Study of Externally Waste-gated Turbine Performance under Steady and Pulsating Inlet Conditions for Improved Turbocharger Matching

By

Wan Saiful-Islam Wan Salim

This thesis is submitted for the award of Doctor of Philosophy (Ph.D.)

Department of Mechanical Engineering

Imperial College London

Buat Ayahanda dan Bonda…

Declaration

This thesis represents my account of the work that I have undertaken over the course of the registration period for this degree. Relevant citations have been included to acknowledge the contribution of others. Parts of the work that has been published in conference proceedings have also been clearly mentioned.

Wan Saiful-Islam bin Wan Salim

Copyright Declaration

Acknowledgements

I wish to record my special thanks my supervisor Professor Ricardo Martinez-Botas for his constant guidance, advice and encouragement throughout the course of this study. Needless to say, the flaws in this thesis whether in fact or style are entirely my own.

My gratitude is also extended to Universiti Tun Hussein Onn Malaysia (UTHM) for funding my studies here at Imperial College London. I would also like to acknowledge the UK Technology Strategy Board (TSB) for funding part of the experimental work carried out in this thesis through the Ultraboost project.

I am forever indebted to Dr Peter Newton, Dr Yang Mingyang and Dr Alessandro Romagnoli for their contribution in assisting me with the experimental work despite their own busy schedules. Peter especially dedicated a lot of his time in helping with the analysis and final write-up of this thesis. My thanks are extended to Dr Apostolos Pesiridis, Dr Srithar Rajoo and Dr Colin Copeland for their invaluable ideas and critical comments. I wish to also acknowledge the contribution of Mr Haminder Flora and Mr Asanka Munasinghe who has been instrumental in setting up the turbocharger test facility and Mr Tariq Rasheed for his assistance in software installations.

I also wish to thank my colleagues, Dr Aman Mohd Ihsan Mamat, Dr Hasbullah Padzillah, Dr Adam Malloy, Dr Johnathan Hey, Dr Clemens Lorf, Nicola Terdich, Balamurugan Gurunathan, Mohd Ibtisham Ardani, Mohd Izzal Ismail, Uswah Khairuddin, Jose Cortell, Marie-Therese Srbik and Maria Barrera-Medrano for their friendship and assistance throughout the duration of my studies. My gratitude is also extended to colleagues outside the turbocharger group for all their help and support throughout the duration of my study here at Imperial College London. My great friend and mentor Dr Vijay Raghavan has always been inspiring and has taught me the conceptual approach to understanding scientific problems. For this, I thank him with a humble heart.

I wish to thank my wife Nor Hafidzah for her love and patience. My children Daniya Kauthar and Muhammad Ikhlas have brought joy to my life and have made my stay in London ever so memorable. This thesis is especially dedicated to my parents. My father Wan Salim Wan Mohd Noor, has always taught me the importance of knowledge and good values. My mother Jariah Md Noh, with her constant love and prayers, has endowed me with the strength to complete this study.

Abstract

The demand for drastic reduction in CO_2 emission among road vehicles has seen downsizing becoming a megatrend in modern engine developments due to its benefits in reducing throttling loss and improvement in engine efficiency. In light of this, turbocharging is seen as one of the key enabling technologies and therefore carries along with it an ever-increasing challenge in terms of system-matching as the device is required to operate in ranges never encountered before. The increasing reliance on 1-D engine performance simulation tools calls for more accurate representation of the turbocharger model. The present study assessed the turbocharger turbine maps for use in commercial 1-D gas dynamics engine code from several aspects, namely the width of the map and the representation of turbine unsteady performance in the virtual environment. Furthermore, the present work assessed the performance of turbine under waste-gated operations. For this, an experimental work has been carried out on a bespoke waste-gated turbine layout over a wide range of operating conditions. The performance of the radial turbine under steady inlet conditions was evaluated for different waste-gate openings, at various points along several speed-lines. Then the unsteady tests saw the turbine performance evaluated at various sets of pulse frequencies, turbine loadings and waste-gate openings. Analysis of this study include the impact of turbine map width on the turbine performance modelling in a commercial 1-D gas dynamics engine simulation software and subsequently the prediction of the engine's performance. This simulation work is carried out based on an actual heavily downsized gasoline engine with a series super-turbocharging system. The study also examined the method of incorporating the effects of turbine unsteady performance under waste-gated and non-waste-gated conditions in the performance maps used in 1-D code and evaluate its impact on the engine performance prediction. The outcome of the study aims at providing a deeper understanding on the unsteady performance of a turbocharger turbine which will lead to improved turbocharger-engine matching methods in the future.

Contents

List of Figures

List of Tables

Nomenclature

Abbreviations

BMEP	Brake mean effective pressure
BSFC	Brake specific fuel consumption
CAHU	Charge air handling unit
cDAQ	Compact DAQ
cRIO	Compact RIO
CTA	Constant temperature anemometer
CVT	Continuously variable transmission
DF	Downsizing factor
DI	Direct injection
EGR	Exhaust gas recirculation
FIFO	First in, first out
FPGA	Field programmable logic array
GDI	Gasoline direct injection
HP	High pressure
IFCE	Fuel conversion efficiency
IMEP	Indicated mean effective pressure
LP	Low pressure
MFP	Mass flow parameter
MFR	Mass flow ratio
NA	Naturally aspirated
NEDC	New European driving cycle
PFI	Port fuel injection
PR	Pressure ratio
PRF	Pressure ratio factor
RPM	Revolutions per minute
RSS	Root sum square
RT	Real-time
SI	Spark ignition
VCR	Variable compression ratio
VGT	Variable geometry turbocharger

Notations

A, B	Hotwire constants
C_D	Discharge coefficient
C_f	Friction coefficient
C_{is}	Isentropic velocity
C_p	Coefficient of pressure
c_p	Specific heat capacity
d_w	Wire diameter
e	Total internal energy
F_a	Material expansion factor
h	Enthalpy
I	Moment of inertia
I_{el}	Electrical current
I_{MFP}	Influence factor
K	Constant
K_S	Loss coefficient
l_w	Wire length
l_{wg}	Waste-gate valve lift
$\dot{m}$	Mass flow rate
Ma	Mach number
N	Rotational speed
Nu	Nusselt number
P	Pressure
Re	Reynolds number
R_w	Wire electrical resistance
s	Entropy
St	Strouhal number
T	Static temperature
T_0	Total temperature
T_{meas}	Measured temperature
U	Rotor tip velocity
U/C_{is}	Velocity ratio
V_c	Clearance volume
V_d	Displacement volume
$\dot{W}_{act}$	Actual power
$\dot{W}_{is}$	Isentropic power
Y	Gas expansion factor
γ	Specific heat ratio
Δ	Difference
η	Efficiency
η_{TS}	Total to static efficiency
η_{TT}	Total to total efficiency
μ	Dynamic viscosity
ρ	Density
τ	Torque

P_0	Total pressure
P_s	Static pressure
Q	Heat transfer rate
R	Universal gas constant
r	Recovery factor

φ	Phase angle
ϕ	Pulse period fraction (duty cycle)
Ω	Amplitude-weighted Strouhal number

Subscripts and Superscripts

‘	Fluctuating parameter
1, 2	Location of measurements
act	Actual condition
avg	Average value
C	Compressor parameter
cold	Cold condition
cyc	Cycle average
exit	Exit
hot	Hot condition
in	Inlet
inst	Instantaneous value
isen	Isentropic condition

max	Maximum value
meas	Measured parameter
norm	Normalized value
opt	Optimum value
pred	Predicted value
QS	Quasi-steady
ref	Reference condition
SC	Supercharger parameter
T	Turbine parameter
US	Unsteady
WG	Waste-gate parameter

Chapter 1 Introduction

1.1 General overview

Modern road vehicles are required to meet stringent emission and fuel economy demands and as a consequence, the optimization of engine performance becomes a crucial process in vehicle development programs. One of the key legislations approved by the European Union and Council is the reduction in tailpipe CO_2 emission to an average of 95 g/km CO_2 of newly registered cars by 2025 through technological advances (The European Commission, 2009).

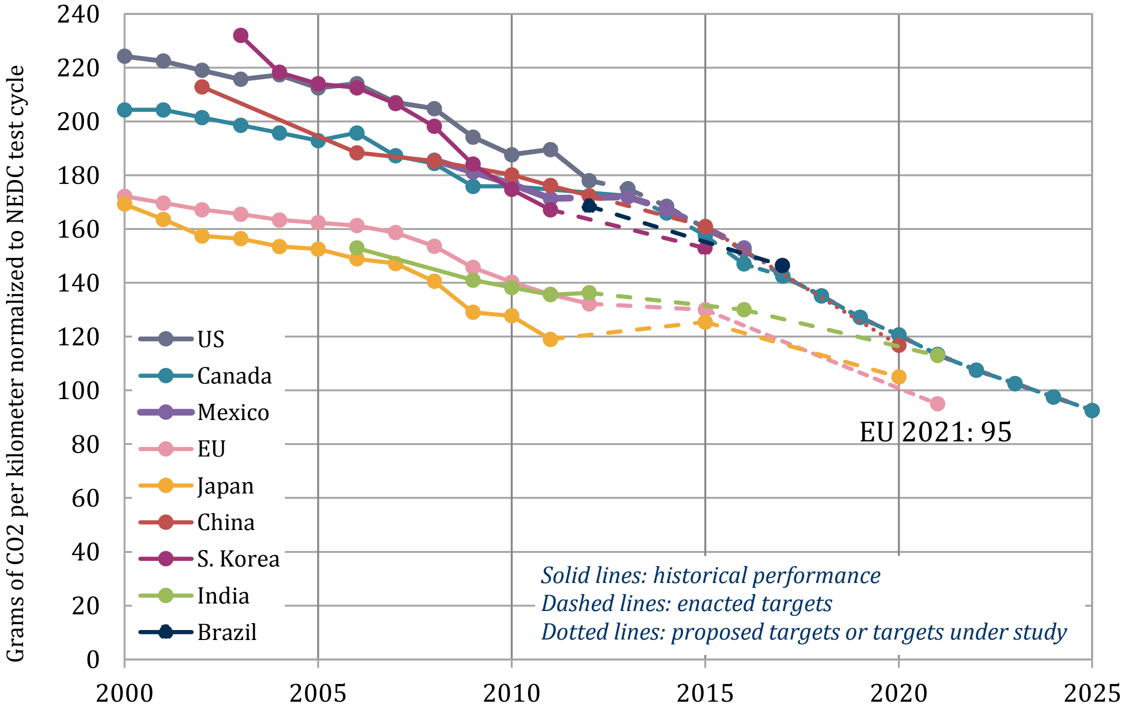

Figure 1.1 Market road map for CO_2 emissions from passenger cars (ICCT, 2014)

Figure 1.1 shows the roadmap to reduction and projected reduction of CO_2 on the New European Driving Cycle (NEDC) for various market fleets across the world from the year 2000 until 2025 (ICCT, 2014). CO_2 emission indicates a measure of how much fuel a vehicle consumes and therefore reflects on the efficiency of the engines. The figure reflects the commitment from the industry whereby steady improvements has been made towards achieving the 2015 target. Higher rate of improvement is required for manufacturers to achieve the 2020 targets (2025 for the US). Clearly, pursuing such a steep progress calls for more rigorous approach in engine development. Figure 1.2 shows that several manufacturers have already made progress towards achieving the set targets for 2020 (ICCT, 2014). This improvement comes either through the introduction of plug-in hybrid and electric vehicles or via the route of boosting and optimization of various engine components and controls.

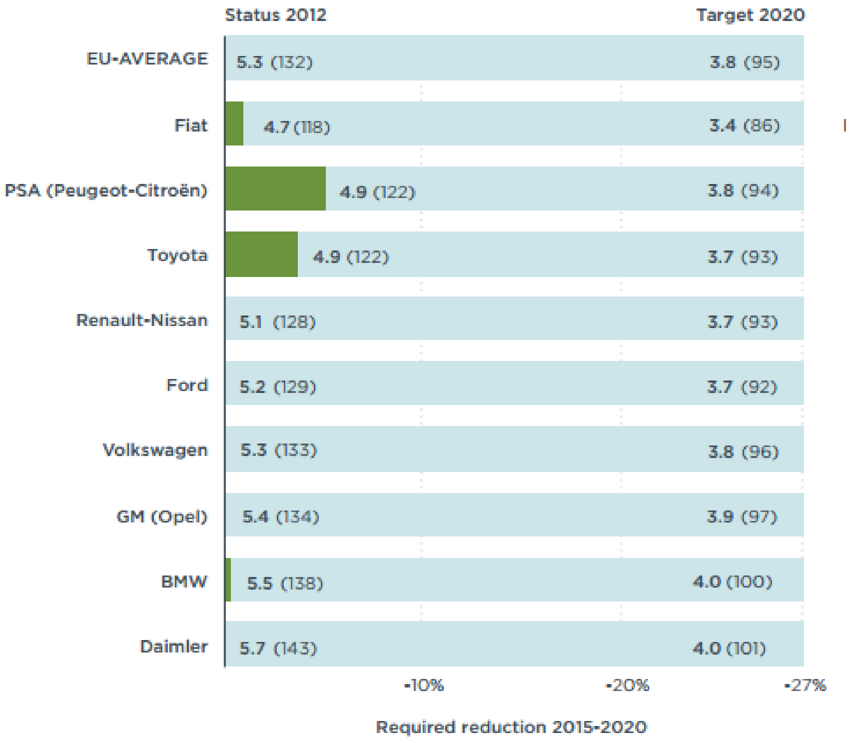

Figure 1.2 Average 2012 fuel consumption and CO_2 emission level of main EU passenger car manufacturers shown with target for 2020 (ICCT, 2014)

While the current state-of-the-art have seen growing trends in development of alternative low carbon technologies such as hybrid fuel cell and electric vehicles, the conventional internal combustion engine remains at large the key form of road vehicle propulsion system. For these propulsion systems, CO_2 emissions relate directly to the capacity of the engine. Therefore, manufacturers are actively reducing the size of their engines, replacing them with more efficient smaller units for a specific vehicle platform.

The choice of engine operating cycle namely fuel selection also dictates the downsizing strategy. While the CO_2 reduction in the European Union shown in Figure 1.1 above is largely contributed by Diesel-based engines, recent years have seen the development of fuel economy improvement technologies focusing on gasoline engines. These technologies include gasoline engine downsizing, gasoline direct injection (GDI), exhaust gas recirculation (EGR), variable valve trains, controlled auto-ignition (CAI) and friction reduction (Fraser et al, 2009). The demonstrator engine developed by Fraser et al (2009) has managed a 15% potential reduction of CO_2 through adoption of the technologies mentioned above with a further 10% possible reduction when a start-stop function is included.

Having a smaller engine helps improve fuel economy by reducing pumping, friction and heat losses within the engine architecture. In addition, a smaller engine would reduce the overall volume and thus it's overall mass. Therefore, the engine compartment within a vehicle platform can be minimized, resulting in a more compact and lighter vehicle. On the other hand, a smaller engine will also exhibit depreciation in the engine torque output. To compensate this inherent loss in performance, forced induction systems are introduced and the efficiency of the small engine is enhanced by "boosting" the intake air. This would increase the volumetric efficiency of the engine and raise the maximum torque output to a level that is similar to its larger counterpart. This exercise of seeking the same level of performance from a smaller engine with a specified larger counterpart is known as "engine downsizing". Forced induction systems such as turbochargers play a vital role in engine downsizing and a lot of research is being carried out to improve the design and selection of the components involved as well as to control and optimize the engineering package.

1.2 The Concept of Engine Downsizing

A well accepted definition of engine downsizing is the method of changing the speed and load operating point of an engine by replacing a large engine with a smaller engine. The smaller engine is boosted to enable operation at a higher specific load to maintain the same torque output. At present, several developers have demonstrated successful engine downsizing up to 50% the displacement of a comparable naturally aspirated (NA) version while achieving the same full-load torque output with significant improvement in fuel economy (Lumsden et al, 2009). The term "down-speeding" is also widely used referring to the ability of the engine to operate at higher gear ratios (low speeds) as a result of the high brake mean effective pressure (BMEP).

Forced induction systems play a central role in the development of downsized engines. For an engine to achieve its target performance output, the process of selecting, matching and control of a boosting system to the engine are crucial in the development process. These devices are required to deliver the high flow capacity at high pressure ratio as demonstrated by Arnold et al (2005) and Lumsden et al (2009). Salamon et al (2012) reported that air pressure charging of

3.5bar is required to boost a 2.0 litre engine to achieve 35 bar BMEP for a 60% level of downsizing. At these conditions, the technical challenges involved are vast. A more aggressive downsizing practice or those carried out on larger engines will inherently require higher boost pressure. This brings about other issues such as charge-air cooling, high exhaust gas temperatures, high cylinder pressure, knock mitigation and control, vehicle drivability, mechanical and thermal stresses. In order to achieve sufficient boost from the boosting systems, larger turbochargers which operate at extremely high speeds and able to withstand higher temperatures will be required.

1.3 Forced Induction Systems and Turbochargers

As mentioned earlier, forced induction system play a central role in engine downsizing development to provide the necessary boost pressure. Forced induction technologies are nothing new as far as the automotive engines are concerned. Spark ignition (SI) engines has seen the use of turbochargers or superchargers in niche markets and applications such as in performance and racing vehicles as well as in several passenger cars and it has become difficult to find successful NA compression ignition engines in the market today.

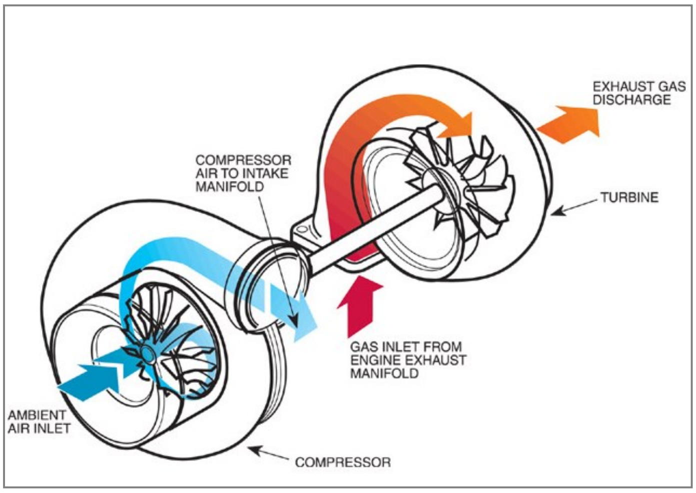

Figure 1.3 Basic components of a turbocharger (Raunekk & Stonecypher, 2009)

Forced induction systems are methods to increase the mass flow rate of air entering the combustion chamber in order to increase the efficiency of the engine. The types of forced induction systems most widely used in automotive engines include turbochargers and superchargers. The present work focuses on the analysis and performance of the former. A turbocharger, shown in Figure 1.3 is a turbomachinery device which is connected to an internal combustion engine at the exhaust manifold to extract the energy available in post-combustion exhaust gas and uses it to increase the intake air pressure of the engine.

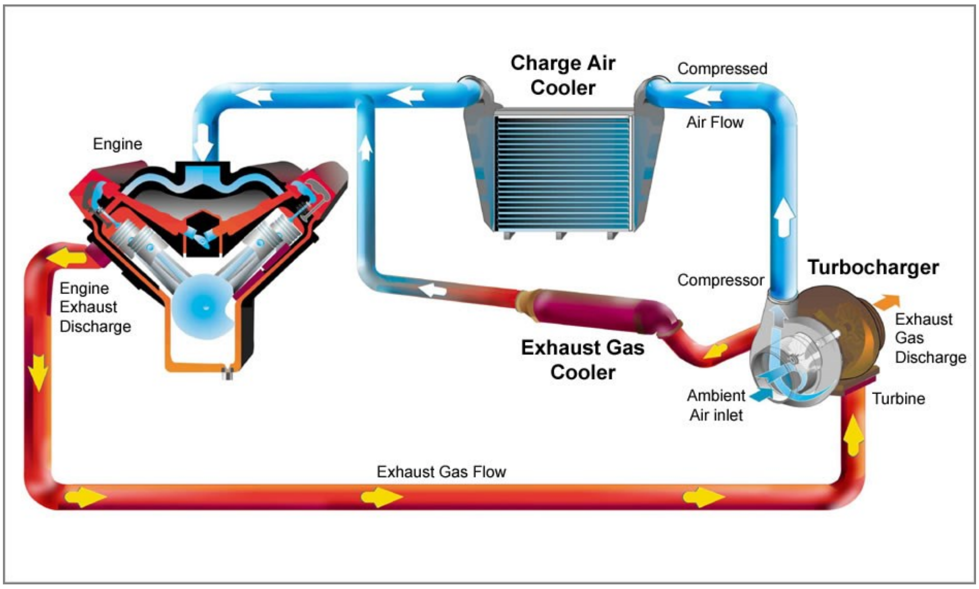

Figure 1.4 Schematic diagram of a turbocharged engine showing the flow of hot exhaust gas and cold intake air (Honeywell, 2009)

1.3.1 Turbochargers

Figure 1.4 shows how the turbocharger is connected to the engine. The pressure energy available in the exhaust gas is utilized to drive a turbine, which in turn drives an air compressor. The compressor increases the intake air density to a higher-than-ambient value, allowing the combustion to take place at a higher volumetric efficiency. Also shown in the figure is the presence of a charge air cooler seen as a rectangular box located between the compressor exit and the intake manifold. The role of the charge-air cooler is to reduce the temperature of the compressed air thereby increasing its density. This will result in higher air mass flow rate entering the engine cylinder.

Figure 1.5 shows the work available in ideal exhaust process in an internal combustion engine on a pressure versus volume (p-V) diagram. V_d and V_c denotes the swept volume and clearance volume of the combustion chamber. The hatched area represents the energy available from the exhaust blow-down process (area 1-2-3) and the piston work done to discharge the remaining exhaust gas (area 3-4-5-6), which would otherwise be unused and released in an open engine cycle. Turbochargers fundamentally exploit this unused energy to provide higher pumping power for the engine thereby increasing the net work produced over the cycle.

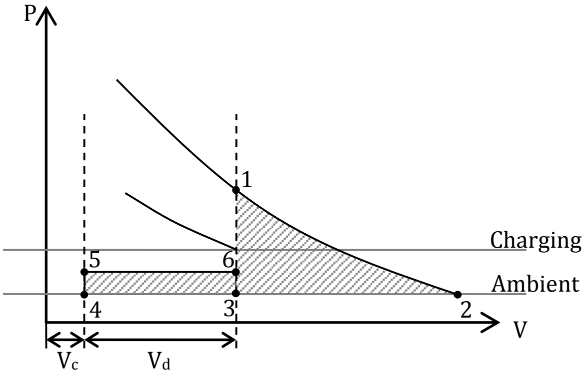

Figure 1.5 Work available from an ideal exhaust process

Superchargers in its current definition[1] are compressors which are connected and driven directly by the engine crankshaft. As a consequence, the potential power increase may be slightly lower in comparison with turbochargers, which have the luxury of utilizing the 'free' pressure energy from the exhaust gas flow. On the other hand, superchargers are superior to turbochargers in terms of their transient response. Since the device is directly connected to the engine crankshaft, there is virtually no lag involved and the rate of torque-climb would be identical to that of a NA engine.

The main components of a turbocharger shown in Figure 1.3 include a turbine, a compressor, a shaft and bearing housing. In high speed applications such as turbochargers, centrifugal compressors are normally used due to their flow capacity. The compressor wheel or the rotor is enclosed in a volute forming forms a closed passage between the atmosphere and the intake manifold. The shaft which connects the compressor to the turbine is housed in a bearing unit which can either be of oil or of ball type. Cooling is provided to maintain the suitable temperature for the shaft and lubrication system.

The turbocharger turbine comprises of a rotor which is housed in a volute. The rotor can be of axial, radial or mixed flow type. Some designs may include guide nozzles at the inlet of the rotor. The inlet end of the turbine volute is connected to the exhaust manifold of an engine and is therefore made of high temperature resistant materials.

---

[1] The general term "supercharging" was defined as the introduction of air into an engine cylinder at a density greater than ambient (Watson & Janota, 1982). However, in its contemporary definition, the term supercharger refers to mechanically driven compressors which draw its power from the crankshaft of the engine.

1.3.2 Boost control and the waste-gate system

Turbocharger performances has always been designed and tested as separate units and its interaction with the engine is often analysed in the matching process. Often, the installation of a turbocharger on an engine is accompanied by additional boost control mechanisms such that the two machines operate in harmony with each other. A variety of boost control mechanisms exist in with each having their own specific tasks. Variable geometry turbines for instance are mainly used on diesel engines to achieve good transient response at low and medium range engine speeds. Turbocharged gasoline engines which tend to operate over wide speed ranges often utilize the use of waste-gate valves for boost control. This device is found to be effective due to its relatively low cost and capable of operating in high temperature environments. These valves may be incorporated into the turbine housing designs (internal waste-gate) or as a separate unit and linked to the turbine flow via additional plumbing (external waste-gate valves). In internal waste-gates, the boost is controlled pneumatically by actuating a flapper valve connected to the actuator via a crank arm. External waste-gates are installed with installed upstream of the turbocharger turbine to bypass the exhaust gas flow around the turbine stage. The flow is reintroduced into the exhaust stream downstream of the turbine.

1.4 Research Motivation

A turbocharger turbine performance which characterises its swallowing capacity and efficiency is represented by a set of data called maps. These performance parameters are measured in turbocharger test facilities at various ranges of shaft speeds and pressure ratio across the device. Therefore, the range of data in a typical turbine map is limited by points of experimental measurements. Besides indicating the performance of a particular turbine, the map may also be used in predicting the performance of the engine which the turbocharger is matched to through computational simulations. The calculations performed by these codes range from mean-value models to full 3-D computational fluid dynamics. Nowadays, advanced 1-D engine gas dynamics codes such as GT-Power developed by Gamma Technologies, Ricardo Wave by Ricardo and LES by Lotus Engineering are capable of predicting the engine performance along with wave dynamics within the system layout at relatively low computational cost, thus making it favourable among engine developers.

1.4.1 Turbine map prediction in 1-D gas dynamics engine simulation software

In most commercial 1-D gas dynamics codes, the turbocharger maps are entered in engine simulation codes in a form of look-up tables. During a simulation of a turbocharged engine, it is not uncommon for the operating conditions of the running engine or the turbocharger to extend beyond the points that are obtained from experiments. This will numerically destabilize the solution and lead to errors in the simulation output. To prevent this, the maps have to be extended to include the range of operations that are beyond those in the data range. In other words, there is a need for these maps to be pre-processed prior to a simulation such that turbocharger component in the software reads these extended maps rather than the original user-input versions. The current method of map prediction used by commercial engine simulation software is based on various curve fitting techniques which are used to interpolate and extrapolate the original data. While extending the range of the map is needed to ensure the stability of the simulation, the map extension methods are developed based on limited range of experimental data, hence the need for experimental validation against wider data range. Therefore, the current study aims at evaluating the capability of turbine map extrapolation method employed by mainstream 1-D gas dynamics engine simulation software, namely GT-Power. It is crucial to point out that the reliability of any map prediction methods is only as good as the experimental data that validates them. In most cases, the range of empirical data is small due to the lack of accurate measuring tools at extreme operating ranges; an issue addressed by Martin et al (2009). The majority of current models fall short in this aspect. The availability of test facilities which yield a wider spread of data range means that existing map extrapolation methods can be evaluated.

1.4.2 Impact of boost control mechanism on turbocharger behaviour

Technological advancements in the production of key enabling technologies such as boosting systems, direct fuel injection and intelligent valve-trains has made downsizing a megatrend in automotive engine developments. Smaller, more efficient engines are being built with increased levels of boost. As such, the control of the boosting systems becomes more crucial. In a highly boosted gasoline engines, the boost produced by turbochargers are regulated by means of exhaust gas bypass systems or waste-gates. Previously, it was assumed that the interaction between the flow through the turbine and the waste-gate during operation has minimal impact on the performance of the boosting system. Recent studies on internally waste-gate turbines have revealed that this assumption was inaccurate and that there are indeed, interactions between the two devices (Capobianco & Marelli, 2007). This provides the impetus for an investigation to be performed on a turbine system with an external waste-gate bypass system. This part of the study aims to determine experimentally the effect of external waste-gating on the performance of a turbine. The study will allow better understanding of how a turbocharger turbine behaves under such conditions, thus improving turbocharger matching process and boost control methods.

1.4.3 Turbine behaviour under pulsating inlet conditions

Another aspect worth discussing with regards to engine downsizing is that the reduction in engine capacity is usually accompanied by the reduction in the number of engine cylinders. As a consequence, the pulsating nature of the exhaust gas becomes more prominent. This implies that the inlet of the turbine will be subjected to a highly pulsatile flow of various pressure and frequency levels. With this in view, the measurement of turbine characteristics must also account for the effect of pulsating inlet conditions. This scenario serves as another motivation for research carried out in this thesis. In addition to varying inlet pressure and pulse frequencies, the characterization of the turbine also has to include the effect of waste-gate openings, which adds another dimension to what is already a complex system.

1.4.4 Performance prediction of a heavily downsized boosted engine

Modern engines have become more complex in design due to incorporation of various technologies within the system. The use of computational tools to predict the performance of an engine has become increasingly popular due to the advantages which they can offer over tradition methods in terms of development time and cost. Moreover, these control-based engine simulation codes allow an engine developer to model and assess at an early stage the interactions between the engine components. In a downsized engine, the interactions include those between the engine and the boosting system. To achieve accurate prediction of the engine performance, it is paramount for the boosting system performance to be accurately represented within the computational environment. This can be assessed by evaluating the performance of the boosting system predicted through computations. The application aspect of the present study is achieved by way of implementing engine performance simulations based on an actual heavily downsized engine which employs an advanced boosting system, which are used in this study.

1.5 Thesis Objectives

The aim of the present work sets out to study, implement and model novel boosting systems to enable aggressive downsizing of internal combustion engines. This will be carried out by means of experiments and simulations using state-of-the-art methods and tools including an advanced turbocharger testing facility and engine simulation software. As part of the turbocharger boost control elements, the effect of a waste-gate valve on the characteristics of the system is also considered in the study.

The following objectives have been laid down for this thesis.

1. The first objective set for this study is to evaluate the effect of turbine map width on map extrapolation procedures commonly used in turbocharger matching and explain its effect on the prediction of engine performance.
2. The second objective of the thesis is to develop an experimental method to establish and explore the effect of an external waste-gate on steady turbocharger turbine performance.
3. The third objective is to investigate the unsteady pulsating flow performance of a waste-gated turbine experimentally and provide an insight into the effect of various operating parameters (pulse frequency, turbine loading and degree of waste-gate opening) and investigate how it can be represented in 1-D engine simulation codes.

1.6 Thesis Outline

The content of this thesis is distributed within six chapters as described below:

Chapter 1: Introduction

This chapter presents the background and overview of the research at hand and explains the rationale behind the work carried out. The objectives and scope of work are also laid out and the structure of the thesis is explained.

Chapter 2: Literature Review

Various publications and previous work related to the present study are discussed and reviewed in this chapter. These include discussions on various boosting systems adopted in engine downsizing, turbine performance modelling and map extension methods. This chapter also reviews the previous work related to turbine performance under various operating conditions.

Chapter 3: Test Facility and Steady State Turbine Performance

This chapter describes the experimental facility and method of measuring the turbine performance under steady inlet conditions and its results analysed and discussed. In addition to the standard steady state conditions, the experiments to measure the performance of a waste-gated turbocharger turbine was also performed and the findings of this work are presented and discussed. Besides this, the chapter describes the characterization of an external waste-gate valve used in the experiments. The evaluation of a map extrapolation method employed in 1-D gas dynamics engine simulation code is also presented in this chapter. This involves the comparison between extrapolations carried out on performance maps with wide and narrow experimental data range.

Chapter 4: Turbine Performance under Pulsating Inlet Conditions

The method of testing a waste-gated turbocharger turbine under unsteady pulsating inlet conditions is described in this chapter. This includes the description of the various instrumentation and calibration procedures used in the experiments. The effects of waste-gate area opening on the unsteady turbine performance are also discussed in the chapter. Then, the level of unsteadiness in the turbine behaviour under pulsating inlet conditions are analysed based special dimensionless parameters. Also included in the chapter is the description of a simulation work conducted to predict performance of waste-gated turbine under pulsating inlet conditions. This part of the study was performed using a commercial 1-D simulation code.

Chapter 5: One-Dimensional Gas Dynamics Simulation of Engine and Turbocharger Performance

This chapter primarily discuss the simulation work carried out using the turbine performance maps obtained from the experimental work. A description on the commercial GT-Power engine simulation software used for this investigation is provided. Then, the impact of map width on the prediction of engine performance by the 1-D engine simulation code is presented and discussed in the chapter. Another part of this chapter describes the simulation work based on an actual boosted downsized engine that deploys a dual-stage boosting system comprising of a supercharger and a turbocharger. Here the performance targets and the layout of the engine and the individual boosting devices are described. This includes a supercharger unit and a turbocharger turbine that was experimentally tested at Imperial College. The simulation is carried out to predict the performance of the engine and the boosting system. In discussing the simulation output, a new method of averaging the fluctuating pressure ratio is proposed and described in the chapter. Finally, 1-D calculations carried out to compare the impact of different waste-gate modelling methods on the prediction of turbocharger performance on the engine is reported.

Chapter 6: Conclusion and Future Work

The final chapter of the thesis highlights the significant findings in the thesis and suggests recommendations for future work.

Chapter 2 Literature Review

2.1 State-of-the-art Engine Downsizing Technologies

Over the years, many efforts have been made to address the challenges faced by automotive engine developers in increasing the efficiency of the internal combustion engine. In combination with other key technologies, downsizing offers the most practical short to medium term measure to drastically reduce CO_2 emissions and improve fuel economy of road vehicles (Walzer, 2001, Leduc, 2003 and Petitjean, 2004). In real world driving scenarios or representative drive cycles such as the New European Drive Cycle (NEDC) (Barlow et al, 2009), the operating points of an engine falls mostly in the low-speed and low-load regions where fuel economy is generally lower. This low efficiency or high brake specific fuel consumption (BSFC) results from friction and, in the case of SI engines, throttling losses (Kleeberg et al, 2006). Reducing the swept volume of the engine will shift the operating points of the load-speed curve to higher efficiency regions of the BSFC by reducing pumping and friction losses. However, this has to be done without sacrificing the performance of the engine. Therefore, it is necessary for the reduced swept-volume engine to produce torque characteristics on par with its larger counterpart. In order to achieve this, the brake mean effective pressure (BMEP) has to be increased, usually by means of boosting the amount of air being delivered to the combustion chamber. The method of reducing the capacity of an engine while maintaining its performance is called "downsizing" which has now become a megatrend in current engine developments and is predicted to continue to be so in the near future. In order to evaluate the level of downsizing, it is inevitable that the small engine be compared to a larger naturally aspirated (NA) counterpart thereby establishing the definition of the *downsizing factor* (*DF*) as follows:

$$DF = \frac{V_{d,NA} - V_{d,DS}}{V_{d,NA}} \quad \ldots (2.1)$$

where V_d is the engine displacement (swept volume) and the subscripts NA and DS refer to "naturally aspirated" and "downsized" respectively (Turner et al, 2014).The principle of downsizing is explained and demonstrated by several authors such as Walzer (2001), Leduc et al (2003), Lecointe and Monnier (2003), Clenci et al (2007) and Königstein et al (2008). Over the years, many downsized engines have been developed and several examples are reported by Lumsden et al (2009), King et al (2012) and Salamon et al (2012).

Turner et al (2005) mentioned downsizing as one of the key technologies for improving fuel economy of internal combustion engines and discussed several other key technologies. The authors also discussed the compression ratio limit as the main issue associated with highly downsized, high BMEP engines. The high propensity of the air-fuel mixture to reach the self-ignition limit before the actual ignition process leads to occurrence of engine knocking. This in turn limits the compression ratio of an SI engine hence preventing higher thermal efficiencies being achieved. Therefore, engine knocking has to be supressed by increasing the knock resistance of the fuel (Edson, 1962) and/or that of the design of the engine itself. The knocking phenomena in multi-cylindered engines was investigated by Leppard (1982)who discussed the randomness of knock events between individual cylinders and found that reducing this variation would lead to lower octane number requirements for SI engines. Investigation by Muranaka et al (1987) revealed that for a pre-mixed SI engine the improvements of thermal efficiency, by increasing engine compression ratio, are limited primarily by capability of a combustion chamber to remove heat (cooling loss) and excess unburned fuel. In addressing the key features and technologies for development of downsized turbocharged GDI engines, Bandel et al (2006) explained the different types of knock events and auto-ignition phenomena that occur inside the combustion chamber of high BMEP engines. Besides conventional knock which is normally triggered by advanced spark timing, irregular combustion is more unpredictable and occurs from different sources and locations. Advanced engine management systems (EMS) were suggested by the author to manage these phenomena and enhance low end torque of the engine. Other technologies suggested for reducing knock include variable compression ratio (VCR), exhaust gas recirculation (EGR), turbo-expansion and novel turbocharger technologies (Turner et al, 2005).

In the attempt to improve fuel economy of turbocharged engines, it is necessary for the boosting strategy to be accompanied by other technologies. Bandel et al (2006) evaluated the combined effects of technologies for efficiency improvements of gasoline engines and boosting as highlighted in Figure 2.1. The work demonstrated that besides driving pattern, fuel consumption is also highly influenced by load profile of the engine, which is determined by the engine displacement, the gearbox and overall vehicle size. Downsizing by reducing the displacement and downspeeding by having longer drive ratio enables the shift of the load profile to better fuel consumption regimes. The combined effects of advanced gasoline engine technologies and boosting was discussed. The work demonstrated a 15% improvement in fuel economy over the NEDC by downsizing a 2.2 litre NA to a turbocharged 1.8 litre GDI using homogeneous DI, advanced cam phasing and a single scroll turbocharger. The turbocharged GDI was comparable to a Diesel engine in terms of engine efficiency at medium to high vehicle speeds.

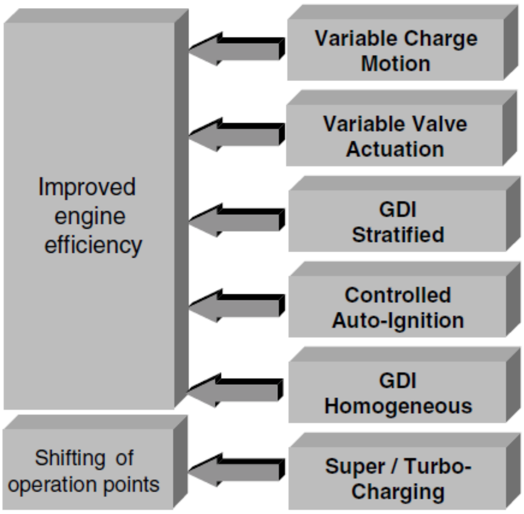

Figure 2.1 Types of technologies for improving fuel economy of gasoline engines (Bandel et al, 2009)

The technical challenges for advanced boosting technologies were addressed by Fraser et al (2009). The comparison of performance in terms of BMEP using state-of-the-art technologies was made along potential improvements as shown in Figure 2.2. Five main technical challenges needed to be met in order to achieve the target performance level (35 bar, peak BMEP). These include combustion limitations, low speed torque, transient response, combustion chamber geometrical layout and part-load fuel economy. In gasoline engines, the role played by direct injection (DI) combustion system in reducing knock tendency by way of reducing charge air temperature was presented. Compared to the conventional port fuel injection (PFI) system, the cooler gas temperatures in the cylinder of DI combustion systems allow for higher compression ratios and therefore, higher thermal efficiency. The authors pointed out that a potential increase of full load BMEP by up to 60% and a 10 to 17% improvement in fuel economy over a drive cycle is obtainable with use of recent technologies such as gasoline direct injection (GDI), exhaust gas recirculation (EGR), variable valve trains, controlled auto-ignitions and friction reduction. It was also demonstrated that for a greater degree of engine downsizing, the use of a single charging unit is no longer sufficient. This is partly due to the performance being restricted by the availability of the exhaust energy at low engine speeds as well as the width of the compressor operating range. Additional charging methods can be incorporated, including the use of multi-stage charging systems with several layouts shown in Figure 2.3. The boosting systems include the use of a combination or combinations of turbocharger and superchargers which can be mechanically or electrically driven.

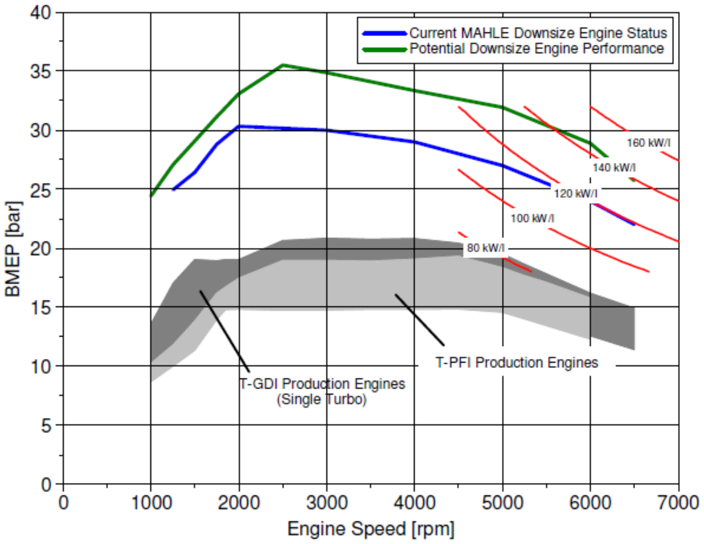

Figure 2.2 Full load performance of gasoline downsized engine (Fraser et al, 2009)

In order to explore the limits of gasoline engine downsizing, Leduc et al (2003) demonstrated through simulation that for the same platform, downsizing a 1.6 litre engine to a 50% level can reduce fuel consumption by as much as 18% on the NEDC cycle, with high benefits seen at near-urban driving conditions. At high speeds such as motorway driving, the benefit of downsizing diminishes. The authors went on to demonstrate the use of the two main driving technologies, namely GDI and turbocharging along with advanced valve timing and combustion systems to attain 80 kW/l specific power output and 175 Nm/l specific torque, which corresponds to 22 bar BMEP.

2.2 Boosted Downsized Engines

Walzer (2001) discussed the progress made in terms of technology development and future development of vehicle powertrains. It was mentioned that future downsized gasoline engines will require boost up to 2.5 bar at low loads and operating at low compression ratio at high loads. Part load BSFC for a 50% downsized boosted 1.5 litre engine may be reduced by 25%. The use of electromechanical type, fully variable valve trains was predicted to improve fuel economy by 15 to 20% through reduction of throttling loss. The new technologies introduced for Diesel engines include fuel injector systems, EGR control systems and catalysts for NOx reduction and particulate filter regeneration systems. The role of future intelligent drive trains, alternative fuels and hybrid and fuel cell systems in future powertrains was also described by the author.

To explore the potential of a heavily downsized turbocharged engine, a demonstrator 1.2 litre three-cylinder direct injection gasoline engine with a single and a two-stage turbocharging was developed at MAHLE Powertrain and was reported by Hancock et al (2008) and later by Lumsden et al (2009). The two-stage layout is shown as configuration (B) in Figure 2.3. The performance of the engine here was benchmarked against a larger 2.4 liter V6 port-fuel-injected (PFI) naturally aspirated counterpart translating to 50% degree of downsizing. A high pressure turbine was used at low engine speeds to provide better transient response whereas a low pressure turbine was used at high engine speeds to produce maximum power output. Performance characteristics such as the mean effective pressures and specific fuel consumption at partial and full loads were also evaluated and have shown significant improvements. Despite the torque target being surpassed for the most of the operating range with the use of the two-stage boost system, the authors admitted that there is room for improvement in terms of transient response characteristics especially at throttle-snap condition.

King et al (2012) described the development of a 50% downsized GDI engine for use in C-segment passenger car. The three-cylinder 1.0 litre engine features a fixed geometry turbocharger, start-stop technology, electric supercharger and electric turbo-compounding unit. Fuel consumption was reduced by 27% compared to the baseline 2.0l engine through powertrain downsizing with a further 4% reduction achieved through use of a higher gear ratio (downspeeding). Further improvements in fuel economy were obtained by means of micro-hybrid system.

An extreme downsizing exercise was carried out on a 2.0l and was reported by Salamon et al (2012) and Turner et al (2014). The aim was to achieve a BMEP output equivalent to a modern NA 5.0 litre V8 engine translating to a 60% downsizing factor. This extremely downsized engine adopts a series supercharger-turbocharger forced induction system which is capable of providing up to 3.5 bar (abs.) boost level. Crucial to any downsizing practice, the engine was set to obtain a 35% reduction in tailpipe CO_2 at a vehicle level, relative to its NA counterpart over the NEDC cycle. This translates to approximately 23% of fuel economy at the engine level. Besides boosting, other state-of-the-art technologies including a combination of GDI and PFI system, variable valve timing, water-cooled charge-air coolers (CACs) and a highly knock tolerant combustion chamber. The engine features a clutched supercharger unit at the HP stage and a fixed geometry turbocharger at the LP stage. The operation of the boosting system was regulated by means of the turbine wastegate and the HP bypass valve. In addition, the drive ratio of the supercharger unit can also be set providing an extra degree of freedom over the control of the boosting system.

2.3 Forced Induction Systems as Key Enabling Technology

A direct effect of boosting on the performance of an internal combustion engine is the reduction in pumping losses. Without forced induction, the air entering the combustion chamber is always going to be limited due air being inducted at atmospheric pressure. Boosting allows the air to be compressed to a higher density, hence resulting in more power. This principle of increasing intake air density through, or boosting, to increase the power output of a combustion engine has been well understood and put to practice (Heywood, 1988). Reports on the use of boosting methods to increase the performance of passenger car engines can be found even at the dawn of the 20th century. For instance, Gregg (1928) studied the effect of supercharging on the performance of passenger car engines and showed that the power can be increased up to 59% using a chained-driven, positive displacement supercharger. From the chronological perspective, the efforts to incorporate turbochargers in automotive engines were well on the way ever since Buchi introduced the device before World War I. An article by Birman (1954) provides an insight into the early works on technological developments of turbocharging. The author discussed the technological challenges associated with turbocharging at the time, pointing out the impacts of turbocharging on engine thermal efficiency, the need for efficient turbines and compressors at high pressure ratios, the issue of pre-turbine temperatures, in-cylinder gas scavenging and the issue of pulse phasing in multiple-cylinder reciprocating engines. In addition, the author correctly predicted an increase in the use of turbochargers in small engines as a result of improved manufacturing techniques for mass production of turbocharger units.

Since then, turbocharging has seen extensive use in high performance vehicles and automobile racing. Mezger (1978) reported on the application of turbochargers in various Porsche race engines such as those used in the Lemans series and discussed several issues associated with turbocharger matching and drivability of these engines. In addition, the transfer of turbocharging technologies to their high performance passenger cars was also discussed. The use of waste-gates to control the boost pressure along with the compressor pressure relief valves to maintain compressor rotational speeds at closed throttle positions or during vehicle braking were also described. What is interesting was the prospect of turbocharging as a means of reducing emissions and improving fuel economy was put forth. In this regard, a 20 to 30%

fuel consumption reduction was suggested albeit at the cost of a 10% increase due to reduction in compression ratio. Nonetheless, it is evident that, the idea of using boosting technologies to improve fuel economy is nothing new.

The work by Schweikert and Johnson (1973) demonstrated the potential of improving fuel economy through boosting. Evaluation was done on a multi-cylinder turbocharged engine with exhaust gas recirculation (EGR) operating at steady state, part-load conditions over several engine speeds. The finding of this work was that turbocharging a small engine can provide 20% improvement in fuel economy whilst maintaining the same power output and emission levels similar to those of a larger NA engine. In addition, the overall engine weight can be lower than the NA counterpart.

In the historical context, the energy crisis in the early 70's was the main driver behind the efforts to turbocharge gasoline engines as an alternative to larger NAs. The extensive use of turbochargers in gasoline engines was forecasted by Watson (1979) with the limited manufacturing technique for mass production of turbochargers being the only constraint at the time. The investigation by Watson et al (1983) was among the pioneering work demonstrating the application of turbocharging for fuel economy in SI engines. The work indicated that it is possible to replace a 2.0 litre NA engine with a turbocharged 1.3 litre engine and achieve similar performance with 11 to 22% potential fuel reductions. Boosting enables an increase of peak torque and power output by up to 40%.

Schruf and Mayer (1981) demonstrated the use of pressure-wave charging to increase torque at low engine speeds for a Diesel engine. The method of engine downsizing and downspeeding by reducing the swept volume and reducing overall numerical gear ratio respectively were laid out by the authors. The outcome of this investigation led to further work by Mayer et al (1982) which revealed a potential improvement of 20 to 25% in fuel economy depending on the drive cycles. More recently, simulation based study by Wetzel (2013) revealed the potential of downsizing and downspeeding in improving fuel consumption over the NEDC through various boosting strategies.

Wirth et al (2000) studied the combination of DI engines with other fuel-saving technologies including charging the intake air via forced induction systems. The author mentioned downsizing via turbocharging as one of the most effective methods for fuel economy improvement but pointed out the issue of transient response and real-world driving characteristics as the major obstacle in such development. Nonetheless, it was shown that the part-load transient response of a turbocharged engine can benefit from different modes of DI system operating modes. This is achieved by extending operation in stratified mode to higher IMEP regions with the NOx emission as the primary limiting factor.

Analysis on the effect of turbocharging on fuel economy of passenger cars over a ten-year period between 1992 and 2002 was carried out by Petitjean et al (2004). This investigation by Garrett Engine Boosting Systems at Honeywell International, Inc. compared the fuel consumption of turbocharged to non-turbocharged engines with the same power output. The work revealed that the CO_2 levels of turbocharged direct injection Diesel engines were 30 to 50% lower than gasoline engines for a given vehicle curb weight which drives the need to improve the fuel economy of the latter. For gasoline engines with the same power outputs, turbocharged engines offer up to 12.5% reduction in fuel consumption for a given rated power. It was also shown that turbocharged engines are 30 to 50% smaller than NA engines for the same power output. Another noteworthy outcome of the work was that it depicts the flexibility of a turbocharged engine in terms of the range of its application. A base engine with different levels of boosting is able to provide a wide range of power output to cater for more than one family of vehicles, thereby serving as potential for reducing development and manufacturing cost.

The need to limit the compression ratio in boosted engines has always been the critical factor which limits the thermal efficiency of boosted engines. Stokes et al (2000) introduced the lean boost system via direct injection and homogeneous lean operation to allow higher compression ratios in gasoline engines. Lake et al (2004) adopted this concept for a boosted three-cylinder 1.12 litre engine using a variable nozzle turbine and achieved 20% fuel economy benefit over the NEDC with a comparable 1.6 litre NA vehicle.

2.4 Multistage Boosting

As the level of downsizing increases single-stage boosting systems are no longer able to deliver an adequate amount of air for the entire range of operation. Thus, there is a shift towards using multiple stage boosting systems. Multi-stage boosting involves the use of more than one boosting system with many variations of system types, combinations, sizes, layouts and operations. Description of these variations is given by Martinez-Botas et al (2011). Often, the choice of individual boosting devices in a multi-stage system is made such that they complement each other during operation and mitigate each other’s weakness. For instance, a supercharger offers lag-free performance and is able to deliver high boosts at low engine speeds, whereas a turbocharger offers boost at higher engine speeds where more pulse energy are available.

Consequently, a combination of the two systems should be able to accommodate a wider range of boost demand from an engine.

Fraser et al (2009) laid out several options of multiple-stage boosting systems to deal with this shortcoming as shown in Figure 2.3 (a). For the 1.2 litre downsized engine used in their work, it can be seen in Figure 2.3 (b) that a two-stage turbocharger system proved to be superior in terms of delivering the BMEP compared other systems in comparison, namely a single-stage turbocharger system and a two-stage electric supercharger with variable torque enhancement system (VTES) and a low pressure turbocharger. The two-stage turbocharger system utilizes a high-pressure (HP) unit for low engine speed operations and a low-pressure (LP) unit for high speed operations. Turbine bypass valves (waste-gates) are used to control the turbocharger speeds and prevent over-speeding.

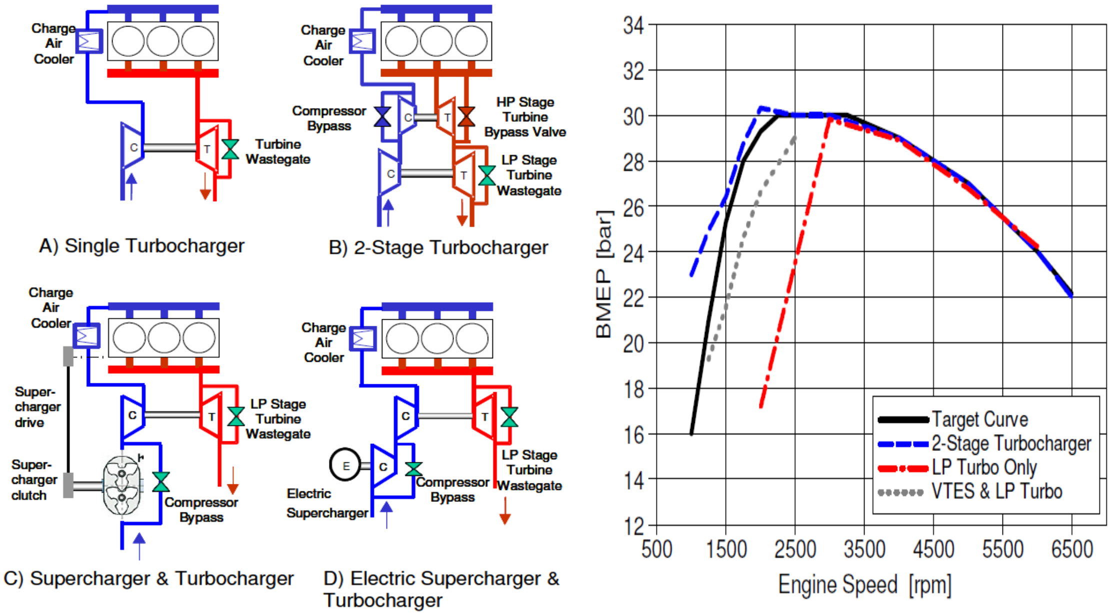

(a) **(b)**

Figure 2.3 (a) Boosting system options for downsized engines and (b) Performance of various boosting systems (Fraser et al, 2009)

Saulnier and Guilain (2004) conducted a computational study on downsized Diesel engine with dual-stage turbocharging to evaluate the potential of such systems for passenger car applications. Recent generations of Diesel engines with specific power up to 70kW/l require boost pressures above 3 bars. The limitation of turbocharger operating ranges calls for the use of two-stage turbocharging systems. Another issue investigated by the author is the low speed torque and transient response. A commercial one-dimensional gas dynamics code was used for the investigation.

A three-stage boosting system with extensive multi-stage cooling was suggested by Gheorghiu (2011) for downsizing of Atkinson cycle engines for further efficiency enhancements. The simulation work uses an Atkinson engine with high boost pressures to increase the indicated mean effective pressure (IMEP) of the engine and high volumetric compression ratio to enhance fuel conversion efficiency (IFCE).

Keidel et al (2012) explored the benefits of using two-stage boosting systems with supercharger-turbocharger combinations for application in a large (15 litre) Diesel engine. The idea behind using a supercharger was to improve transient response due to turbo lag associated with solely turbocharged engines. Building on the same principle, Wetzel (2013) evaluated three different two-stage boosting systems used in downsizing and downspeeding a small Diesel passenger car engine. A series twin turbocharger baseline configuration was compared to two series supercharger-turbocharger configuration. The supercharger-turbocharger combinations comprise of mechanical superchargers and turbochargers that are arranged in series, either upstream or downstream of the other. It was shown that both supercharger-turbocharger configurations offer better BSFC compared to the sequential twin turbocharger configuration at low engine speeds. Between the two turbocharger-supercharger configurations, it was shown that utilizing the mechanical supercharger system in the high pressure stage and the turbocharger for the low pressure stage offers better BSFC due to the smaller supercharger size required for a given boost demand. The supercharger-turbocharger systems were shown to have superior vehicle acceleration compared to the series twin turbo system. Downspeeding can be implemented such that the acceleration time becomes equal to that of the baseline model with further reduction in fuel consumption. A steady state fuel economy comparison for the configurations over the NEDC showed a reduction of 4.5% in fuel consumption with a downsped turbocharger-supercharger configuration over the baseline sequential turbocharger layout.

Various multi-stage boosting options were assessed by Pohorelsky et al (2012) in development of a two-stroke two cylinder diesel engine. To achieve the engine power target the multi-stage system needed to deliver very high boost pressure with low mass flow. These include waste-gated and VGT turbochargers, positive displacement and centrifugal compressors, and various electrical boosting systems. The authors found the best system suited for their application to be the supercharger-turbocharger layout with a HP stage dual-drive positive displacement supercharger and a waste-gated turbocharger as the LP stage.

The work by King et al (2012) described earlier, adopts a less than conventional boosting system comprising a fixed geometry turbocharger, an electric driven supercharger and an electric turbocompounding system. The electric supercharger unit was used to mitigate the inadequate steady state and transient torque at low engine speeds which arises due to fitment of a large fixed geometry turbocharger. As a result, the engine torque was increased by 29 - 47%.

2.5 Other Enabling Technologies

Besides boosting, the success of engine downsizing applications also rely on accompanying technologies such as the employment of DI systems, advanced valve systems, variable compression ratio systems etc. It is extremely difficult to achieve the theoretical benefits of downsizing merely by boosting without the combination of the aforementioned systems.

DI systems have long been used in Diesel engines and an example of the early application of DI systems in small Diesel engines is given by Kawamura et al (1982). Turner et al (2005) and Leduc et al (2003) both explained the benefits of GDI used in downsizing application. Instead of mixing the air-fuel mixture in the intake port as in port fuel injection (PFI) systems, the fuel is directly injected in to the combustion chamber, thus lowering the charge temperature through absorption of latent heat during vaporization of fuel. This offers two advantages in the form of higher charge density and lower average gas temperature in the combustion chamber. The former increases the volumetric efficiency of the engine while the latter improves the knock limit of the combustion. With a higher knock-tolerant combustion chamber, higher thermal efficiency can be achieved by increasing the compression ratio. The knock-on effect of these advantages is that smaller turbochargers can be matched to the engine thereby improving low end boost and transient response. Fraser et al (2009) stipulated that for an equivalent specific power output, the compression ratio can be increased by a factor of one. An example of the work related to development of GDI systems in operation with high output turbocharging is Luttermann and Mährle (2007). The use of high-precision fuel injector to further enhances the fuel distribution in the combustion chamber. This injection system was used together with twin-scroll turbocharger and high compression ratio combustion chamber (10.2:1) enabling high torque and power outputs as well as excellent fuel efficiency for their 3.0 litre engine.

Lang et al (2005) produced initial results in terms of performance and fuel economy benefits obtained from DI turbocharged engines. Later Kleeberg et al (2006) presented the optimization efforts carried out on improving the low end torque and transient response of the DI turbocharged engine for downsizing applications. Similar work was carried out by Clenci et al (2007) who studied the potential of using variable compression ratio (VCR) and variable intake valve lift in gasoline engines for potential application in downsizing.

It can be seen that seen that the advancement of valve train designs and operation also play a crucial role in developments of GDI boosted engines. As opposed to fixed cam timing, advanced valve systems allow the variation of lift, duration and timing. Systems such as the VIVL adopted by Clenci et al (2007) show improvement to transient response by reducing turbo-lag. Other examples of advanced valve systems are described by Hosaka et al (1991), Flierl et al (2000) and Luttermann et al (2006). The optimization process by means of high valve overlaps with a variable valve timing to allow a high degree of fresh air scavenging in the cylinder was presented by Kleeberg et al (2006). This leads to less residual gas and reduced knock sensitivity. Scavenging also helps to maintain high turbocharger turbine mass flow and ensures high efficiency turbocharger operations. Furthermore, the transient response of the engine can be improved by optimizing the valve overlap settings and manifold-integrated charge cooling systems. Recent work by Bucker et al (2013) looked at the influence of VVT on the flow field inside the engine cylinder and the possibility of using it to control the flow tumble and turbulent flow characteristics.

2.6 Modelling of Turbocharged Engines

The use of simulation tools to predict the performance of turbocharged engines can be traced back to the early works of Watson and Marzouk (1977) where a quasi-steady, filling and emptying method was employed to analyse transient performance of turbocharged Diesel engines. This was followed by other works carried out by the author to improve performance prediction and Diesel engine, turbocharger matching (Watson, 1981).

Later, Watson (1984) demonstrated the use of computational methods to predict the performance of a turbocharged SI engine. The main aim of the work was to resolve the issues associated with interaction between the engine and turbocharger components in a control volume based simulation environment. The approach adopted by the author in the model structure ensures flexibility in terms of change in designs of various engine components. Components such as the engine cylinder and manifolds are modelled as variable and fixed volumes respectively. Flow devices such as throttles and valves are modelled as orifices with varying areas. Boosting devices such as turbochargers appear in the model as boundary conditions within the manifolds. One of the key features of the model was its ability to predict gas dynamics effects arising from unequal lengths of manifold piping layouts, hence the ability to model cylinder to cylinder variations. Another noticeable feature regarding the model was the use of turbocharger performance maps (turbine and compressor), which are imposed directly as boundary conditions within the manifold architecture. Twin entry and variable geometry turbochargers were also considered and methods to model them were addressed by the author. The speed of the turbocharger is calculated by balancing the torques produced and consumed by the turbocharge turbine and compressor respectively. The simulation manages to predict the changes in engine performance due to change in geometrical layout of the engine and the presence of the turbocharger. The method used by the author has seen widespread use over the years in commercial wave action codes.

2.7 Turbocharger Performance Prediction

The most common types of turbocharger performance prediction models that are used in gas dynamics codes are discussed by Moraal and Kolmanovsky (1999). Mean-line models of turbocharger performance are developed based on physical gas dynamics equations which are correlated with empirical data. Models utilizing this approach often require, to a certain extent, inputs of turbine aerodynamic and geometrical properties. A classic example of this approach is to model the turbine as an adiabatic nozzle of effective area equal to that of the corresponding turbine. The basic concept of this model is elaborated in Watson and Janota (1982) and its application in control based engine simulation codes was first demonstrated by Jensen et al (1991) for a mean-value engine modelling procedure, which is widely referred to by the industry (Eriksson, 2007).

Map-based turbocharger models are popular in one-dimensional engine modelling wave-action codes. Here, the practice is to have the maps stored in the form of reference (look-up) tables. Then, mathematical algorithms are used to interpolate and extrapolate these data points and extend the range of the maps. This approach to modelling turbocharger performance is therefore independent of any aero-thermo-physical characteristics of the turbine at hand.

As mentioned above, the model proposed by Jensen et al (1991) which is based on the adiabatic nozzle concept is considered as a standard model to which many authors compare their results. The same model for mass flow prediction was later adopted by subsequent authors, amongst them, Moraal and Kolmanovsky (1999), Martin et al (2009) and Liang et al (2009). Based on the relationships between turbine performance parameters, a third order polynomial is used to fit the isentropic efficiency from existing empirical data as a function of velocity ratio. With regards to turbine mass flow, Jensen et al (1991) utilizes the concept of effective area which is imposed as a multiplier to the isentropic flow (adiabatic nozzle) mass flow parameter equation as shown below:

$$MFP = A_t\sqrt{\left\{\frac{2\gamma}{(\gamma-1)R}\left[\left(\frac{P_{out}}{P_{in}}\right)^{2/\gamma}-\left(\frac{P_{out}}{P_{in}}\right)^{(\gamma+1)/\gamma}\right]\right\}}\text{for}\frac{P_{out}}{P_{in}}<P_{crit}\quad \dots (2.2);$$

$$MFP = A_t\sqrt{\left\{\frac{2\gamma}{(\gamma-1)R}\left[(P_{crit})^{2/\gamma}-(P_{crit})^{(\gamma+1)/\gamma}\right]\right\}}\quad\text{for}\frac{P_{out}}{P_{in}}>P_{crit}\quad \dots (2.3);$$

where P_{crit} is the critical pressure ratio defined as:

$$P_{crit}=\left(\frac{P_{out}}{P_{in}}\right)_{crit}=\left(\frac{2}{\gamma+1}\right)^{\gamma/(\gamma-1)}\qquad \dots (2.4);$$

and A_t is the effective turbine area as a function of turbine ratio and is given as:

$$A_t=k_{t1}\left(\frac{p_{in}}{p_{out}}\right)+k_{t2}\qquad \dots (2.5);$$

with k_{t1} and k_{t2} as constants. This approach was further augmented by Eriksson (2007) in his control-based code. The author assumed the degree of reaction for radial turbines to be 0.5 whereby the total pressure ratio is halved between the stator and the rotor. The choking condition therefore takes place when flow reaches critical pressure ratio either in the stator or the rotor. The predicted mass flow using this approach has seen to show better agreement to experimental data to earlier models. A similar concept was adopted by Serrano et al (2008) where the turbine is represented by two nozzles, which reproduce the pressure drops across the stator and the rotor, and at an intermediate cavity where mass accumulation in the system takes place. The efficiency prediction proposed by Martin et al (2009) was adopted by the authors; firstly, by establishing a fit between pressure ratio and mass flow at various turbine rotational speeds and extrapolation of the fit towards lower rotational speed. Once the fit is obtained, the value of specific enthalpy and efficiency are calculated. The main limitation of the adiabatic nozzle assumption can be traced back to the definition of critical pressure ratio P_{crit} whereby choke conditions are predicted at substantially lower pressure ratios using this model for a radial turbine than in reality (Watson and Janota, 1982). To obtain a good agreement with a turbine mass flow, the specific heat ratio has to be set to a value of $\gamma\approx5$, which is physically unjustified.

Moraal and Komanovsky (1999) provided an overview of different parameterization methods of turbocharger modelling. A method worth mentioning is the use of artificial neural network for mass flow prediction. Here, the network output which is the mass flow parameter is predicted with speeds, pressure ratios and, if needed, the nozzle vane settings as inputs. The network is trained to associate the output with trained input patterns and subsequently predict the parameter values for given new maps. This method was applied to a compressor and was reported by Ghorbanian and Gholamrezaei (2009). The disadvantage of this method is that the training of the input neurons will have to rely heavily on a great quantity of existing data in order to accurately predict new map. With the absence of such data, the model will not offer reliable results.

A detailed modelling of turbine performance is described by Romagnoli and Martinez-Botas (2011) for turbines with and without nozzles. This mean line loss model is based on conservation of mass and energy calculations of flow parameters at several stations throughout the turbine assembly. Coefficients of losses are calculated for each station and imposed on the calculated flow parameters. Later, Chiong et al (2013) attempted to couple this mean-line method with a wave action 1-D code to enable the use of a more physical-based model engine simulations.

The preceding discussion signifies the importance of turbine map accuracy and range. With regards to the latter aspect, turbocharger experimental facilities which use compressors to balance the turbine power fall short. As acknowledged by several authors such as Moraal and Kolmanovsky (1999) and Jung et al (2002), this shortcoming is due to the lack of sensor resolution and sensitivity to capture flow characteristics at low speeds.

2.8 Unsteady Turbine Performance

Discussions thus far have been mainly on steady state maps and methods to predict and extend them. Little information is available in the public domain for methods of modelling unsteady turbine operation. It is a well-known fact that there is a high degree of interaction between the engine and the turbocharger. Since turbochargers are designed based on steady conditions, the highly pulsating exhaust flow may affect the turbocharger performance in actual operations. The maps generated for unsteady turbine operations are not so commonly available. Unsteady turbocharger experiments such as those reported by Karamanis and Martinez-Botas (2002), Copeland et al (2011) and a review by Rajoo and Martinez-Botas (2008) shows that the performance parameters exhibits hysteresis loops around the steady state points on the maps due to the filling and emptying process of the flow and the wave dynamics within the turbine volumes.

This behaviour of turbocharger turbines under unsteady, pulsating inlet conditions have been studied for various types of turbines. Rajoo and Martinez-Botas (2010) carried out experimental investigations on the unsteady behaviour of nozzled turbocharger turbines which revealed a higher effect of unsteadiness on efficiency compared to a nozzle-less turbine. Other investigations include the unsteady performance of multiple entry turbines such as those presented by Copeland et al (2011) for a double entry turbine and Costall et al (2010) and Rajoo et al (2012) for twin entry turbines.

Capobianco and Marelli (2007) studied experimentally the performance of an internally waste-gated turbocharger turbine under steady and unsteady inlet flow conditions. Among the findings in this work was that under steady state inlet flow conditions, the actual mass flow rate through the turbine rotor was found to be lower by as much as 10 – 25% compared to the mass flow rate estimated by taking the summation of flows through the rotor and the waste-gate at the same pressure ratios. The authors attributed this to the drop in effective pressure ratios across the device. Later Marelli and Capobianco (2011) evaluated the efficiency of a small turbocharger turbine under unsteady flow conditions. This work, which was also carried out on an internally waste-gated turbine, reveals that the efficiency computed directly through measurements of thermodynamic parameters through the turbine gave different results when compared to that obtained through calculation based on turbine power absorbed by a loading device (a compressor) due to inaccuracy in temperature measurements at the exit of the turbine. With the integrated waste-gate valve in opened positions, the calculated efficiency is increased due to the increase in the total overall mass through the system. From this work, the authors stressed on the difficulty in measurement of instantaneous turbine parameters under unsteady flow conditions as well as the inadequacy of the quasi-steady approach in estimating the turbine efficiency. Besides the work presented by the authors above, other work related to waste-gated turbocharger turbines involve the effect of a waste-gate on the engine intake air (Andersson and Eriksson, 2001) and the modelling of the waste-gate control system (Thomasson, et al, 2013).

2.9 Summary

A review of literatures have been carried out in this chapter, covering topics that are relevant to the current work. These include the state-of-the-art and related issues pertaining to boosting systems in downsized automotive engines. Reviews are also carried out on investigations into the steady and unsteady performance of turbocharger turbines leading to performance measurements and modelling on different types of turbines. The literature review can be summarized as follows:

1) The main drive behind engine downsizing is the practical need for a short to medium term solution for automotive engines to reduce CO_2 emissions and conform to the targets set by emission standards and regulatory bodies. At the same time, downsized engines have to maintain the same level of performance as its NA benchmarks. Boosting the engines enable the operating points to be shifted to a higher specific load to maintain the torque output while achieving the desired fuel economy. Aggressive levels of downsizing with boosting systems brings about inherent issues which are mostly related to high cylinder temperatures (leading to knock in SI engines) and the limitation of the boosting system itself. The introduction of direct injection systems, variable valve timing mechanisms and advanced combustion systems, together with supercharging and turbocharging allows further levels of downsizing to be implemented in SI engines. As far as the boosting systems are concerned, the way forward is to employ multistage systems which ensures sufficient boost to be delivered across the whole engine operating speeds.
2) One of the issues pertaining the boosting system, in particular, the turbocharger is the process of matching. This matching process carried out using engine simulation codes requires the use of turbocharger performance data which are available in the form of manufacturer maps. These maps have to be extrapolated due to its limited range of data because of the limitations in conventional turbocharger test facilities. Without a facility that is able to obtain a map with a wide range of data, it is impossible to ensure the validity of the extrapolation methods carried out to extend the map data range. This evaluation of map extrapolation methods in mainstream 1-D engine simulation codes has yet to be done in any previous studies. Furthermore, the impact of any errors in the extrapolated manufacturer maps with actual turbine performance on the prediction of engine performance by the software itself has to be investigated in greater detail.
3) Following the above points, it was also found that very limited work has been carried out to investigate the performance of a waste-gated turbine. Where such investigations exist, it was restricted to turbine with internal waste-gates. The tests itself were carried out on facilities using compressors as a loading device where issues of turbine power and consequently efficiency measurements and the data range itself are present. Until such studies are carried out, then only the validity of various turbocharger modelling methods can be validated with reliable experimental data. The studies on the performance of internally waste-gated turbines indicate that there is a strong

interaction between the flow inside the bypass waste-gate valve and the turbine which affects the turbine performance. Therefore, the valve and the turbine itself cannot be treated as two devices operating independently at a given system pressure ratio; an assumption which is commonly adopted in most turbocharger models thus far.

Chapter 3 Test Facility and Steady State Turbine Performance

3.1 Introduction

One of the specific objectives of this thesis is to obtain the steady state performance of an externally waste-gated turbine. In pursuance of this, a major part of this study comprises experimental investigations carried out on a dedicated turbocharger test facility at Imperial College London. The methodology for steady state testing is explained followed by test results and discussions.

In the following sections, the turbocharger turbine performance, which is represented by non-dimensional parameters are presented. This is followed by the description of the test facility and instrumentations used for measurement of these performance parameters. The steady state test configurations and the method used for characterization of the waste-gate valve ensue, followed by experimental results and discussions. Included in the discussion is the pertinent issue of turbine map extension, where different methods employed in turbocharger matching procedures are evaluated. Finally, the chapter is concluded with a summary of the important findings.

3.2 Turbine Steady State Performance

In general, the performance of a turbocharger turbine is evaluated on its ability to “swallow” mass and the efficiency of its power delivery. The term swallowing characteristics/capacity and mass flow is interchangeably used throughout the analysis and discussion within this thesis. These performance parameters are often presented as functions of several other parameters in dimensionless forms which encompass the turbine geometrical and operational properties. With reference to Watson and Janota (1982), the mass flow rate ($\dot{m}$) and efficiency (η) of a turbine can be expressed as functions of several independent variables including the gas properties, turbine geometry and operating flow conditions as follows:

$$\dot{m}, \eta = f\left(P_{0,in}, P_{S,exit}, T_{0,in}, N, D, R, \gamma, \mu\right) \quad \ldots (3.1);$$

where, $P_{0,in}$ and $T_{0,in}$ are inlet total pressure and temperature respectively, $P_{S,exit}$ is the exit static pressure, N is the turbine rotational speed, D is the rotor wheel diameter, R is the universal gas constant, γ is the gas specific heat ratio and μ is the dynamic viscosity of the gas. Through the

Buckingham Pi method of dimensional analysis, these parameters can be reduced to a set of non-dimensional parameters as given below:

$$\frac{\dot{m}\sqrt{RT_{0,in}}}{P_{0,in}}, \eta = f\left(\frac{ND}{\sqrt{RT_{0,in}}}, \frac{P_{0,in}}{P_{S,exit}}, \frac{\dot{m}}{\mu D}, \gamma\right) \ldots (3.2);$$

The effect of the Reynolds number term ($\dot{m}/\mu D$) is often negligible due to the highly turbulent nature of the gas flow in turbochargers during normal operation and can therefore be dropped from the expression. With turbocharger operating on a specific gas, the values of γ and R are assumed to be constant. Furthermore, the wheel diameter (D) is unique to a particular turbine and therefore is constant. These assumptions further reduce the non-dimensional parameters above to become functions of two variables as follows:

$$\frac{\dot{m}\sqrt{T_{0,in}}}{P_{0,in}}, \eta = f\left(\frac{N}{\sqrt{T_{0,in}}}, \frac{P_{0,in}}{P_{S,exit}}\right) \quad \ldots (3.3)$$

It follows that two terms, namely mass flow and speed, become pseudo-dimensionless as a result of these assumptions, hence they are now respectively referred to as the mass flow parameter (*MFP*) and speed parameter ($N/\sqrt{T_0}$) throughout the thesis. The ratio of inlet to exit pressures ($P_{0,in}/P_{S,exit}$) indicates the expansion within the turbine and aptly denoted as the expansion ratio or pressure ratio (*PR*). The choice of static pressure rather than stagnation pressure is made on the basis that the kinetic energy available at the exit of the rotor is usually not recovered (Watson and Janota, 1982). Therefore, efficiency here is evaluated on total-to-static basis and is denoted by (η_{TS}).

The isentropic total-to-static enthalpy drop from the turbine expansion process can be used to define the isentropic velocity (C_{is}) for a given pressure ratio. Using the rotor tip velocity (U) to non-dimensionalize this isentropic velocity gives rise to another important parameter related to turbine operation called the velocity ratio (U/C_{is}), which is defined as the ratio between the rotor tip speed (U) and the isentropic speed (C_{is}) shown below:

$$\frac{U}{C_{is}} = \frac{(\pi ND/60)}{\sqrt{2c_p T_{0,in}\left[1-(PR)^{(1-\gamma/\gamma)}\right]}} \quad \ldots (3.4);$$

where c_p is the specific heat capacity and *PR* is the pressure ratio. Often, it is more convenient to plot the turbine efficiency against velocity ratio as opposed to pressure ratio since efficiency does not vary significantly with turbine speed. It is also used to assist turbine-compressor and turbocharger-engine matching. For optimum performance, the matching is carried out such that the operational boundaries of the turbine fall mainly on the high efficiency region of the efficiency-velocity ratio curve.

3.3 Similitude and Equivalent Conditions

In contrast to the hot inlet conditions in an actual engine (or in a hot-flow test facility), the present experiments are carried out on a cold-flow test facility. In view of this, appropriate similitude approach has to be adopted such that the parameters measured in the facility are in equivalence with on-engine conditions. The similarity between the measured parameters in cold and hot inlet conditions is achieved through the following relationships for mass flow and speed parameters with the “cold” and “hot” subscripts denoting the test conditions:

$$\left[\frac{\dot{m}\sqrt{T_{0,in}}}{P_{0,in}}\right]_{cold} = \left[\frac{\dot{m}\sqrt{T_{0,in}}}{P_{0,in}}\right]_{hot} \quad \dots (3.5)$$

$$\left[\frac{N}{\sqrt{T_{0,in}}}\right]_{cold} = \left[\frac{N}{\sqrt{T_{0,in}}}\right]_{hot} \quad \dots (3.6)$$

The similitude achieved through the above relationships allows the turbine to be tested at a lower temperatures and rotational speeds within the operational limits of the measurement instruments.

3.4 Overview of the Turbocharger Test Facility

The turbine performance in this study is measured on a dedicated turbocharger test facility developed at Imperial College London. This cold-flow facility uses air as working fluid and is capable of testing different types of turbocharger turbines under various inlet conditions. Figure 3.1 shows the overall layout of the facility.

The main air supply is provided by three *Ingersoll Rand* screw-type compressors capable of delivering a maximum of ≈1.2 kg/s (0.4 kg/s of air each) at 4 bar pressure. The air is fed through a pipe (internal diameter = 101.6mm) and is regulated by a main valve (101.6 mm diameter) and a smaller (38.1 mm diameter) secondary valve. Electric actuators enable these valves to be controlled remotely from a computer interface while in operation. A 72 kW heater controlled by a single-loop *West 6001+* controller is placed after the main valves to heat the incoming air and prevent water condensation at the exit of the turbine due to flow expansion. In addition, the heater allows for the turbine inlet temperature to be held at a constant value during operation so that the inlet temperatures for a given set of test points can be made consistent. Tests are carried out with inlet turbine temperatures in the range of 320 – 350 K.

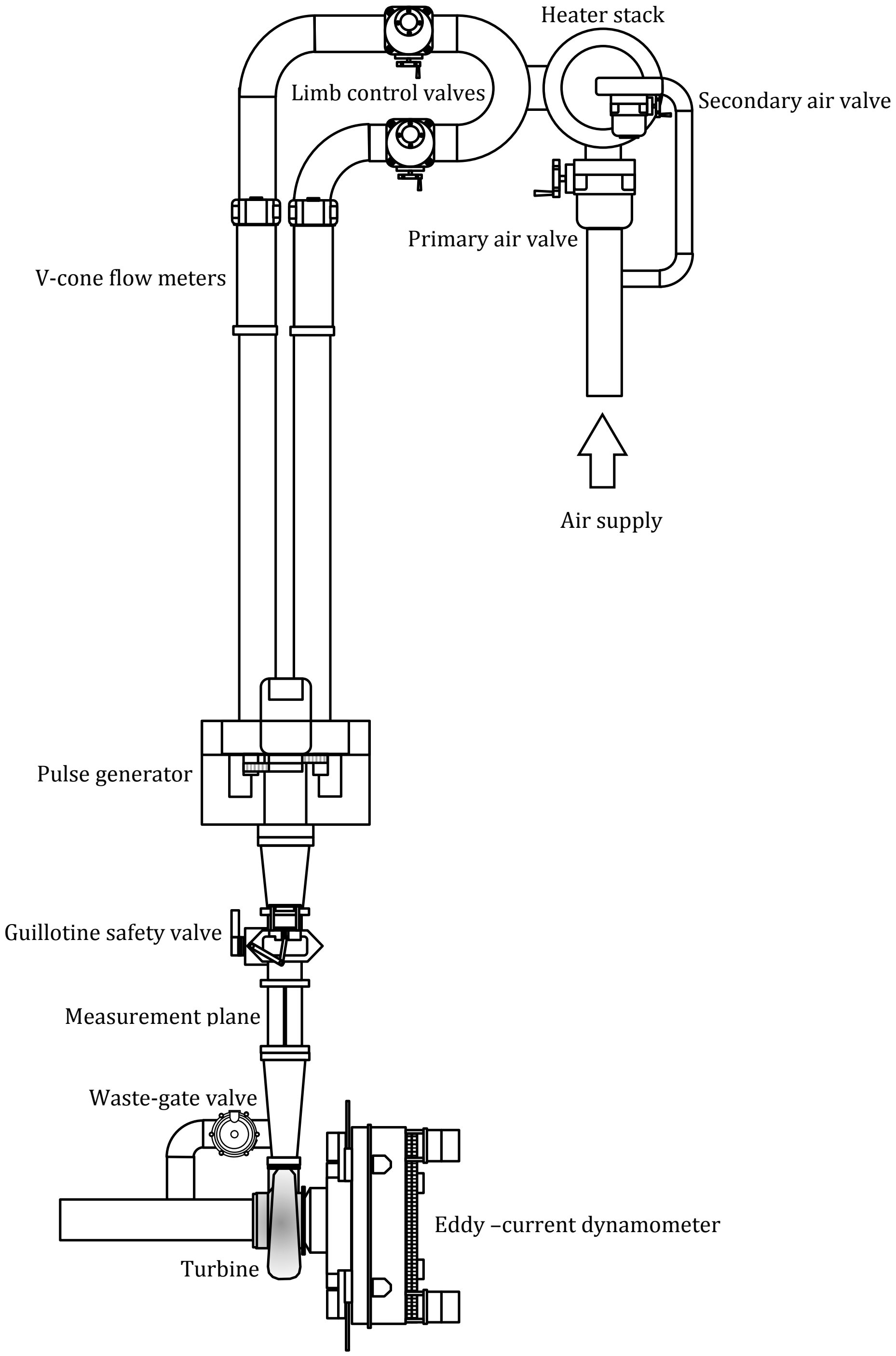

Figure 3.1 Schematic layout of turbocharger test facility

After the heater, the flow is split into two 76.2 mm diameter branches (limbs), each having separate valves to allow independent flow control. Based on the piping layout, the corresponding limbs are referred to as *inner* and *outer* limbs. This setup enables testing of partial or unequal flow admissions for multiple entry turbines. Similar to the main valves, these individual limb control butterfly valves can be controlled remotely via a computer. The mass flow rates of air are measured by *McCrometer* V-cone flow meters placed in each limbs. This type of flow meter offers better flow measurement over a wide range of steady state operation compared to a conventional orifice-plate system.

Downstream of the V-cone meter, is a pulse generator system consisting of an electric motor and two pulleys to rotate two solid plates with cut-outs. The plates are aptly referred to as chopper plates as they block (chop) the air flow temporarily during a cycle, inducing pressure pulses within the flow. This system is operated during unsteady tests to simulate the pulsating flow from the exhausts of a reciprocating engine. In addition, the pulsations in each limb can be made to be either in-phase or out-of-phase with each other to adhere to different pulse overlaps from an actual engine. During steady state tests, the plates are aligned such that the flow areas of the plates are in the fully-opened configuration.

The gas leaving the pulse generator then flows through a guillotine safety valve which is magnetically armed during testing and activated whenever any of the pre-set safety limits of the rig are breached. This spring-loaded valve ensures rapid cut-off of the air supply to the highly instrumented components further downstream. An instrumented section referred to as the measurement plane is located after the guillotine valve with the flow from the individual limbs still separated from each other. In a normal test, the inlet isentropic conditions of the turbine are measured in this section. Besides pressure and temperature, the measurement plane is also equipped with a hotwire system including a traverse mechanism in one limb for measurement of instantaneous mass flow in unsteady tests.

Turbines are installed on a dynamometer located after the measurement plane. Bespoke adaptor ducts are made to connect the flow in the measurement plane to various turbine entry geometries. As such, designs of these adaptor ducts may be tailored to suit single or multiple entry turbines with the former allowing the flow through the individual limbs to be merged in a single stream before entering the turbine. The adaptor duct may also incorporate connections for additional flow devices such as turbine bypass pipes, waste-gate valves, EGR system etc.

An in-house designed eddy-current high-speed dynamometer is used to measure turbine shaft power up to 60 kW using the magnetic reaction between a rotor and two stator plates as a loading system, described below. The turbine bearing housing is oil-cooled via an oil flow circuit which delivers oil at a flow rate of ≈16 l/min during experiments. The whole setup is suspended on a gimbal system which allows the entire device besides the turbine volute to rotate and torque to be measured directly via a load cell. The power in the form of heat produced by the turbine is absorbed by cooling water from a cooling circuit. A digital counter comprising an optical sensor and a ten-toothed encoder is used to measure shaft speed and acceleration of the shaft during unsteady testing. A *Bently Nevada* piezo-velocity sensor is used to monitor vibration levels of the dynamometer and to trigger the activation of the guillotine valve when vibrations exceed a pre-set limit. The test rig is operated and monitored remotely via a PC through a LabVIEW interface. All data logging process and storage are done via the same PC.

3.4.1 Description of the eddy-current dynamometer

The design of the dynamometer (Figure 3.2) used in this study was carried out by Szymko (2006) with initial aim of overcoming the inadequacies associated with load range and accuracy of conventional test facilities such as compressor-loaded and hydraulic dynamometers. With this system, a wide range of load can be applied to the turbine with accurate measurement of turbine swallowing capacity and power.

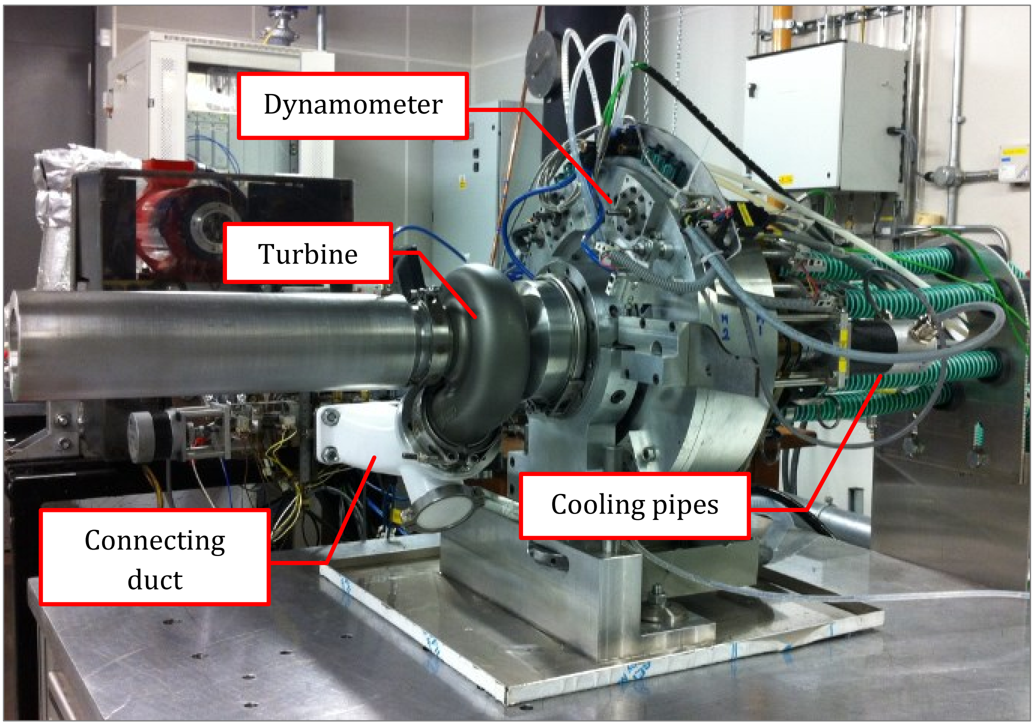

Figure 3.2 Photo showing the eddy current dynamometer

The loading method adopted by the dynamometer is based on the eddy-current principle. Here, the basic construction comprises of a permanent magnetic rotor made attached to the turbine shaft with two stationary, electrically-conducting discs (stator plates) on either sides of this rotor. This magnetic rotor consists of permanent magnet buttons made of Neodymium-Iron-Boron (NdFbB) embedded in an aluminium disc as shown in Figure 3.3. The rotating motion of the magnetic rotor driven by the turbine will change the magnetic field over its surface, inducing eddy-currents within the stators plates. These eddy-currents, in turn, generate their own magnetic field that will react to the source field generated by the rotor and resist its motive force, hence acting as a brake. As the stator plates are brought axially closer to the source magnet, this braking force increases due to increased magnetic flux experienced by the conductors, consequently increasing the load exerted on the rotor and vice-versa. The gap between the stators and rotor is controlled by two stepper motors mounted on the dynamometer. Multiplying this braking force with the relative velocity between the rotor and the stators yields the power absorbed by the stators which is dissipated as heat through Ohmic losses. Considering the vast amount of heat generated at peak power (≈62 kW), the cooling requirement for conductors is extremely large, given the small surface area of the stators. In order to achieve adequate amount of cooling, water is forced over the surfaces of the stator plates via a 3 kW pump and a cooling circuit and stator to water heat exchange is achieved through nucleate boiling. Cooling of the rotor is achieved by imparting high-pressure air over its surface.

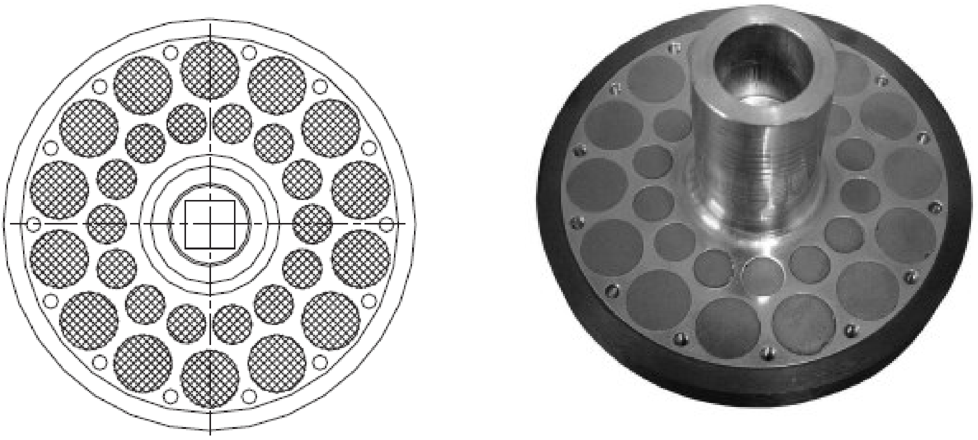

Figure 3.3 Schematic diagram and photo showing the arrangement of permanent magnets on the rotor (Szymko, 2006)

In principle, the torque produced by the eddy-current is equal to that generated by the turbine. With the whole arrangement including the bearing housing being mounted on a gimbal system and are allowed to rotate freely on its horizontal axis, this torque can be measured directly by means of reacting the dynamometer against a load-cell which is attached to the dynamometer through a lever arm. Because the whole turbine system rotates freely, this method of measuring turbine power allows for the aerodynamic performance of the turbine to be evaluated. For a fixed shaft speed, the range of mass flow rate and turbine power that can be measured from this is system is far wider than those measured on a conventional turbocharger test facility where compressors are used to load the turbine. This is primarily because the loading is not limited by the aerodynamic constraints, namely surge and choke characteristics of the compressor. Furthermore, the direct measurement of turbine power eliminates the uncertainty found in compressor-based systems which relies on thermodynamic measurements on the compressor flow.

3.4.2 The *Garrett* GT30R turbocharger turbine

The turbine used for experiments is from a *Honeywell Garrett* GT30R turbocharger unit. The main turbocharger assembly comprises of a radial type turbine with 60mm wheel diameter paired to a 67mm wheel diameter compressor capable of delivering boost up to 3.5bar absolute. The choice of this unit is based on a matching procedure carried out by Copeland et al (2012) for a 2.0 l gasoline engine which is designed to produce 35 bar brake mean effective pressure (BMEP). The photo in Figure 3.4 shows the turbine unit installed on the dynamometer. Only the turbine rotor and shaft assembly and the volute housing are needed for the present experimental setup. Thus these components are separated from the turbocharger unit, and several adaptations are made in order for the turbine to be fitted on to the dynamometer.

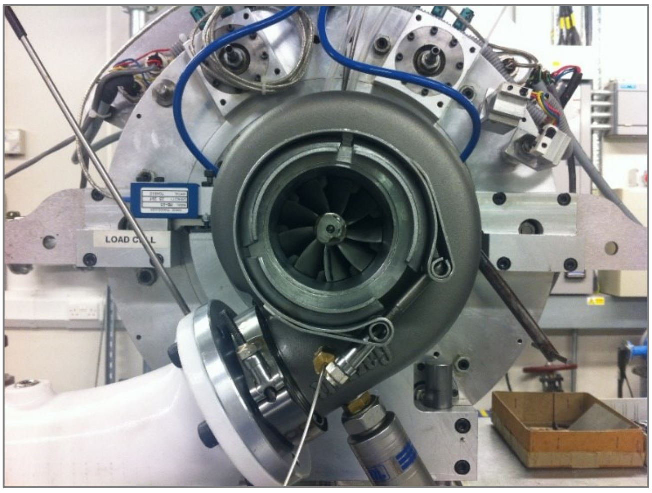

Figure 3.4 Photo showing the GT30R turbine installed on the dynamometer

3.4.3 The *Ti-AL* MV-R external waste-gate valve

A *Ti-Al* MV-R series external waste-gate is used to regulate the amount of air bypassing the turbine stage during testing. This type of waste-gate uses a poppet valve which is acted against a spring. Above the valve is a boost-sensing chamber which is connected to the compressor exit via pressure feed lines. A diaphragm is placed between this chamber and the spring such that a sufficient amount of pressure in the chamber will result in compression of the spring and the subsequent lifting of the poppet valve. This pressure, often referred to as "cracking" pressure is the threshold value of boost pressure which is required to overcome the spring force. When placed upstream of the turbine, the gas will flow through the waste-gate valve thus bypassing the turbine whenever the cracking pressure is exceeded. In the current setup, the waste-gate valve is installed at the end of a secondary branch of the transfer duct that connects the turbine housing to the measurement plane. To replicate realistic engine conditions, the flow through the bypass valve is reconnected back into the main flow downstream of the turbine stage in what is referred to as the exit duct.

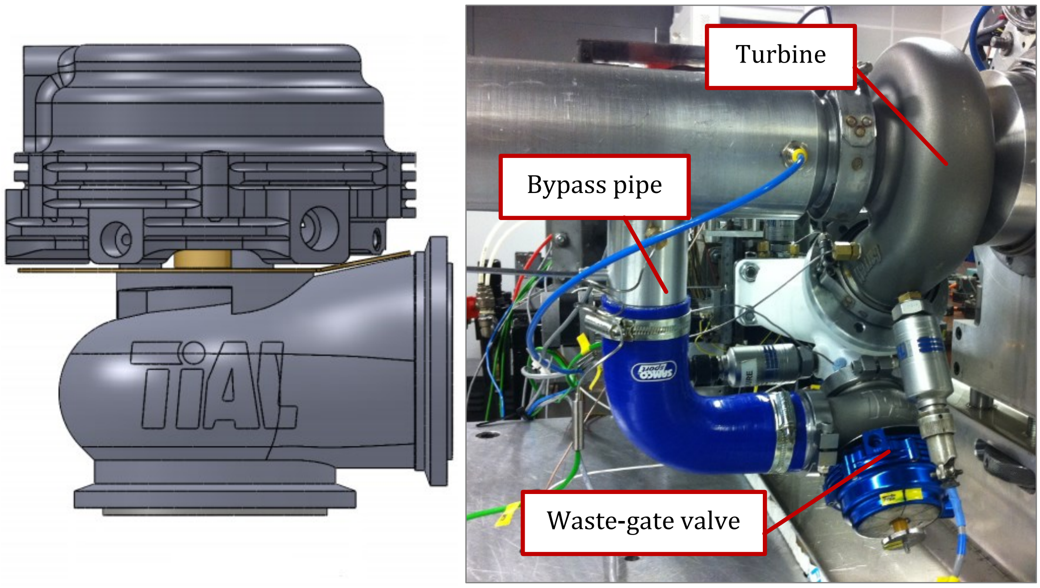

Figure 3.5 Schematic drawing and photo of external waste-gate valve used for the experiments

Under opened waste-gate test conditions, the waste-gate opening areas are set at fixed set of values by way of adjusting the valve lifts rather than exerting pressure into the pressure-sensing chamber. To do this, several modifications are made to the waste-gate valve used in this experiment. Firstly, the original waste-gate spring was replaced with a stiffer spring capable of withstanding more than 5bar of pressure before lifting. This is to avoid unwanted lifting of the valve at high pressure ratios. Secondly, a lead screw assembly was attached to the waste-gate valve so that the lift could be accurately controlled by a screw dial. The screw has an M4 x 0.7mm thread pitch, thus one revolution of the dial corresponds to 0.7mm of valve lift. The mass flow rate across the waste-gate is then recorded for several points at a given lifts in the range of 1.0mm to 10.0mm.

3.5 Data Acquisition and Rig Control

The main control of the rig operation and acquisition of data is performed by National Instruments CompactRIO system (cRIO) comprising a real-time (RT) controller, a field programmable logic array (FPGA) chassis and eight C-series I/O modules where the various sensors and actuators are connected. The I/O modules are directly accessed by the FPGA, which then sends the signal to the RT controller via a high speed bus based on a FIFO (first in, first out) queuing system. The data from RT controller is relayed to the host PC which the operator uses for rig control and data logging. For low speed data such as thermocouple readings, oil flow and water flow frequency measurements, the readings are passed to the host PC as network global variables. High speed data acquisition such as the chopper plate frequency sensor and the instantaneous speed measurement are acquired at a rate of 25 kHz and are passed to the host PC from the RT controller via a network stream to ensure that the data maintains temporal alignment. Besides the cRIO, the host PC is also served by two CompactDAQ (cDAQ) systems for measurement of atmospheric pressure, vibration monitoring and valve controls.

3.6 Steady Measurement

The test facility described above is highly instrumented to enable measurement of various quantities that relate to the gas flow, turbine characteristics and rig safety. To obtain the performance parameters defined for the turbine in Section 3.2, the measurements of pressure, temperature, rotational speed and torque are performed. The location of each measurement point is shown in Figure 3.6. The mass flow rate of the incoming gas is measured upstream via two V-cone flow meters.

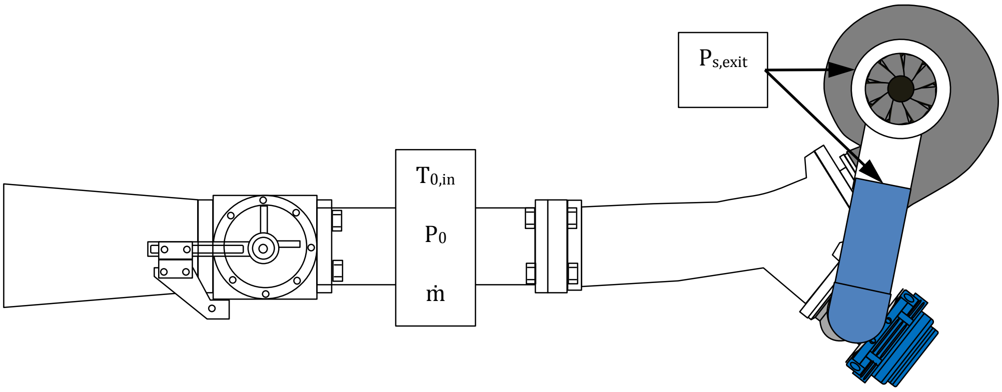

Figure 3.6 Measurement locations for steady experiments

3.7 Uncertainties of Measurement

It is important that the uncertainty in measurement of individual parameters be accounted for when analysing the data. Hence, a statistical-based approach was used to evaluate the inherent uncertainty of the parameters during the calibration process of the relevant parameters based on Kirkup (1994) and adopted by Newton (2013). A measured parameter Y can be defined as a function of variable x, such that $Y = f(x)$. The standard deviation of the recorded data points from the defined function (σ) for n number of data can then be estimated by:

$$\sigma_Y = \sqrt{\frac{\sum_{i=1}^{i=n}[Y_i - f(x_i)]^2}{n-\nu}} \quad \text{... (3.8);}$$

where v is the number of degrees of freedom defined as the number of data points minus the number of restrictions placed on possible Y values for a given function f(X). A linear function $Y = mx + c$ reduces the value of v to two. The uncertainty U of measurement is taken as twice the standard deviation for the variable Y as follows:

$$U_Y = \pm 2\sigma_Y \quad \text{... (3.9)}$$

If the deviation of measurement from the trend follows a normal distribution, this results in 95.4% probability that the true value lies within the calculated uncertainty.

There are instances where a measured parameter is a function of several other independent quantities $X_1, X_2, \dots X_k$. This can be written as follows:

$$Y = f(X_1, X_2, \dots, X_k) \quad \text{... (3.10)}$$

The standard deviation for Y is given by (British Standards Institution, 1983):

$$\sigma_Y = \sqrt{\left(\frac{\partial Y}{\partial X_1}\sigma_1\right)^2 + \left(\frac{\partial Y}{\partial X_2}\sigma_2\right)^2 + \cdots + \left(\frac{\partial Y}{\partial X_k}\sigma_k\right)^2} \quad \dots (3.11);$$

where, $\frac{\partial Y}{\partial X_1}, \frac{\partial Y}{\partial X_2}, \dots \frac{\partial Y}{\partial X_k}$ are partial derivatives of Y with respect to X. In this case, the combined uncertainty for the measure Y parameter employs the Root Sum Square (RSS) method of uncertainty estimation, which was commonly used in previous works of Szymko, 2006 and Newton, 2013. This RSS uncertainty (U_{RSS}) for parameter Y above can be expressed in absolute form by:

$$U_{RSS,Y} = \sqrt{\left(\frac{\partial Y}{\partial X_1}U_1\right)^2 + \left(\frac{\partial Y}{\partial X_2}U_2\right)^2 + \cdots + \left(\frac{\partial Y}{\partial X_k}U_k\right)^2} \quad \dots (3.12)$$

3.8 Steady Pressure Measurement

In steady state testing, the pressure is measured at the inlet and exit of the system including the waste-gate. All steady state pressure measurement is carried out using a *Scanivalve* system. Static-hole taps on the desired pressure measurement locations are connected via pneumatic tubes to the channels on the *Scanivalve* system. A total number of 32 pressure readings can be simultaneously taken from the four DSA3016 modules, each having eight pressure connections. Two banks operate in a low pressure range of 0 to 1psi (≈0 – 6894.75 Pa) and the other two, at high pressure range of 0 to 100 psi (0 – 689475 Pa). An Ethernet connection is established within the *Scanivalve* system and the host PC where the pressure readings and recordings are performed via a LabVIEW interface. A TCP connection is used within Labview to obtain the pressure measurement from the *Scanivalve* system. The *Scanivalve* is calibrated by an automatic procedure with their bespoke software, *Presscal*. The accuracy is reported as ±0.08% of the full scale reading by *Scanivalve*.

3.9 Steady Temperature Measurement

The measurements of temperature are taken at various locations within the test rig for the purpose of evaluation of turbine performance as well as to monitor safe operation of the turbine and rig components. The temperature measurements are carried out using K-type and T-type thermocouples which are linked to the thermocouple module on the cRIO chassis. Table 3.1 shows the types of thermocouples used at various locations in the test rig. The air temperature downstream of the heater is monitored using K-type thermocouples to avoid overheating and risk of damaging the heater elements. The pre-set heater temperature is maintained via a PID controller incorporated into the heater power supply. Further downstream, a K-type thermocouple is used for measurement of air temperature inside the V-cone flow meter. Safe operation of the bearing housing and dynamometer is ensured by monitoring the temperatures of the stator plates using K-type thermocouples whereas T-type thermocouples are used to monitor the temperature of the cooling water. For calculation of turbine performance, the air temperature is measured by T-type thermocouples at the measurement plane.

Table 3.1 Types of thermocouples used in steady state experiments

Measurement Location	Type of thermocouple
Heater section	K-type
V-cone flow meter	K-type
Measurement plane	T-type
Stator plates (dynamometer)	K-type
Cooling water (dynamometer)	T-type
Bearing system	K-type

In a fluid flow, the static and stagnation temperatures (T and T_0) can be related to each other through Mach number (Ma) using isentropic flow relationships shown below:

$$\frac{T}{T_0} = 1 + \frac{\gamma - 1}{2} Ma^2 \quad \ldots (3.13)$$

The compressibility within the flow causes the measured temperature values to fall between static and total temperatures. To account for this, a temperature correction procedure used by Szymko (2006) is employed wherever the flow Ma exceeds 0.3. Here, a recovery factor (r) is defined and its relationship with measured temperature (T_{meas}) actual temperatures is shown below:

$$r = \frac{T_{meas} - T}{T_0 - T} \quad \ldots (3.14)$$

Therefore the actual static temperature is calculated from the following expression:

$$T = \frac{T_{meas}}{1 + r\left(\frac{\gamma - 1}{2}\right) Ma^2} \quad \ldots (3.15)$$

Since the Ma itself is also a function of temperature, the values of the correction factor, r, are obtained iteratively within the post-processing software.

3.10 Steady Mass Flow Measurement

In the steady state experiments, the measurement of mass flow rate is carried out using a *McCrometer* V-cone differential pressure flow meter (Figure 3.7) located at the individual flow limbs downstream of the limb control valves. A cone, centrally located inside a pipe alters the flow by accelerating it and creating a low pressure region downstream. By measuring the difference in pressure at the upstream high pressure port (P_1) and the downstream low pressure port of the cone (P_2), the mass flow rate of the gas through the V-cone can be determined by the following expression:

$$\dot{m} = F_a C_D Y k_1 \sqrt{\Delta P \rho} \quad \ldots (3.16);$$

where, F_a is the material expansion factor, C_D is the discharge coefficient, Y is the gas expansion factor, k_1 is the flow constant, ΔP is the pressure difference and ρ is the gas density. The differential pressure is measured through a built in pressure measurement unit which feeds the signal to the *National Instrument* analogue input module.

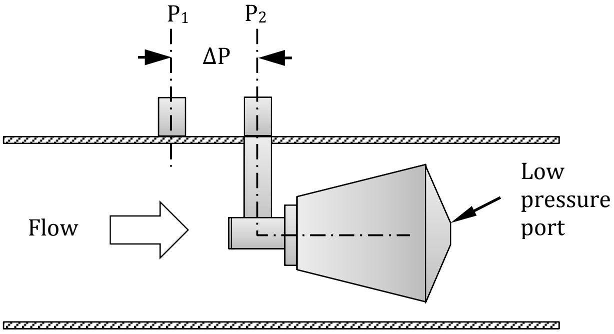

Figure 3.7 Schematic diagram of the V-Cone flow meter (McCrometer Inc., 2011)

The thermal expansion factor (F_a) accounts for material geometrical changes with temperature and is often very close to unity. The flow constant (k_1) is given by:

$$k_1 = \frac{\pi\sqrt{2U_3}}{4U_2} \cdot \frac{D^2\beta^2}{\sqrt{1-\beta^4}} \ldots (3.17);$$

where U_2 and U_3 are unit conversion constants prescribed by *McCrometer*, D is the internal diameter of the pipe, and β, defined below, is the beta ratio which is a function of the cone outside diameter (d) and the pipe internal diameter (D):

$$\beta = \sqrt{1 - \frac{d^2}{D^2}} \quad \ldots (3.18)$$

The V-cones in both flow limbs in the test rig has a k_1 value 0.0139. The gas expansion factor (Y) in Equation 3.11 is obtained by the following expression:

$$Y = 1 - (0.649 + 0.696\beta^4)\frac{U_1 \Delta P}{P} \quad \ldots (3.19);$$

where U_1 is a unit conversion factor and P is the operating temperature.

The discharge coefficient C_D is a function of Re and therefore has to be calibrated. However, it was found that C_D is constant from Re range of 17000 to 430000, which in mass flow rate terms is in the range of 20g/s to 500g/s through each meters. Anticipating that the mass flow rate during testing is within this range, C_D is taken as constant at 0.8385 and 0.8472 for the individual limbs.

3.11 Measurement of Shaft Speed

Another important parameter with regards to turbine performance is the rotational speed. This parameter is measured by an optical sensor attached to the end of the magnetic rotor. The optical signal is repeatedly obstructed by a ten-toothed encoder at the end of the rotor shaft. The rotational speed of the shaft can be worked out from the frequency of the interference caused by the toothed encoder. The sensor is calibrated against a 5 kHz square wave signal produced by a signal generator which produces an equivalent rotational speed of 30000 RPM. The accuracy of the reading was found to be within ±1 RPS.

3.12 Steady Torque Measurement

The turbine torque along with speed is integral in defining the power output of a turbine. The steady state torque generated by the turbine is determined through direct measurement of torque which is reacted against dynamometer via a load cell system. In the experiment, the load cell is of an Interface Miniature Beam force transducer with a capacity of 11.3 kg.f. This device is connected to a bridge module on the cRIO system. During testing, the load cell reading was logged along with other steady state parameters once the desired turbine speed stabilizes for a prescribed dynamometer load. The turbine was then brought to rest by closing the main valves that feeds air into the turbine and the subsequent torque reading at this point was taken as the zero offset for the actual torque calculation.

The calibration of the load cell was carried out by way of loading known set of loads at the end of a cantilever arm which is attached to the dynamometer. The resulting moments generated by the loads are recorded as voltage readings and a linear relationship between the moment and voltage was found as shown in Figure 3.8. The torque calibration process results in a standard deviation of 0.0108 Nm giving an uncertainty of ±0.0217 for a 95.4% confidence interval.

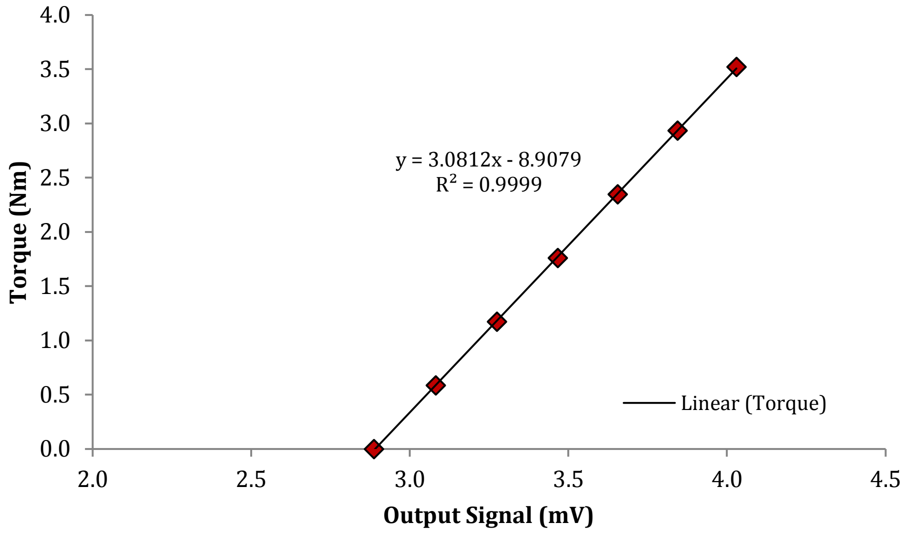

Figure 3.8 Calibration of the load cell for torque measurement

3.13 Experimental Layout and Test Configurations

The primary aim of the experiment is to obtain the steady state characteristics of the turbine in the form of performance maps. The maps are useful, not only from a turbocharger design standpoint, but also in the process of matching a turbine to a particular engine. Central to the theme of the thesis, the map obtained from the test will be used in 1-D engine simulations, which will be discussed in Chapter 5.

In the present work, measurements were taken at five different speeds ranging from $N/\sqrt{T_0}$ =1531 RPM/√K to $N/\sqrt{T_0}$ =2755 RPM/√K. This speed range is selected based primarily on the operational limits of the test facility with the level of vibrations during high speeds being the most influential factor. In addition to what is considered as "standard" steady state testing, further experiments are conducted with an amount of mass bypassing the turbine rotor stage. This involves installation of a bypass waste-gate valve between the turbine inlet and the rotor. To date, a waste-gated turbine is assumed to behave like a normal turbine without the bypass flow having any significant effects on the turbine performance. It is interesting to find out whether this assumption is adequate, especially from the perspective of turbocharger modelling and engine matching. In view of this, the steady state experiments are conducted with different waste-gate area openings which are regulated by varying the lift of the waste-gate poppet valve. The steady state tests are carried out at five levels of waste-gate lifts ranging from 1.0mm to 9.0mm.

3.14 Characterization of the Waste-gate Valve

Figure 3.9 shows the waste-gate mass flow characteristics of the waste-gate valve used in this investigation. To establish equivalent conditions with the turbine characteristics, the mass flow parameter (*MFP*) as defined earlier in Section 3.2 is also used for the waste-gate. As expected, the mass flow curve shows resemblance to that of a nozzle. A more specific comparison can be made with the findings of Woods and Khan (1965) who studied the characteristics of flow through poppet valves where a similar trend is observed. This is typified by the increase in mass flow as the pressure ratio is increased. The flow begins to show signs of choking at pressure ratios beyond ≈2.0.

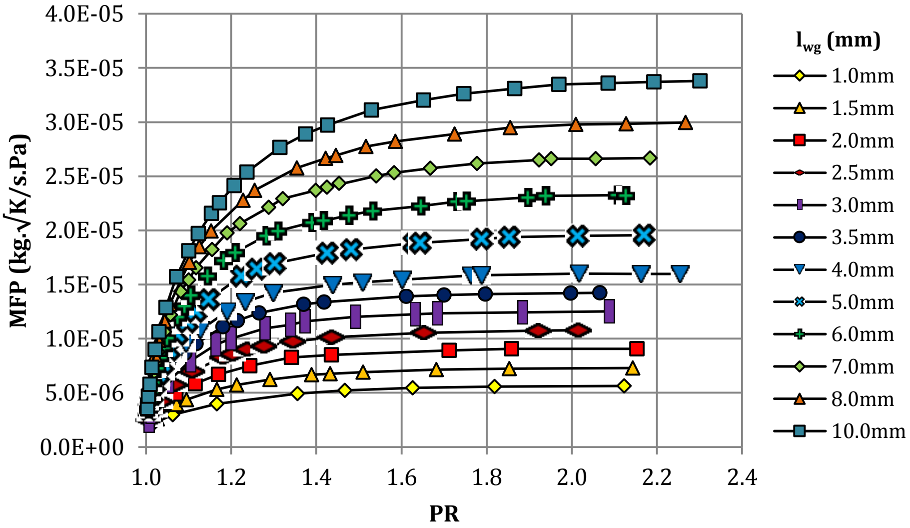

Figure 3.9 Waste-gate mass flow characteristics obtained at ten various waste-gate lifts

For the sake of convenience, the degree of waste-gate valve opening is represented henceforth simply in the form of valve lift. The corresponding valve lift to the lift parameter (l/d_{ref}) which is defined as the ratio between the valve lift and a reference diameter (diameter of the valve inlet port) is presented in Table 3.2. A_{eff} in the table is the effective flow area which is the product of the valve flow coefficient (C_f) and reference area (A_{ref}), these are described below.

Table 3.2 Flow coefficient and effective area measured for waste-gate valve tabulated for different valve lift and (l/d_{ref})

***l* (mm)**	**l/d_{ref}**	**C_f**	**A_{eff} (mm^2)**
1.0	*0.025*	*0.112*	*136.721*
1.5	*0.038*	*0.149*	*182.629*
2.0	*0.051*	*0.191*	*233.872*
2.5	*0.063*	*0.231*	*282.660*
3.0	*0.076*	*0.267*	*326.884*
3.5	*0.089*	*0.300*	*368.043*
4.0	*0.101*	*0.333*	*407.841*
5.0	*0.127*	*0.397*	*486.823*
6.0	*0.152*	*0.466*	*571.508*
7.0	*0.177*	*0.530*	*649.944*
8.0	*0.203*	*0.584*	*716.151*
10.0	*0.253*	*0.634*	*776.593*

3.14.1 Waste-gate flow coefficient

Once the mass flow characteristics are known, it is now possible to determine the flow coefficient (C_f) of the waste-gate, which is defined as the ratio of actual to ideal mass flow rates. The mass flow through a poppet valve can be represented by the following expression for (Heywood, 1988):

$$\dot{m} = C_f A_{ref} \frac{P_{0,in}}{\sqrt{RT_{0,in}}} \left(\frac{P_{S,exit}}{P_{0,in}}\right) \sqrt{\frac{2\gamma}{\gamma-1}\left[1-\left(\frac{P_{S,exit}}{P_{0,in}}\right)^{(\gamma-1/\gamma)}\right]} \quad \ldots (3.20a)$$

For choked flow where:

$$\frac{P_{exit}}{P_{0,in}} \leq \left(\frac{2}{\gamma+1}\right)^{(\gamma/\gamma-1)} \quad \ldots (3.20b)$$

The mass flow rate is calculated by:

$$\dot{m} = C_f A_{ref} \frac{P_{0,in}}{\sqrt{RT_{0,in}}} \sqrt{\gamma} \left(\frac{2}{\gamma+1}\right)^{\gamma+1/2(\gamma-1)} \quad \ldots (3.20c);$$

where $P_{0,in}$ and $P_{S,exit}$ are the inlet total and exit static pressure respectively, R is the gas constant and γ is the specific heat ratio. The reference area A_{ref} in the above equations is taken as the inlet area of the inlet port which is measured to be 1225.4 mm^2. Through this expression, the mass flow characteristics of the waste-gate valve can be represented by the average C_f for a given valve lift, plotted against the parameter l/d_{ref} which is the ratio of the valve displacement, or lift (l) to the reference diameter (d_{ref}) as shown in Figure 3.10. The product of flow coefficient and reference area ($C_f.A_{ref}$) is referred to as the effective area as previously defined and is included in Table 3.2 above for each valve lift.

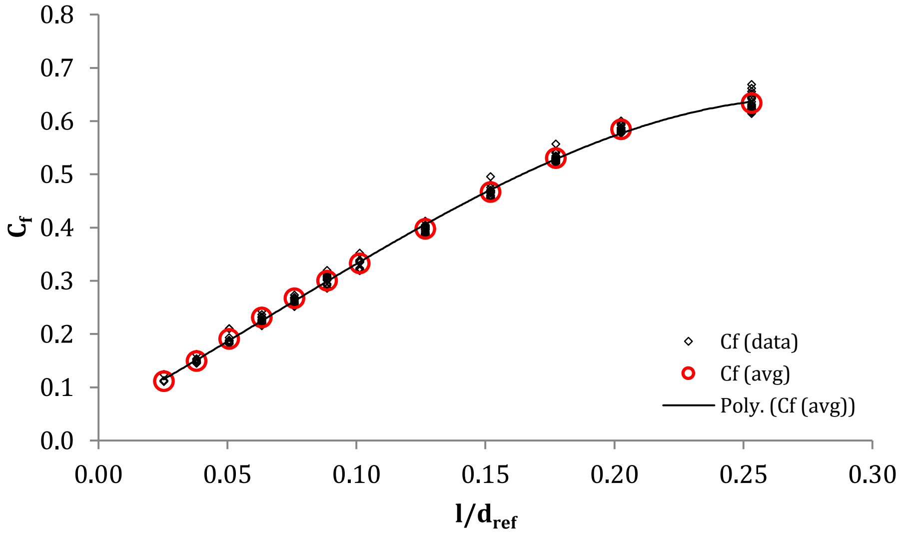

Figure 3.10 Flow characteristics of waste-gate valve represented by C_f versus l/d_{ref}

The characteristics established above allow the valve component to be defined in a 1-D engine simulation code. This procedure will be discussed later in the thesis.

3.15 Results for Steady State Experiments

The following sections discuss the steady state performance of the turbine under closed and opened waste-gate conditions with regards to its swallowing characteristics and efficiency. As mentioned, the experiments are carried out at five speed parameters. For every speed, the load imparted by the dynamometer is varied by adjusting the gap between the stator plates and the magnetic rotor. Once the load is applied, the air delivery valves are opened and adjusted until the turbine steadily rotates at the prescribed speed followed by subsequent logging of the relevant quantities for evaluation of turbine performance.

3.15.1 Swallowing characteristics

Figure 3.11 presents the mass flow parameter plotted against the measured total to static pressure ratio across the turbine. As seen in the "map", the measured swallowing characteristics conform to the characteristics of a typical radial turbine. For increasing pressure ratios (load), the rate of mass flow parameter increases as a function of speed until the flow begins to show signs of choking at higher pressure ratios, where the mass flow parameter lines converge asymptotically along the horizontal axis. The maximum value of mass flow parameter recorded occurs at PR = 2.87 for 2146 RPM/√K speed parameter. The highest measured pressure ratio is found to be 2.93 at 2462 RPM/√K with a mass flow parameter value of 3.068 x 10^{-5} kg.√K/s.Pa.

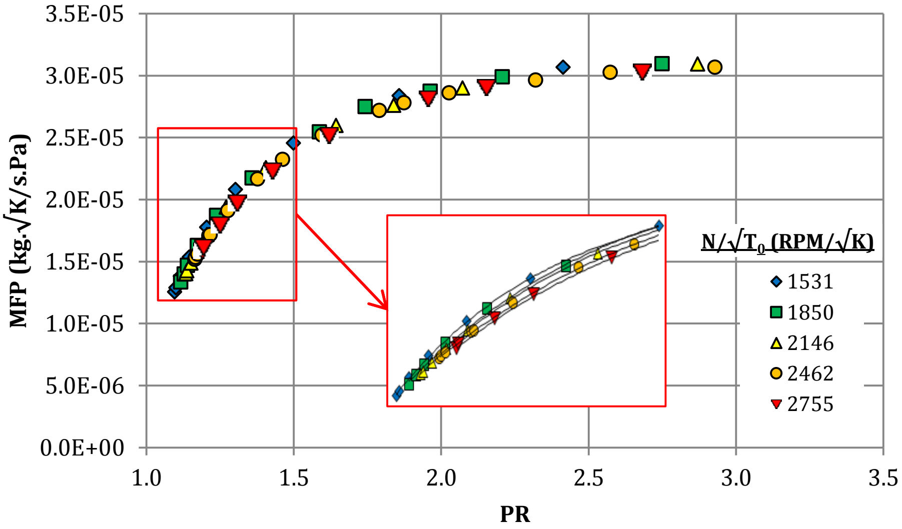

Figure 3.11 Steady state swallowing characteristics of the turbine and the spread of mass flow parameter measurement caused by the centrifugal field created by the rotor

One of the characteristics of a radial turbine is that the effect of the centrifugal field created by the turbine rotor results in mass flow rate being spread out and dependent on turbine speed. While this effect is rather minimal due to the small turbine size, it can still be seen at low pressure ratio regions as shown in the magnified section within Figure 3.11, where mass flow parameter curves seem to shift to higher pressure ratios for high speeds lines. The centrifugal effects become less significant as the pressure ratio is increased.

Another feature that can be observed is the significant width of the mass flow parameter measurement for a single speed line, demonstrating one of the advantages of the current test facility. In Figure 3.12 the same map is superimposed on a map provided by the turbine manufacturer (OEM) which was obtained from a conventional turbocharger facility and scaled here to achieve equivalent conditions. Taking the 2146 RPM/√K speed parameter as an example, the map covers the pressure ratio range of 1.73, between a minimum of 1.13 to a maximum of 2.87. For the sake of comparison, the OEM data spread at 2018 RPM/√K only accounts for 4.5% of this range. This is largely due to the loading device not being restricted by the aerodynamic limits of a compressor based system used in other facilities. The availability of a wider map is extremely helpful in engine simulation environments, which traditionally requires extensive extrapolation of the existing maps to encompass the whole operating range of the turbine on an engine. The OEM map does however encompass higher speed parameter range. In this respect, the OEM data was obtained at a maximum speed parameter of 4969 RPM/√K with highest recorded pressure ratio of 3.65.

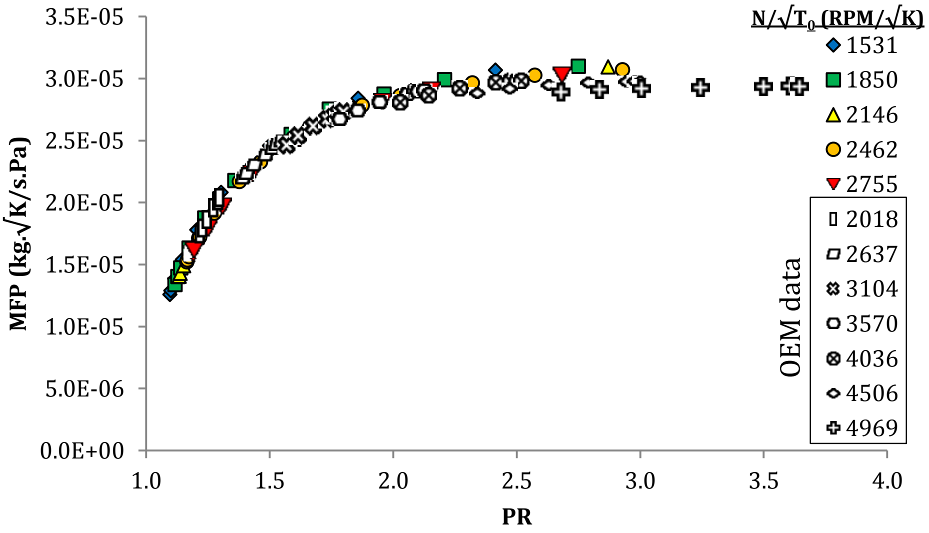

Figure 3.12 Comparison of swallowing characteristics with manufacturer map

3.15.2 Efficiency

The total-to-static efficiency of a turbine η_{TS} is given by the ratio of actual work ($\dot{W}_{act}$) produced by the turbine to the ideal isentropic work ($\dot{W}_{is}$) shown below:

$$\eta_{TS} = \frac{\dot{W}_{act}}{\dot{W}_{is}} \quad \dots (3.21)$$

The actual work (power) is obtained by direct measurement of torque and multiplying it with the angular velocity of the rotor as follows:

$$\dot{W}_{act} = \tau\omega = \frac{2\pi N}{60}\tau \quad \dots (3.22);$$

where *N* is the rotational speed in RPM.

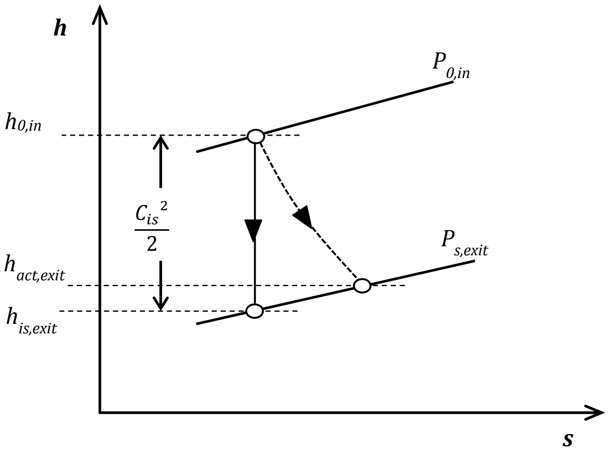

Figure 3.13 *h*-*s* diagram for turbine expansion

With reference to a turbine enthalpy versus entropy (*h*-*s*) diagram shown in Figure 3.13, the isentropic work (power) which is the ideal work produced from an isentropic expansion can be expressed as follows:

$$\dot{W}_{is} = \dot{m}\left(h_{0,in} - h_{is,exit}\right) \dots (3.23)$$

This can be expressed in terms of isentropic velocity C_{is}, to give:

$$\dot{W}_{is} = \dot{m}\frac{C_{is}^2}{2} \quad \dots (3.24)$$

$$C_{is} = \sqrt{2c_p T_{0,in}\left[1 - \left(\frac{P_{0,in}}{P_{S,exit}}\right)^{(1-\gamma/\gamma)}\right]} \dots (3.25)$$

The total-to-static efficiency of the turbine measured in the experiments is plotted against the velocity ratio and is shown in Figure 3.14 along with a third order polynomial fit applied to the data for reference. The efficiency curve is representative of a typical radial turbine where peak values are seen to occur close to 0.7 velocity ratio although the peak value of 0.713 is found at velocity ratio 0.627 for 2755 RPM/√K speed parameter. As with the mass flow parameter, the width of the efficiency data is also apparent and is seen to span between 0.223 (at 1531 RPM/√K) to 0.877 (at 2755 RPM/√K) velocity ratios. To give a more specific example, at 2462 RPM/√K, the data spreads from 0.337 velocity ratio up to 0.839.

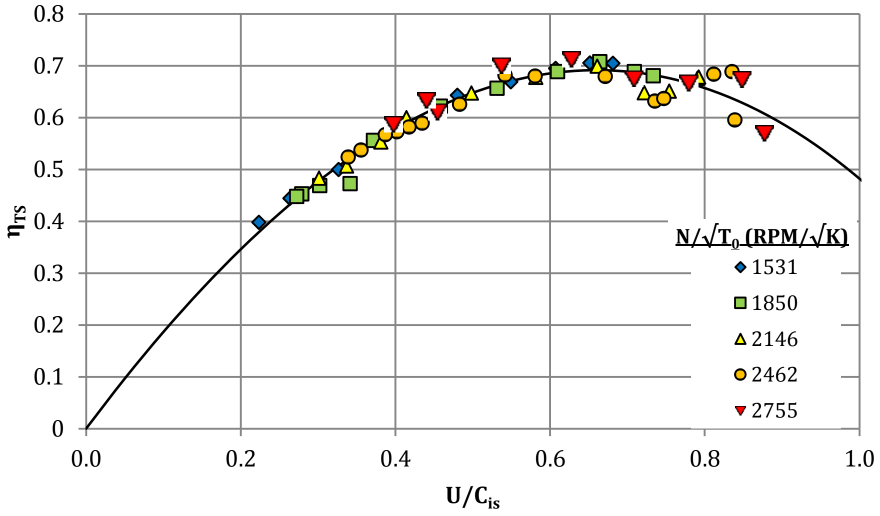

Figure 3.14 Total-to-static efficiency of the turbine plotted against velocity ratio

The uncertainty of efficiency is shown as error bars in Figure 3.15 below for two speed parameters. The measurement of total-to-static efficiency is seen to be more scattered at high velocity ratios. This is attributed to the uncertainty in the calculation of actual power at low loads which is largely due to uncertainty in torque measurement. For instance, at the highest velocity ratio for 2146 RPM/√K speed parameter, the computed actual power, calculated using Equation 3.22 is only 0.736 kW at 0.792 velocity ratio compared to 20.563 kW generated at velocity ratio 0.301.

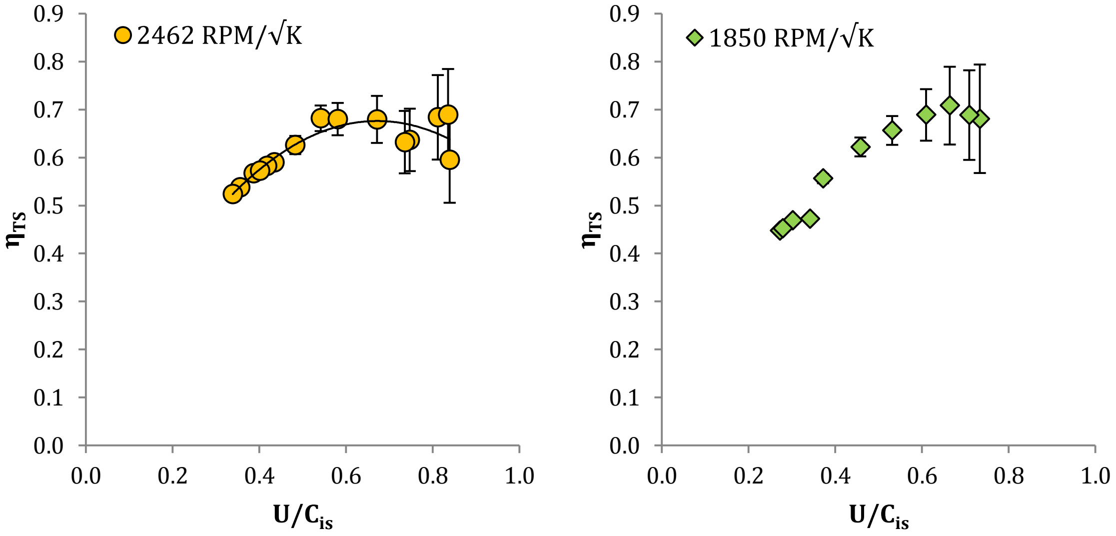

Figure 3.15 Efficiency shown with uncertainty bars for two speed parameter cases

For comparison, the range of performance parameters measured at minimum and peak power and peak efficiency for each corresponding speed parameters in the steady state experiments is summarized in Table 3.3.

Table 3.3 Range of measured parameters in steady state tests

$N/\sqrt{T_0}$ (RPM/√K)	Condition		PR	MFP (kg.√K/s.Pa)	U/C_{is}
1531	Max η_{TS}	*0.706*	*1.100*	1.289×10^{-05}	*0.654*
	Max $\dot{W}_{act}$ (W)	*12396.49*	*2.413*	3.068×10^{-05}	*0.223*
	Min $\dot{W}_{act}$ (W)	*461.13*	*1.096*	1.256×10^{-05}	*0.681*
1850	Max η_{TS}	*0.708*	*1.140*	1.470×10^{-05}	*0.677*
	Max $\dot{W}_{act}$ (W)	*18031.01*	*2.749*	3.097×10^{-05}	*0.272*
	Min $\dot{W}_{act}$ (W)	*581.94*	*1.116*	1.336×10^{-05}	*0.733*
2146	Max η_{TS}	*0.699*	*1.206*	1.720×10^{-05}	*0.659*
	Max $\dot{W}_{act}$ (W)	*20563.46*	*2.870*	3.094×10^{-05}	*0.301*
	Min $\dot{W}_{act}$ (W)	*697.75*	*1.133*	1.405×10^{-05}	*0.790*
2462	Max η_{TS}	*0.689*	*1.164*	1.519×10^{-05}	*0.837*
	Max $\dot{W}_{act}$ (W)	*23561.35*	*2.928*	3.068×10^{-05}	*0.339*
	Min $\dot{W}_{act}$ (W)	*840.98*	*1.166*	1.536×10^{-05}	*0.839*
2755	Max η_{TS}	*0.713*	*1.429*	2.233×10^{-05}	*0.620*
	Max $\dot{W}_{act}$ (W)	*21907.07*	*2.683*	3.030×10^{-05}	*0.398*
	Min $\dot{W}_{act}$ (W)	*978.59*	*1.190*	1.591×10^{-05}	*0.877*

As expected, the minimum power output occurs at the lowest speed and load. This is found to be 461.13 W at 1531 RPM/√K where the pressure ratio is measured as 1.096. The maximum power is recorded at 2462 RPM/√K and was found to be 21907.07 W.

As will be shown later in this chapter, the values of the performance parameters at maximum efficiency shown in Table 3.2 are useful in one of the map extrapolation procedures. These "optimum parameters", are used for normalizing the data and for curve-fitting purposes. A detailed description of this procedure is described later in the chapter.

3.15.3 Swallowing characteristics in opened waste-gate conditions

Steady state experiments are carried out at five intervals of waste-gate valve lifts ranging from 1.0mm to 9.0mm with the corresponding flow coefficient and effective flow area shown in Table 3.2. During the experiment, the measurement for each valve lift is carried out at consistent set of loads applied by the dynamometer. Figure 3.16 presents the swallowing characteristics of the turbine for 1850 RPM/√K for five levels of waste-gate lifts. The closed waste-gate map denoted as WG=0.0 mm is also included in the figure for reference.

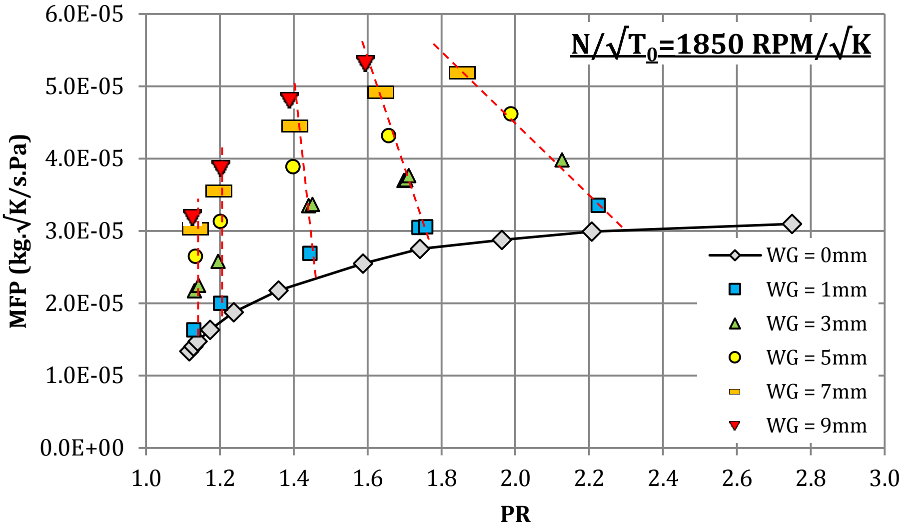

Figure 3.16 Mass flow parameter plotted against pressure ratio at different waste-gate valve lifts at constant 1850 RPM/√K speed parameter

The result show that mass flow parameter, which was recorded at the measurement plane, upstream of the waste-gate valve and the turbine, increases with the higher valve lift. This is anticipated since that more delivery air is required to drive the turbine at a prescribed speed and load due to some of the air bypassing the turbine stage. The highest recorded mass flow parameter for the 1850 RPM/√K shown in the Figure 3.16 was found to be 5.316x10^{-5} kg.√K/s.Pa observed at 9.0mm valve lift. This was attained at a pressure ratio of 1.593.

It is noticed that at high valve lifts, the gradient of the mass flow curves become higher and the choking mass flow increases. For a given dynamometer load applied to the turbine by adjusting the gap between the stator plates and the magnetic rotor, the measured pressure ratio across the turbine was found to decrease as the waste-gate opening was increased. This is shown in Figure 3.16 where dotted lines linking the mass flow parameter points for opened-waste-gate conditions indicate the same dynamometer gap. This effect was found to be more pronounced as the turbine load was increased. In other words, for the same turbine output power and speed the increase is mass flow parameter caused by opening the waste-gate is also accompanied by reduction in pressure ratio as more flow is bypassing the turbine. To further investigate the behaviour of pressure, the inlet total pressure is plotted against static exit pressure for different waste-gate lifts at the same speed parameter (1850 RPM/√K). This is shown in Figure 3.17.

It is rather interesting to note from Figure 3.17 that exit pressure of the turbine is no longer close to atmospheric at high loads. This behaviour is more distinct as the valve lift is increased.

The high pressure at the exit means that higher inlet pressure is required to deliver a given pressure ratio. Taking the extreme case in the measurement, the highest exit pressure is measured to be 154684.4 Pa at 7.0 mm valve lift. It can be drawn that the presence of the waste-gate induces back pressure at the turbine exit with the effect more noticeable as more flow is waste-gated. This is due to the present experimental setup with the waste-gate flow reconnected to the turbine exit duct at a 90° angle. A higher waste-gate flow results in higher pressure stagnating at the flow junction, thereby inducing higher back pressure at the turbine exit region.

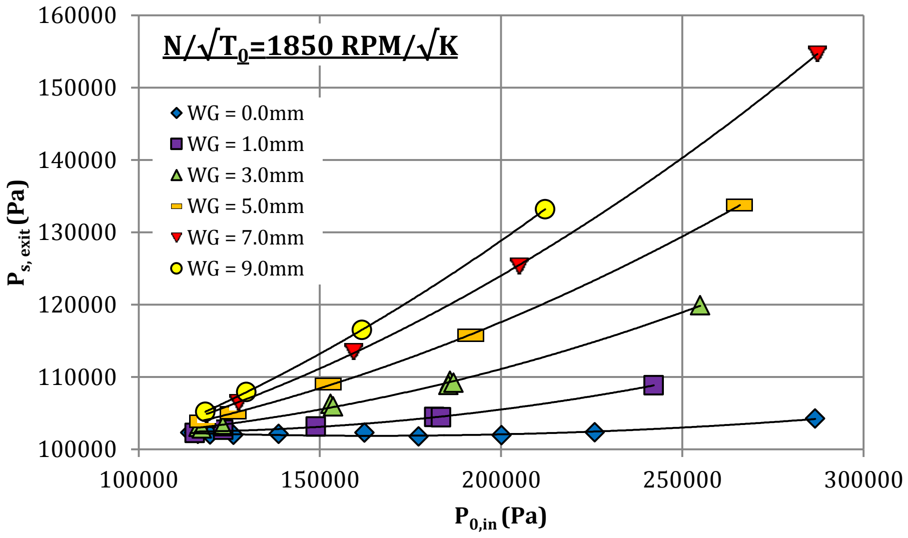

Figure 3.17 Turbine exit static pressure plotted against total inlet pressure at constant speed and different waste-gate valve lifts

3.15.4 Interaction between waste-gate and turbine swallowing characteristics

With the measured mass flow characteristics of the turbine under closed and opened waste-gate conditions and those of the waste-gate, it is possible to carry out further analysis to see the interaction between the two devices. The aim is to examine whether or not the waste-gated turbine characteristics can be estimated by a standard mass flow map.

Figure 3.18 compares the swallowing characteristics of the turbine under closed and opened waste-gate conditions along with waste-gate mass flow characteristics at 3.0mm and 5.0mm valve lift. It is initially thought that the mass flow rate going through the turbine under the waste-gated condition (MFP_{wg}) can be predicted by summation of mass flow rate through the turbine and the waste-gate ($MFP + MFP_{wg}$). However, this does not seem to be the case as the predicted mass flow parameter (MFP_{pred}), shown as dotted line in the figure, is higher than the actual measurement. Taking the case of the 3.0mm valve lift, at *PR*=1.5, the predicted turbine mass flow is found to be 3.6747x10^{-05} kg.√K/s.Pa as opposed to a measured value of 3.4420 x10^{-05} kg.√K/s.Pa yielding a 6.76% difference. Similar findings are also experienced by Capobianco and Marelli (2007) for their internally waste-gated turbine. The authors attributed this to the reduced effective pressure ratio across the rotor passage and the waste-gate port. The authors remarked that a higher pressure drop exists between the inlet measurement plane and the entry section of both the turbine stage and the waste-gate section when the mass is flowing in both devices. This however can only be confirmed by having additional pressure measurements along the system.

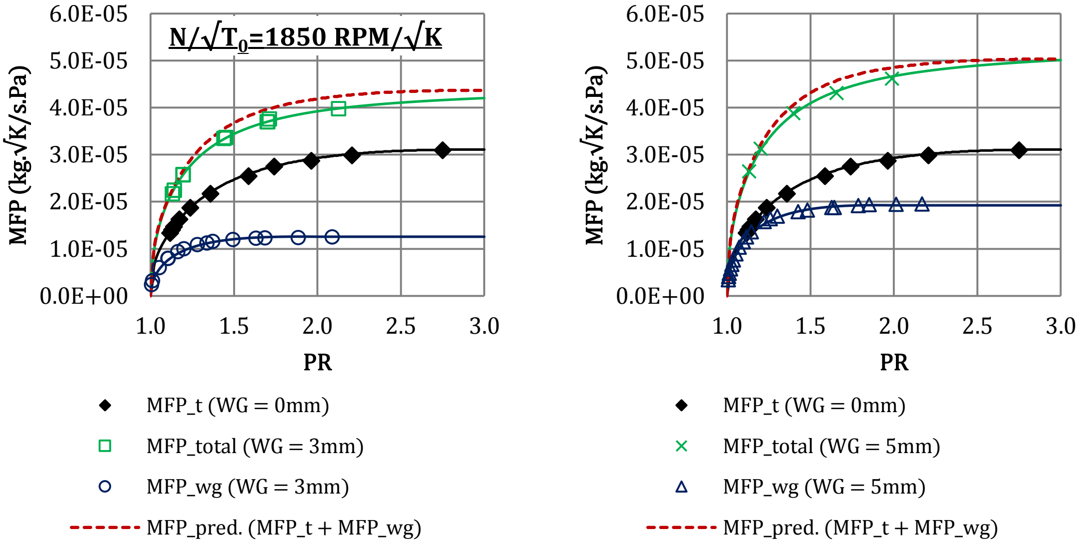

Figure 3.18 Prediction of mass flow parameter compared values recorded for turbine under closed and opened waste-gate conditions along with waste-gate mass flow parameter

In any case, it can be deduced that the swallowing characteristics of a waste-gated turbine cannot be adequately predicted by adding the mass contributions through the each devices. On this account, the conventional practice of modelling a waste-gate flow as simply a leakage of mass through the turbine is inadequate in representing the actual behaviour of the system.

3.15.5 Effect of waste-gate on turbine efficiency

Similar to closed-waste-gate conditions, the efficiency of the turbine under waste-gated conditions can be evaluated. This is presented by plotting the turbine efficiency against velocity ratio and pressure ratio as shown in Figure 3.19 for speed parameter 1850 RPM/√K.

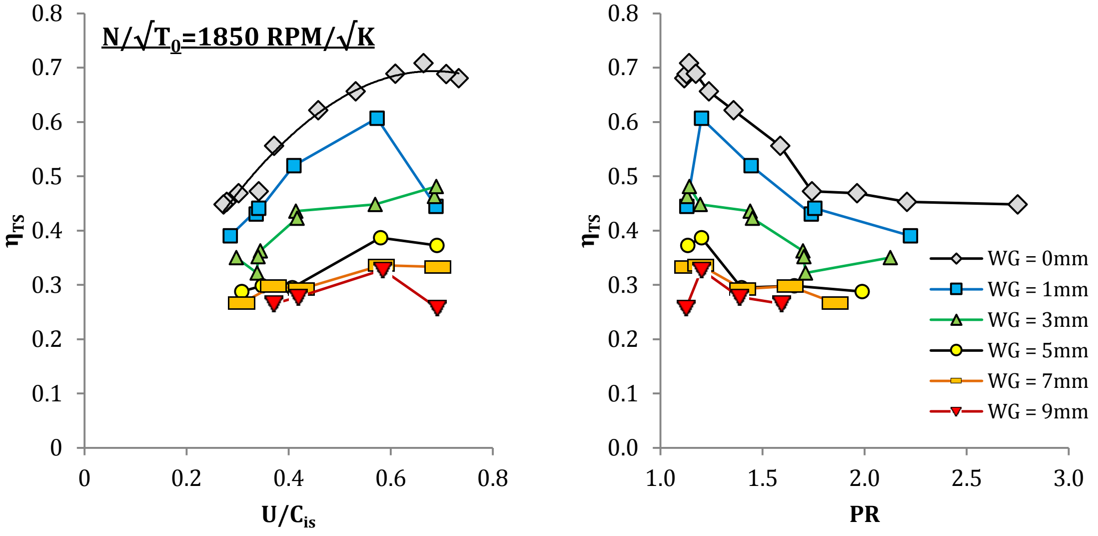

Figure 3.19 Efficiency characteristics of waste-gated turbine at constant speed parameter under different levels of waste-gate valve lift

The measured turbine efficiency is seen to drop as the waste-gate valve lift increases. This is consistent with the findings of Marelli and Capobianco (2011) for an internally waste-gated turbine. Due to increased mass flow rates at the inlet, the available isentropic power also increases with increasing valve lift. Since the turbine is producing the same amount of actual power regardless of waste-gate lift, the resulting efficiency will therefore decrease. In Figure 3.19 the apparent efficiency of the turbine can be seen to drop by 53.7% from 0.708 down to 0.328 at the peak efficiency point from the closed waste-gate condition to a 9mm lift.

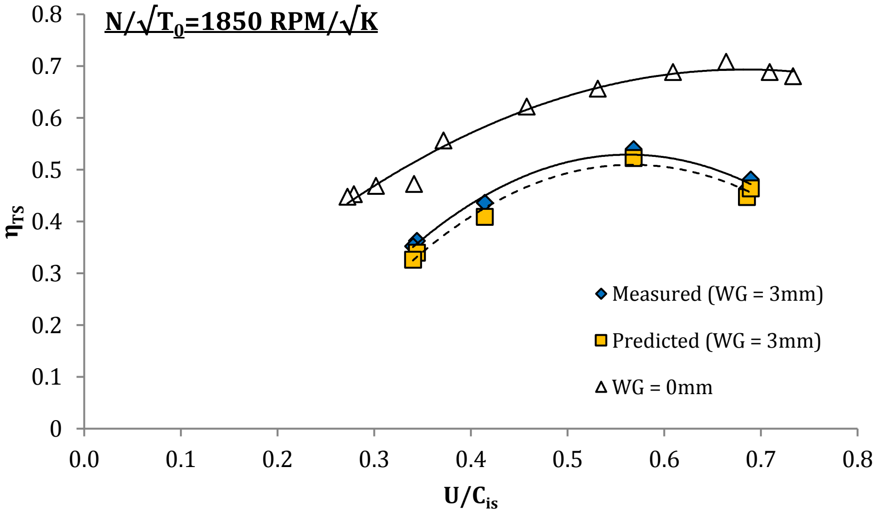

Figure 3.20 Comparison between measured and predicted efficiency through summation of turbine and waste-gate mass flow rate

In the preceding section, it was demonstrated that the actual mass flow through the turbine in waste-gated conditions is different to that predicted by summing the mass flow through the individual flow components, i.e. the turbine and the waste-gate valve. The higher mass flow rate predicted will result in lower calculated values of efficiency due to the mass flow rate being a component in the calculation of isentropic power. This can be demonstrated for the 3.0 mm valve lift case and is shown in Figure 3.20 below. For the specific case shown, the deviation of predicted efficiency is in the range of 3.0% to 7.4%.

3.16 Effect of Experimental Data Range on Turbine Map Extrapolation

In modern engine simulation software, it is common for the turbocharger system to be represented as a boundary within the engine piping layout, in the form of look-up tables. During a simulation, it is not uncommon for the engine to run in conditions where the turbocharger operating points are outside those defined in the maps. This will numerically destabilize the solution and lead to errors in the prediction of the engine performance. To prevent this, the maps have to be extended to include the range of operations that are beyond those in the limited data range.

The current method of map prediction used by engine simulation software is based on various curve fitting techniques which are used to interpolate and extrapolate the original data. While extending the range of the map is necessary to ensure the stability of the simulation, the map extension methods are developed based on limited range of experimental data, hence the need for experimental validation against wider data range. Therefore, this section of the chapter aims at evaluating the current method employed by a mainstream 1-D engine simulation code by way of comparing the predicted map with experimentally measured data. When considering turbocharger map prediction methods for use in 1-D simulation codes, great emphasis has to be given to the simplicity as well as the accuracy of the model. In view of this, the present work involves the evaluation of a model that is adopted by a commercial engine simulation software, namely GT-Power. The approach taken for the present work is to focus the investigation on this modelling method and evaluate its accuracy and its impact on the overall engine performance calculation which will be discussed in Chapter 5.

The concept of GT-Power map fitting is based on the normalization of efficiency, velocity ratio and mass flow parameters by their values at maximum efficiency for all speed lines. The rationale behind this is that the data points of efficiency and mass flow for all speed line will end up being on a single line thus allowing the map to be extended by fitting a single curve on respective efficiency and mass flow against velocity ratio plots.

3.16.1 Map extrapolation method

From a turbine performance map, the maximum efficiency points are identified for all speed lines giving and the "optimum" values of pressure ratio (*PR_{opt}*), velocity ratio ($U/C_{is,opt}$) and mass flow parameter (*MFP_{opt}*). The mass flow ratio (*MFR*) is then defined as the optimum mass flow parameter divided by the largest among all of the optimum mass flow parameter values among the speed lines (*$MaxMFP_{opt}$*) as shown below:

$$MFR = \frac{MFP_{opt}}{MaxMFP_{opt}} \quad \ldots (3.26)$$

The optimum velocity ratios for each speed line is identified and divided by the largest value amongst them (*$MaxU/C_{is\,opt}$*), giving the (*U/C_{is}) Ratio* as follows:

$$\left(\frac{U}{Cis}\right) Ratio = \frac{U/C_{is_{opt}}}{MaxU/C_{is_{opt}}} \quad \ldots (3.27)$$

Following this, polynomial curves are fitted on the optimum pressure ratios (3rd order polynomial), the mass flow ratios (3rd order polynomial) and maximum efficiencies (linear fit) versus speed parameter as demonstrated in Figure 3.21(a). This gives each optimum parameter in the map a corresponding speed parameter value. Another curve is fitted on the (*U/C_{is}*) *Ratio* against optimum pressure ratio shown in Figure 3.21(b) based on the assumption that the optimum velocity ratio for each speed line increases proportionally with optimum pressure ratio.

From the data, normalized values of velocity ratio, (U/C_{is})$_{norm}$, and efficiency (η_{norm}) are calculated for each pressure ratio point in the map. The normalized velocity ratio is the velocity ratio of each data point in the map divided by the optimum velocity ratio.

$$\left(\frac{U}{Cis}\right)_{norm} = \frac{U/C_{is}}{U/C_{is_{opt}}} \quad \ldots (3.28)$$

The normalized efficiency is the efficiency at each point divided by the corresponding maximum efficiency of all speed lines.

$$\eta_{norm} = \frac{\eta}{\eta_{max}} \quad \ldots (3.29)$$

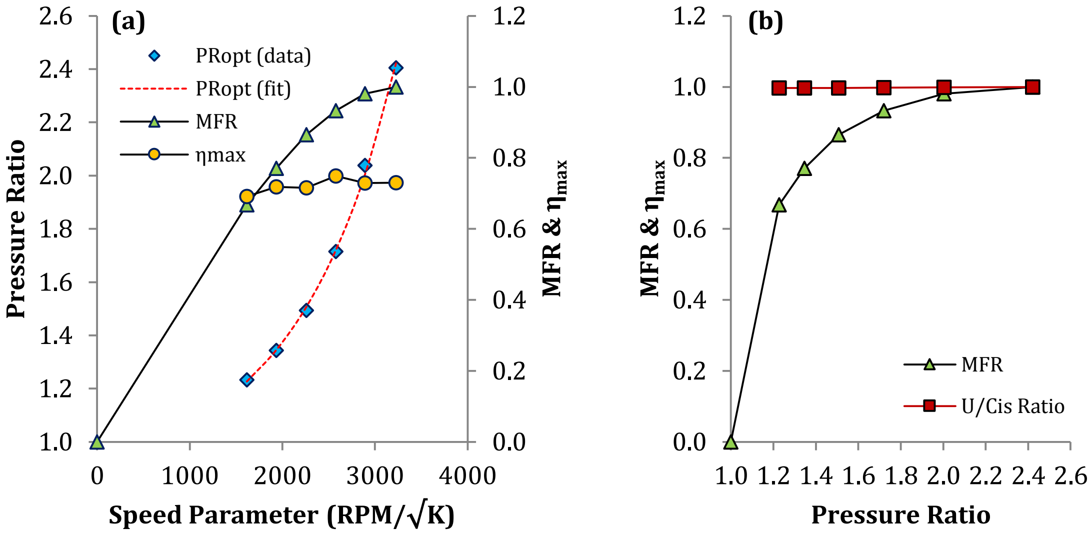

Figure 3.21 Optimum values plotted against (a) Speed parameter and (b) Pressure ratio

At this stage in the procedure, all the derived mass flow ratios and normalized efficiencies should lie on single lines in order for the extrapolation to be carried out. The normalized efficiency is plotted against $(U/C_{is})_{norm}$ after which two curves are fitted for low velocity ratios $(U/C_{is})_{norm} < 1$, and high velocity ratio, $(U/C_{is})_{norm} \geq 1$ as follows:

$$\eta_{norm} = 1 - \left[1 - \left(\frac{U}{Cis}\right)_{norm}\right]^{b} \qquad \left(\frac{U}{Cis}\right)_{norm} < 1 \qquad \text{... (3.30);}$$

$$\eta_{norm} = 1 - c\left[\left(\frac{U}{Cis}\right)_{norm} - 1\right]^{2} \left(\frac{U}{Cis}\right)_{norm} \geq 1 \qquad \text{... (3.31);}$$

where *b* is the constant to control the curve of the low $(U/C_{is})_{norm}$ efficiency fit and *c* controls the fit of the efficiency curve at high $(U/C_{is})_{norm}$. The constant *c* is calculated from intercept of the efficiency curve with the $(U/C_{is})_{norm}$ axis, Z_0; this has a value of 1.92 in Figure 3.24. The relation between *c* and Z_0 is given as:

$$Z_0 = 1 + \frac{1}{\sqrt{c}} \qquad \text{... (3.32)}$$

Similarly, a curve is fitted to the *MFR* against $(U/C_{is})_{norm}$ plot using the following equation:

$$MFR = cm + \left(\frac{U}{Cis}\right)_{norm}^{d} (1 - cm) \quad \text{... (3.33);}$$

where the mass coefficient cm is the intercept of the curve at 0.0 $(U/C_{is})_{norm}$ and d is an exponent coefficient that controls the curvature of the curve. The values of efficiency and mass flow are extrapolated over the entire range of pressure ratio.

3.16.2 Comparison between wide and narrow map extrapolations

To evaluate the map extrapolation method employed in engine simulation codes, an investigation into the effect of map width on the prediction of turbine performance by a 1-D gas dynamics code was carried as part of this study and its findings were published by Pesiridis et al (2012)[2]. The work was based on the performance data of a mixed flow turbine tested by Szymko (2006) as part of the development of the dynamometer used in this study. The aim of the investigation is to see if the extrapolation carried out on a typical turbine map with a limited range of data can accurately represent the actual characteristics of a turbine. Therefore, two maps of the same turbine with different range (width) of data are needed.

To obtain different map data widths, the dataset of the experimental map is reduced to represent a typical narrow map that would normally be provided by manufacturers. The comparison between the original wide map and the reduced narrow map is shown in Figure 3.22 and Figure 3.23 for mass flow parameter and efficiency respectively. Following this, the maps are extrapolated using the extrapolation method described above and the output is compared with the original experimental map.

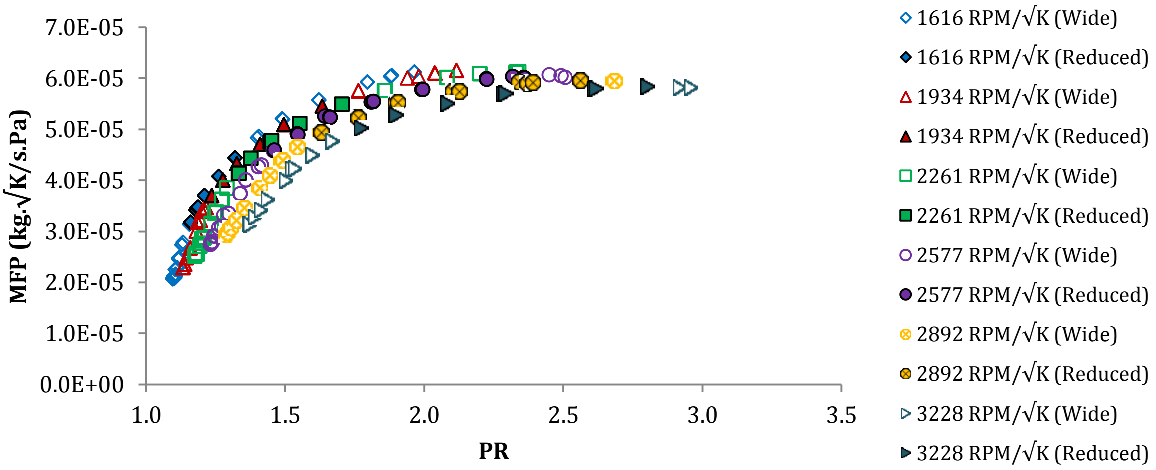

Figure 3.22 Wide and reduced (narrow) swallowing characteristics map used for map extrapolation analysis

---

[2] This part of the study was presented at the 10th International Conference on Turbochargers and Turbocharging, 15-16th May 2012, London. The work was carried out by Salim and intended from the outset to be part of this thesis, Pesiridis and Martinez-Botas acted in supervisory roles.

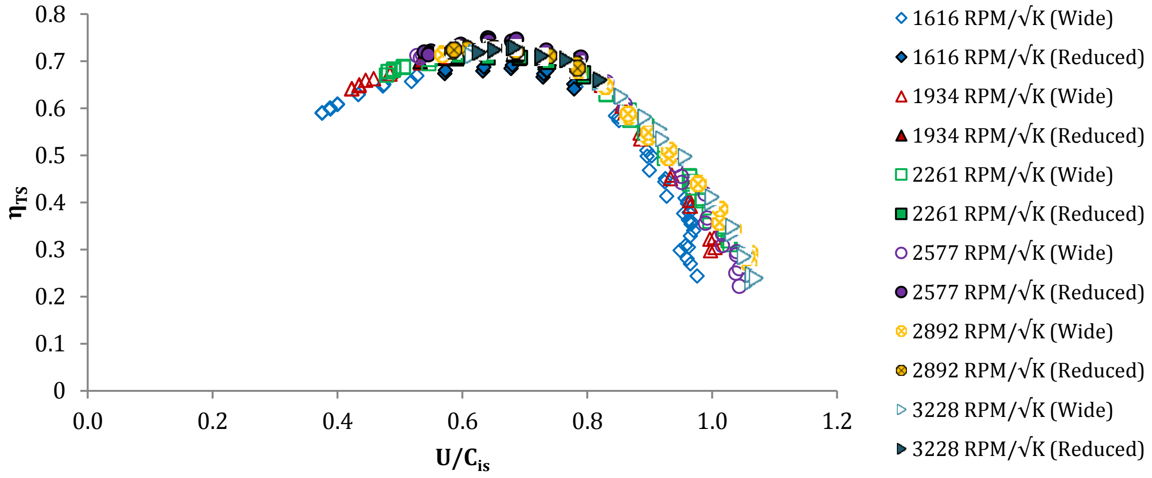

Figure 3.23 Wide and reduced turbine efficiency map used for map extrapolation analysis

3.16.3 Predicted turbine performance through extrapolations

The extrapolation for mass flow ratio against velocity ratio is shown in Figure 3.24 for the reduced map. Also included in the graph, is the extrapolation line based on the wide data set labelled as "fit (wide)". Clearly, it is seen that the use of different map ranges has produced a significant difference in the extended region of the data. The use of the narrow map data range results in approximately 5.4% higher mass flow ratio intercept at zero normalized velocity ratio compared to that obtained with wider map data. At high velocity ratios, the effect of using a narrower map ranges is more pronounced; again with the narrow map intercepting higher normalized velocity ratio. This effect is likely due to failure of the procedure to take into account the curvature within the experimental data, hence the flatter mass flow ratio curve compared to that of the wide map. Consequently, the procedure will predict higher mass flow rates as the velocity ratio point is shifted away from the maximum efficiency points. The same effect is observed for the extrapolation of efficiency in Figure 3.24. In terms of efficiency, there is only a slight difference in the extrapolated curves at low normalized velocity ratio. However, at high velocity ratios the reduced map results in the over-prediction of Z_0 (see Equation 3.32), that is the zero efficiency intercept at high velocity ratio. For the wide map, the extrapolated line intercepts the normalized velocity ratio at 1.747 while the reduced map extrapolated line intercepts at 1.915.

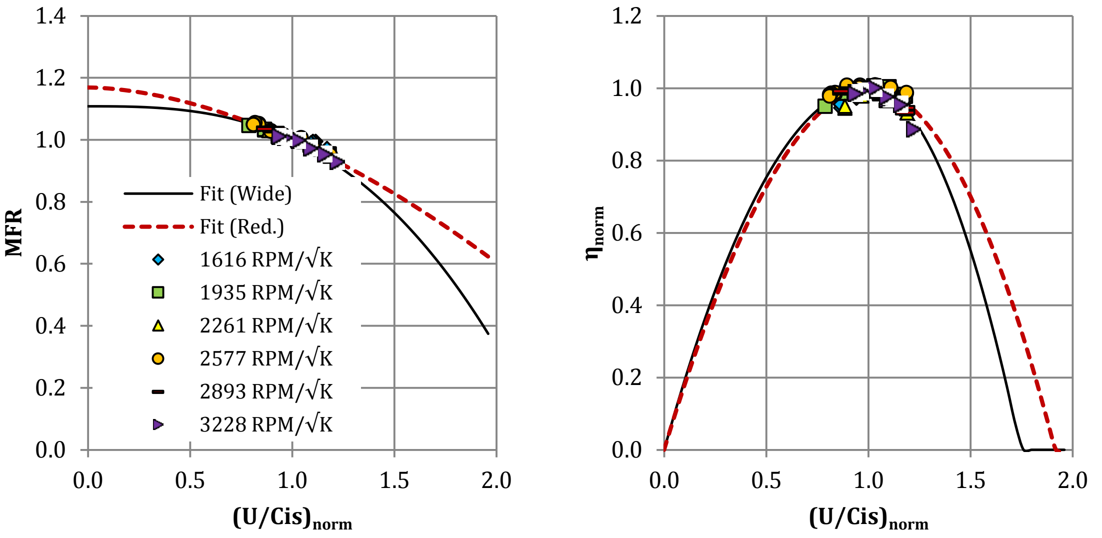

Figure 3.24 Mass flow ratio and normalized efficiency extrapolation

The shapes of the curves depend on the coefficients imposed in the equations that are used for the extrapolations. The values of these coefficients which are imposed by the map processor are shown in Table 3.4 for the different maps used in this investigation. Clearly, with limited data range, the failure of the extrapolation method to account for the curvature of the mass flow ratio data has resulted in extrapolation points to be more spread out over the velocity ratio.

Table 3.4 Values of coefficients used in map extrapolation

Coefficient	**Values used in extrapolation**	
	Wide map	**Reduced map**
MFR: (cm)	*1.10824*	*1.1689*
MFR: (m)	*2.84423*	*1.74188*
η_{norm}: (b)	*2.01765*	*1.87024*
η_{norm}: (z_0)	*1.74707*	*1.91531*

When compared with the actual data, it can be seen in Figure 3.25 that at low speeds, the predicted mass flow parameter agrees well with the experimental data. However, at higher speeds, the difference in mass flow prediction is slightly higher in the low pressure ratio region. The maximum discrepancy between the extrapolation, based on the narrow map, and the experimental data was found at a pressure ratio of 1.352. The extrapolation procedure at this point predicts a 7.3% higher mass flow. This was anticipated earlier as the *MFR* extrapolation for the narrow map sat above that for the wide map in the high velocity ratio region.

The prediction of efficiency parameter based on the reduced map is shown in Figure 3.26 with experimental data points for two speed-lines. It was explained earlier that efficiency-velocity ratio fit is carried out separately for low and high normalized velocity ratio values. The results in this figure show that at high pressure ratios (low velocity ratios), the predicted efficiency curve from the reduced map is slightly lower than experimental results but generally fits well to the measured data. For the 2892 RPM/√K case, above a pressure ratio of approximately 1.90, the difference was found to be less than 2% in all cases and less than 1% in most cases. For the 1934 RPM/√K case between pressure ratios of 1.33 and 1.95 the difference between the experimental results and the extrapolation is less than 2%. At higher pressure ratios the extrapolation falls below the experimental data, the discrepancy is -2.7% at the highest measured pressure ratio of 2.11. These results suggest that for the high pressure ratio region of the maps the prediction of the efficiency curve is relatively insensitive to the width of the available data with the narrow map allowing a reasonable extrapolation to predict the full turbine map.

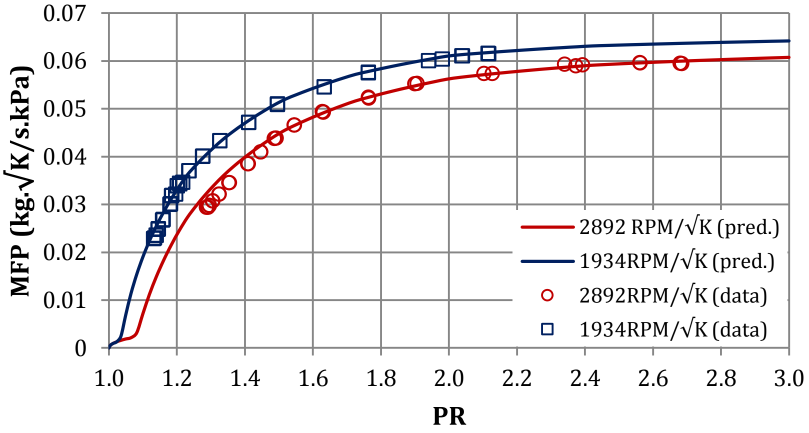

Figure 3.25 Mass flow parameter predicted based on reduced map compared with experimental data

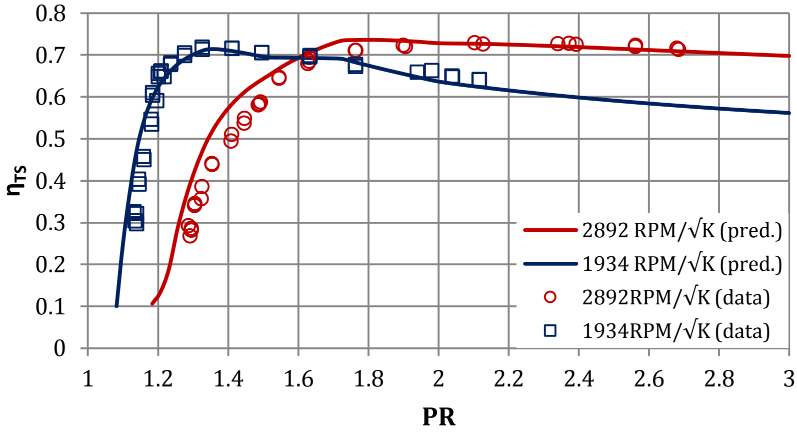

Figure 3.26 Efficiency predicted based on reduced map compared with experimental data

At high velocity ratio (low pressure ratio) a greater difference is found between the experimental results and the extrapolation. For the 2892 RPM/√K case the maximum discrepancy was found to be 45% between the extrapolation and the experimental data, this was at a pressure ratio of 1.29. For the lower speed case the greatest discrepancy was 58% at a pressure ratio of 1.13. It can be seen from Figure 3.21 that the value of Z_0 is drawn outwards due to the absence of data points, thereby predicting higher efficiency compared to the wide map case. Because of the steep nature of the efficiency curve in this region a small difference in pressure ratio, or velocity ratio, can lead to a large difference in the predicted turbine efficiency. This makes the extrapolation of the turbine map in this region particularly sensitive to the width of the available data. In the context of engine simulations, such large difference between the predicted and actual turbine efficiency would lead to errors in the prediction of engine performance and consequently affecting the later stages of engine design, development, testing and homologation. Having an accurate representation of the turbine performance in the simulation stage will minimize the need for re-matching of the engine boosting systems and engine calibrations.

3.17 Summary

This chapter reports the experimental work that has been carried out to evaluate the steady state performance of an externally waste-gated turbocharger turbine. It then goes on to study the effect of experimental data range on the extrapolation of turbine performance in relation to the numerical simulation of a turbocharged internal combustion engine. The description of the test facility was provided along with the necessary instrumentation for measurement of turbine performance parameters.

3.17.1 Effect of waste-gating on turbine performance

Two sets of experiments have been carried out. The first set of experiments was performed to obtain the standard turbine characteristics under closed waste-gate conditions on the Imperial College dynamometer. This allowed a much wider range of data to be collected than was available from the manufacturer-supplied turbine maps. The second set of experiments was performed on an externally waste-gated turbine. A waste-gate valve was installed upstream of the turbine and the method of characterizing the waste-gate valve was demonstrated. The experiments were carried out at various levels of waste-gate valve opening areas, which are represented by the valve lift. A summary of the results are listed below:

1. The steady state experiment carried out on the turbine under closed waste-gate conditions enabled the characterisation of the turbine performance over a wide range of conditions in comparison to the map provided by the manufacturer for the same turbine. Swallowing characteristics of the turbine were obtained at pressure ratios ranging from 1.09 to 2.92. Efficiency data is spread between 0.2 to 0.8 velocity ratios.
2. Under waste-gated conditions the turbine was tested at five waste-gate valve lifts. The results show that the system mass flow increases with the increase in valve lift due to gas flow bypassing the turbine stage through the waste-gate. Results showed that for a given load, set by adjusting the dynamometer magnetic brake (gap between the stator plates and the magnetic rotor), the turbine pressure ratio decreases along with the increase in turbine mass flow parameter. Closer examination of the pressure measurements at the inlet and exit of the system reveal that the exit static pressure increases under waste-gated conditions. This was caused by the flow stagnating at the junction in the exit pipe where the flow from the waste-gate is reconnected to the main flow downstream of the turbine stage.
3. It was also revealed that the mass flow rate through the system under waste-gated conditions cannot be assumed as the summation of mass flow passing through the turbine stage and the waste-gate valve if they were operating independently of each other. What is seen in the experiment is that as the waste-gate area is increased, the mass flow rate through the system is actually lower than that predicted by adding the mass flow rate from the waste-gate characteristic data and the turbine mass flow rate obtained under closed waste-gate conditions. This can be attributed to the flow losses within the additional piping setup and the added geometrical complexity of the system. A similar finding was also encountered by studies on internally waste-gated turbines by Capobianco and Marelli (2007) although the close arrangements of components in such devices is expected to be more susceptible to further losses due to flow mixing at the turbine exit.

3.17.2 Effect of experimental map width on turbine performance extrapolation

An evaluation of the map prediction procedure employed by a commercial 1-D gas dynamics code was carried out and was presented in this chapter. The map extrapolation procedure was described and its accuracy at predicting a turbine map was assessed. For this purpose, a wide experimental map was reduced such that its data range is similar to a typical manufacturer map. Then, the map extrapolation method was carried out on the wide and reduced map and the results are compared with experimental data. The outcome of this analysis reveals that there is indeed a difference in the predicted maps. The summary are given as follows:

1. The extrapolation method, when imposed on the narrow map results in prediction of higher mass flow rates at low pressure ratio. The maximum difference between extrapolation on the wider experimental data and the extrapolation based on the narrow map was found to be 7.3% at a pressure ratio of 1.352.
2. The predicted efficiency was also affected by the map width. Without the availability of experimental data at high velocity ratios, the extrapolation method over-predicts the intercept of the zero efficiency at higher velocity ratio, leading to an overestimate of efficiency in the high velocity ratio region. Using the narrow map, the zero efficiency point was predicted at a velocity ratio of 1.915. Using the wide map, this value was predicted to be at a velocity ratio of 1.747. In the low velocity ratio region, the agreement between the wide and narrow map extrapolations fared better. At high pressure ratios, the efficiency predicted by the extrapolation is less sensitive to the width of the data. At low pressure ratios, the discrepancy in prediction of efficiency can be as large as 58% observed at the low speed case.

Chapter 4 Turbine Performance under Pulsating Inlet Conditions

4.1 Introduction

This chapter discusses the work undertaken to investigate the effects of unsteady inlet conditions on the behaviour of the turbocharger turbine. The experiments are carried out under various conditions with regards to the characteristics of the inlet flow and waste-gate configurations. In the sections to follow, the experimental test configurations are described followed by necessary procedures taken to calibrate the various instruments used in the experiment. Following this, the results of the experiments are presented and discussed. This begins with the results of testing under closed waste-gate conditions where the performance of the turbine is measured under different loads and inlet pulse frequencies. Included in the discussion is the evaluation on the level of unsteadiness observed in the turbine behaviour. Then, the test results for unsteady performance of the turbine under waste-gated conditions are analysed. The discussions address the effects of varying waste-gate openings on the behaviour of the turbine. One-dimensional prediction of turbine performance under waste-gated conditions forms the final section of the chapter.

4.2 Test Configurations

The experiments are carried out to analyse several aspects of unsteady waste-gated turbine performance under various inlet conditions. Therefore, the unsteady test conditions are configured to include variations of turbine speeds, operating loads, pulse frequencies and waste-gate openings and are shown in Table 4.1 below.

Table 4.1 Test configurations

Speed Parameter (RPM/√K)	**Waste-gate valve lift (mm)**	**Turbine Load (PR)**	**Pulse Frequency (Hz)**
1850	0, 1, 3, 5	Low, Medium, High	20, 40, 60, 80
2146	0, 1, 3, 5	Low, Medium, High	20, 40, 60, 80

The test configurations above result in a total of 96 test points. The range of test points is limited by factors related mostly to operational capability of the test facility and safety procedures. For instance, the turbine rotational speed limit and vibration levels have to be observed during testing. It was often found that the bearing temperatures and vibration levels are relatively high during high speed operations in this test facility. In addition, the test configurations also have to take into account the increase in the amount of delivery air during waste-gated operations, especially at high turbine loads and large waste-gate openings. However, the dominating factor governing the limit of unsteady testing is the durability of the instruments, in particular, the sensitive hotwire probes. It was observed during the tests that the 10μm Tungsten hotwires tend to reach their operational limits at mean mass flow rates of ≈ 0.18 kg/s before breaking. It should be noted that over a pulse cycle during unsteady tests, the peak mass flow rate can be much higher than this value.

4.3 The Pulse Generator System

To achieve realistic flow conditions experienced at the turbocharger turbine inlet, it is necessary to replicate the pulsating nature of the exhaust gas in the test facility. This is achieved by means of a pulse generator located immediately upstream of the measurement plane. A CAD drawing of the system is given here in Figure 4.1. The device consists of two counter-rotating chopper plates with specific cut-outs to produce the desired pulse shape. The pulse is generated through linear opening and closing of cut-out flow area which occupies one-third (120°) of the pulse cycle (Figure 4.2). A DC motor is used to drive two belts which rotate the chopper plates via a pulley system. Another special feature of the pulse generator system is that the chopper can be configured to be out of phase with each other. Photos of the different chopper plate configurations are included in Figure 4.1. This is particularly useful when replicating real engine conditions where valve overlaps may incur out-of-phase exhaust gas flow conditions.

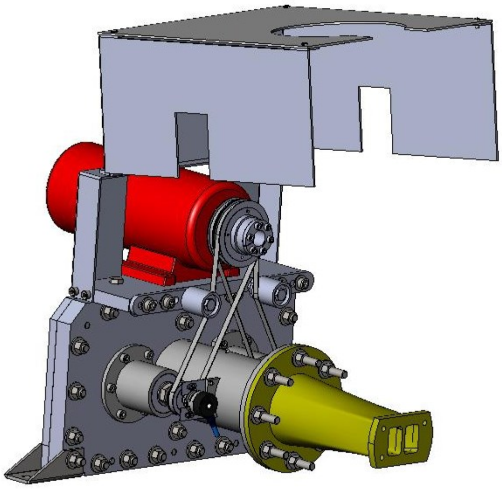

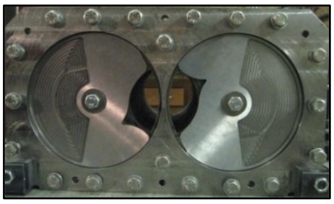

In-phase configuration

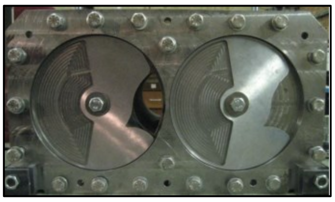

Out-of-phase

Figure 4.1 CAD drawing of the pulse generator shown with photographs of chopper plate configurations

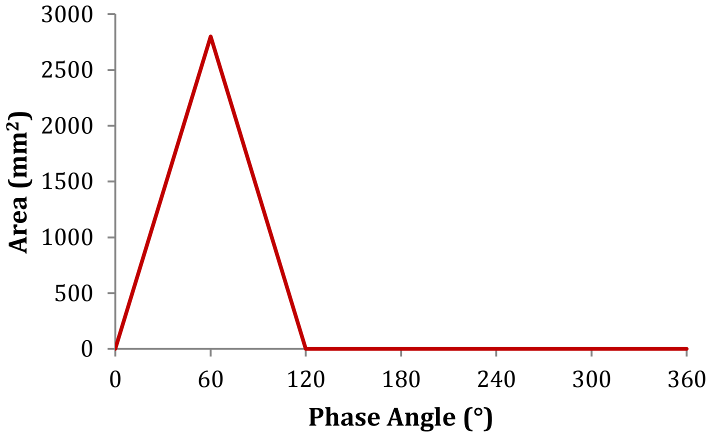

Figure 4.2 Chopper plate opening area with respect to angle of rotation

4.4 Measurement of Unsteady Parameters

The measurement of instantaneous quantities under pulsating flow conditions was carried out at various locations along the experimental layout. The measurement points are shown schematically in Figure 4.3 and the description of each measurement system is provided in the following sections.

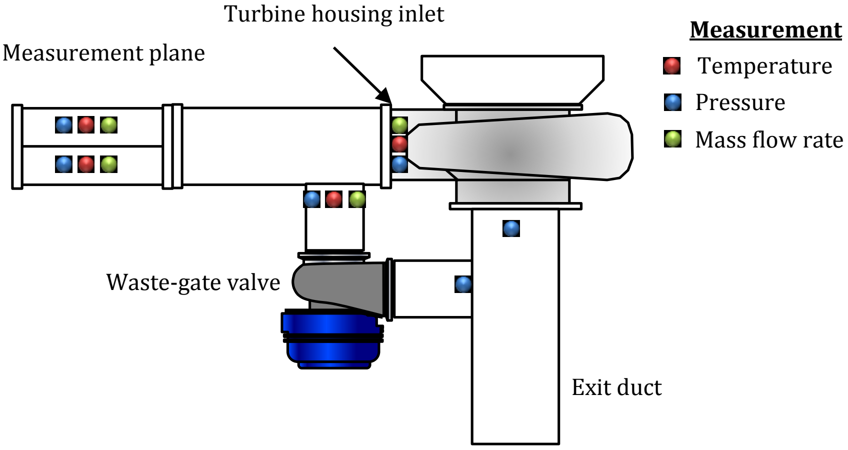

Figure 4.3 Schematic diagram showing measurement locations for testing of waste-gated turbine unsteady performance

4.4.1 Instantaneous pressure measurement

Instantaneous pressure is recorded using strain gauge pressure transducers (*Schaevits* P704-0001), which are rated for the range of 0 to 3.5 bar gauge pressure. The pressure transducers are connected directly to a high speed bridge input module (NI 9237) on the cRIO chassis. These pressure transducers were calibrated using a portable calibration unit (*Druck* DPI 610). The pressure transducers gave a linear correlation between pressure and voltage outputs as shown for the unit installed for the outer limb pressure measurement in Figure 4.4.

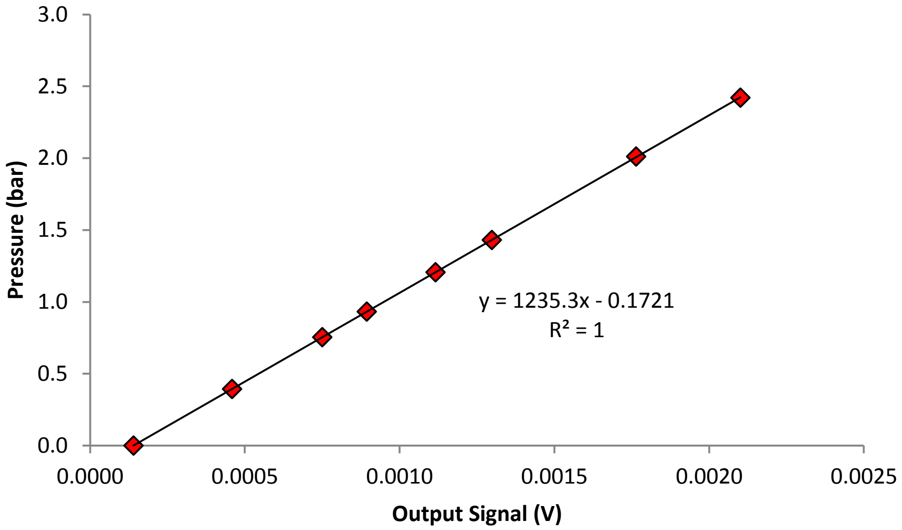

Figure 4.4 Calibration of pressure transducer for unsteady measurement

The calibration above gave a standard deviation of ±473.4 Pa with ±943.8 Pa uncertainty for a confidence interval of 95.4%. Using the same calibration procedure, the uncertainty levels of other transducers are found to be in the range of ±241.4 Pa to ±946.8 Pa at 95.4% confidence interval.

4.4.2 Instantaneous temperature

During experiments, static temperatures of gas are measured at the measurement plane, and the inlets of the turbine housing and the waste-gate. Due to the presence of thermal inertia in the thermocouples, the direct measurement of instantaneous temperature is not possible in unsteady testing. Rather, the instantaneous temperature is inferred from the instantaneous and mean pressure measurements (P_{inst} and $\bar{P}$) by assuming an adiabatic relationship as follows.

$$T_s \approx \bar{T}\left(\frac{P_{inst}}{\bar{P}}\right)^{\frac{\gamma-1}{\gamma}} \quad \dots (4.1);$$

where $\bar{T}$ is the time averaged temperature. The time mean pressure ($\bar{P}$)is taken as the time average pressure over a pulse cycle. This method of instantaneous temperature approximation was proposed by Dale and Watson (1986) and later validated by Szymko (2006).

4.4.3 Instantaneous torque

An indirect method was adopted for measurement of instantaneous torque. This is achieved by taking the sum of two components, namely the mean toque ($\bar{\tau}$) measured by the load cell similar to steady state testing and the fluctuating torque (τ').

$$\tau_{inst} = \bar{\tau} + \tau' \quad \dots (4.2)$$

The fluctuating component shown below is calculated from the angular speed variation (dω/dT) over a pulse cycle and the polar moment of inertia (*I*) of the rotating system:

$$\tau' = I\left(\frac{d\omega}{dT}\right) \quad \dots (4.3)$$

The trifilar suspension method is used to measure the polar moment of inertia of the rotor wheel (Anderson, 1987), giving a value of 3.6667 x 10^{-4} kg.m^2. This value is combined with the moment of inertia for the rest of the rotating assembly (Rajoo, 2007), giving a total value of 7.2436 x 10^{-4} kg.m^2. The rotor angular acceleration is obtained through central differencing described in the expression below:

$$\left(\frac{d\omega}{dT}\right) = \frac{\omega_n - \omega_{n-1}}{t_n - t_{n-1}} \quad \dots (4.4)$$

where subscripts *n* is and *n-1* denote the current and previous measured values respectively (Szymko, 2006).

4.4.4 Unsteady mass flow rate measurement with constant temperature anemometer hotwire system

The fluctuating mass flow rate of the gas stream during unsteady testing can no longer be measured accurately using the V-cone due to the low frequency response of such systems. Therefore, a high-speed mass flow rate measurement system having a frequency response higher than that of the unsteady pulses is required for this purpose. This is obtained using a constant temperature anemometer (CTA) hotwire system which has been proven to fulfil this requirement (Szymko, 2006). For this device, Joule heating is applied to a probe comprising a fine cylindrical 10μm Tungsten wire fixed between the tips of two support prongs as shown in Figure 4.5.

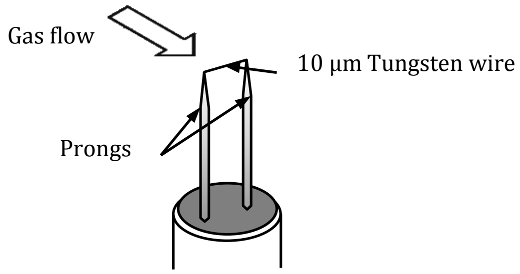

Figure 4.5 Schematic diagram of the CTA hotwire probe

When immersed in a fluid flow, the heat transfer between the wire and the fluid stream will result in the change of voltage reading across this wire. At constant wire temperature, the voltage measuring the heat transfer between the wire and the gas is proportional to the velocity of the gas stream. It is this therefore possible to obtain the mass flux from the measured velocity for a given flow area. The constant temperature hotwire type used in this study implies that the probe is operated at constant electrical resistance adhering to the Wheatstone bridge concept. Assuming zero heat storage within the wire, the electrical power provided to the wire is equal to convective heat transfer rate (Q) over the surface area of the wire, according to the following relationship:

$$Q = {I_{el}}^2 R_w = hA_w(T_w - T_\infty) \quad \text{... (4.5);}$$

where I_{el} is the electrical current, R_w is the electrical resistance, h is the convective heat transfer coefficient, A_w is the surface area of the wire, T_w is the wire surface temperature and T_∞ is the free stream gas temperature. The heat transfer characteristics represented by the Nusselt number (Nu), which is the ratio of fluid convective to conductive heat transfer, can be used with the above relationship giving:

$$\dot{Q} = {I_{el}}^2 R = Nu\, k\, \pi l_w (T_w - T_\infty) \quad \text{... (4.6);}$$

$$Nu = \frac{hd_w}{k} \quad \text{... (4.3);}$$

where l_w and d_w are the wire length and diameter respectively and k is the thermal conductivity of the gas. For an infinitely long cylinder, as is the case for a very small diameter wire, the heat transfer in the form of the Nusselt number (Nu) and flow characteristics which is represented by the Reynolds number (Re) can be related by King's law as shown below (King, 1914):

$$Nu = \boldsymbol{A} + \boldsymbol{B}.Re^{1/2} \quad \text{... (4.7)}$$

$$Re = \frac{\rho U d_w}{\mu} \quad \text{... (4.8);}$$

where $\boldsymbol{A}$ and $\boldsymbol{B}$ are power law constants, ρ is the gas density, U is the gas velocity and μ is the gas dynamic viscosity.

Incorporating the temperature correction into the above equation and accounting for the influence of Mach number and Prandtl number results in the final expression relating mass flux (ρU) to the anemometer voltage E as follows (Newton, 2013):

$$\rho U = \frac{\left[\frac{\left(\frac{T_w - T_{ref}}{T_w - T_\infty}\right)^{1+\boldsymbol{m}} \left(\frac{T_{ref}}{T_\infty}\right)^{0.83} E^2 - \boldsymbol{a}}{\boldsymbol{b}}\right]^{1/\boldsymbol{n}}}{\left(\frac{T_{ref}}{T_\infty}\right)^{0.73}} \quad \text{... (4.9);}$$

where (T_{ref} – T_w) term is the overheat temperature and T_{ref} being the reference temperature at the initial hotwire calibration taken as 222K and T_w being the wire temperature taken as 512K. The addition of the constant m to the temperature correction term and the constant n instead of the value of ½ are to account for the expression not fully adhering to the infinitely long wire assumption and to account for the influence of Mach number and Prandtl number of the flow.

4.5 CTA Hotwire Calibration Procedure

The experimental setup uses a total of four hotwire probes with two placed inside the inner and outer limbs at the measurement plane (inner and outer hotwires), one at the inlet of the turbine volute (volute hotwire) and another one at the branch where the flow splits from the main pipe to the waste-gate valve (waste-gate hotwire) as shown in Figure 4.3. The following paragraphs describes the procedure established to calibrate the hotwires in this experiment.

The standard procedure for calibrating the hotwires is to do so against the value of steady state mass flow rate measured by the V-cone meters placed in each limb of the intake pipes upstream of the measurement plane (Figure 3.1). The calibration of the two hotwires in the measurement plane is straight forward since the mass flow rate at each limb in the measurement plane must be equal to those measured by the corresponding upstream V-cone meters. Calibrating the additional two hotwires placed further downstream of the measurement plane at the turbine inlet and in the branch before the waste-gate valve is problematic since there are no direct measurements of the mass flowing through each component. However, with the current setup, the volute hotwire can be directly calibrated against the total mass flow rate measured by the V-cone meters with waste-gate flow fully closed, although the absence of a traversing mechanism due to the complexity and limited mounting space, may introduce a degree of uncertainty as the velocity profile of the flow entering the volute alters in this condition. Similarly, the waste-gate hotwire was initially calibrated by entirely blocking the flow to the turbine and adjusting the calibration constants such that the mass flow through the waste-gate equals that measured by the V-cone meters. This method of calibration results in a good relationship between the voltage readings and the mass flow rates in both conditions above.

Following this method of calibration, the turbine flow was unsealed and the waste-gate valve was opened allowing gas to flow simultaneously through both components. It was found that the use of this calibration method results in the waste-gate hotwire giving too high a mass flow rate (almost twice as much) for the same waste-gate valve lift as it would be expected from the independently measured waste-gate swallowing characteristics. This was observed despite the hotwire measuring the mass flow rate into the volute giving consistent swallowing characteristics regardless of whether the waste-gate is opened or closed. The discrepancy in the mass flow measurement is deemed to be caused by the difference in the local flow structure at the waste-gate branch during opened and closed waste-gate operations.

A simple CFD calculation was carried out separately to compare the flow around the waste-gate branch at conditions when the valve is opened and closed. This was carried out using a commercial CFD code called NUMECA. The flow equations were discretized over a 300,000 node grid with y+ = 3 (a dimensionless distance of the first cell from the wall), ensuring grid independency of the simulation. This structured grid was generated using IGG 3-D grid generator software. Total pressure and temperature were imposed as boundary conditions at the inlet and ambient conditions are imposed at the exits of the flow domain and the flow solver EURANUS was used to solve the 3-D steady flow equations. Three cases were evaluated here. First, the branch leading to the waste-gate was sealed and flow was allowed to exit only through the branch which leads to the turbine. Then, the turbine flow was blocked and the flow was left to exit the domain only through the waste-gate branch. Finally, both the turbine and waste-gate branches were opened simulating an opened waste-gate operating condition. The result is shown in Figure 4.6 for an inlet total pressure of 120 kPa and temperature of 323K. It is seen that indeed, there is a significant change in flow structure at the flow branch leading to the waste-gate valve during the two said conditions, thereby further supporting the reason behind the discrepancy in the hotwire mass flow rate measurement.

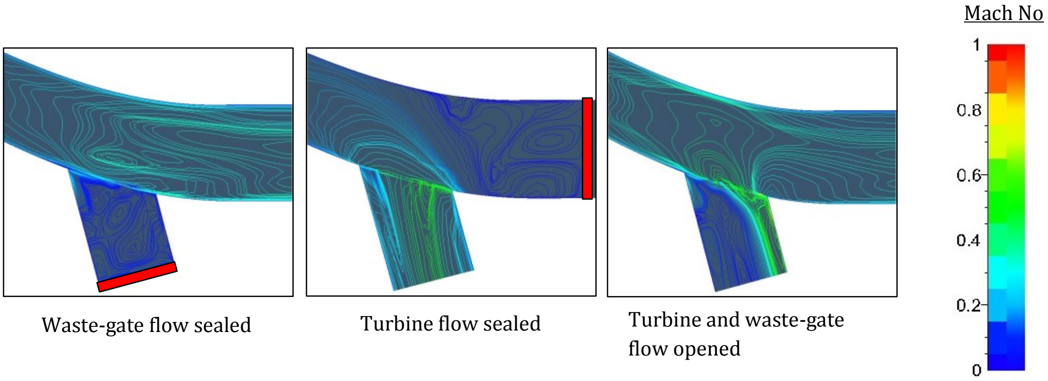

Waste-gate flow sealed

Turbine flow sealed

Turbine and waste-gate flow opened

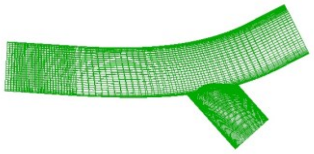

Computational grid

Figure 4.6 CFD flow visualization showing the Mach number contours around the waste-gate branch at different conditions

In the absence of direct mass flow rate measurement for waste-gate flow calibration, an alternative method, which was adopted in this experiment, was developed. This involves the use of the steady state characterization of the waste-gate flow described earlier in Section 3.14 where mass flow rate across the waste-gate was obtained for different valve lifts. If the swallowing characteristic of the waste-gate is assumed to remain the same regardless of whether the turbine flow is blocked or unblocked, it is thus possible to calculate the mass flow rate through it by measuring the pressure ratio across the waste-gate and the pressure and temperature of the incoming flow. The hotwire within the waste-gate branch can then be calibrated against this value of this mass flow rate. Figure 4.7 shows the waste-gate mass flow measurements after calibrating against the waste-gate steady flow characteristics following the procedure described above.

When the turbine is then run in the opened-waste-gate condition, the mass flow rate into the volute can be deduced by subtracting the waste-gate mass flow rate, calculated as described above, from the total mass flow rate through the system. The turbine mass flow rate calculated via this method can be compared to the values obtained from the volute hotwire measurement, as calibrated under the closed waste-gate condition (described above). A good match is observed when these two values are compared, as shown in Figure 4.8.

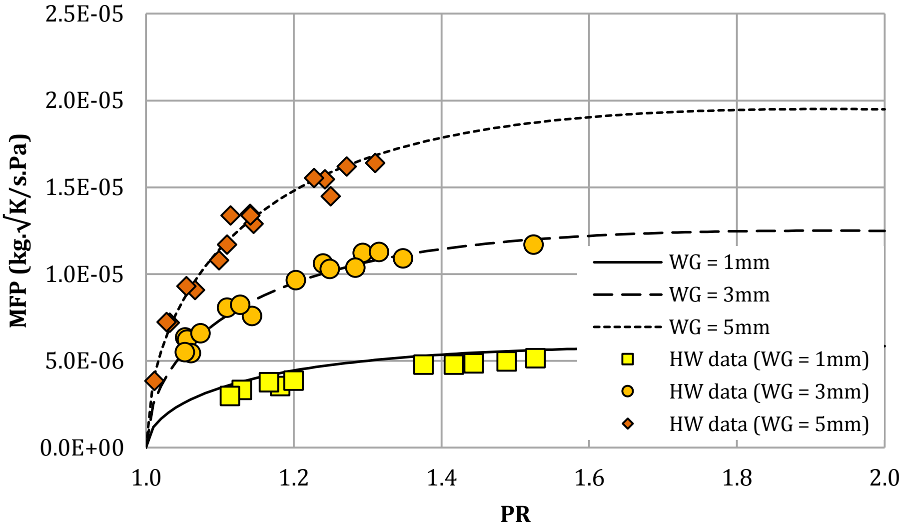

Figure 4.7 Waste-gate hotwire data compared to steady state characteristics

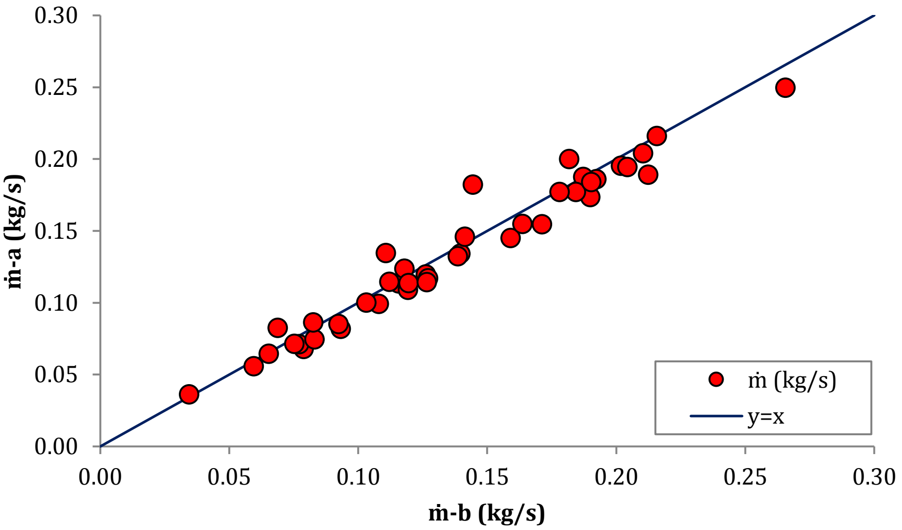

Figure 4.8 Variation of turbine mass flow rate using subtraction method (ṁ-a) against volute hotwire mass flow (ṁ-b)

The difference between these two measurements was used to calculate the uncertainty in mass flow rate measured with the hotwire in both the volute and the waste-gate. This was done by calculating the standard deviation of the difference between these two methods of measurement. Figure 4.9 shows the mass flow characteristics for the volute when the calculated waste-gate mass flow rate is subtracted from the total measured mass flow rate (a) and that measured using the volute hotwire calibration (b). Uncertainty bars are included for the former; these demonstrate a 95% confidence interval (i.e. 2σ) calculated from the difference between these two methods. The figures also include the turbine steady state swallowing characteristics for two turbine speed parameters.

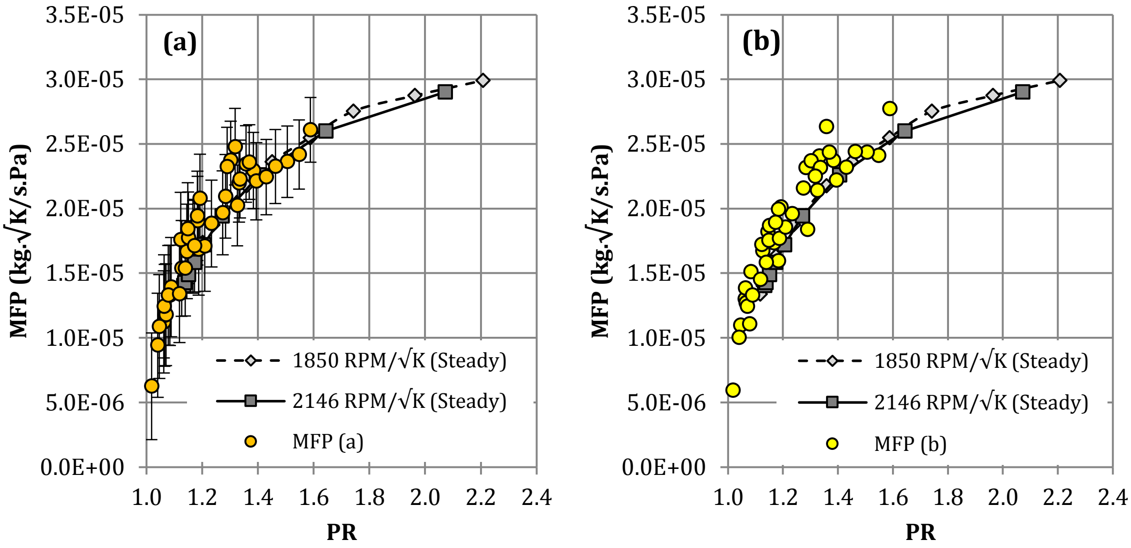

Figure 4.9 Comparison of turbine mass flow parameter measurements by (a) subtracting the waste-gate mass flow rate from the total mass flow rate and (b) direct measurement of mass flow rate by hotwire at turbine volute

4.6 Results and Discussion

Presented in following sections are the results of the unsteady tests undertaken for the test configurations given in Table 4.1. The influence of various inlet conditions, turbine operation and waste-gate settings will be discussed. In the following analysis and discussions, the respective terms “steady” and “unsteady” are used to denote measurements that are taken under steady state and pulsating inlet flow conditions. The results are analysed for testing under closed waste-gate conditions followed by waste-gated conditions. The effects of speed, turbine load, pulse frequency and waste-gate opening are evaluated and presented in the subsequent sections.

When comparing a particular instantaneous parameter against each other at different test configurations, it is convenient to have them plotted over a common reference scale. Therefore, the measured instantaneous data are distributed along 360° phase angle of the pulse generator where zero degrees indicate the start of the pulse generator rotation (the start of the area opening of the pulse generator).

4.6.1 Unsteady characteristics of turbine performance

The tests for closed waste-gate conditions are carried out at different turbine speeds, loads and pulse frequencies. To begin, it is necessary to describe the behaviour of the turbine under pulsating inlet conditions. Figure 4.10 below compares the instantaneous mass flow characteristics from hotwire measurements at 1850RPM/√K and 2146RPM//√K speeds, 40Hz pulse frequency, and approximately the same turbine load superimposed on steady state mass flow curves for the corresponding speeds. The arrows on the loops indicate the direction of data progression around the corresponding loops. It is apparent that under pulsating inlet flow conditions, the mass flow characteristics differ from steady state performance confirming the departure from quasi-steady behaviour. Instead, the instantaneous mass flow forms a characteristic loop around the steady curve and a trend in terms of shape can be observed. This is a typical characteristic of mass flow under pulsating conditions observed by preceding researchers in the field (Rajoo, 2008 and Baines, 2010). The size of the area encapsulated by the loop depends on the magnitude of mass flow parameter and pressure ratio fluctuations for a given unsteady condition. Over a pulse cycle, higher pressure ratio and mass flow amplitudes will cause the loop to expand along their corresponding axis. This can be seen in the figure where the area encapsulated by the loop is larger for the higher speed case by ≈28.5%.

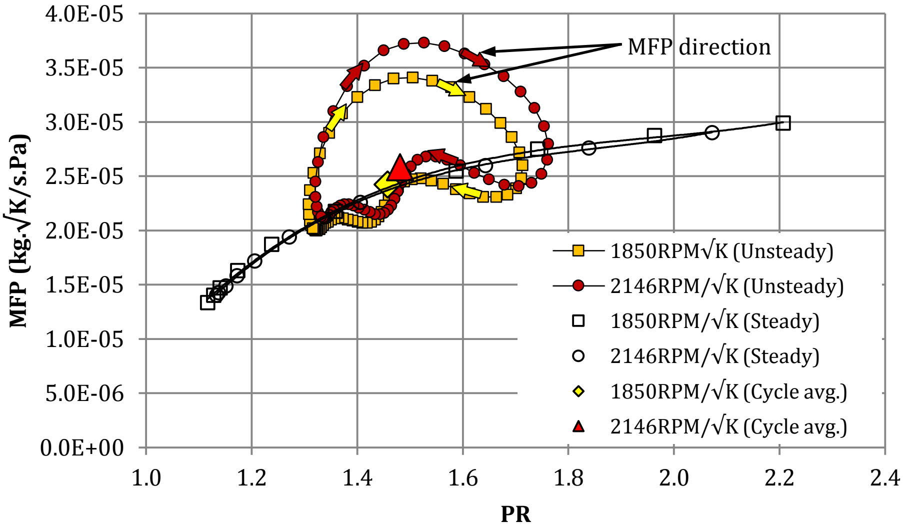

Figure 4.10 Unsteady mass flow parameter against pressure ratio for two different speeds at ≈1.45 pressure ratio and 40Hz pulse frequency

The profile of the mass flow characteristics seen here can be described by the “filling and emptying” process undergone by the gas within the volume of the turbine. With the turbine stage acting as a reservoir, a residence time is required for an amount of mass to accumulate (filling), and leave (emptying) this volume. This filling and emptying process depends on the volume of the stator which is effectively a plenum chamber, and the rotor passage acting a flow restrictor. As flow is initiated at the pulse generator, it enters an empty volume downstream which is at a relatively low pressure due to flow discharge in the previous cycle. The low pressure region offers less resistance for the incoming flow to pressurize and fill up the volume. As a consequence, the measured mass flow is expected to be higher than that seen in an equivalent steady state operation. Beyond the peak pressure ratio inside the volume, the rate of mass flow should begin to decline, thus initiating the emptying process.

The rotational direction of the loop profile is dictated by the propagation speed of mass flow parameter and pressure ratio over the cycle. If mass flow parameter peaks faster than pressure ratio, the direction of the loop will be clock-wise and vice-versa. Although it may appear from Figure 4.9 that the loop is largely dominated by the filling phase due to the portion of the loop being mostly above the steady state curve, the residence time of mass (represented by number of points, which are equally spaced temporally) is shorter than that in the emptying regime, thus the total mass should lie close to the steady state curve. This can be verified by calculating the average values of mass flow parameter over the pulse cycle. For the specific points selected, the cycle average mass flow parameter values based on cycle average pressure ratios are included in the graph and can be seen to fall very near to, although slightly above, the corresponding steady curves for both speeds lines. The cycle average values of mass flow parameter for the turbine under waste-gated and non-waste-gated conditions are discussed further in Section 4.8.

4.6.2 The effect of turbine load on swallowing characteristics

Figure 4.11 shows the unsteady mass flow plotted against pressure ratio for at different turbine loads under the same pulse frequency at 2416 RPM/√K speed parameter. The load is varied by adjusting the gap between the stator plates at either sides of the magnetic rotor. For the sake of clarity, the measurements of instantaneous data are plotted here as continuous lines.

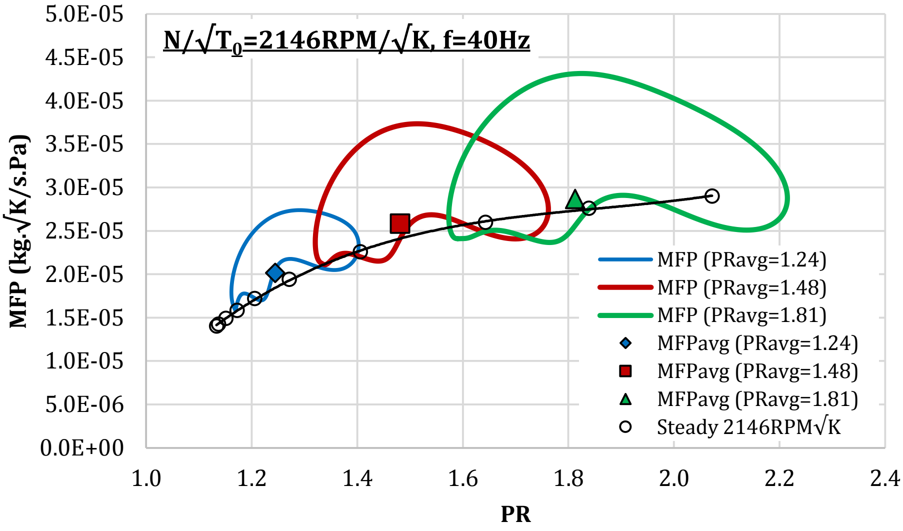

Figure 4.11 Unsteady mass flow parameter plotted against pressure ratio for three different turbine cycle average pressure ratios

The area encapsulated by the loop increases with as the turbine load is increased and this behaviour was found to be consistent throughout the experiment. For the case shown in the figure, the area of the loop is increased by ≈216% from low to medium load, and by ≈82% from medium to high load[3]. To explain this behaviour, the traces of mass flow parameter and pressure ratio, plotted against the phase angle, are shown Figure 4.12 for the same test conditions.

It can be gathered from the traces that the amplitudes of pressure ratio and mass flow parameter increases with increased turbine load. The pressure ratio amplitudes from low to high turbine loads are 0.24, 0.44 and 0.64 respectively. As for the mass flow, the amplitude increases from 1.15x10^{-5}kg.√K/s.Pa at low load, 1.62x10^{-5} kg.√K/s.Pa at medium load and 1.95x10^{-5} kg.√K/s.Pa at high load. This increment in amplitudes of both pressure ratio and mass flow parameter explains the expansion of the areas encapsulated by the mass flow parameter loops in Figure 4.11 above. The profiles of the traces remain similar implying that the turbine load has no influence over the dynamics of the mass flow characteristics. At this point, it can be said that, if the amplitudes of the fluctuating parameters are any indicator of the unsteadiness in the turbine behaviour, then this attribute increases as turbine load is increased. Also shown in Figure 4.11, are the cycle average mass flow parameter values for the corresponding instantaneous conditions. The values, although consistent along the steady mass flow parameter

---

[3] The mass flow parameter loop area is approximated numerically by estimating the area encompassed by the top section of the loop between the extremities of the PR values and subtracting with the area covered by the bottom curve.

curve at this specific speed line, are slightly higher compared to the equivalent steady state values.

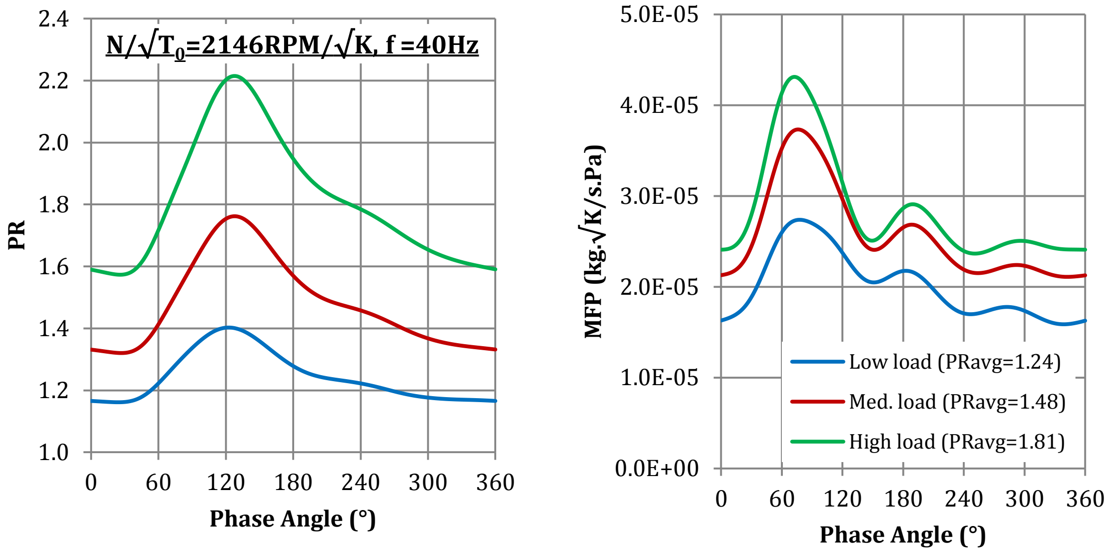

Figure 4.12 Profiles of pressure ratio and mass flow parameter plotted against phase angle for three different turbine loads at 2146 RPM/√K and pulse frequency = 40Hz

4.6.3 Effect of load on instantaneous power

It is also interesting to see the characteristics of instantaneous torque as the load of the turbine is varied. This is shown in Figure 4.13 for the three different loads at 2146 RPM/√K and 40Hz frequency. The instantaneous torque in the figure are normalized by the corresponding mean values. The turbine load indicated by the pressure ratios in the range of 1.24 to 1.81 are labelled as low, medium and high respectively. It can be seen that the higher turbine loads are accompanied by higher instantaneous torque amplitudes. The measured torque amplitude is 0.404 Nm at low load and increases to 1.104 Nm and 2.041 Nm at medium and high loads respectively. With the instantaneous torque known, it is then possible to compute the power generated by the turbine at the same condition and comparing it to the corresponding isentropic power at each load points. This is shown in Figure 4.13.

Clearly, as the turbine load increased, the isentropic power increases since more mass at higher pressure ratio is needed to drive the turbine at higher power. It is also noticed that as load increases, the difference in magnitudes between isentropic and actual power is more pronounced. At these conditions, the turbine is operating away from its design point and therefore is operating at low efficiencies. It can be drawn that varying turbine load will only affect the magnitude of torque but does not change its instantaneous behaviour.

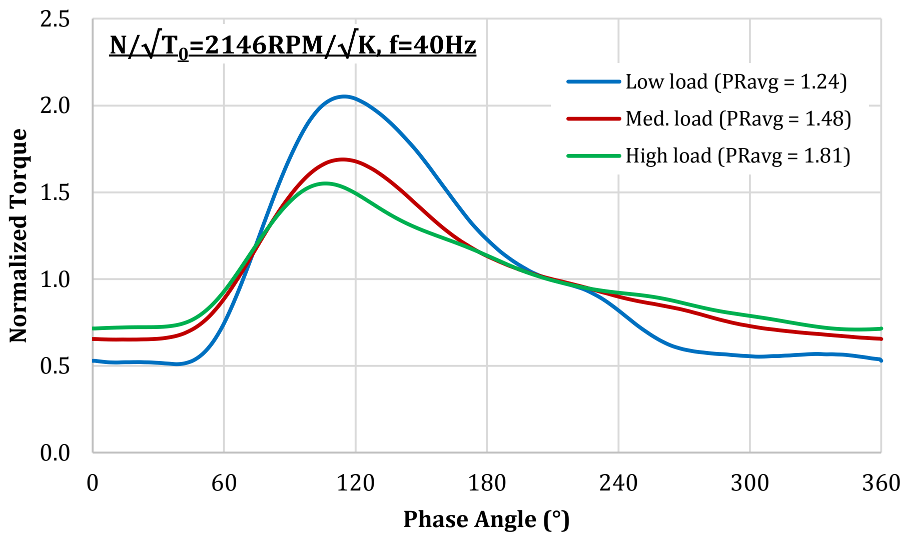

Figure 4.13 Instantaneous torque measurement carried out at 2146 rpm/√K speed and 40Hz pulse frequency at different turbine loads

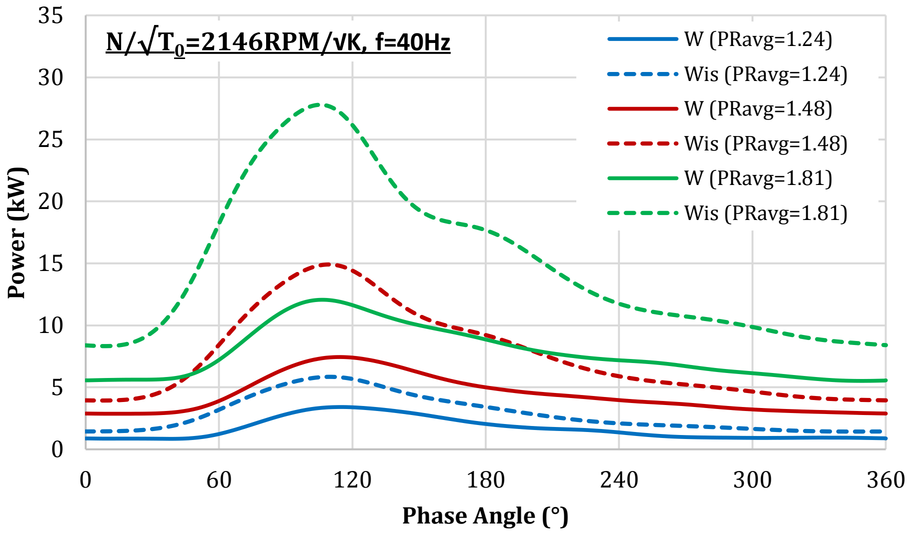

Figure 4.14 Comparison of turbine instantaneous actual and isentropic power at different turbine loads for 2146 RPM/√K speed and 40Hz pulse frequency

4.6.4 Effect of pulse frequency on turbine unsteady performance

To investigate the effect of pulse frequency, the turbine is driven at similar equivalent steady state pressure ratios at the same speed. This is shown in Figure 4.15 for a set of instantaneous mass flow measurements carried out at mean $PR_{avg} \approx 1.50$ for four frequency levels (20, 40, 60 and 80Hz) at a turbine speed of 2146 RPM/√K. In an actual four-cylinder, four-stroke engine, these frequencies correspond to engine speeds of 600[4], 1200, 1800 and 2400 RPM respectively. Again, the steady mass flow curve is superimposed on the graph for reference along with the cycle average mass flow parameter for each case. A clear distinction in the unsteady mass flow characteristics is observed for the different frequency levels although their corresponding cycle average values are almost identical.

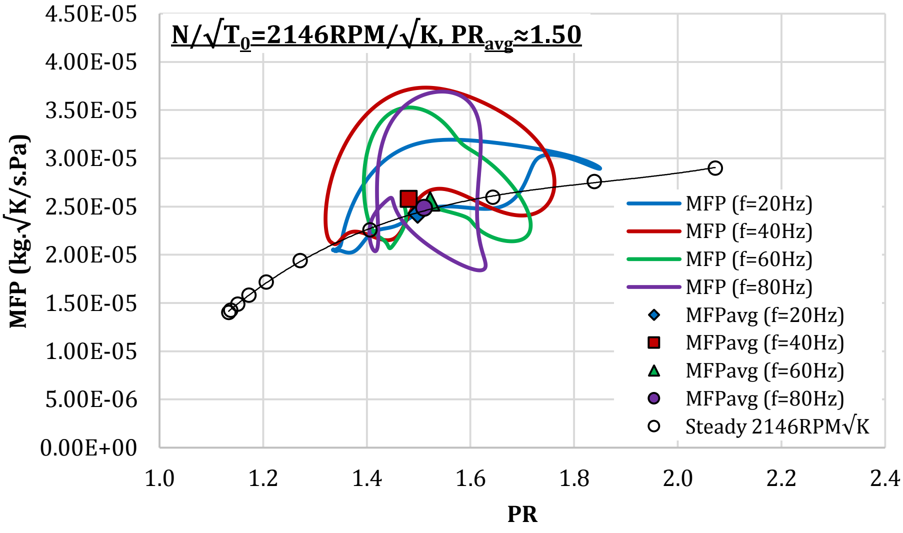

Figure 4.15 Instantaneous mass flow characteristics against pressure ratio for different pulse frequencies

By observing the features of the instantaneous loops, it can be noticed that their overall width decreases as frequency increases. Comparison of the instantaneous mass flow and pressure profiles at different frequencies are shown in Figure 4.16. The chopper plate opening area is also indicated in the graphs. The figures reveal the influence of pulse frequency on the shifting of the pressure ratio peaks along the cycle phase. A relatively small shift is seen for the peaks of instantaneous mass flow compared to those of pressure ratio as the frequency level increases. Taking the f = 20Hz case here, the mass flow rises along with increase in pressure ratio until a

---

[4] It is highly unlikely that a modern automotive engine using this turbocharger would operate at this low a speed in normal operating conditions as it would normally fall below the engine's idling speed. Nevertheless, the initial aim of having the turbine tested at this frequency is to establish whether or not different pulse frequencies exhibit a significant trend in terms of its shape.

peak value of 3.19x10^{-5} kg.√K/s.Pa at 41.8° phase angle. This observation suggests the influence of wave actions within the volume where a pressure wave travelling in direction of the flow will result in the increase of fluid velocity. Beyond this point, the mass flow decreases with the pressure ratio still increasing until it reaches the value of 1.85 at 75.3° phase angle. However, this is not the case for instantaneous measurements seen in the figure (at 20Hz pulse frequency). In fact, the opposite is true where the mass flow is reduced as the pressure ratio continues to rise.

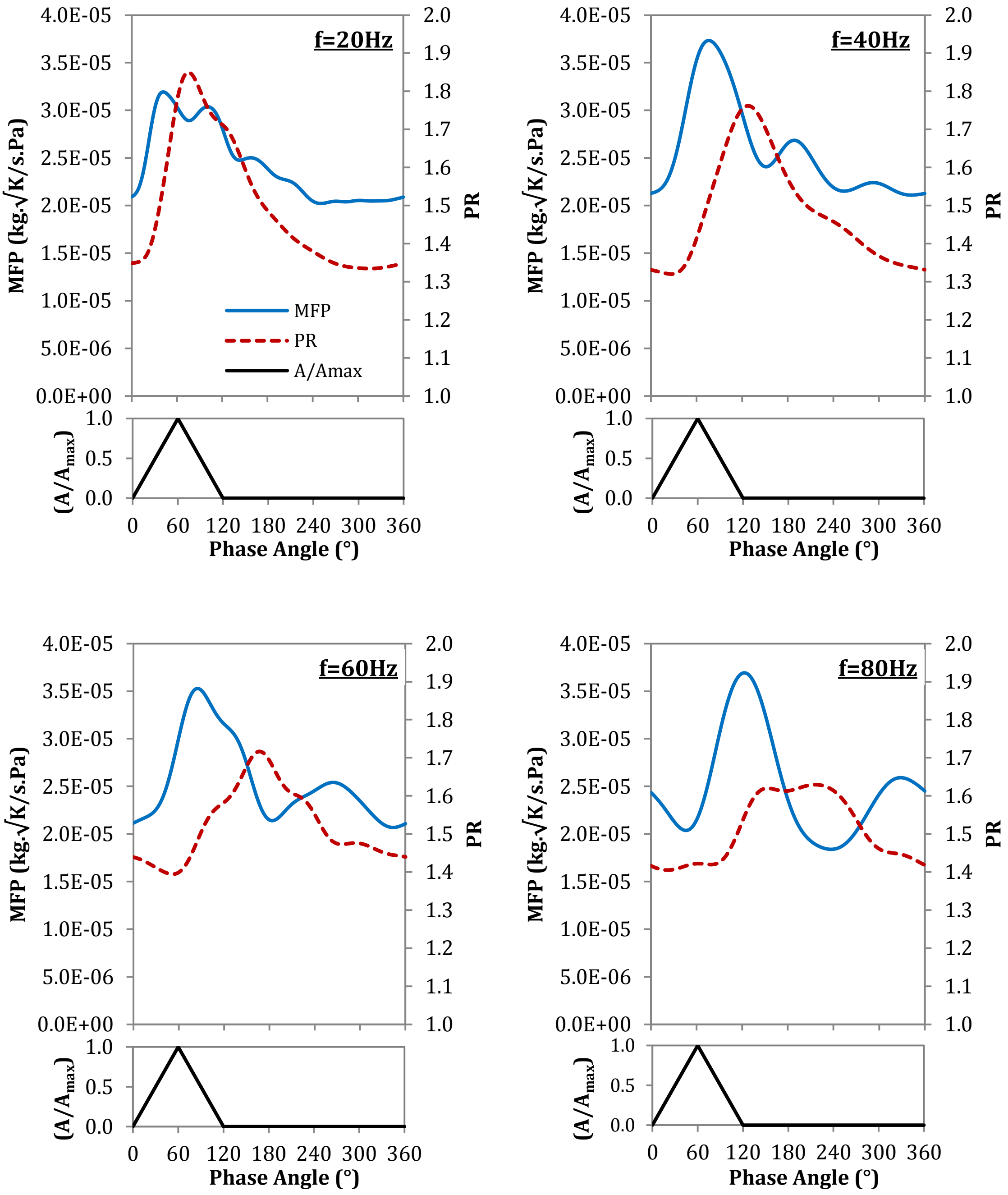

Figure 4.16 Pressure ratio and mass flow parameter traces plotted against phase angle for different pulse frequencies

This continued rise in pressure ratio is likely to be caused by a superposition of the pressure wave from the pulse generator with a reflected wave propagating in the opposite direction and consequently reducing mass flow rate. This behaviour has been observed by many previous studies such as Rajoo (2007), Mamat (2012) and Newton (2013). A closer look at the pressure trace indicates a second peak appearing on the trailing side of the wave, indicating the presence of the reflected, weaker pressure wave super-positioning on the primary wave.

The same explanation can be extended to other cases shown in Figure 4.16. For instance, at 60Hz frequency, several peaks are observed along the pressure ratio trace and the peak value is lower than that observed for lower frequencies. At 80Hz, the value of maximum pressure ratio is reduced to 1.63 and there seems to be two pressure ratio peaks of almost similar magnitudes occurring over the cycle. In relation to mass flow, the first pressure ratio peak occurs when the mass flow is close to its peak value during the filling phase of the cycle while the second peak coincides with the minimum mass flow in the emptying phase. This observation appears as an almost vertical decline in the swallowing characteristic plot shown in Figure 4.15 for 80Hz pulse frequency case. The relative drop in peak pressure ratio again can be associated with the wave reflections from the downstream of the flow path. An increase in frequency may result in more waves being reflected back towards the source, which increase the likelihood of a diminishing effect on the primary wave as opposed to wave amplification seen for 20Hz pulse frequency case.

4.6.5 Effect of pulse frequency on turbine power

Similar to the turbine swallowing characteristics, the effect of pulse frequency on instantaneous turbine power can be evaluated. This is done by running the turbine at the same speed and average load, and varying the frequency of the pulse generator. The instantaneous power recorded at 2146 RPM/√K speed and medium load with PR ≈ 1.50 is shown in Figure 4.17.

From the figure, it can be seen that the peak power is reduced and shifted towards larger phase angles as frequency is increased. Peak power values decrease from 8.11kW at 20Hz, 7.44kW at 40Hz, 6.79kW at 60Hz and 6.52kW at 80Hz. In terms of phase, the peaks are spread along 106.4° between 20Hz and 80Hz pulse frequency. This is a direct result of the peaks' phase angle dependency on frequency and the time taken for the pulse energy to propagate from its source (pulse generator) to the measurement location (at the turbine rotor). Since the time for the pulse energy to travel is roughly the same for the speed and pressure ratio, the change in frequency will result in an increase in phase angle of the pulse peaks.

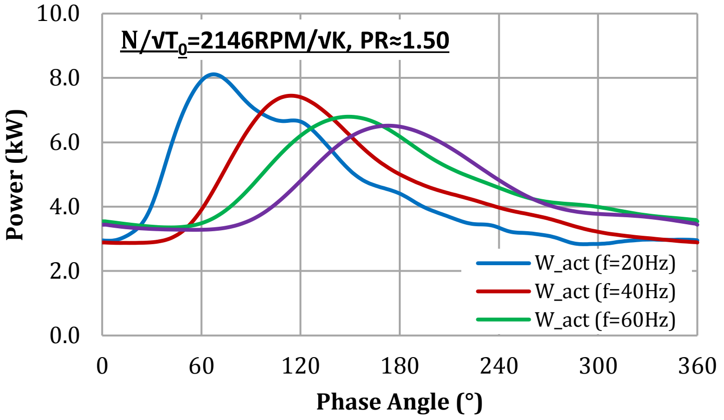

Figure 4.17 Comparison of instantaneous power at different pulse frequencies

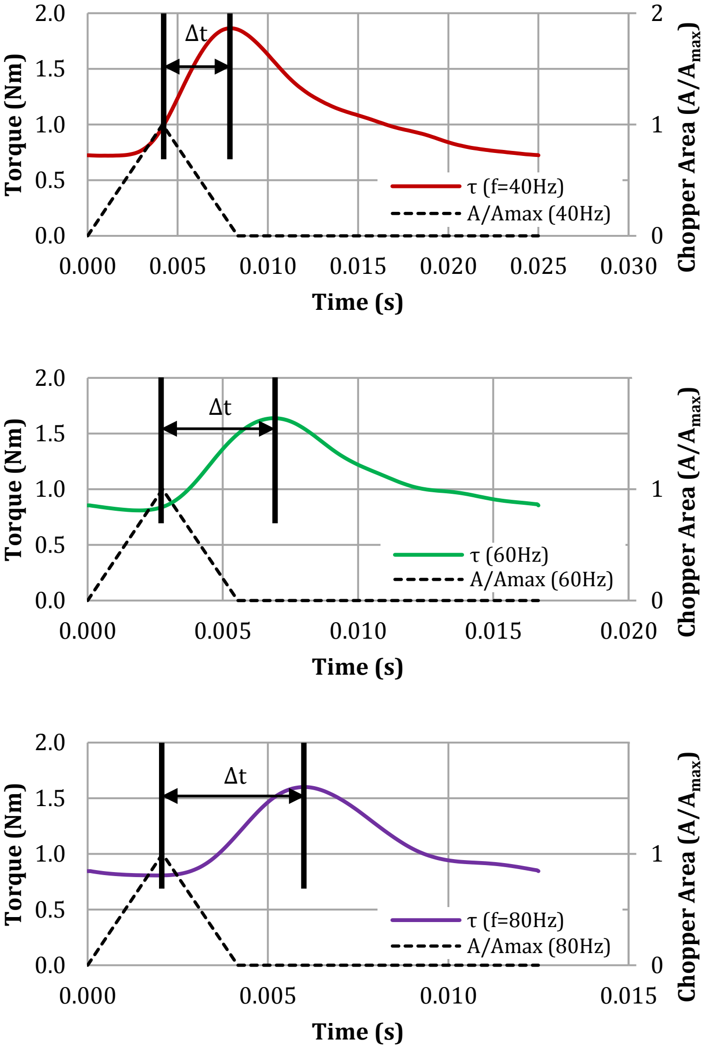

Figure 4.18 Time lag between chopper opening and peak instantaneous torque measured at the rotor wheel

To demonstrate this effect, the instantaneous measurements of torque at three different pulse frequencies (20 to 40Hz) are plotted against time along with the chopper opening area and is shown below in Figure 4.18. These are torque traces for the same test case given in Figure 4.17 above. The time shift (Δt) between the maximum chopper opening areas and the peak torque values for every case are almost similar at approximately 0.004 seconds. This time shift can be related to the phase angle (φ) and frequency (f) through the following equation:

$$\Delta t = \frac{\varphi}{360 \cdot f} \quad \text{or} \quad \varphi = 360 \cdot \Delta t \cdot f \quad \ldots (4.10)$$

It is clear from this relationship that for a fixed time shift, the increase in frequency will result in the shift in the phase of the peak torque and subsequently peak power to greater angles.

4.6.6 Quasi-steady analysis

From the perspective of turbine modelling, it is inevitable that performance under unsteady pulsating condition be compared to the equivalent steady condition. As most engine simulation tools adopt the quasi-steady approach in modelling turbocharger behaviour, it makes sense to compare the unsteady turbine performance with the predicted quasi-steady behaviour. To form the basis for discussions, the quasi-steady analysis is carried out at test configurations selected when analysing the impact of turbine loads and pulse frequencies in the preceding sections.

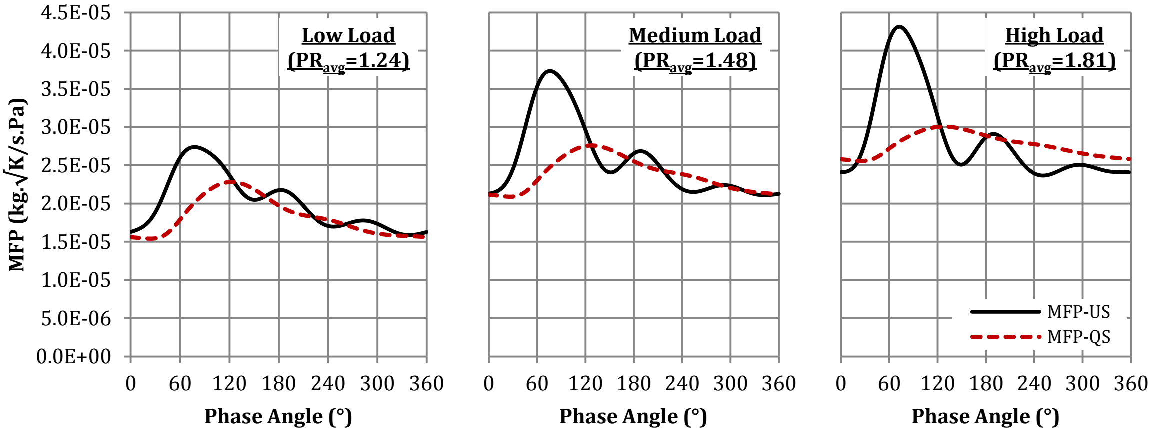

Figure 4.19 Comparison of unsteady mass flow parameter with predicted quasi-steady values for three turbine loads

Figure 4.19 shows quasi-steady mass flow parameter (MFP_{QS}) compared to unsteady mass flow parameter (MFP_{US}) for three different turbine loads at 2146 RPM/√K and 40Hz pulse frequency.

The MFP_{QS} for each pressure ratio over a pulse is obtained via interpolation of the mass flow parameter values measured in steady state experiments.

As previously discussed, there is a trend seen in the unsteady behaviour of the turbine in that the amplitudes of mass flow traces increases along with the increase in turbine load. From Figure 4.19, this variation is clearly not captured by the quasi-steady prediction. In fact, the amplitude of the mass flow parameter seems to decrease as load is increased. This is not surprising since the amplitude of the quasi-steady mass flow depends on where the range of pressure ratio lies on the steady curve. At low loads, the higher variation of mass flow parameter with pressure ratio would therefore lead to higher mass flow parameter amplitude and vice versa.

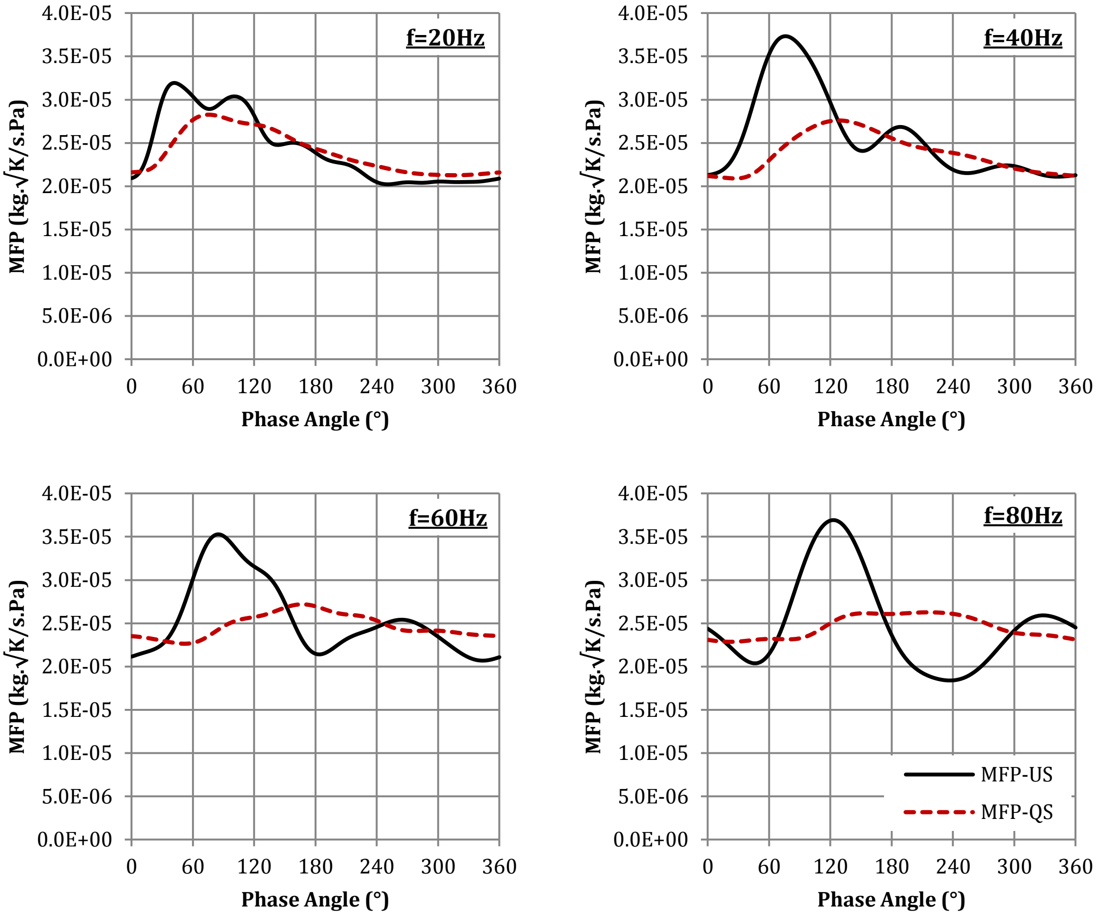

Figure 4.20 Comparison of quasi-steady mass flow parameter with measured data at different frequencies

The quasi-steady analysis can be extended for evaluation of pulse frequency impact on turbine unsteady behaviour. Similarly, the quasi-steady mass flow parameter values are calculated and compared to unsteady experimental values for four different pulse frequencies (20Hz to 80Hz) at 2146 RPM/√K speed and approximately 1.50 mean pressure ratio and is shown in Figure 4.20.

While the mass is significantly influenced by pulse frequency in the unsteady measurement, such is not the case for the quasi-steady values. Rather, the form of the quasi-steady MFP follows that of the instantaneous pressure ratio, with the 20Hz pulse having the smallest amplitude (followed by 40Hz, 60Hz and 80Hz). This is also not surprising since, it was earlier established that pressure ratio amplitude decreases as pulse frequency is increased. Without the influence of the slope of the steady mass flow parameter curve due to each cycle having identical pressure ratios, the form of the predicted quasi-steady mass flow parameter will solely depend on that of the corresponding instantaneous pressure ratio. As such, it can be drawn that the quasi-steady prediction is inadequate in representing the unsteadiness of the turbine behaviour with regards to mass flow amplitude change at different frequencies. Nonetheless, this approach serves as a useful indicator when evaluating unsteadiness on a cycle average basis.

4.7 Performance of Turbine in Opened Waste-gate Conditions

This section discusses the experimental results obtained from tests of the waste-gated turbine under pulsating inlet conditions. Altogether, the tests are carried out at three waste-gate opening areas which are regulated by adjusting the lift of the waste-gate valve. Similar to the non-waste-gated test conditions, the experiments are carried out over two turbine speeds and at various loads and pulse frequencies. Waste-gates are used to ensure that the turbocharger is providing the exact amount of boost demanded from the engine. Whenever this demand is reached, the waste-gate bypasses the exhaust gas flow from the turbine and maintains the turbine operating condition until the boost demand changes. The range of waste-gate opening depends largely on how the turbocharger is matched to the engine. In most cases, the waste-gate flow area is normally at its largest at high engine speeds and at high loads to prevent over-boosting, excessive cylinder and exhaust gas temperatures, turbocharger shaft over-speeding etc.

In the experiment, the level of opening is set by three valve lift values (l_{wg} = 1.0, 3.0 and 5.0mm). The lift is adjusted manually by rotating a screw, which displaces the valve rod vertically and consequently increases or decreases the flow area through the valve.

4.7.1 Effect of waste-gate opening area on turbine mass flow characteristics

Figure 4.21 shows the system mass flow characteristics recorded at the measurement plane at different waste-gate valve lifts plotted along with the corresponding steady state characteristics. This system mass flow rate refers to the total mass flow rate passing through the whole arrangement, which include the waste-gate flow that bypasses the turbine. Similarly, the pressure ratio indicated here represents the ratio of total pressure at the entry of the system with the exit static pressure. All the cases shown in the figure are obtained at 2146 RPM/√K speed, equal pulse frequency (20Hz) and at approximately the same average pressure ratio ($PR_{avg} \approx 1.25$). The unsteady mass flow characteristics exhibit a familiar behaviour whereby loops are formed around the steady state curve. As expected, the system swallowing characteristics is increased along with waste-gate lift due to the higher mass flow needed to drive the turbine and the mass bypassing the turbine via the waste-gate system. It can be noted that increasing the waste-gate opening results in the increase in the area encapsulated by the mass flow loops. In general, the loops stretch in both the mass flow parameter and pressure ratio directions as more mass bypasses the turbine. This indicates that greater amplification of the mass flow parameter and pressure ratio occurs as the waste-gate area is increased; an effect similar to increasing the turbine load as discussed earlier.

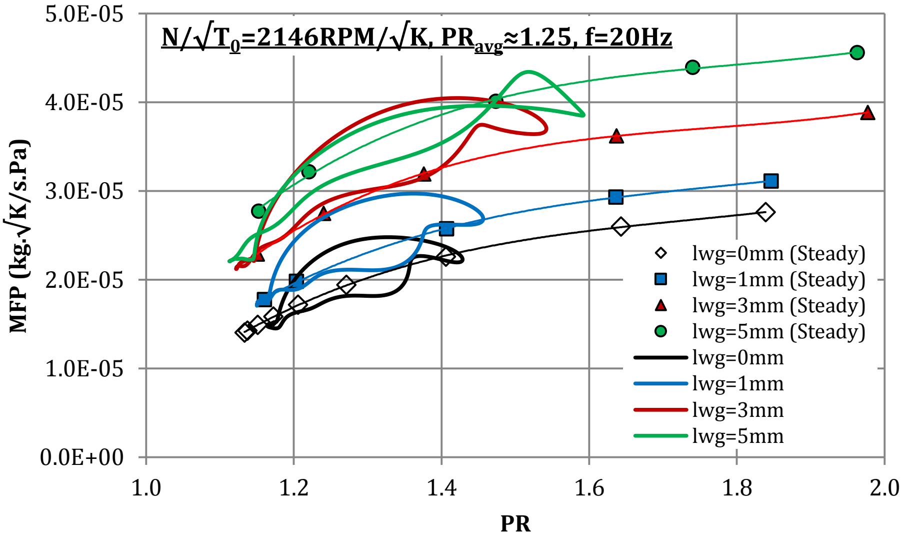

Figure 4.21 Mass flow characteristics of the turbine at different waste-gate lifts

The features of the loops remain largely similar to that of the closed waste-gate condition with the exception of the highest valve lift case (5.0mm) where it takes a more dynamic form. In addition, it is seen that as waste-gate area is increased, the shape of the loop becomes more slender with larger pressure ratio amplitudes. The individual mass flow parameter and pressure ratio amplitudes can be assessed in Figure 4.22. Looking at the pressure ratio traces, there seems to be no significant change in terms of its form other than the change in amplitude corresponding to each waste-gate lift. For the specific conditions demonstrated here, the pressure ratio amplitude increases from ≈0.264 at closed waste-gate conditions to 0.307, 0.420 and 0.480 respectively for 1.0mm, 3.0mm and 5.0mm waste-gate lifts. This can be attributed to the increased swallowing capacity of the turbine system as the waste-gate is opened. This means that during the latent period of the pressure pulse, when the chopper plate is closed, the turbine will be able to empty a greater amount of mass, leading to a greater depressurisation of the turbine stage volume. The average pressure ratio is kept similar in each case as the turbine load was kept constant. A similar trend is observed for the mass flow parameter for 1.0mm and 3.0mm waste-gate lifts. However, at 5.0mm lift, the mass flow parameter is seen to depart from the trend where the peak is shifted to higher phase angle. Closer observation on the individual mass flow traces shows that the maximum values occur at the first mass flow peak in the region of 47° to 50° phase angle in all cases except that of the 5.0mm waste-gate lift, where the maximum arises from its second peak at 107° angle.

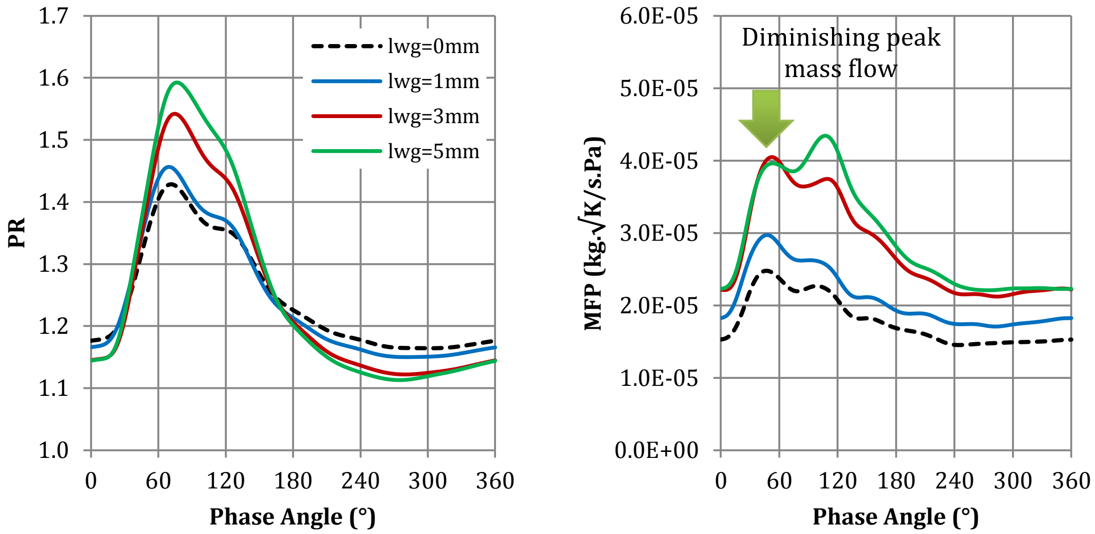

Figure 4.22 Pressure ratio and mass flow parameter traces at different waste-gate valve lifts

What seems to be a rise in magnitude of the second peak for the 5.0mm lift case is in fact a rather substantial drop in magnitude at the first peak as indicated in the figure. This can likely be attributed to the presence of a stronger reflected pressure wave, which diminishes the mass flow at this section of the pulse cycle[5].

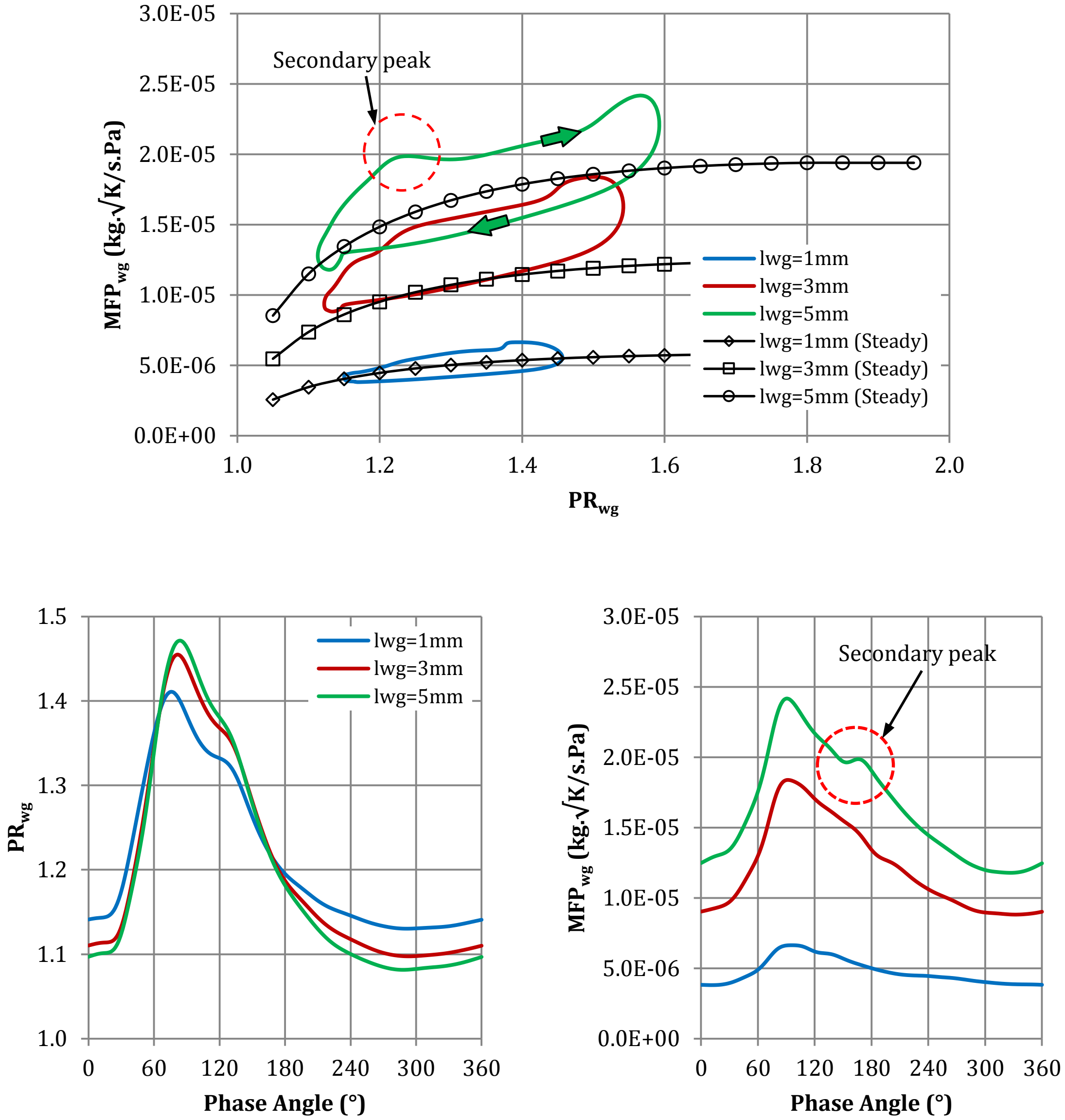

Figure 4.23 Waste-gate unsteady swallowing characteristics (top) shown with pressure ratio and mass flow parameter traces (bottom)

With the cases above tested at a similar turbine operating condition (i.e. equal turbine speed, pressure ratio and pulse frequency), it is also interesting to look at the unsteady characteristics

---

[5] To quantify the unsteadiness of the turbine behavior, a separate analysis based on dimensionless parameters called "Analysis on the level of unsteadiness" is carried out based the experimental results here and is given in Appendix I.

of the waste-gate mass flow. Instantaneous measurements of pressure and mass flow rate at the waste-gate allow further assessment on how the two components, namely the turbine and the waste-gate, interact with each other. For the same set of cases, the flow characteristics of the waste-gate are shown in Figure 4.23.

The traces show the higher amplitude for pressure ratio experienced by the waste-gate at larger opening. The pressure ratio peaks, which occur at 75°, 81° and 83° phase angles, are trailed by secondary peaks at approximately 130° phase angle hinting at the presence of wave reflections within the device. Another feature observed is that instantaneous pressure ratio peaks before mass flow parameter causing the loop to circulate the steady curve in a counter-clockwise direction as opposed to the instantaneous mass flow recorded at the measurement plane.

Mass flow amplitude increases by more than two-fold (≈237%) as waste-gate lift increases from 1.0mm to 3.0mm. From 3.0 mm to 5.0mm increment of waste-gate lift, the amplitude increase is relatively small (≈30% over the 1.0mm to 3.0mm lift case). It is interesting to note that for 5.0mm waste-gate lift, the mass flow trace exhibits a secondary peak occurring at ≈167° phase angle. It is possible that the peak observed in the measured static pressure at the waste-gate comprise of both travelling and reflecting waves. As such, the reflected wave, although increases the measured value, actually decelerates the flow. This effect is rather prominent in the 5.0mm lift case.

4.7.2 Effect of varying turbine load and inlet pulse frequency on waste-gated turbine swallowing characteristics

The effect of turbine load on the unsteady performance of the waste-gated turbine can be analysed by having the turbine run at constant speed, waste-gate lift and pulse frequency. Figure 4.24 shows the swallowing characteristics of the system for two different values of waste-gate lift at two different frequencies. The first case is for the system at 1.0mm waste-gate valve lift and 40Hz pulse frequency while the second is for 5.0mm waste-gate lift, at 80Hz pulse frequency. In both cases, the turbine is tested at three different loads varying between 1.14 to 1.42 and 1.12 to 1.39 cycle average pressure ratios for the former and latter case respectively. Also included in the graphs above are the corresponding swallowing characteristics for the waste-gate labelled in the figures as “WG” at different loads and their steady state curve.

It seems that under waste-gated conditions, the effect of varying loads is similar to that observed for closed waste gate conditions. The hysteresis loops are ever-present and are seen to encapsulate the quasi-steady lines. Again, it is seen that both pressure ratio and mass flow parameter amplitudes expand as load is increased. The area encapsulated by the mass flow loop grows by 106% from low to medium load and 207% from medium to high load for the 1.0 mm waste-gate lift case. For the 5.0 mm waste-gate lift, the area increases by 52% from low to medium load and 110% from medium to high load. For both cases shown above, the pressure ratio amplitude across the waste-gate is identical to the system pressure ratio taken at total to static conditions between the measurement plane and the turbine exit.

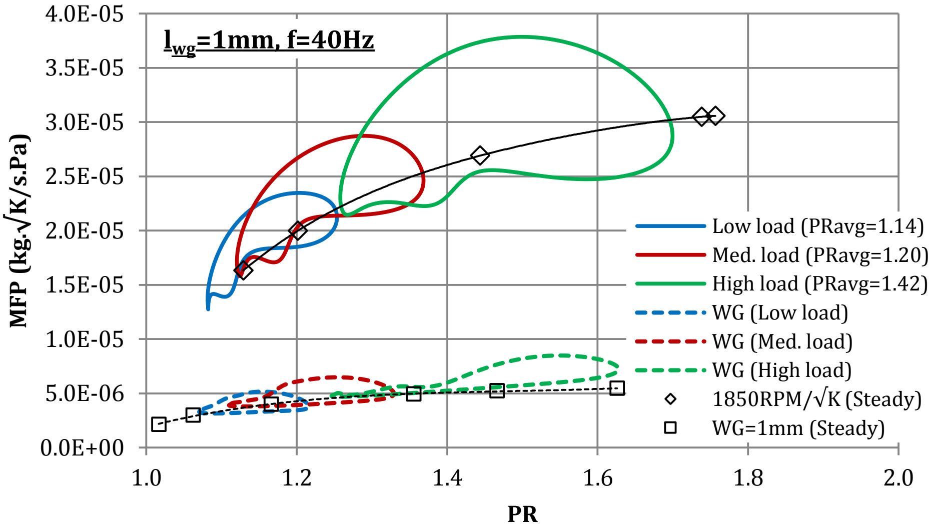

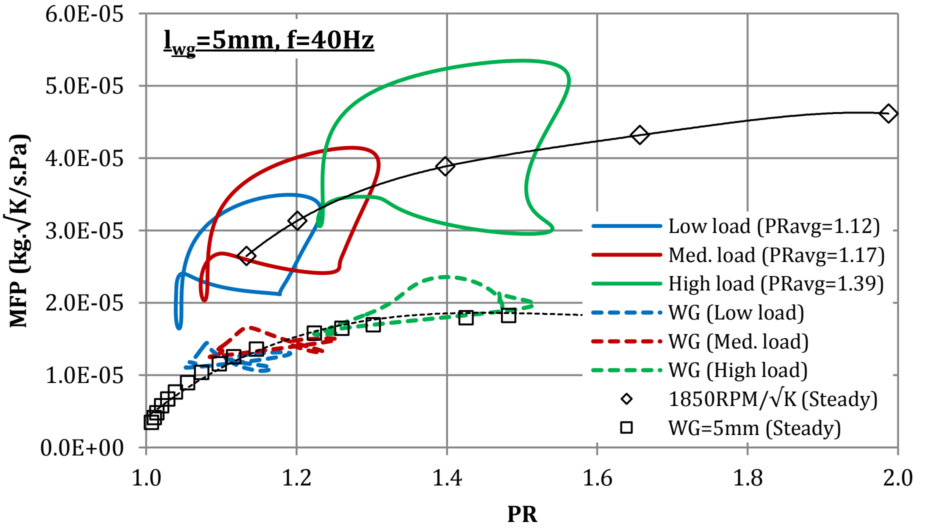

Figure 4.24 Unsteady swallowing characteristics for waste-gated turbine with 1.0 mm valve lift (top) and 5.0 mm valve lift (bottom)

The fact that the area of the loops increases with load agrees with the findings of Yang et al (2014) who suggested that the level of unsteadiness can be represented by the area encapsulated by the mass flow loops. For a nozzled turbine, the same authors showed that increasing the swallowing capacity by increasing the nozzle area would lead to a decrease in the unsteadiness. They attributed this to the low gradient of the steady state mass flow curve, which increases the mass imbalance within the system. What is observed in the work of Yang et al (2014) is a connection between the steady state mass flow parameter curve and unsteady mass flow parameter amplitudes with unsteadiness of the system. In the condition where pressure ratio amplitude occupies the flatter section of the steady state curve, the mass imbalance created during pulsating condition is greater. In the case of the waste-gated turbine, the gradient of the steady state curve encapsulated by the unsteady loop increases as waste-gate area opening is increased suggesting that the mass imbalance should be smaller, according to the findings of Yang et al (2014). However, because the pressure ratio amplitude is also larger, it covers a larger portion of the steady state curve, thus the corresponding mass flow amplitude also increases. This enhancement of mass flow amplitude along with that of the pressure ratio is only broken as the wave dynamic effects dominate the shape of the loop as seen earlier Figure 4.23.

4.7.3 Torque characteristics of waste-gated turbine under pulsating inlet conditions

Just as it is interesting to see the effect of waste-gating on the swallowing characteristics of the turbine, it is also important to look at its instantaneous torque behaviour. Again, the analysis is based on varying waste-gate openings via the corresponding valve lifts, turbine loads and pulse frequencies. As the load of the turbine is increased, it is expected that the mean torque would increase too. The experiment confirms this trend as is shown in Figure 4.25, which compares the instantaneous torque values for closed and opened waste-gate conditions (l_{wg} = 3.0 mm) at 1850 RPM/√K . At the two corresponding turbine loads (PR_{avg} ≈1.20 & 1.40), the cycle average values for closed and opened waste-gate conditions are identical at 0.38 Nm and 1.07 Nm respectively for the low and high load cases. The amplitudes of torque increase along with waste-gate opening. For the specific case shown in the figure, the amplitudes increase by 38.9% (0.56 Nm to 0.79 Nm) at low loads and 126.9% (from 0.68 Nm to 1.53 Nm) at high loads.

Shown in Figure 4.26 are the instantaneous torque measurements made at different waste-gate openings with fixed speed, pressure ratio and inlet pulse frequency. The measurements are sampled at two sets of conditions at 1850 RPM/√K speed; the first set is carried out at ≈ 1.20 pressure ratio and 40 Hz pulse frequency while the second set is carried out at ≈ 1.40 pressure ratio and 60 Hz pulse frequency. It can be observed that the torque amplitude increases as the waste-gate area is increased and is found to be consistent for both sets of samples. Case (a) in the figure has a mean torque value of 0.38 Nm. In case (b) where the torque profile seems to be more dynamic in form, the cycle average torque varies from 1.02 Nm at 3.0 mm waste-gate lift to 1.07 Nm at 1.0 mm waste-gate lift.

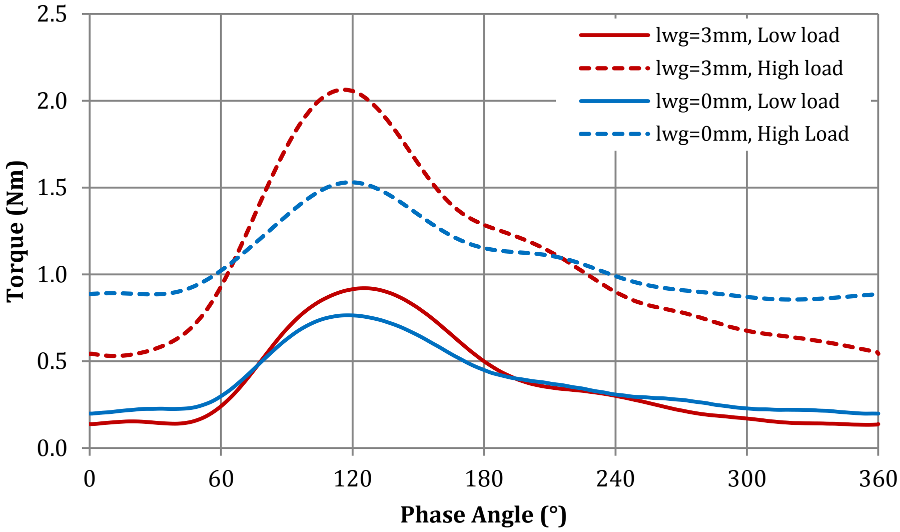

Figure 4.25 Comparison of instantaneous torque at opened and closed waste-gate for two different turbine mean loads

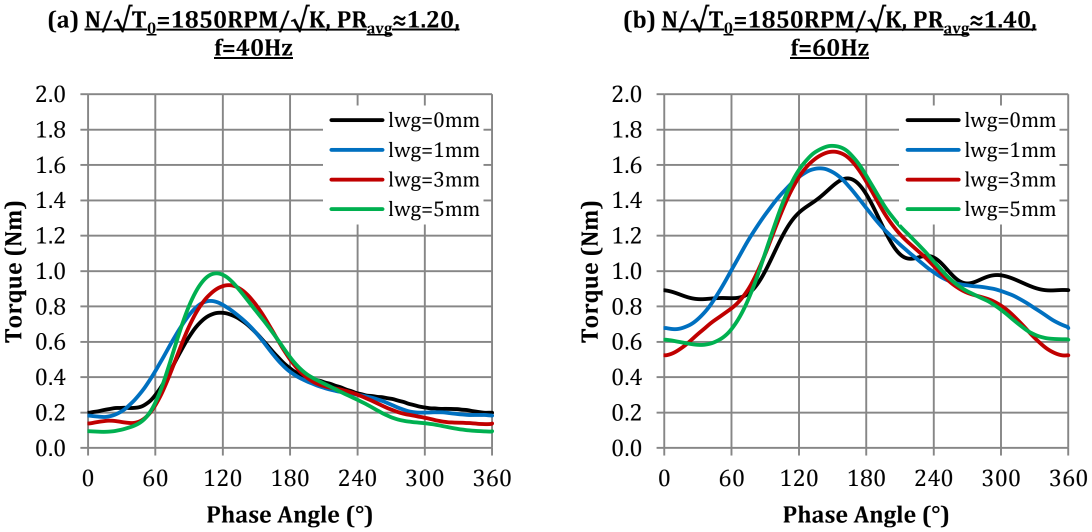
(a) $N/\sqrt{T_0}$=1850RPM/√K, PR_{avg}≈1.20, f=40Hz

(b) $N/\sqrt{T_0}$=1850RPM/√K, PR_{avg}≈1.40, f=60Hz

Figure 4.26 Torque profiles for different waste-gate openings shown for two cases

4.7.4 Frequency effect on torque behaviour at various waste-gate opening

As has been demonstrated for closed waste-gate conditions, pulse frequency has significant impact on the unsteady torque profiles. Here, the torque profiles for different cases of various waste-gate openings are compared. Figures 4.27 to 4.29 depict traces of torque at different pulse frequencies at three waste-gate lift settings in comparison with closed waste-gate measurements. Measurements in the figures are all carried out for four pulse frequencies (20, 40, 60 and 80 Hz) at equal average turbine load (PR ≈ 1.20) and speed parameter 1850 RPM/√K.

A common trend can be seen in these figures in that the amplitude of the torque trace is reduced as pulse frequency is increased. This is consistent with the findings for closed waste-gate conditions. The peak value of torque for each frequency case is also reduced. Another observation from the figures is that the torque signals are out of phase each other, with high frequencies being more delayed in phase. This is caused by the time delay present as the pulse travels from the measurement plane to the rotor wheel where the torque is measured. This travelling time for the wave to reach the rotor wheel constitutes a greater portion of the total cycle time as the pulse frequency is increased. With exception of amplitude, the dynamics of the torque profiles at different frequencies between closed and opened waste-gate conditions show strong resemblance with each other. For example, in the case of 20Hz pulse frequency, the second peak in the torque trace at closed waste-gate condition is also present in all the waste-gated cases. However, it is observed that the torque curve under closed waste-gate conditions appears to be smoother than for the non-waste-gated case.

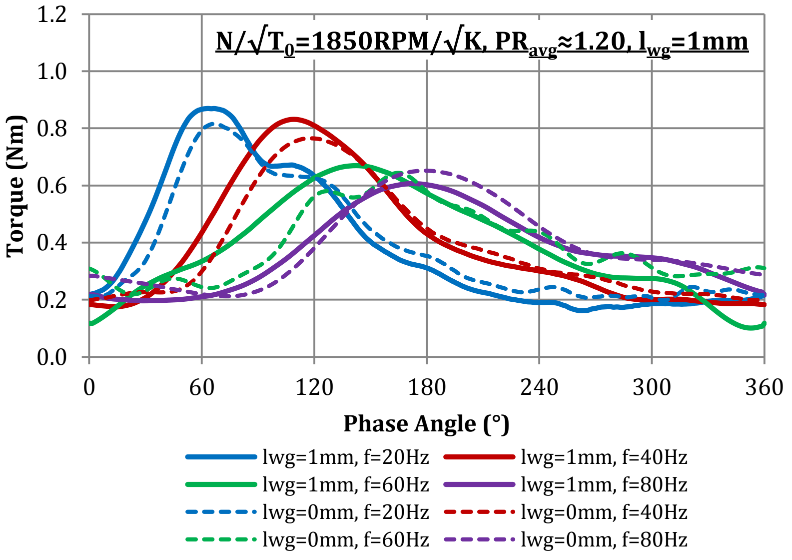

Figure 4.27 Effect of pulse frequency on torque at 1.0mm waste-gate lift

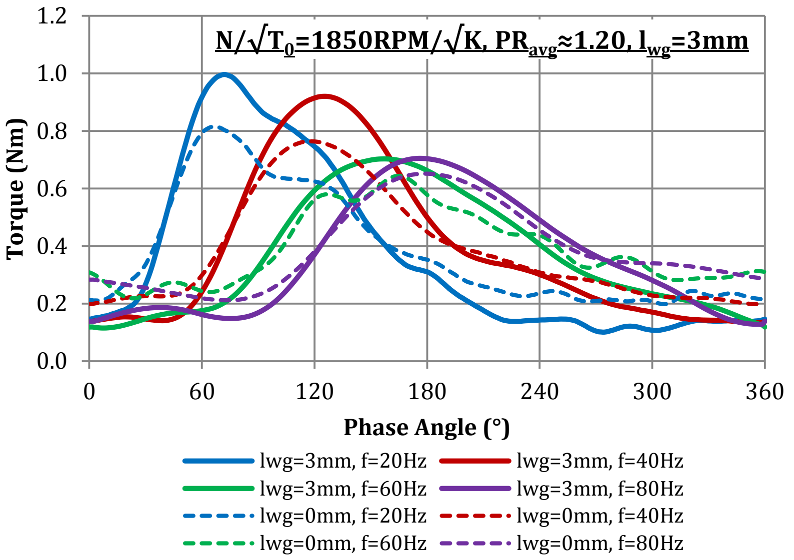

Figure 4.28 Effect of pulse frequency on torque at 3.0 mm waste-gate lift

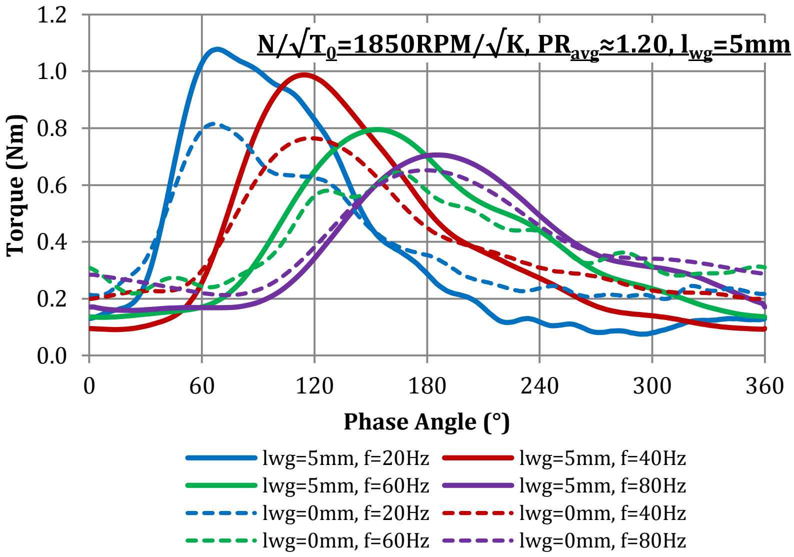

Figure 4.29 Effect of pulse frequency on torque at 5.0 mm waste-gate lift

4.7.5 Evaluation of turbine power output

With the knowledge of instantaneous torque, it is then possible to compute the power output generated by the turbine through the following expression:

$$Instantaneous\ Power, \dot{W} = 2\pi N_{inst}\tau_{inst} \quad \dots (4.11);$$

where is the N_{inst} is the instantaneous rotational speed of the turbine and τ_{inst} is the instantaneous torque.

With the torque measurement available, it is now possible to evaluate the power output of the turbine operating with different waste-gate openings. This can be done by evaluating the power traces at equal turbine speed, load and pulse frequency as shown in Figure 4.30 (a) below. The power output under the closed waste-gate condition is also given in the figure. Since power is directly related to torque as shown in Equation 4.11 above, it is not surprising that the two parameters exhibit the same behaviour. Peak power in the pulsating inlet conditions is observed to be increased as waste-gate area is increased. For the set of cases in consideration, peak power of 3.47 kW occurs at 5.0 mm waste-gate lift with power amplitude of 3.15 kW as compared to 2.56 kW peak power and 1.92 kW amplitude for closed the waste-gate condition. On a cycle average basis, the calculated power varies slightly between all cases between 1.23 to 1.59 kW.

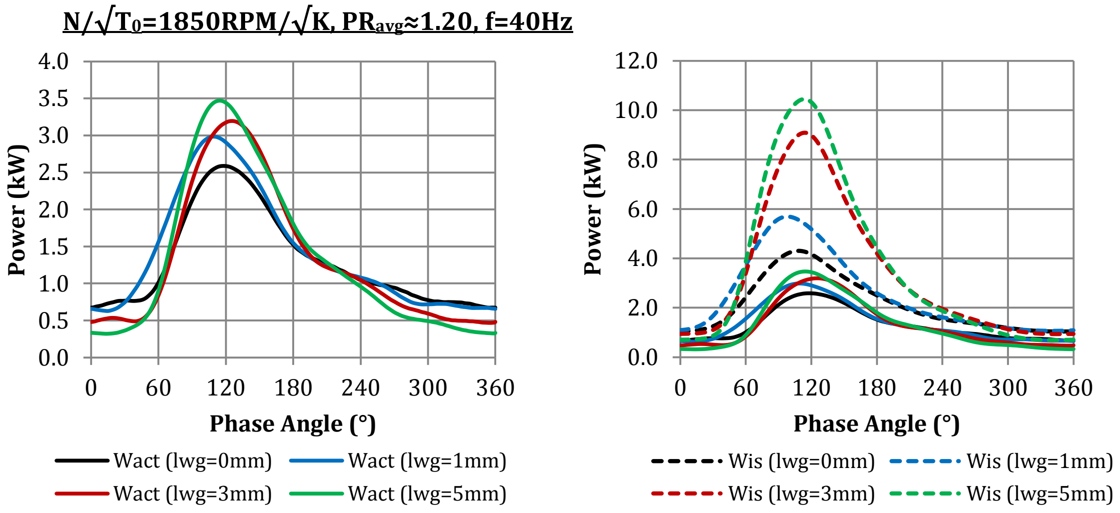

(a) **(b)**

Figure 4.30 Comparison of power characteristics of the turbine under waste-gated conditions

Figure 4.30 (b) compares the same set of actual instantaneous power profiles with corresponding isentropic power. Evidently, the isentropic power of the system rises as the waste-gate area is increased due to higher rate of mass flow bypassing the turbine rotor passage. The fact that actual power is obtained from torque which is measured downstream at the rotor rather than at the measurement plane (where quantities for isentropic power are measured) results in a slight phase difference between the two parameters. For the above set of results, the peak torque for the closed waste-gate case occurs at 117.8° phase angle and 109.3°, 125.2° and 114.8° for subsequent waste-gate openings. This can be attributed to the isentropic power being a function of both mass flow rate and pressure ratio across the system. As such, its profile is also subjected to the unsteadiness observed in mass flow behaviour as well as the pressure wave interactions within the system. It is also interesting to note that the profiles of the actual power trace share commonalities with its corresponding isentropic power in terms of form. Regardless of waste-opening, the torque and therefore the actual power features remain closely linked to its isentropic counterpart, but at lower magnitudes.

4.8 Cycle Average Performance

Earlier, it was demonstrated how a quasi-steady analysis was carried out as means of comparing unsteady to steady state performance. Another convenient way of comparing unsteady and steady state performance of the turbine is to use cycle average values of the pertinent turbine parameters.

This analysis brings forth the issue of averaging the relevant instantaneous parameters because in averaging, a single value which is representative of the whole cycle is sought after. In this work time averaging has been used. The cycle average mass flow parameter is obtained as follows:

$$\overline{MFP}_{cyc} = \frac{\sum_0^T MFP\,\Delta t}{T} \quad \text{... (4.12);}$$

where Δt is the time step and T is the total time taken by the pulse. The cycle average pressure ratio is calculated by taking the ratio of the integral of the total inlet pressure and static exit pressure over a pulse cycle as given in the expression below:

$$\overline{PR}_{cyc} = \frac{\sum_0^T P_{0,inlet}\,\Delta t}{\sum_0^T P_{s,exit}\,\Delta t} \quad \text{... (4.13)}$$

4.8.1 Cycle average swallowing characteristics

The graphs in Figure 4.31 shows the cycle average performance compared to steady state characteristics of mass flow parameter and total-to-static efficiency for turbine running at 2146RPM/√K with closed waste-gate and with opened waste-gate at 3.0mm valve lift. In Figure 4.30 (b), the total steady state mass flow characteristics of the system, which represent the mass flow through both the turbine and waste-gate is also included. This is marked as marked as "2146 RPM/√K, l_{wg} = 3mm (Steady)" in the graph. The points in each of the plots show cycle average values measured at different turbine loads and pulse frequencies.

The cycle average values for mass flow are seen to fall very close to the steady state mass flow parameter curves; this was also shown in Section 4.6.2. This is consistent in both closed and waste-gated conditions. For a give turbine load, the cycle average *MFP*s are almost similar at all inlet pulse frequencies. In the case of waste-gated turbines, this parameter is seen to coincide with the steady state waste-gated *MFP* curve. Indeed, this shows that there are still strong links between the characteristics of the turbine under pulsating and steady state conditions.

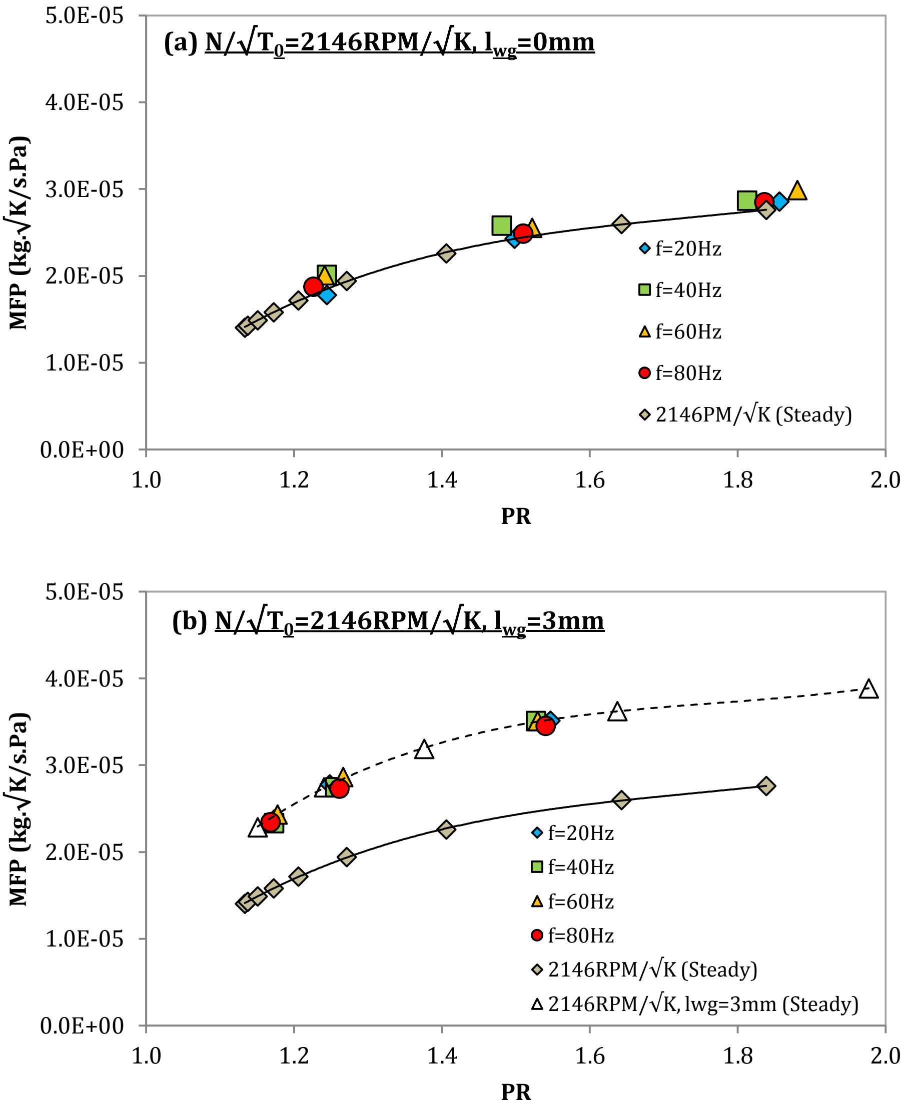

Figure 4.31 Cycle average swallowing characteristics for (a) closed waste-gate condition and (b) waste-gated condition with 3.0 mm valve lift

4.8.2 Cycle average efficiency

It is also interesting to compare turbine efficiency in the same manner as that undertaken for mass flow parameter. The known instantaneous values, the cycle average efficiency ($\bar{\eta}_{cyc}$) may be evaluated by integrating the actual and isentropic power over a pulse cycle as follows:

$$\bar{\eta}_{cyc} = \frac{\sum_0^T \dot{W}_{act}\,\Delta t}{\sum_0^T \dot{W}_{is}\,\Delta t} \quad \ldots (4.14)$$

where $\dot{W}_{act}$ is the actual power, $\dot{W}_{is}$ is the isentropic power. To enable comparison with steady state characteristics, the efficiency computed through the above expression is plotted against cycle average velocity ratio. This cycle average velocity ratio is weighted by isentropic power and is calculated by the following expression:

$$\overline{\left({}^{U}\!/_{C_{is}}\right)}_{cyc} = \frac{\sum_0^T \dot{W}_{is}(U/C_{is})\,\Delta t}{\sum_0^T \dot{W}_{is}\,\Delta t} \quad \ldots (4.15)$$

An advantage of evaluating the unsteady efficiency in time average form is that it eliminates the inherent phase shifting issues associated the different locations of measurement points. This is not an issue for swallowing characteristics since the measurement of inlet pressure, temperature and mass flow are all carried out at the same reference plane and the exit pressure being atmospheric is almost constant throughout the cycle. On the other hand, the parameters for efficiency calculation are obtained at different locations within the system with torque being measured at the rotor, further downstream of the inlet parameters. Similar to the mass flow characteristics, the cycle average efficiencies are plotted against velocity ratio for the turbine operating at 2146 RPM/√K under closed and opened waste-gate condition (l_{wg} = 3.0mm) with different selected loads and four pulse frequency levels as shown in Figure 4.32 below.

In general, it is observed that the cycle average efficiencies are higher at higher pulse frequencies. Other authors have observed similar results with the cycle averaged efficiency being higher for higher pulse frequency (Mamat, 2012). This may be attributed to the mass flows being slightly lower and more influenced by the wave dynamics within the volume than at lower frequency cases, giving rise to the calculation of efficiency. Overall, the cycle average efficiency points are lower than the steady state characteristics, but follow the trend quite closely. In the waste-gated condition shown above, the cycle average points again, are observed to be lower than the steady state curve. Nonetheless, a trend can be seen in that the peak efficiencies are shifted towards the low velocity ratio region in the opened waste-gate condition. At high velocity ratios, there is a tendency for efficiency at high frequencies to be higher than that at low frequencies.

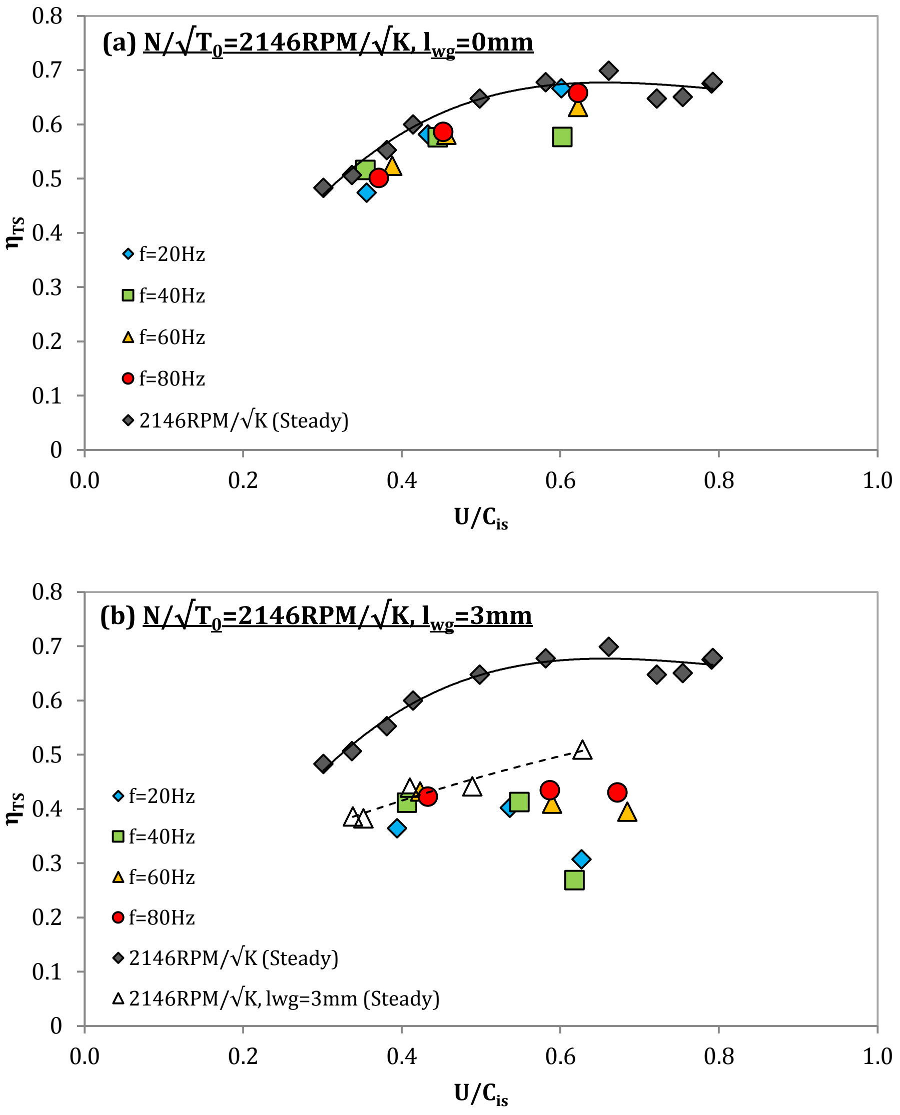

Figure 4.32 Cycle average total-to-static efficiency for (a) closed waste-gate condition and (b) waste-gated condition with 3.0 mm valve lift

4.9 One-Dimensional Simulation of Waste-gated Turbine Performance

With the experimental results at hand, it is interesting to assess whether or not the behaviour of the turbine under pulsating inlet conditions can be represented in a 1-D simulation environment. This attempt is implemented in a 1-D, gas dynamics, commercial engine simulation software namely GT-Power. The piping layout of the experimental setup from the exit of the pulse generator downstream is modelled as 1-D pipes with appropriate equivalent one-dimensional geometry. The turbine volute section is simplified as a straight pipe with uniform diameter, having a length equal to the meridional distance between the tongue and 180° rotor azimuth angle as proposed by Costall and Martinez-Botas (2007) and later demonstrated in the work of Chiong et al (2013) and Yang et al (2014). The flow through the rotor passage is assumed to be quasi-steady considering the flow length being relatively small compared to the rest of the pipe sections. This enables the use of a steady state turbine performance map as a boundary within the layout in the form of a look-up table. Total pressure and temperature profiles measured during experiments are imposed at the inlet boundary while atmospheric pressure is imposed at the exit. These inlet pressure and temperature profiles are distributed over 360° profile angle and are driven by a prescribed cyclic frequency. The 1-D, compressible, unsteady Navier-Stokes equations are solved using explicit time integration scheme (Gamma Technologies, 2011). These equations are shown in Section 5.2.

In a typical simulation routine, a compressor part is linked to the turbine via a shaft component and steady state convergence is reached when the power produced by the turbine and that absorbed by the compressor is balanced. However, in the absence of a compressor, a torque element counteracting against that produced by the turbine is used as a substitute. A corresponding mean torque value equal to that recorded in the experiments are set and solution convergence is met whenever the predicted cycle average torque output is equal to this mean torque value.

Simulations are first performed for closed waste-gate condition followed by two opened waste-gate conditions of 1.0 mm and 3.0 mm valve lifts. Two sets of experimental cases are simulated here based on the experimental average turbine speed and pulse frequency. The first set of case simulates the turbine which is operating on the dynamometer at 2146 RPM/√K and 20 Hz pulse frequency whereas the second set of case, at 1850 RPM/√K and 60 Hz pulse frequency. The values of pertinent parameters are compared at locations similar to those in the experimental setup. Table 4.2 shows the predicted average turbine speeds for the two cases described above. It is seen that the average speed was very well predicted by GT-Power, giving confidence in the prediction of other turbine performance parameters.

Table 4.2 Predicted turbine rotational speeds for two simulation cases (38500 and 33000 RPM)

Simulation Case	**Predicted Speed (RPM)**		
	WG = 0 mm	**WG = 1 mm**	**WG = 3 mm**
Case 1: Average speed (38,500 RPM)	38492.8	38477.1	38477.8
Case 2: Average speed (33,000 RPM)	32996.7	32974.5	32981.2

The computed mass flow parameter and torque are compared with experimental values and area shown in Figure 4.33 and Figure 4.34 for both sets of cases.

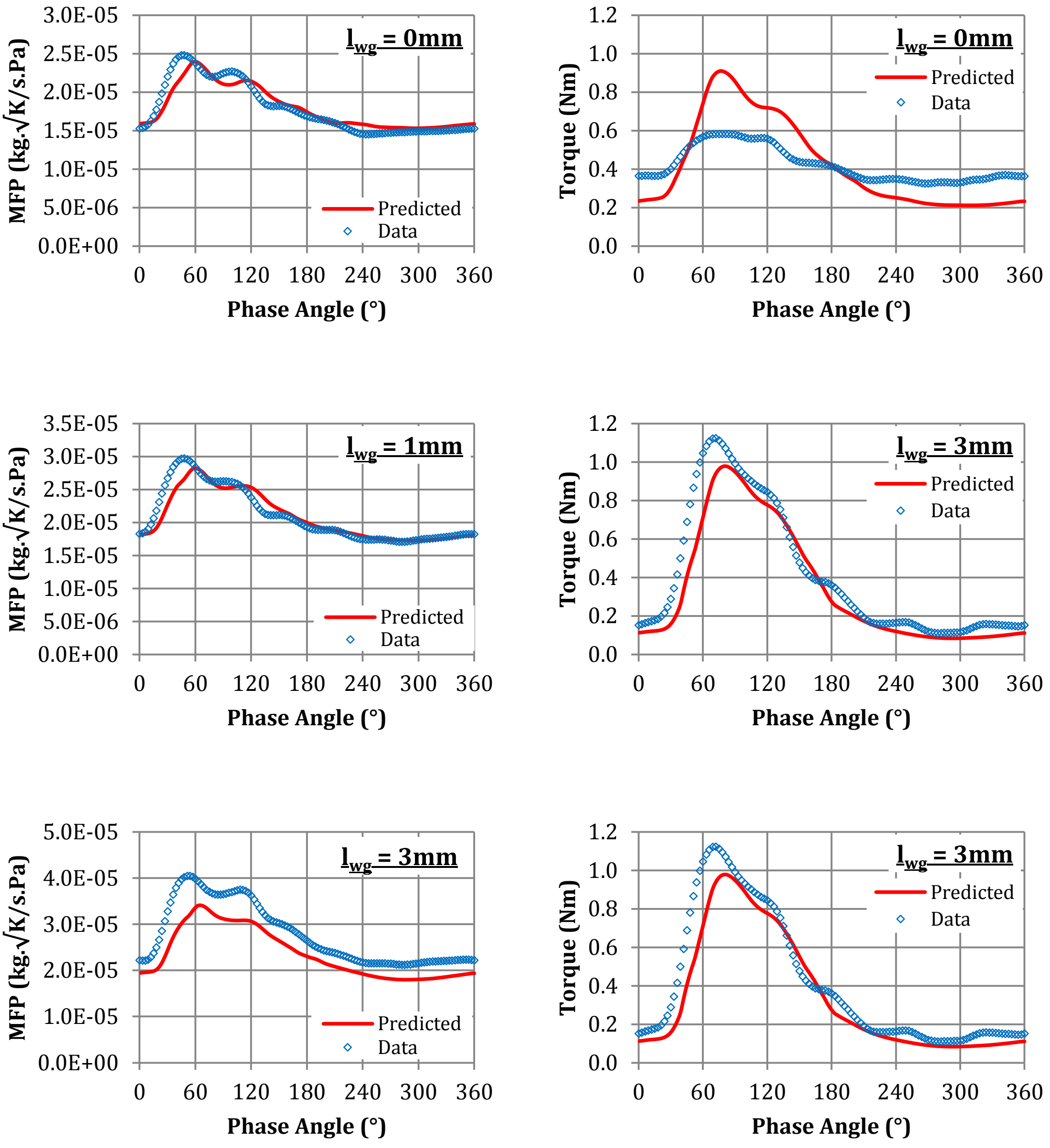

Figure 4.33 Comparison of predicted mass flow parameter with experimental data at various waste-gate valve lifts. (Case: N = 38500 RPM, f = 20 Hz)

Qualitatively, the predicted performance is in good agreement with experimental data even with minimal tuning of the model. At closed waste-gate conditions the prediction of mass flow parameter follows the profile of the experimental data. A slight lag in phase of approximately 10° is seen in the predicted results. This is can be associated with the simplistic representation of the piping geometry. Torque at the closed waste-gate condition is notably over-predicted by the simulation for this case although the mean value remains the same due to it being imposed as a boundary condition. The torque prediction at opened waste-gate conditions is slightly lower, but shows good agreement with the experimental data.

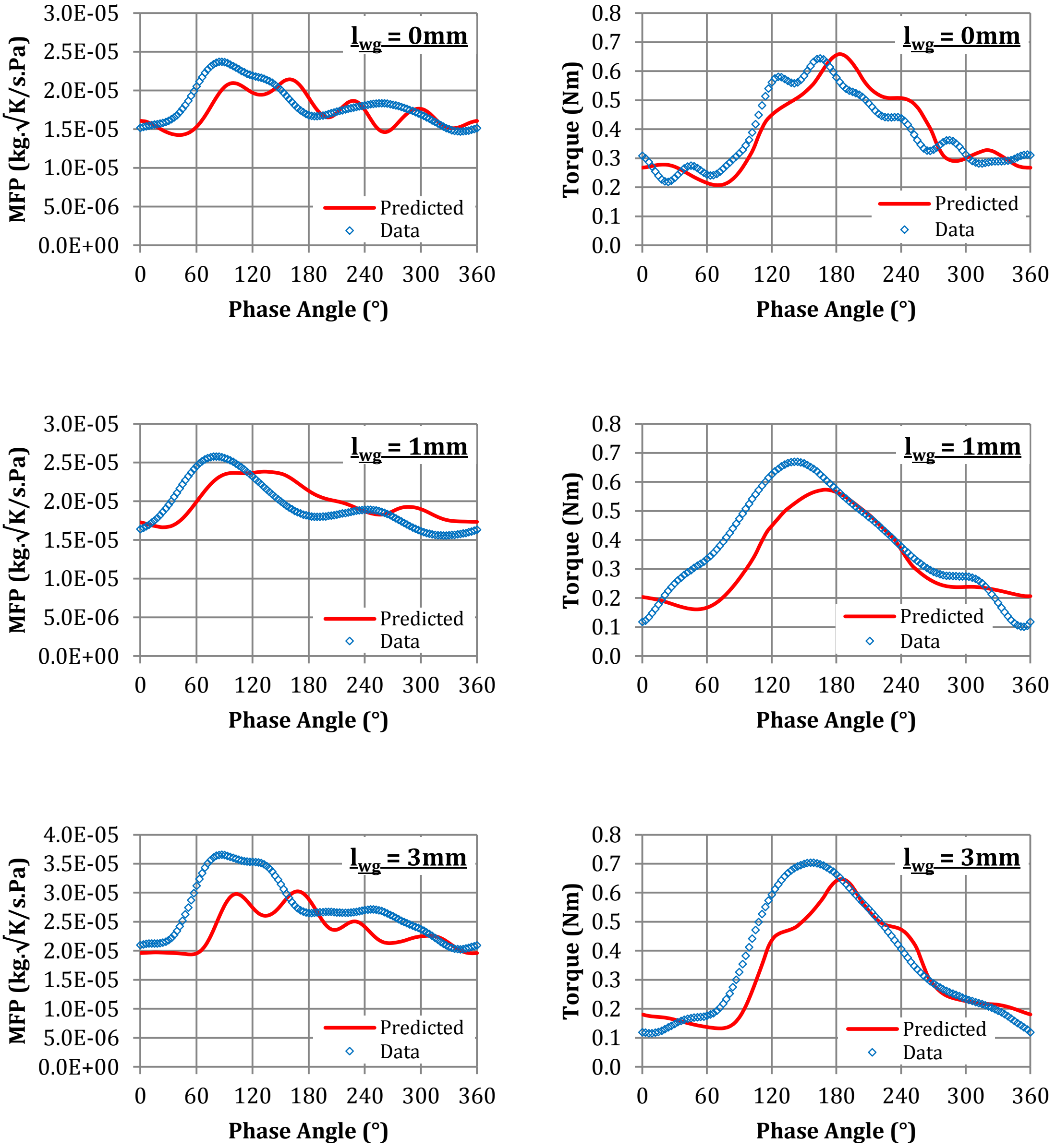

Figure 4.34 Comparison of predicted mass flow parameter with experimental data at various waste-gate valve lifts. (Case: N = 33000 RPM, f = 60 Hz)

The second set of simulations is carried out at 33000 RPM shaft speed with 60 Hz pulse frequency. The phase lag observed for predicted data is also present in this set of data. Compared to the prediction at lower frequency in the first case above, the mass flow trace is less well predicted by the simulation. The traces show that mass is under-predicted in all cases and appears to be more dynamic in shape compared to the actual data. The traces of instantaneous torque is seen to agree well with the experimental data. In the closed waste-gate condition the predicted torque is 6.0% higher than that measured during experiments. At opened waste-gate conditions, the predicted torque amplitude is lower than the actual measurement by 27.4% and 12.6% at 1.0 mm and 3.0 mm valve lifts respectively.

4.10 Summary

An experimental investigation has been undertaken to obtain the characteristics of an externally waste-gated turbine under unsteady pulsating inlet flow conditions. The methods that were adopted and the instrumentations that were used to perform the experiments were described in this chapter. Unsteady measurements were performed at various waste-gate openings, turbine loads and inlet pulse frequencies over two turbine speed parameters. A quasi-steady analysis was carried out on the unsteady measurements and finally, 1-D gas dynamics calculations were performed to model the performance of the turbine under waste-gated conditions. A summary of the important findings is given below.

1. It was found that under pulsating inlet conditions, the externally waste-gated turbine exhibits the typical feature of turbocharger turbine unsteady behaviour where the measured instantaneous mass flow parameter forms a hysteresis loop encapsulating the steady state curve. Increasing the turbine loads resulted in the increase in the amplitudes of both mass flow and pressure ratio. When viewed on a super-imposed steady state map, this increase in mass flow and pressure ratio amplitudes causes the loop area to expand. This behaviour is associated with the filling and emptying process taking place in the turbine volute. The turbine instantaneous torque measurements also exhibit a similar trend where the amplitudes increase as the load is increased.
2. For different inlet pulse frequency levels, a clear distinction in the unsteady mass flow characteristics was observed. In general, it was seen that the pressure ratio amplitude decreases while the mass flow parameter amplitude increases as frequency levels are increased, indicating a higher departure from quasi-steady behaviour. The wave actions within the turbine volume is prevalent in dictating the dynamics of the flow when the pulse frequency is varied. As a result, the positions of peak mass flow is seen to vary over the pulse cycle depending on the superposition of pressure waves within the flow volume. The torque amplitude decreases with its peak shifted towards higher phase angles as the pulse frequency is increased due to its dependency on the pulse frequency itself and the time taken for the pulse energy to propagate from its source.

3. The quasi-steady analysis was carried out to compare the actual unsteady behaviour of the turbine to that predicted from its steady state characteristics. It was found through this analysis that the quasi-steady assumption is inadequate in representing the unsteadiness of the turbine behaviour with regards to mass flow amplitude change at different loads and frequencies.
4. Under waste-gated conditions, the shape of the unsteady loops is seen to resemble that of a closed waste-gate condition at low waste-gate opening areas with the size of the hysteresis loops increasing as the waste-gate area is increased. At large waste-gate openings, the influence of wave reflections on the dynamics of the flow was observed. The flow through the waste-gate valve itself was also measured where higher pressure ratio amplitudes was observed for higher waste-gate valve lifts. As opposed to what was observed for the turbine, the instantaneous pressure ratio through the waste-gate valve peaks before mass flow parameter causing the loops to circulate the steady state curve in a counter-clockwise direction. Instantaneous torque measurements of the turbine under waste-gated conditions revealed that for constant mean torques, the amplitudes increase as the waste-gate lift is increased. The dynamics of the instantaneous torque are similar to those under closed waste-gate conditions.
5. The waste-gated turbine performance under unsteady inlet conditions is modelled using the GT-Power, 1-D gas dynamics code. Here, the essential elements needed to represent the system in a 1-D virtual environment was identified. These include the 1-D representation of the piping layout and the turbine volute, the turbine steady map and the waste-gate valve flow characteristics. The pressure and temperature profiles are imposed as boundary conditions at the system inlet. A counteracting torque element was used to load the turbine in the absence of a compressor and the cyclic mean torque was specified. The simulation was carried out for different speeds and waste-gate openings. With minimal tuning, the turbine speed, mass flow and torque were predicted well, giving confidence in further implementations of the model in a complete engine environment.

Chapter 5 One-Dimensional Gas Dynamics Simulation of Engine and Turbocharger Performance

5.1 Introduction

The preceding chapters focused on the performance of turbines under steady state and pulsating inlet conditions. This part of the thesis presents the simulation work carried out to evaluate the performance of boosting systems in an on-engine environment. This involves the use of a commercial 1-D gas dynamics code for engine performance simulation. The investigation is divided into two main parts. First, a simulation-based investigation is carried out to investigate the impact of turbocharger turbine map width on the prediction of engine performance.

The second part of the simulation work is carried out as part of an actual engine development program called the *Ultraboost*; a project which aims at exploring the limits of engine downsizing. With regards to this, the main objectives of this work presented in this chapter are to describe the modelling process of a multi-stage boosting system and to assess the performance of the boosting components. This highly downsized engine employs a boosting system that was evaluated by experiments after an elaborate matching process. Discussion of the results emphasizes on boosting system and basic engine performance.

5.2 The GT-Power Engine Simulation Code

As a computational tool, GT-Power, which forms a part of the GT-Suite vehicle simulation package, is selected for the current investigation based on its widespread use by the industry. The concept of flow modelling in GT-Power is based on the solution of the governing equations in one-dimensional form. The conservation of mass, momentum and energy (the Navier-Stokes equations) are solved with all quantities averaged across the direction of flow. The software is an industrial 1-D gas dynamics code developed by *Gamma-Technologies* with built in predefined template objects of individual engine components such as flow components, piping system and manifolds, combustion system, valvetrain, cranktrain, heat exchangers, rotating elements, control elements, boosting components etc. (Gamma Technologies, 2010). This object-based code allows users to arrange the individual components based on the actual engine and specify their geometrical and aero-thermodynamic properties.

The code adopts a staggered grid discretization method whereby the system is divided into volumes and sub-volumes with mean values (1-D) of scalar and vector flow variables solved at the centroid and the boundaries of each sub-volume respectively. The simulations carried out in this thesis are set to run in 'speed' mode which implies that the brake torques is calculated for imposed engine speeds. The 1-D, compressible, unsteady form of the Navier-Stokes equations is solved using explicit time integration method with the size of each time step limited by the Courant time step condition:

Continuity

$$\frac{dm}{dt} = \sum_{boundaries} \dot{m} \quad \text{... (5.1a);}$$

Momentum

$$\frac{d\dot{m}}{dt} = \frac{dpA + \sum_{boundaries}(\dot{m}u) - 4C_f \frac{\rho u|u|}{2}\frac{dxA}{D} - C_p\left(\frac{1}{2}\rho u|u|\right)A}{dx} \qquad \text{... (5.1b);}$$

Energy

$$\frac{d(me)}{dt} = -p\frac{dV}{dt} + \sum_{boundaries}(\dot{m}H) - hA_s\left(T_{fluid} - T_{wall}\right) \qquad \text{... (5.1c);}$$

For clarity, the variables in equation 5.1 above are described in Table 5.1.

Table 5.1 Description of variables in Equation 5.1

$\dot{m}$	boundary mass flux into volume ($\dot{m} = \rho A u$)
m	mass of the volume
V	Volume
p	Pressure
ρ	Density
A	flow area (cross sectional)
A_s	heat transfer surface area
e	total internal energy (internal energy plus kinetic energy) per unit mass
H	total enthalpy ($H = e + p/\rho$)
h	heat transfer coefficient
T_{fluid}	fluid temperature
T_{wall}	wall temperature
u	velocity at the boundary
C_f	coefficient of friction (skin friction coefficient)
C_p	coefficient of pressure (pressure loss coefficient)
D	equivalent diameter
x	discretization length

The Courant number defined below relates the calculation time step to the minimum discretization length of the flow domain.

$$Courant\ number = \frac{\Delta t}{\Delta x}(|u| + c) \leq 0.8 \qquad \ldots (5.2)$$

where, Δt is the time step (s), Δx is minimum discretized element length, u is the fluid velocity and c is the speed of sound. The solution output is retrieved from a built in post-processing software called GT-Post.

5.3 Modelling of Boosting Systems

Boosting components such as turbines and compressors are modelled in the code as boundary systems within the engine architecture. The prediction of charging system performance in is on a quasi-steady basis, which means that the unsteady performance parameters are assumed to be of an equivalent steady value at an instantaneous time. The performance maps in the form of look-up tables comprise data of mass flow and efficiency at constant speed lines which are generated and presented in steady state conditions. At a given time step, the gas conditions at the adjacent pipes are used to read values the values of mass flow, efficiency and shaft speed in the look-up tables.

The isentropic enthalpy (Δh_{is}) change across turbines and compressors are calculated through the following equations:

$$\Delta h_{is,T} = c_p T_{0,in}\left[1 - (PR_T)^{\frac{1-\gamma}{\gamma}}\right] \ldots (5.3)$$

$$\Delta h_{is,C} = c_p T_{0,in}\left[(PR_C)^{\frac{\gamma-1}{\gamma}} - 1\right] \ldots (5.4)$$

with the subscripts "T" and "C" denoting turbines and compressors respectively. The exit enthalpies for turbine or compressor are calculated as follows:

$$h_{out} = h_{in} - \Delta h_{is} \cdot \eta_{TS} \qquad \ldots (5.5);$$

$$h_{out} = h_{in} + \frac{\Delta h_{is}}{\eta_{TT}} \qquad \ldots (5.6);$$

where η_{TS} and η_{TT} respectively denotes the total-to-static and total-to-total efficiencies of the turbine and the compressor. This enables the calculation of turbine and compressor power as shown below:

$$\dot{W}_T = \dot{m}(h_{in} - h_{exit}) \qquad \ldots (5.7)$$

$$\dot{W}_C = \dot{m}(h_{exit} - h_{in}) \qquad \dots (5.8)$$

To reach steady state convergence, it is required that these calculated powers of the two components are balanced over a solution period.

5.4 Effects of Turbine Map Extrapolation on Prediction of Engine Performance

It has been shown in Chapter 3 that the extrapolation method employed by GT-Power, when carried out on a turbine map, is influenced by the width of the map. It may be interesting to see whether this effect has any impact on the prediction of engine performance. To do this, simulations are performed on an engine using both the full “wide” map and the reduced “narrow” map and the predicted basic engine performance are compared for both cases. These maps are the same ones used to demonstrate the extrapolation process in Section 3.19. This investigation along with that presented in Section 3.19 forms the work presented by Pesiridis et al (2012).

The virtual engine model that is used in this study is a 4.7 litre direct injection (DI) Diesel engine with several pertinent specifications shown in Table 5.2. The main engine layout and settings were obtained from an example engine, which was readily available in GT-Power as a template. To isolate the effects of turbine maps on the performance of the engine, the engine layout is kept as basic as possible without the interference of boost control systems.

Table 5.2 Basic engine specification

Parameters	**Specification**
Combustion System	4-Stroke, V6, Diesel DI
Capacity	4.7 litres
Compression Ratio	16.5
Bore x Stroke Dimension	100 x 100 mm
Induction System	Single stage turbocharger

The engine simulation was carried out for engine speeds ranging from 1000 to 3500 RPM to capture the behaviour of turbine over a wide operating range. Figure 5.1 shows the basic predicted performance characteristics of the turbocharged engine compared to the baseline naturally aspirated (NA) engine.

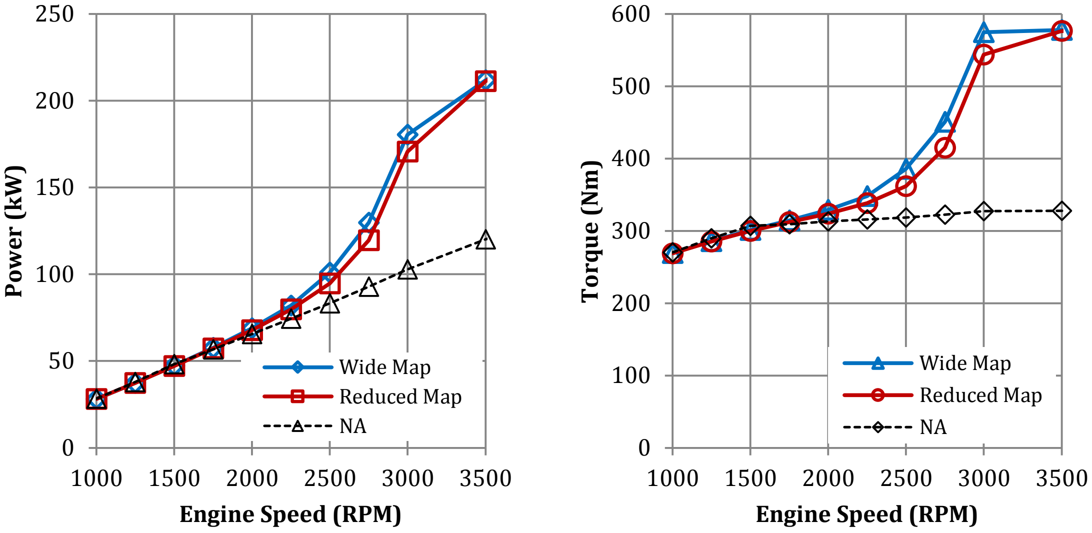

Figure 5.1 Comparison of predicted power and torque characteristics of the engine using different turbine map widths

As expected, the power gain obtained through turbocharging is apparent. In this case, the maximum power output of the engine is increased by 76.2% at 3500 RPM engine speed through turbocharging. Equivalently, the maximum engine torque is also increased by the same margin at 3500 RPM. The torque curve shown above clearly indicates a poor matching of the turbocharger to the engine. This is made clear by the lack of improvement in torque at low end speeds. Nonetheless, the main intention of this exercise is to show the impact of map width on the engine performance prediction and therefore, the issue of matching is not within the scope of discussion here.

The main reason for this substantial increase in performance can be attributed to the improvement in the volumetric efficiency (η_V), defined by the mass flow rate of air inducted into the intake system divided by the volume displaced by the piston. A high pressure flow from the turbocharger is able to deliver higher air mass flow compared to air being inducted at ambient pressure in the naturally aspirated engine, thus attaining higher volumetric efficiency. An engine's relative ability to produce work over a cycle is represented by its mean effective pressure (MEP). The actual power (brake power) produced by the engine is directly related to the engine brake mean effective pressure (BMEP), which is expressed by the equation below:

$$\text{BMEP} = \frac{\dot{W}_b n_R}{V_d N} \quad \ldots (5.9);$$

where $\dot{W}_b$ is the brake power, n_R is the number of crank revolutions for each power stroke, V_d is the displacement volume and N is the engine speed. The increase in volumetric efficiency also affects the fuel consumption of the engine which is represented by the brake specific fuel consumption (BSFC) defined as the ratio of fuel mass flow rate in to the cylinder ($\dot{m}_f$) to the brake power as shown in the equation below:

$$\mathrm{BSFC} = \frac{\dot{m}_f}{\dot{W}_b} \quad \dots (5.10)$$

As a result of the increase in brake power in a turbocharged engine, the brake specific fuel consumption, which is the ratio of fuel mass to power, is subsequently reduced compared to a naturally aspirated engine. The predicted BMEP and BSFC for the engine using both wide and reduced turbocharger maps are shown in Figure 5.2.

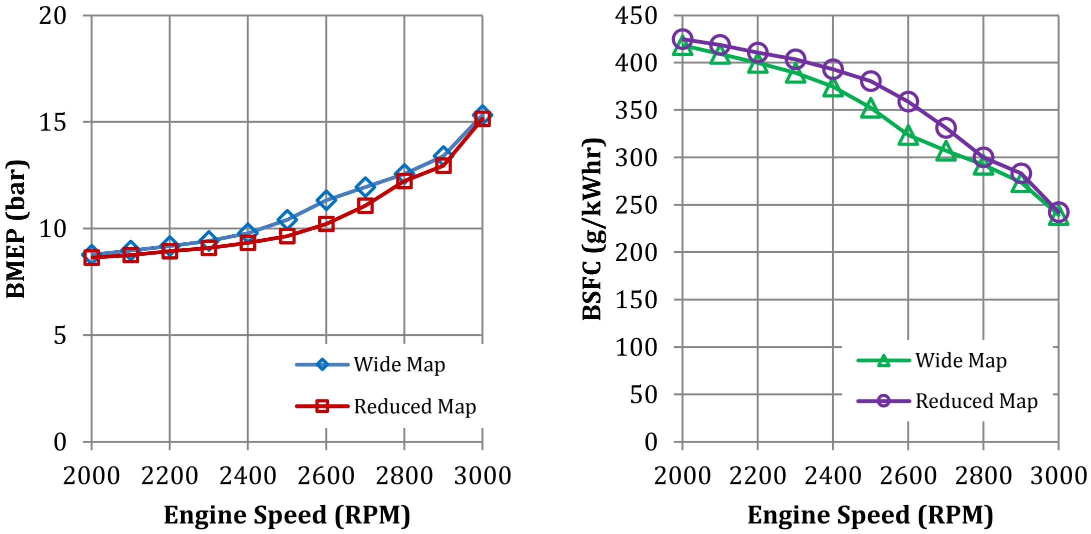

Figure 5.2 Predicted engine BMEP and BSFC using extrapolated wide and reduced turbocharger turbine maps

As can be seen, there is a notable difference in the prediction of BMEP despite the maps being extrapolated from the performance data of the same turbine (the difference being the data range). The maximum predicted BMEP is achieved at 3500 RPM where the values are identical for both maps. A stark difference in BMEP prediction is seen to occur between 2000 to 3000 RPM engine speeds; the largest difference being ≈9.77% seen at 2600 RPM engine speed. Similarly the largest difference in BSFC is seen between 2400 and 2600 RPM where the BSFC a 10.8% reduction in predicted BSFC was seen at 2600 RPM. This can be attributed to the turbocharger operating in a more favourable condition when the turbine performance predicted from the wider experimental map is used, which is discussed below.

Such a large difference in predicted engine performance parameters is directly related to the predicted amount of air being delivered to the cylinder at a particular engine speed. At speed and pressure ratio points in the turbine maps where the values of efficiency and mass flow are different, the computed power and consequently compressor mass flow delivery will also be different. The condition for this to happen is when the simulation runs at the points on the maps which are further away from the maximum efficiency points on the speed lines where the values of mass flow are in the extrapolated region. To examine this further, the predicted turbine speed and pressure ratio are compared for both maps in Figure 5.3. It can be observed that within 2000 to 3000RPM engine speed, the wide map predicts higher turbine speed and slightly higher pressure ratio than the narrow map. This leads to an increase in calculated boost pressures and therefore increased mass flows into the engine cylinder.

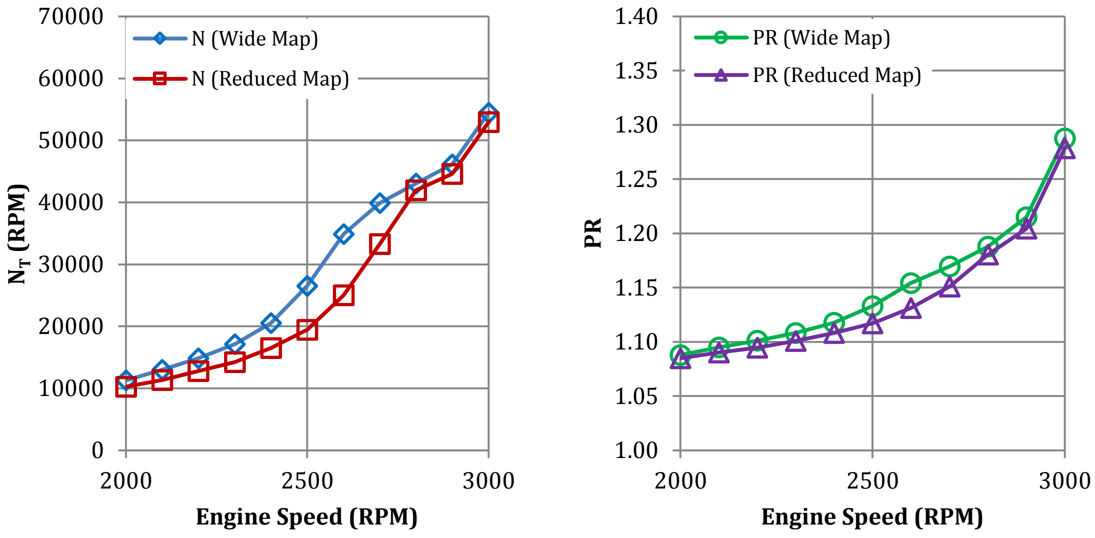

Figure 5.3 Predicted turbine speed and pressure ratio using different map widths

There is a need to explain the source of such a significant difference in prediction using the two maps at hand. To do this, the turbine mass flow parameter and efficiency values at engine speeds of 2000 to 3000 RPM and the corresponding velocity ratio are compared in Figure 5.4. The narrow map predicts lower turbine efficiency over the speed range with a peak value of 10.14% difference at 2500RPM (Figure 5.4a). At 2600RPM where the difference in the predicted turbine speed is at its maximum (Refer to Figure 5.3), the difference in velocity ratio shown in

Figure 5.4b is also at its maximum with the wide map and the narrow map reading values of 0.620 and 0.492 respectively. These velocity ratio values lie at locations where experimental data is present only in the wide map and the velocity ratio for the narrow map is read from the extrapolated data region (see Figure 3.20).

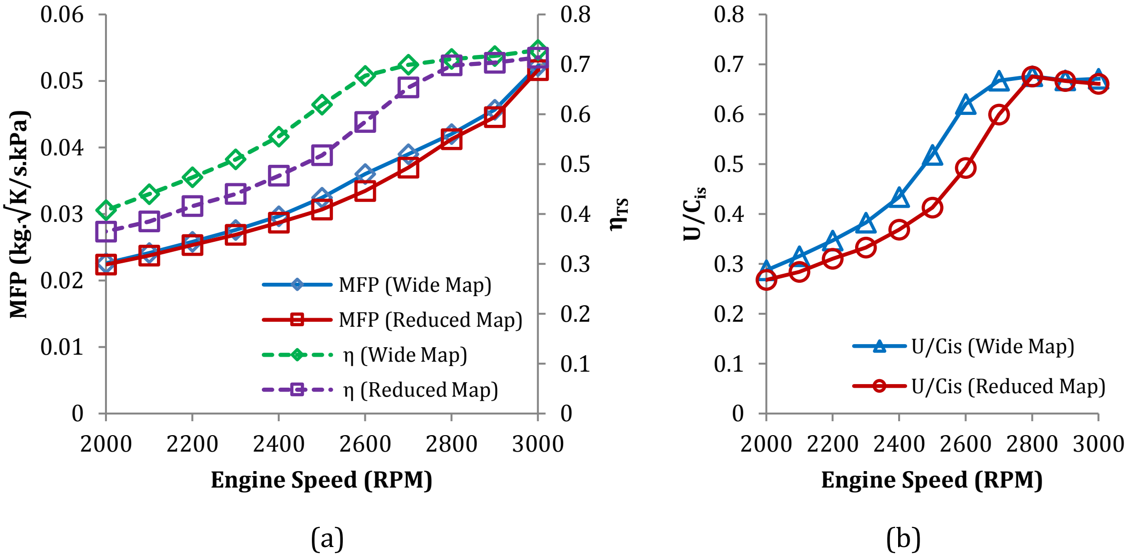

Figure 5.4 (a) Predicted turbine mass flow parameter and efficiency against engine speed (b) Turbine velocity ratio against engine speed

What can be drawn from the above analysis is that using narrow maps, which is usually the case in current practices, may result in under-prediction of the basic performance prediction of an engine. For the specific case shown here, the differences in predicted performance occur in the 'useful' range of the engine speed. This would imply that for a given requested BMEP curve in an engine operation regime, the use of a narrow turbocharger map in a simulation may result in over-specification of a matching turbine. Inconsistencies in predicted and actual engine performance are often mitigated through calibration and appropriate fine-tuning in the later stages of development. The addition of various turbine and engine control mechanisms such as waste-gates may further diminish the impact of these inconsistencies. Nonetheless, the findings from this investigation reveal that these variations can be quite substantial.

5.5 Modelling of Downsized Boosted Engine

The following sections describe the performance modelling of an actual heavily downsized engine. This engine was developed by a consortium of industrial and academic partners led by

Jaguar-Land Rover to demonstrate the possibility of reducing the capacity of an automotive engine by 60% while maintaining the same torque characteristics of the naturally aspirated counterpart. The investigation carried out in this thesis focuses mainly on the modelling and performance prediction of the boosting systems employed by this engine. This involves the GT30R turbocharger which was used in the steady state and unsteady experiments presented in Chapter 3 and 4.

5.5.1 Engine model and performance targets

The ≈60% level of downsizing led to the development of a 4-stroke, 1991 cm^3 (≈2.0 l), inline-4 cylinder, spark ignition prototype engine which utilizes a series configuration, dual-stage forced induction system. Table 5.3 highlights several of the engine technical specifications and a schematic diagram of the engine layout is shown in Figure 5.5. The development of the engine has been described previously by Salamon et al (2012) and Copeland et al (2012) with the latter focusing on boosting system selection. The project is carried out on two versions of the engine designated as UB100 and UB200. The UB100 which is the earlier version was derived from a V8 engine with one of its cylinder bank blanked off. The engine was installed with a new Engine Management System (EMS) module and was matched to the specified boosting systems. Early controls and matching of boosting systems were carried out on this engine and were later carried forward to the UB200 which has its own newly designed block and is closer to a finished prototype than its predecessor. The simulation work described here is based on the UB200 engine.

Table 5.3 Engine specifications

	Specification
Layout	4-Cylinder (Inline)
Firing Order	1-3-4-2
Displacement	1991 cm^3 (≈ 2.0 litres)
Bore x Stroke	83 x 92 mm
Compression Ratio	9.0:1
Fuel Delivery System	GDI & PFI
Valve system	Variable Valve Timing (VVT) with Cam Profile Switching (CPS)
Specific Power Output	142 kW/l at 6500 rpm
Specific Torque Output	255 Nm/l at 3500 rpm
Specified BMEP	≈ 32 bar at 3500 rpm ≈ 25 bar at 1000 & 6500 rpm
Forced induction system	Dual-stage, inter & after-cooled, series boosting system; HP Stage: Roots supercharger LP Stage: Single entry turbocharger with external bypass system

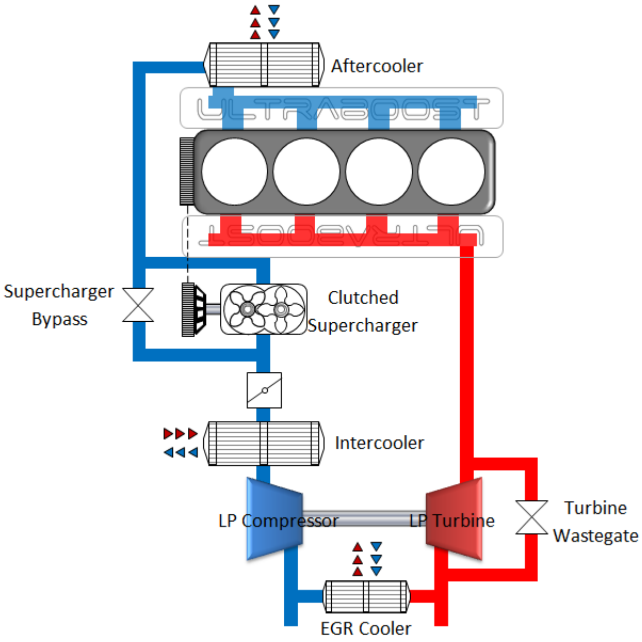

Figure 5.5 Basic layout of the 2.0 litre downsized engine showing dual-stage series boosting system

The engine development was set to achieve three main objectives in areas regarding the combustion system, the boosting system and CO_2 reduction. The high target for brake torque from such as small displacement implies that the cylinders will have to withstand extremely high mean maximum pressures. In this case, the combustion chamber must be able to operate at approximately 135 bar mean peak cylinder pressure. To maintain high thermal efficiency, the combustion system must also operate at relatively high compression ratio thereby making it highly knock tolerant. Besides providing high full load torque characteristics, the boosting system must also be able to provide best-in-class transient response; a typical issue associated with large single stage turbocharger systems. In this aspect, the transient response was targeted to be better than that of a benchmark production 3.0 litre twin-turbo V6 Diesel engine in terms of its time to torque (TTT) value. Essential to an engine downsizing exercise, the third objective, is for the engine to be able to obtain a 35% reduction in tailpipe CO_2 at a vehicle level, relative to the benchmark 5.0 litre NA engine over the NEDC cycle. This translates to approximately 23% of fuel economy at the engine level (Salamon et al, 2012).

The main goal of this downsizing program is to achieve the same performance level as a 5.0 litre V8 NA engine. For a 2.0 litre engine, this translates to a 60% level of downsizing. Figure 5.6 shows the BMEP curve of the said NA engine at full load which the current engine has to match. The performance of this engine is characterized by strong torque characteristic with close to linear power increase over the entire speed range. 510 Nm peak torque was achieved at

3500RPM while a maximum power of 283kW was achieved at 6500RPM. To deliver the same torque characteristics of the NA engine, the current engine has to attain a maximum BMEP of ≈32 bar maximum at 3500rpm and ≈25 bar at 1000 and 6500 rpm. In practice, the only viable way of achieving the mentioned BMEP level at full load is via forced induction as demonstrated by various authors (King et al, 2012, Lumsden et al, 2009 and Wirth et al, 2000).

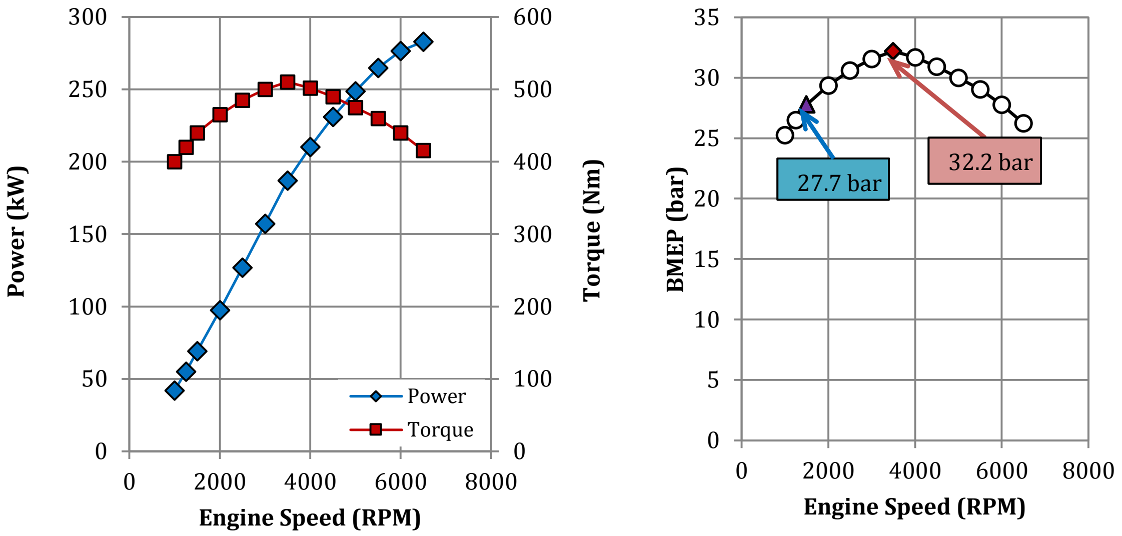

Figure 5.6 Target engine performance based on production NA 5.0 litre V8 engine and BMEP requirements for the downsized engine to reach performance targets

5.5.2 Description of boosting systems

To arrive at the boosting system configuration prescribed for the engine, an elaborate selection process has been implemented as has been outlined by Copeland et al (2012). Essentially, numerous potential boosting systems were required to fulfil a set of performance criteria. Amongst others, the assessment criteria for system selection include achieving the target BMEP, minimum BSFC, transient response and pumping loss. Each of these criteria was assigned a weightage of priority which are linked to another set of requirements at a vehicular level. A method of assessment based on the Quality Function Deployment (QFD) was employed to select the optimum system for the engine.

The target BMEP and BSFC values enable early decision on the size of the boosting system. This is done by estimation of the quantity of air and the boost pressure needed at the inlet manifold for specific points on the speed range based on the required engine torque and power characteristics. This estimation allows for selection of compressor frame size which governs the operational limits of the device. The initial matching process for the Ultraboost engine arrives at the Low Pressure (LP) stage turbocharger system in the form of a Honeywell "GT30R" unit to deliver the required boost for rated power. The main turbocharger assembly comprises of a radial type turbine with 60mm wheel diameter paired to a 67mm wheel diameter compressor capable of delivering boost up to 3.5bar absolute. The turbocharger performance data (maps) were also provided by the manufacturer for use in 1-D calculations.

5.5.3 Boosting strategy

As mentioned, the LP stage is intended to produce the BMEP levels for rated power, thus its operation range is at the high engine speed ranges i.e. above 3000 RPM. The capability of the LP turbocharger at lower engine speeds is restricted by the surge margin of the compressor. Figure 5.7 shows the predicted BMEP curve obtained solely with the LP stage turbocharger (black line). It is seen that the LP stage would be able to deliver the BMEP target at 3000 RPM onwards. Clearly, the use of a single stage system is unable to provide the necessary BMEP over the entire speed range; hence additional boosting (HP stage) at low-end speeds below 3000RPM is needed. On its own, the HP stage selected for this engine is capable of delivering low end BMEP indicated by blue line in Figure 5.7.

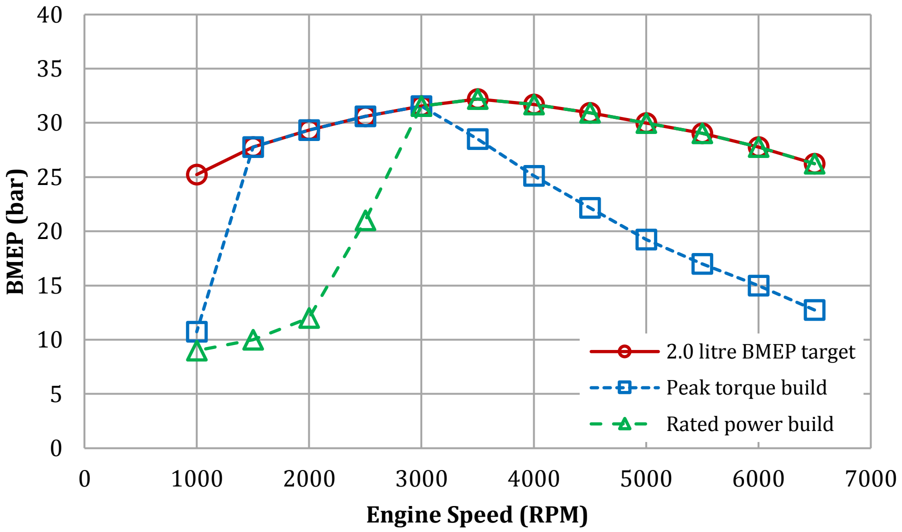

Figure 5.7 Estimated BMEP levels obtained with individual boosting devices (Copeland et al, 2012)

The HP stage boosting is provided by a prototype roots type Twin Vortices Series (TVS) clutched single speed supercharger supplied by *Eaton*. A clutched system allows the device to be detached from the engine crack shaft at engine speeds above 3000 RPM whereby the task of boosting is taken over entirely by the LP stage. A fixed crank-to-shaft gear ratio of 5.9 is set for the supercharger implying a maximum supercharger shaft speed of 17640RPM at 3000RPM. Beyond this point, the supercharger will be declutched and air flow through it will be bypassed. The boost air is cooled via two heat exchangers designated as intercooler and aftercooler located downstream of the LP and HP compressors respectively.

The charge-air coolers (CAC) used to cool the high temperature compressed air from each stage is of water-cooled types. The aim of cooling the charged air is to improve the volumetric efficiency of the engine by increasing the density of air (increasing mass) entering the combustion chamber. The LP stage cooling (intercooler) is carried out by an industrial cooler supplied by *Bowman* whereas that for the HP stage (aftercooler) is a customized unit by *Visteon*. The former was sized to run at heat exchanger effectiveness, ε = 0.85 at the engine's rated power while the latter at the same effectiveness at 3000 RPM engine speed and maximum supercharger speed. The preference of water-cooled heat exchangers over conventional its air-cooled counterpart is mainly because the former offers higher ε thereby allowing a greater degree of compactness and reduced hot side pressure loss over traditional air-to-air CACs. In addition, water-cooled CACs can function effectively independent of its location, cold fluid temperatures and exposed heat transfer areas as opposed to air-to-air types.

5.6 Turbocharger Performance Maps

Typically, the performance parameters are defined within the computational model in the form of pseudo-dimensionless parameters discussed in Section 3.2. In the simulation environment, the boosting systems are represented in the form of look-up tables (maps) which consist of pertinent performance parameters of the devices. A typical map comprises arrays of values for mass flow, pressure/expansion ratio and efficiency at different speeds.

5.6.1 The turbocharger compressor map

The compressor map for the turbocharger unit was provided by the manufacturer and is shown in Figure 5.8. The map presents the compressor pressure ratio, which is the ratio of exit to inlet pressures, plotted against the mass flow rate for different rotational speeds. The compressor total-to-total efficiency contour is superimposed on the map. This is defined as the isentropic work ($\dot{W}_{is,C}$) divided by the actual work ($\dot{W}_C$) across the compressor stage as shown in the equation below:

$$\eta_{TT} = \frac{\dot{W}_{is,C}}{\dot{W}_C} = \frac{\Delta h_{is,C}}{\Delta h_C} = \frac{h_{0s,exit} - h_{0,in}}{h_{0,exit} - h_{0,in}} \quad \dots (5.11)$$

This can also be represented in the form of enthalpy change (Δh) across the compressor as indicated in the definition above with $h_{0,in}$ denoting the total inlet enthalpy, $h_{0s,exit}$ denoting the isentropic exit enthalpy and $h_{0,exit}$ denoting the actual exit enthalpy.

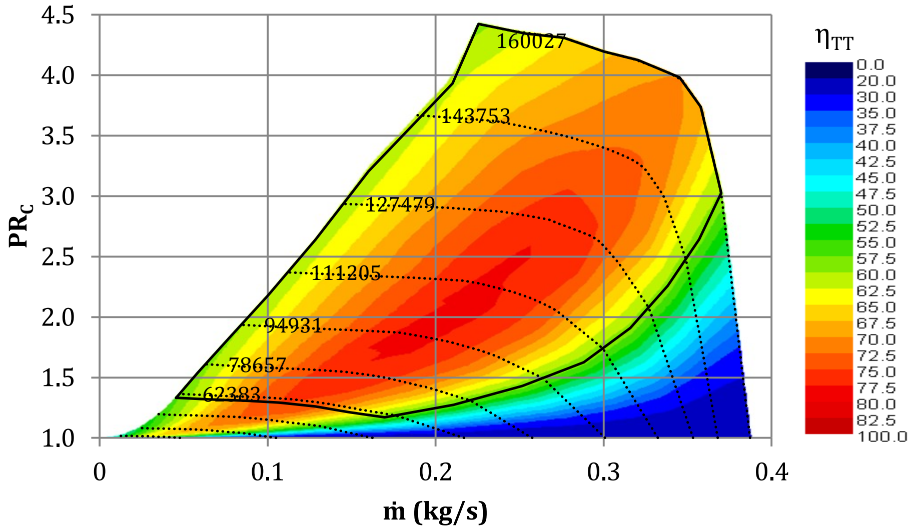

Figure 5.8 Turbocharger compressor map shown with total-to-total efficiency contour

5.6.2 The turbocharger turbine map

The same turbine map obtained from cold-test steady state experiments in Chapter 3 is used here. This map is used to complement the existing manufacturer map especially at low speed parameters which is not covered by the OEM data. The reason for this is the poor map extrapolation carried out by GT-Power on the experimental data due to the inability of the procedure to adequately fit a curve on the mass flow ratio versus normalized velocity ratio data whereby the intercept of the mass flow ratio at zero normalized velocity ratio is at a low value (Figure 5.9a). This results in the output map producing earlier choking conditions at high pressure ratio (low velocity ratio) as shown in (Figure 5.9b). Improving the extrapolation requires substantial tuning of the fit coefficients used in the extrapolation procedure.

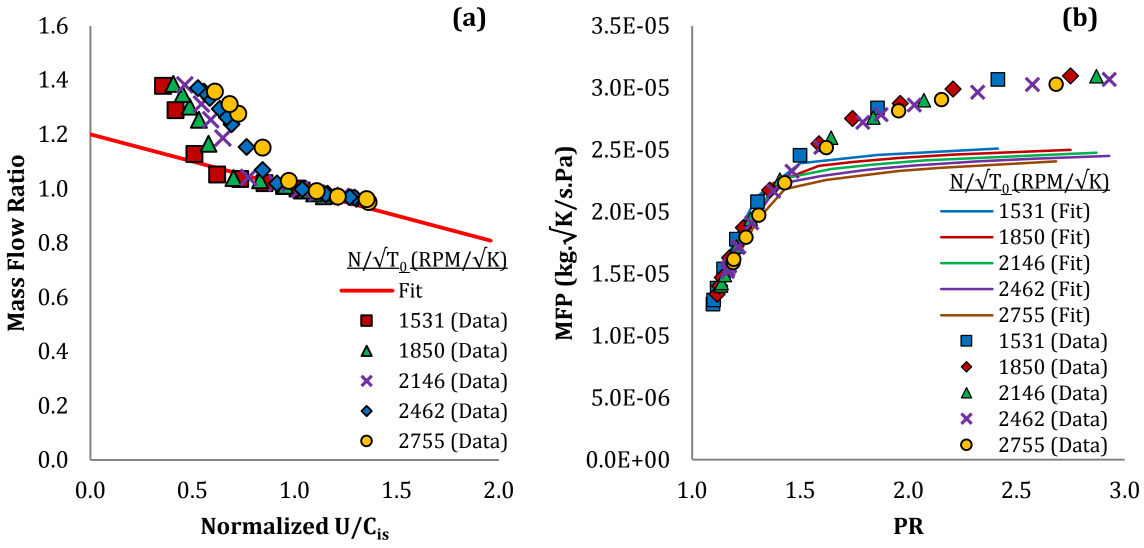

Figure 5.9 GT-Power map extrapolation on cold facility performance data

The map extrapolation using a combination of the maps (cold-test map and OEM map) however yields a much better agreement with experimental data. This is shown in Figure 5.10 below for mass flow parameter.

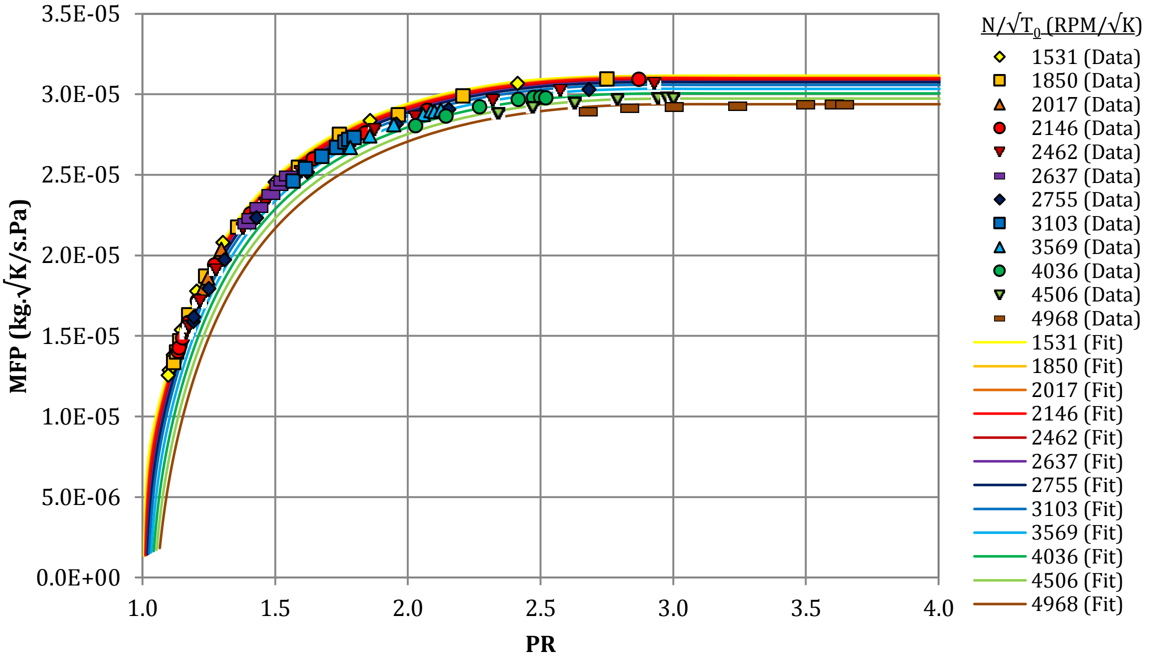

Figure 5.10 Comparison of predicted mass flow parameter and measured data

5.7 Supercharger Testing and Performance Maps

A dedicated supercharger test facility was designed allowing for measurements of its performance (Romagnoli et al, 2014). The mass flow and efficiency parameter of the supercharger is shown here in Figure 5.11. A 100 kW motor with a rated speed of 1800 RPM is used as the driving unit replicating the engine crankshaft rotation. A system of step-up gears is installed allowing the supercharger test speeds to be swept from low speeds up to 20,000 RPM. A pressure loading valve is installed downstream of the supercharger allowing for flow parameters to be varied at different constant speed lines. Thermodynamic measurements recorded for the purpose of map generation include inlet and exit pressures and temperatures, mass flow rate (via a V-cone flow meter). The power absorbed by the supercharger was measured via a torque meter installed at a pulley between the driver motor and the supercharger. The pulley systems including the drive belt was setup such that it replicates the assembly in the Ultraboost engine.

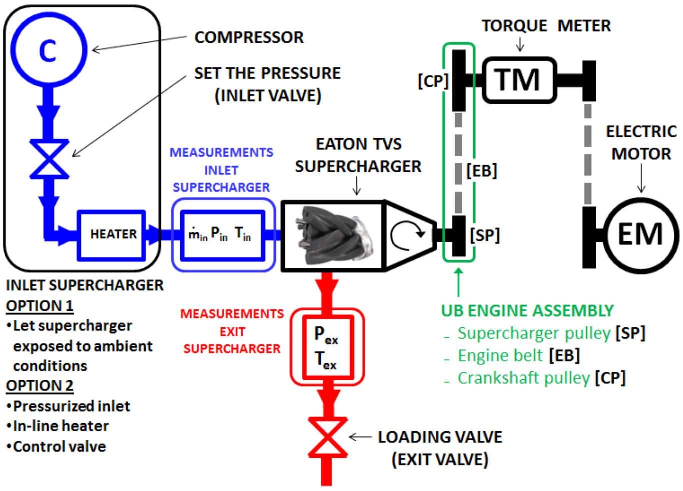

Figure 5.11 Supercharger testing layout (Romagnoli et al, 2014)

The performance map of the supercharger is shown in Figure 5.12 below. The map was obtained at ten supercharger speeds where the values of mass flow rate, pressure ratio and total-to-total efficiency were recorded. The highest recorded efficiency (η_{TT}) was 72.8% for this supercharger unit. The highest mass flow ($\dot{m}_{SC}$) recorded was 1.143 kg/s, occurring at 20101 RPM speed and 1.14 pressure ratio. The supercharger in this engine is modelled similar to the LP compressor but without the presence of the turbine and the connecting shaft. In the simulation, the power consumed by the supercharger is imposed as an auxiliary load on the crank in a form of look up table.

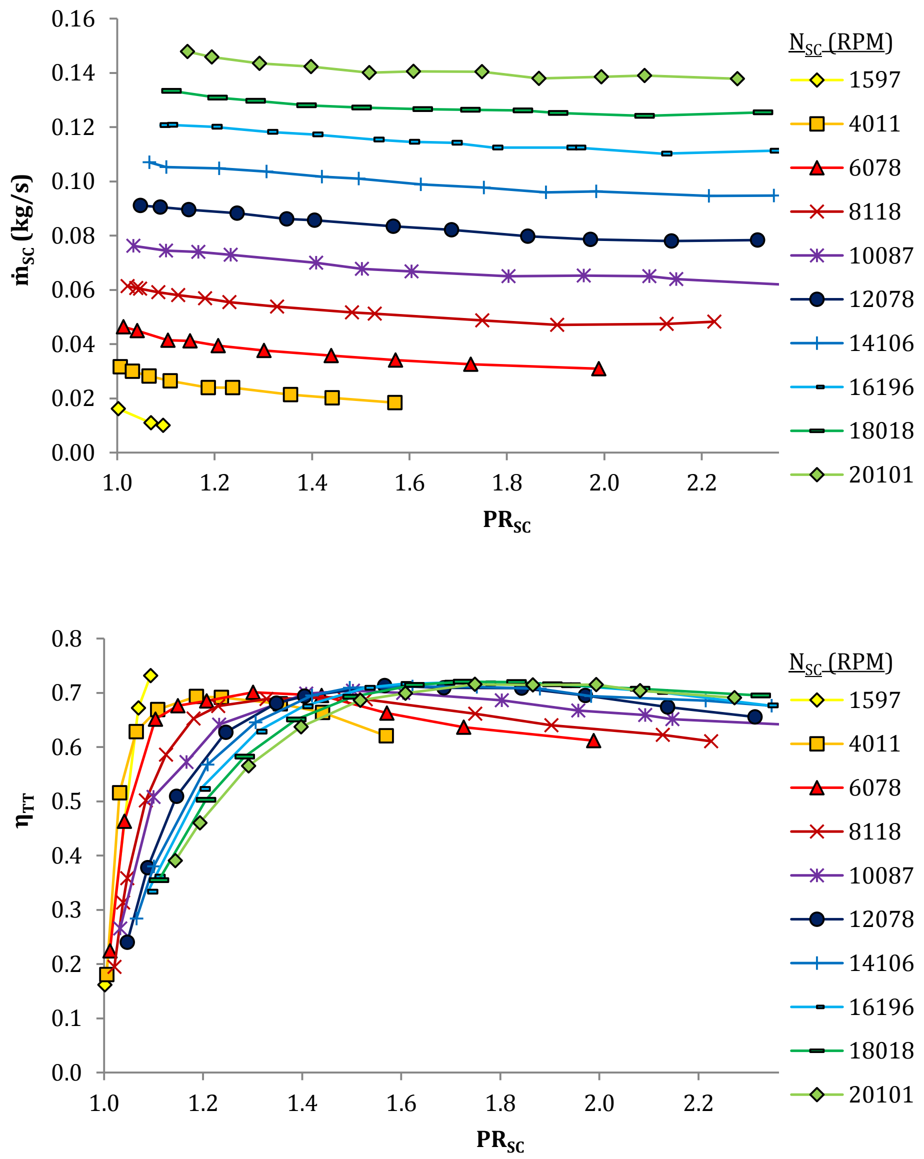

Figure 5.12 Supercharger performance maps obtained from supercharger test facility

5.5.6 Boost level estimation

From 1-D calculations, it is possible to estimate the amount of boost pressure required to deliver the target BMEP level at wide open throttle conditions. This can be achieved by running the 1-D model without the presence of the boosting systems. This setup is realized on the test bed by means of a charge air handling unit (CAHU) which is capable of replicating boosted engine intake and exhaust gas conditions prior to installation of the boosting devices (Turner et al, 2014).

5.6 Compression Stage Control

This estimation of the boost demand allows for the selection and control of the compression devices. Having a series arrangement means that the total pressure ratio is a product of this parameter over each stage. Besides the ability to declutch the HP compressor, the compression levels of each stage can be adjusted via three methods. The turbine waste-gate valve controls the amount of air passing through the turbine impeller passage and allowing control over the LP stage compression level. The HP stage compression is controlled by the supercharger speed which can be achieved via selection of the HP drive gear ratio. Although the HP drive gear in this system is of a fixed ratio type, a variable drive system such as continuously variable transmission (CVT) system to allow a fully flexible supercharger speed control is certainly viable option for the future (Turner et al, 2014). An HP bypass valve which governs the amount of air bypassing the HP stage compressor is placed on the intake pipe at a location between the HP stage intake and exit junctions as shown in Figure 5.5.

5.7 Stage Boost Regulation

In a series charging system, the amount of boost contributed by each stage has to be optimally regulated. This is crucial since the operation of each boosting stage will have a direct impact on the engine performance as well as the performance of the individual boosting device themselves. In addition, the biasing strategy may also affect each stage exit air temperatures for consideration in CAC sizing and operation. The impact of stage boost regulation on engine performance has been demonstrated by the work of Galindo et al, (2010). Zhang et al (2013) provided insight into the control strategies that may be adopted in multistage charging systems.

Since the supercharger drive gear is of a fixed ratio, the stage compression distribution is carried out by controlling the waste-gate and HP bypass. The strategy for the current engine is to have the LP compressor running close to surge line to minimize the engine reliance on the mechanically driven HP compressor to deliver boost when both compressors are in operation and therefore minimizing fuel consumption. The HP stage is declutched at ≥3000 RPM engine speed where the boost is supplied solely by the LP compressor onwards.

5.8 Simulation Setup

Figure 5.13 shows the engine layout in the GT-Power program interface. In this simulation, the engine simulation is run such that the set BMEP target over engine speeds in the range of 1000 to 6500 RPM are achieved. In all cases, the throttle is set to be at wide open condition. The convergence of the solution is based on two variables, namely the average inlet manifold pressure and the BMEP target. The convergence of the solution is met when the cycle-to-cycle average pressure at the inlet manifold are within a fraction of 0.001. The convergence of BMEP is met when the calculated values are within 0.025. This is achieved through the LP-waste-gate and HP-bypass controllers. The simulation setup of the main components within the engine model is described in the following sections.

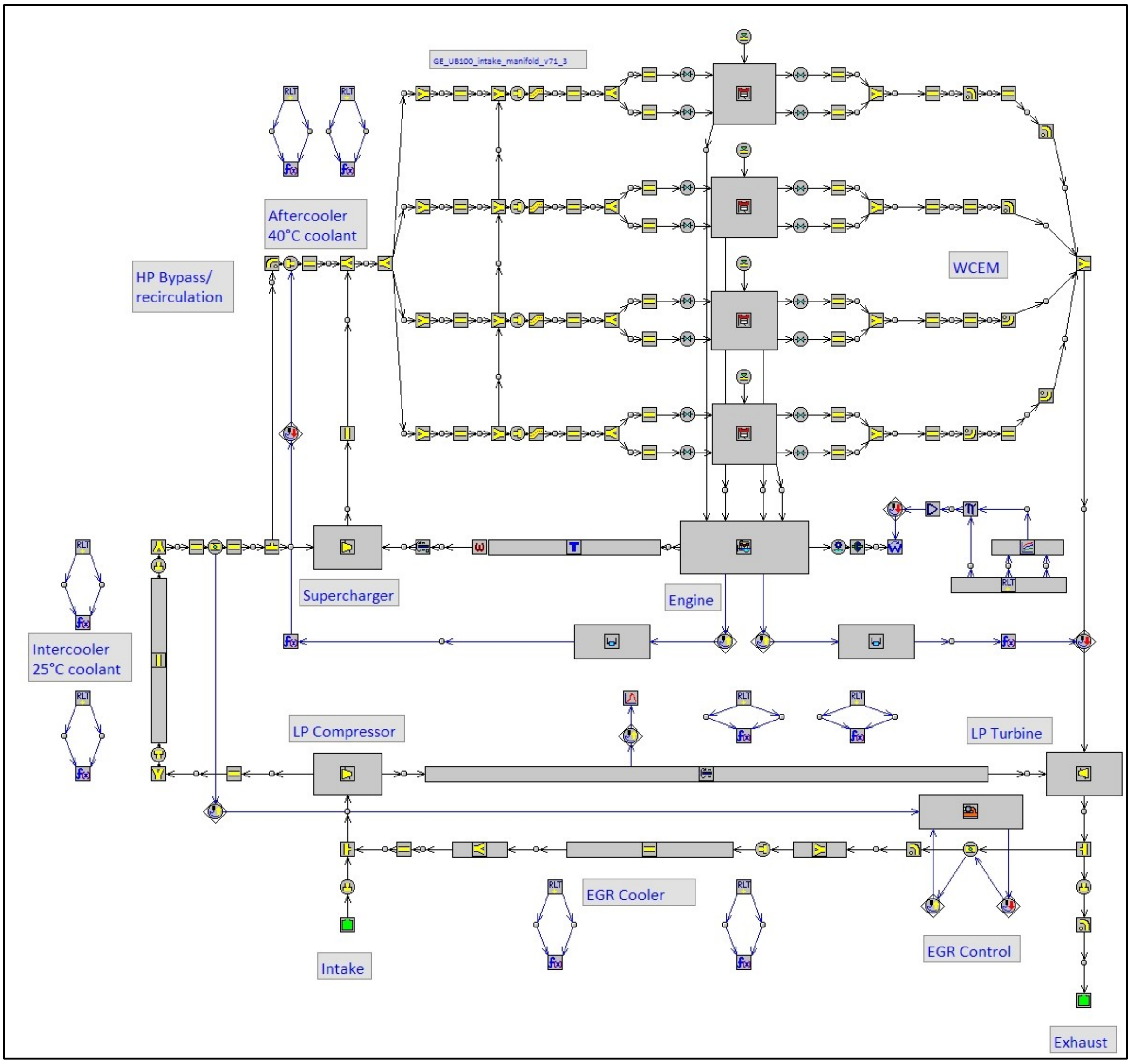

Figure 5.13 Layout of the Ultraboost GT-Power engine model

5.8.1 Combustion system

The engine is represented by four engine cylinder components which represent the individual combustion chambers where the combustion parameters are imposed. These cylinders are attached to a cranktrain element where the main engine attributes such as the engine type (4-stroke or 2-stroke), the cylinder and piston geometries, start of engine cycle and firing order are defined.

The intake and exhaust timing angles and lifts are defined within valve elements attached to the engine cylinders. The engine employs a cam profile switching mechanism whereby the lifts of the intake and exhaust valves cam can be varied based on load demand. Therefore the different valve profiles were defined and appropriately assigned to each speed case. A sequential injector with imposed air-fuel ratio component is used to model the direct injection system of the engine. Each injector consisting of four holes delivers fuel to each cylinder at a rate of 17 g/s. The air-fuel ratio was set to be 14:2 and an appropriate injection timing angle with reference to crank rotation was assigned.

The flow equations are solved to predict the quantity and properties of air and fuel in the combustion chamber. The standard SI Wiebe combustion model is used to predict the amount of energy released from the combustion process by defining the 50% burn anchor angle, the 10 – 90% burn duration in degrees of crank angle and the Wiebe exponent (Heywood, 1988). This yields the Mean Effective Pressure (MEP) in the cylinder from which related performance parameters such as BMEP and BSFC can be derived. The post-combustion properties of the gas flow are then passed on to components downstream of the cylinder via the exhaust valves, ports, manifold, turbocharger turbine, Exhaust Gas Recirculation (EGR), catalytic converter, muffler and finally the atmosphere.

5.8.2 Boosting system representation

The turbine and compressor maps are inserted into the corresponding components to model the LP turbocharger. A shaft element with assigned value of inertia connects the turbine and compressor. The supercharger is modelled similar to the compressor. A rotary element which imposes the supercharger rotational speed was attached to the supercharger component. The crank power consumed by the supercharger was measured through experiments as described in Section 5.7. The mechanical loss due to supercharger clutching is represented by a torque element attached to the engine cranktrain component.

The CACs of the boosting system are modelled by a parallel arrangement of identical pipes with imposed friction and heat transfer losses to calibrate each heat exchangers pressure loss and heat transfer effectiveness respectively.

A Proportional-Integral-Derivative (PID) controller is used to maintain the set BMEP at a particular speed by adjusting the turbine waste-gate area and the HP compressor bypass recirculation area.

5.9 Engine Performance Prediction

The simulation is run for a sweep of engine speeds (1000RPM to 6500RPM) at wide open throttle conditions. The predicted BMEP is compared with the experimental test bed results and is shown in Figure 5.14 below. The predicted and test bed intake manifold pressure is shown in Figure 5.15 which reveals good agreement between predicted and measured data giving a maximum discrepancy of ≈6.5% (1750RPM to 4750RPM engine speed).

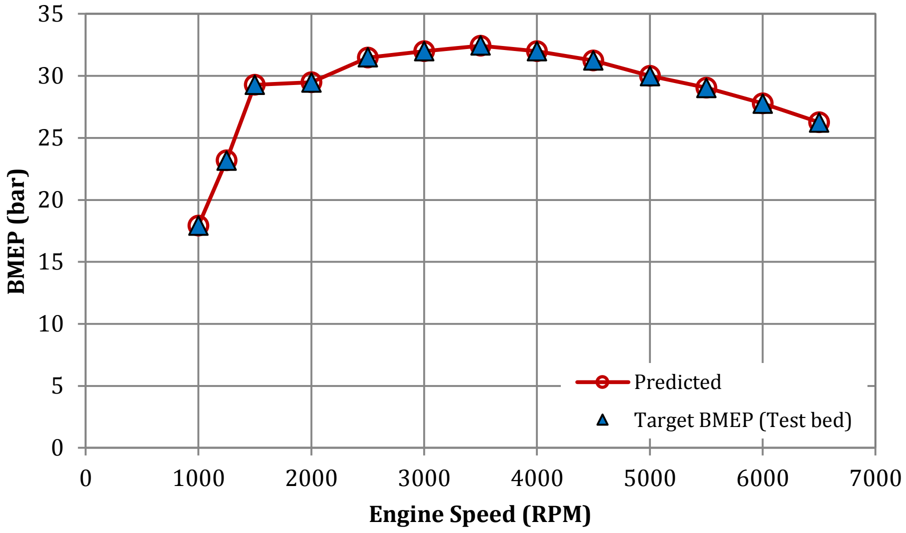

Figure 5.14 Predicted BMEP compared to measured data

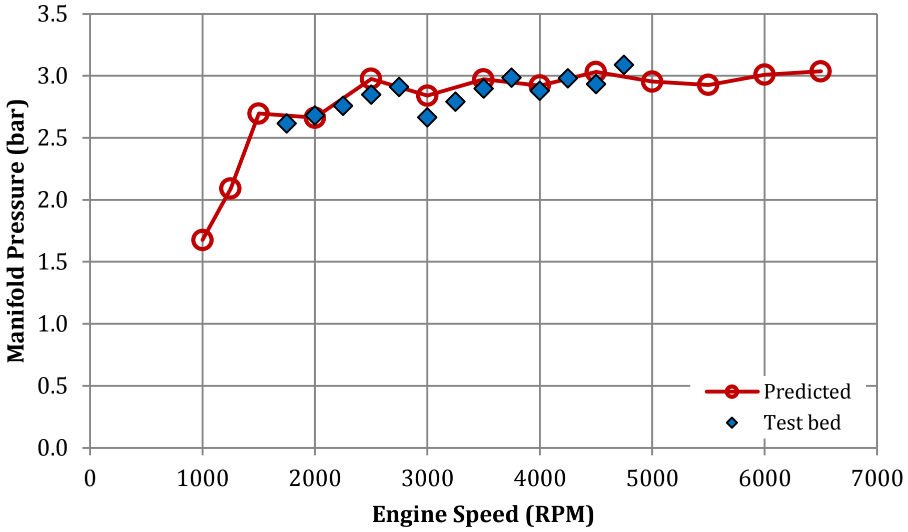

Figure 5.15 Comparison between predicted and measured inlet manifold pressure

The predicted brake specific fuel consumption against test bed data is shown in Figure 5.16. In general, the predicted BSFC is slightly lower than actual test results with maximum discrepancy of ≈13.2% occurring at 3000RPM. The predicted BSFC is slightly higher at engine speeds below 1500RPM by as much as ≈11.9% at 1250RPM. Nevertheless, the trend of the experimental data is captured reliably by the numerical model.

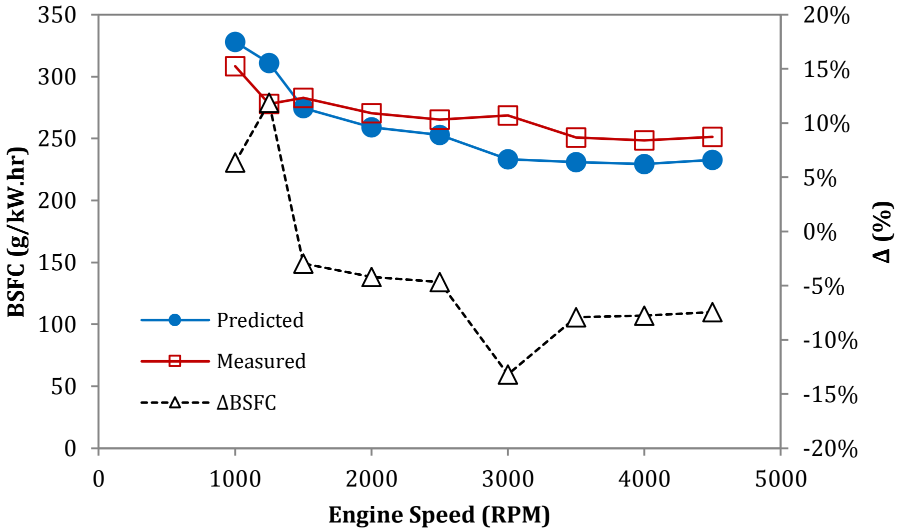

Figure 5.16 Comparison between predicted and measured BSFC

5.10 Boosting System Performance

This section discusses the predicted performance of the individual boosting devices in comparison with measurements made on the engine test bed.

5.10.1 Compressor performance

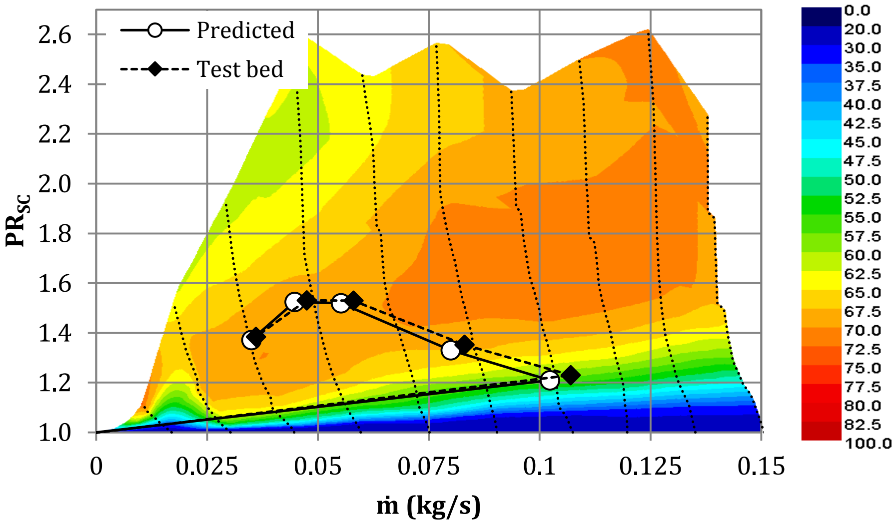

Figure 5.17 Comparison between predicted and test bed supercharger operating points on efficiency contours

Figure 5.17 shows the predicted flow parameters of the HP stage compressor at WOT operation predicted by GT-Power in comparison with test bed data. With the drive gear fixed at a ratio of 5.9, the maximum rotational speed for the supercharger is 14750RPM at 3000RPM engine speed. It can be seen that the predicted and measured values agree well with each other with slightly lower predicted values of mass flow at high supercharger speeds. The highest discrepancy in predicted mass flow (5.8%) occurs at 1500 RPM engine speed. The supercharger running points fall mostly on high efficiency regions in the range of 56.6 to 69.7%.

The LP compressor air mass flow characteristics in comparison with test bed data for WOT operation over a speed sweep is shown in Figure 5.18 below. As mentioned earlier, the boost biasing strategy is such that the LP compressor is set to run close to the surge line and this is exhibited by the predicted points. While this is achieved in the simulation, the actual measurement shows higher mass flow rates typically at mid-range engine speeds (2500 to 3000 RPM). The test bed data shows that the compressor is running at higher efficiency as compared to predicted data between 2000 to 3000 RPM engine speed.

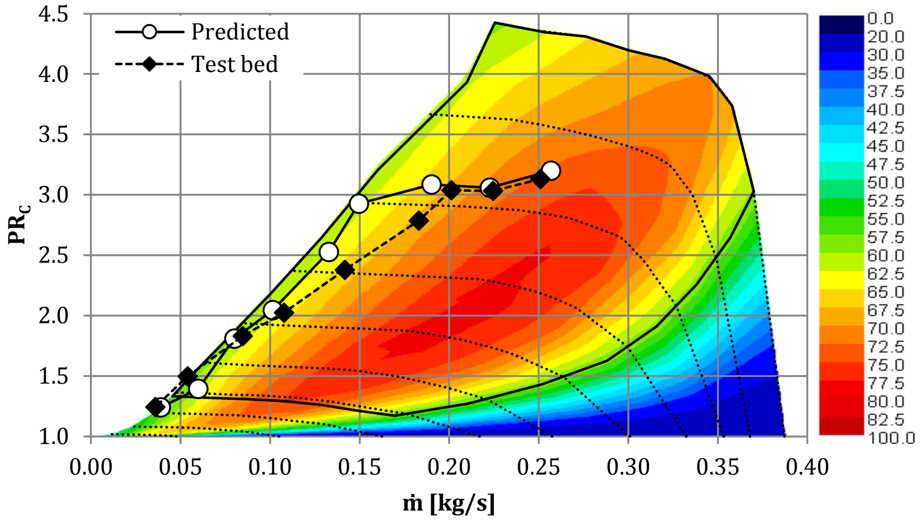

Figure 5.18 Predicted and measured compressor operating points on efficiency contours

By comparing predicted and measured stage pressure ratio and mass flow rate at engine speeds 1000 – 4500 RPM in Figure 5.19, it can be seen that the discrepancy arises from the under-predicted mass flow rate at the said speed ranges. At 3000 RPM, the simulation under-predicts the mass flow rate by ≈18.2%. The pressure ratio is also slightly over-predicted for speeds of 2500 RPM and 3000 RPM where predicted values are slightly higher with discrepancies of ≈6.8% at 2500 RPM and ≈5.0% at 3000 RPM.

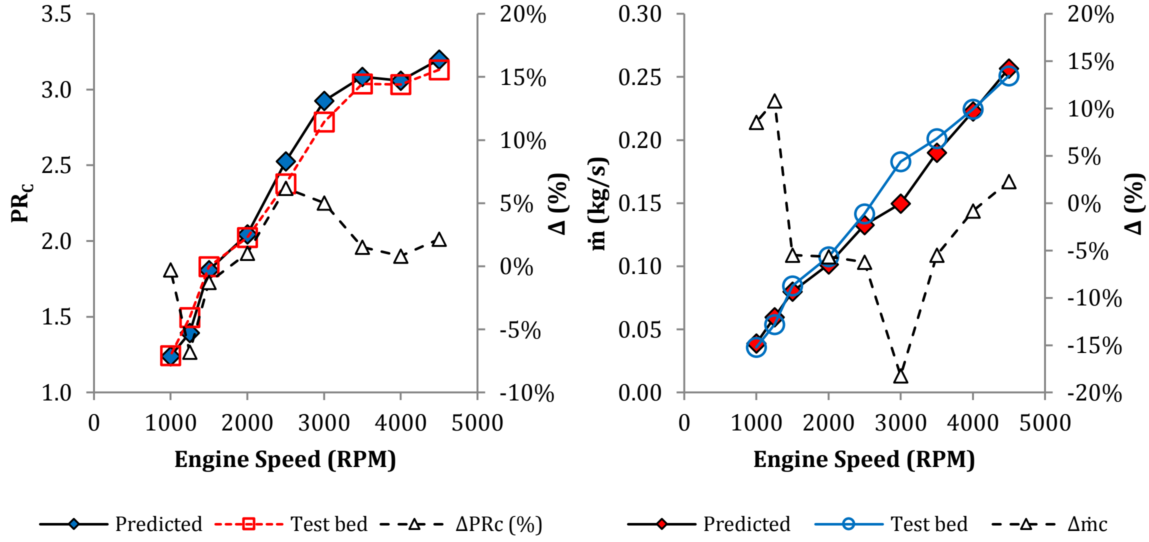

Figure 5.19 Comparison between predicted and measured LP compressor pressure ratio and mass flow rate

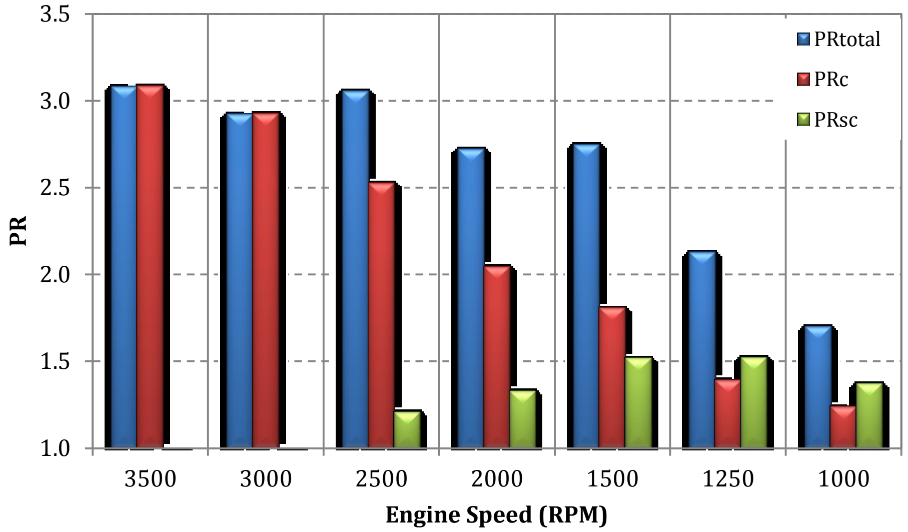

Figure 5.20 Pressure ratio biasing between HP and LP compressors with "SC" and "C" denoting supercharger (HP stage) and turbocharger compressor (LP stage) respectively. PR_{total} denotes to the total PR across the compression stage

Figure 5.20 above compares the pressure ratio across each compression stage to demonstrate the stage boost distribution among the compression stages. The boosting system is LP bias for most WOT speed range except at speeds below 1250 RPM. The HP compressor operates at a maximum pressure ratio of ≈1.52 at 1250RPM and the bias towards HP is reduced as the engine speed increases until 3000RPM when the supercharger is declutched.

5.10.2 Turbine performance

The predicted turbine speed is plotted against engine speed in Figure 5.21 below. The speed was found to be predicted very well by the simulation. The highest discrepancy occurs at 1250 RPM where at 10.7% difference is observed. However, the rest of the cases are between 0.18% to 2.66% discrepancies. The simulation predicts a maximum turbocharger speed of 154494 RPM at 6500 RPM engine speed.

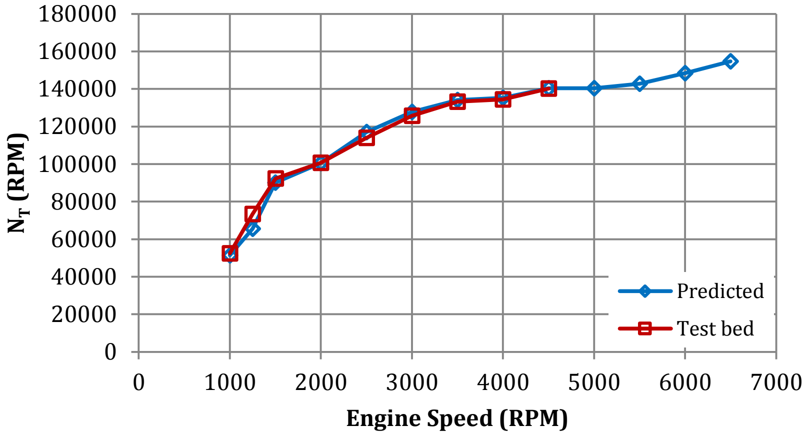

Figure 5.21 Turbine speed predicted by simulations compared to measured data

Besides turbine speed, the predicted pressure ratio across the turbine can also be evaluated. The predicted average pressure ratio values are given by Figure 5.22 along with measured data. It is noticed that the predicted pressure ratio is higher compared to measured data as the speed increases. At 4500 RPM engine speed, the predicted pressure ratio is 18% higher than measured data. The turbine is predicted to operate at 2.46 pressure ratio at maximum speed engine (6500 RPM). The difference in the predicted and measured mass flow could partly be due to the difference in location measurements.

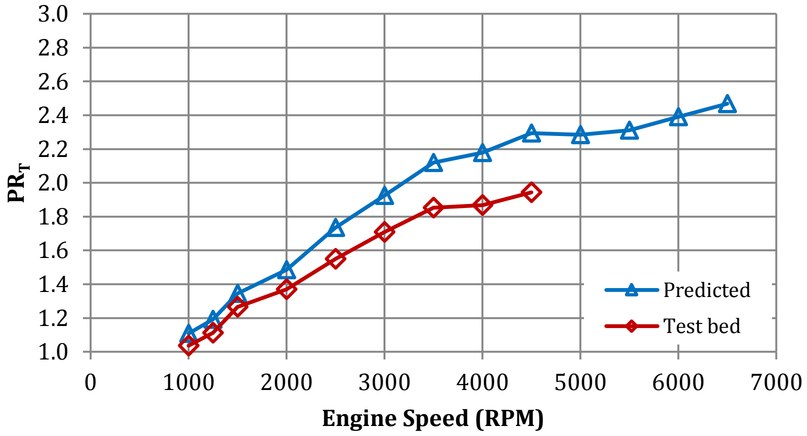

Figure 5.22 Comparison between predicted and measured pressure ratio across the turbine

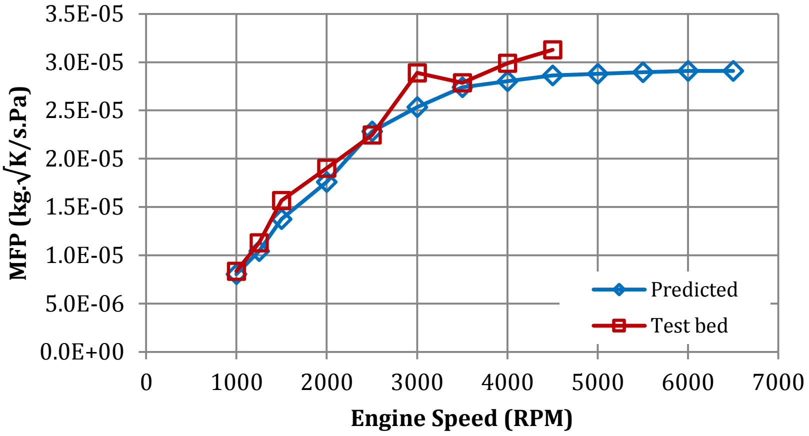

Figure 5.23 Comparison between predicted and measured turbine mass flow parameter

The turbine mass flow parameter predicted by the simulation is compared to test bed results in Figure 5.23. In general, the agreement between predicted and measured mass flow parameter is relatively good with the exception of several points where the actual values are giving higher readings compared to predictions. A 12.3% difference is seen at 3000 RPM engine speed where the measured data shows a rather sharp rise in mass flow parameter reading before decreasing again at 3500 RPM.

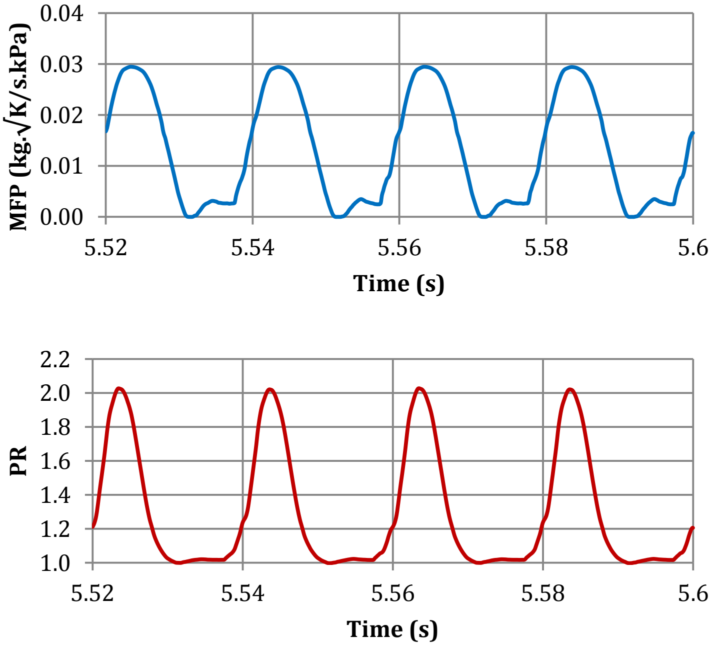

Figure 5.24 Fluctuations of turbine mass flow parameter and pressure ratio over time during a steady state cycle at 1500 RPM engine speed

To evaluate the operating points of the turbine, it is helpful to have the computed values superimposed on a turbine map. This will reveal the specific points on the map which the turbine operates on with respect to speed, pressure ratio and mass flow parameter. The average mass flow parameters obtained by taking the time average value of mass flow parameter over an engine cycle when steady state condition is reached. If the values are obtained at the turbine component in the GT-Power layout, a quasi-steady mass flow characteristic can be observed. This is due to the turbine in GT-Power being represented as a node (boundary condition) within the piping layout. Figure 5.24 shows the mass flow parameter and pressure ratio fluctuations over time during a steady state cycle.

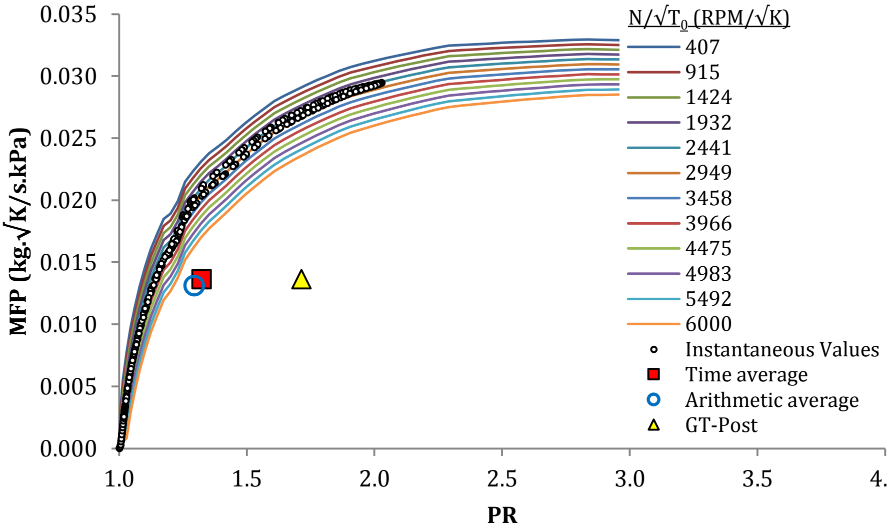

Figure 5.25 Turbine mass flow performance throughout an engine cycle at 1500 RPM plotted on top of the steady turbine performance maps used in GT-Power

The time average values of the mass flow parameter and the pressure ratio can be obtained by integrating the fluctuating values over time. Figure 5.25 shows the time average mass flow parameter plotted on the turbine map along with the instantaneous mass flow parameter trace. The arithmetic average of the mass flow parameter and the GT-Power output is also included in the graph. The GT-Post (post-processing software) computes a mass average pressure ratio which results in the average mass flow parameter point situated at high pressure ratios. The time average mass flow parameter is seen to be relatively close to the arithmetic average. However, in all cases, it is observed that the average value does not fall within the steady state turbine map due to the non-linear relationship between the mass flow parameter and pressure ratio. Evidently, plotting the simulated time average values of mass flow parameter together with the steady state turbine map yields no useful information for the user.

In order for the average mass flow reading to be viewed with respect to the turbine speed, a new method of averaging pressure ratio has to be proposed. This involves the linearization of the relationship between mass flow parameter and pressure ratio by the static pressure loss coefficient suggested for flows through a duct. This loss coefficient (K_s) is expressed by:

$$K_s = \frac{2\Delta P}{\rho {U_2}^2} = \frac{2(P_1 - P_2)}{\rho {U_2}^2} \quad \ldots (5.12)$$

where P_1 and P_2 denotes inlet and exit pressures respectively, ρ is the density and U_2 is the exit gas velocity and . Solving for velocity gives:

$$U = \sqrt{\frac{2}{K_s}\frac{(P_1 - P_2)}{\rho}} = \sqrt{\frac{2}{K_s}} . \sqrt{\frac{(P_1 - P_2)}{\rho}} \quad \ldots (5.13)$$

Equation (5.13) may be multiplied by $\left(\frac{A\rho\sqrt{T_1}}{P_1}\right)$ and rearranged to give:

$$U\left(\frac{A\rho\sqrt{T_1}}{P_1}\right) = A\sqrt{\frac{2}{K_s}} . \sqrt{\frac{(P_1 - P_2)}{P_1} . \left(\frac{\rho T_1}{P_1}\right)} \ldots (5.15)$$

where A is the flow area. The left-hand-side of the equation represents the mass flow function. The equation of state may be used to simplify the equation to:

$$\frac{\dot{m}\sqrt{T_1}}{P_1} = A\sqrt{\frac{2}{K_s}} . \sqrt{\frac{(P_1 - P_2)}{P_1} . \left(\frac{1}{R}\right)} \ldots (5.16)$$

where R is the gas constant. Grouping together the constant terms and further simplifying yields:

$$\frac{\dot{m}\sqrt{T_1}}{P_1} = A\sqrt{\frac{2}{RK_s}} . \sqrt{1 - \frac{1}{PR}} = \boldsymbol{K}\sqrt{1 - \frac{1}{PR}} \ldots (5.17)$$

where $\boldsymbol{K}$ is a constant. The right-hand-side designated as the pressure ratio function (PRF) establishes a linear relationship between the mass flow parameter and pressure ratio. The predicted instantaneous mass flow parameter of the turbine at 1500 RPM engine speed case is plotted against the pressure ratio function in Figure 5.26.

The average pressure ratio based on the pressure ratio function above is calculated by integrating over time. These average pressure ratios are used together with the time average mass flow parameter and are plotted on the turbine map for all speed cases. This is shown in Figure 5.27 along with the mass flow parameter based on time average pressure ratio and the

GT-Power mass averaged pressure ratio. It can be seen now that by using the pressure ratio function, the average mass flow parameters are now representative of the corresponding turbine speeds.

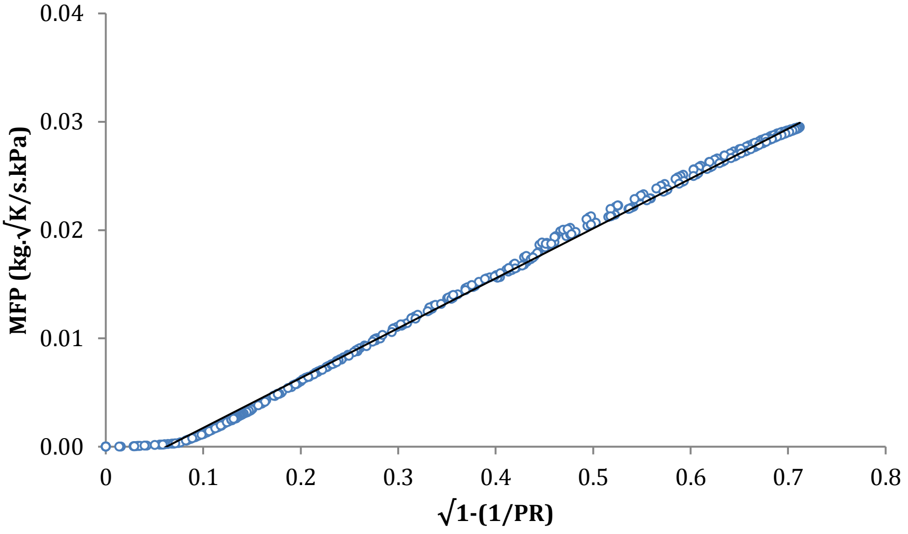

Figure 5.26 Instantaneous predicted mass flow parameter against the pressure ratio function

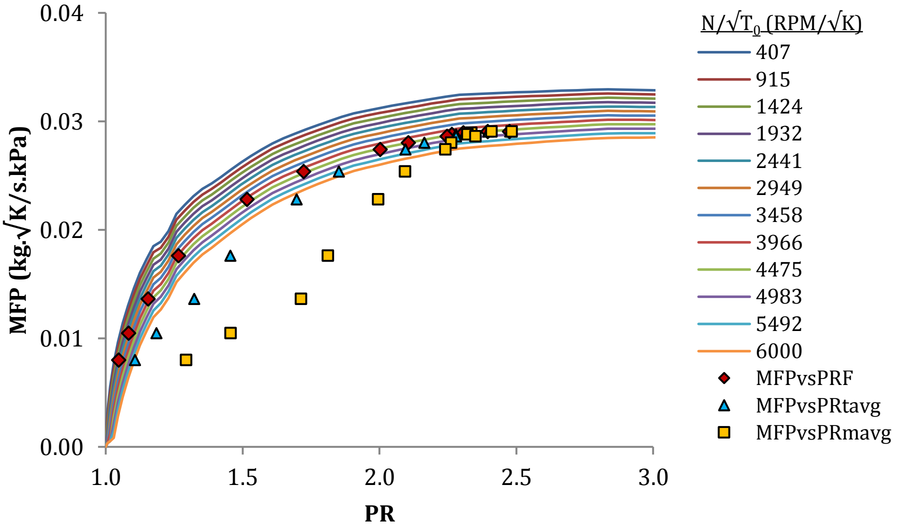

Figure 5.27 Average mass flow parameter plotted on the steady state map using different pressure ratio averaging methods

5.11 Simulation with External Waste-gate

The results reported above was obtained via simulations whereby the external turbine waste-gate installed on the actual engine is not physically modelled. This is based on the assumption that the total mas flow rate through the system (turbine and waste-gate) is calculated by summing the turbine and waste-gate mass flow rates. As has been shown in Chapter 3, this is not necessarily the case where the total flow through the system is actually lower than the sum of mass flow rate through the turbine and waste-gate. It is interesting in the context of this thesis, to see whether modelling the waste-gate system separately has any effect on the predicted performance of the engine the turbocharger system.

An external waste-gate passage was included in the GT-Power engine layout. This involves the use of a pipe junction upstream of the turbine which will split the flow into the turbine and a valve-component. The flow coming out of the valve re-joins the main exhaust gas flow downstream of the turbine. A BMEP sensor and an actuator element are connected to the valve. The BMEP sensor senses BMEP predicted over each cycle and sends the signal to the actuator, which in turn opens or closes the valve accordingly until the cycle-to-cycle BMEP target is met.

5.11.1 Predicted turbine speed and pressure ratio

Figure 5.28 shows the predicted turbine speed and pressure ratio for the externally modelled waste-gate and the standard waste-gate. It can be seen that the turbine speed is predicted to be identical for both cases. The maximum difference between the predicted speeds is less than 1.13% occurring at 6500 RPM engine speed.

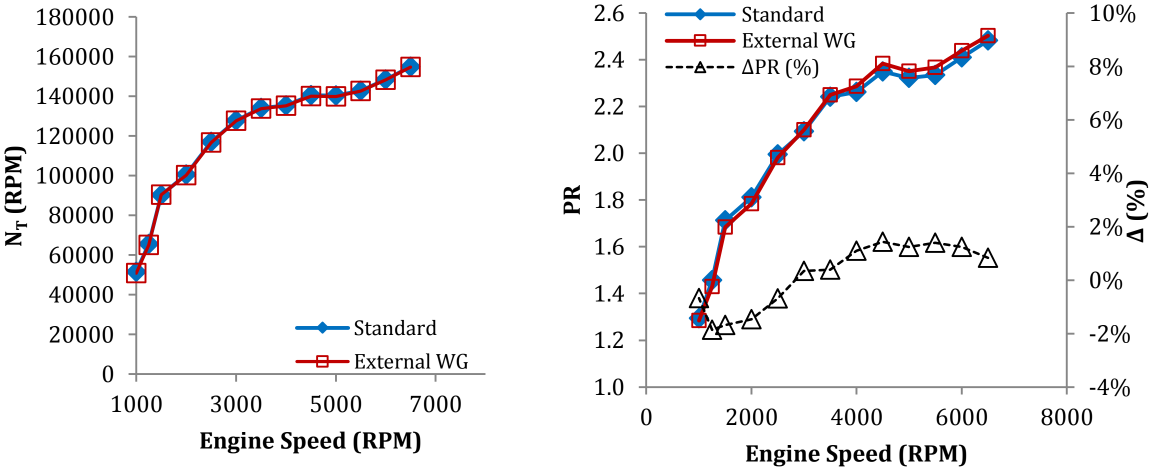

Figure 5.28 Predicted turbine speed and pressure ratio using standard and external waste-gate model

When the pressure ratio is compared between the two cases, the difference between the predicted data is also less apparent with 1.86% maximum discrepancy between them occurring at 1250 RPM engine speed. It is also possible to look at the average values of static pressure across the turbine for both cases. These are shown in Figure 5.29.

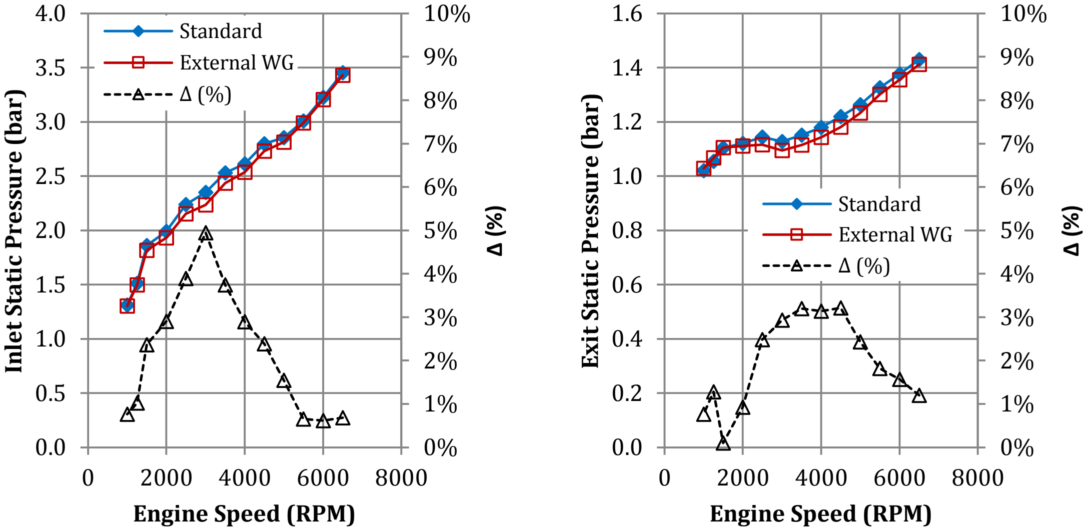

Figure 5.29 Comparison of predicted average turbine inlet and exit static pressures for standard and external waste-gate cases

The figures show slight difference in the prediction of static pressures at the inlet and exit of the turbine component. The maximum difference in the average static pressure occurs at 3000 RPM engine speed (4.94%). At this point, the standard waste-gate model is predicting to give 2.35 bar inlet pressure compared to 2.23 bar for externally waste-gated case. Exit static pressures of 1.22 bar and 1.18 bar at 4500 RPM engine speed for the standard and externally modelled waste-gate respectively gave a maximum difference of 3.22% in the prediction of exit static pressures. From the figures, both the inlet and exit static pressures are seen to be lower if the waste-gate is model externally compared to the standard waste-gate model. The inlet pressure is seen to be lower due to the presence of additional piping system upstream of the turbine. In this case, the drop in turbine inlet static pressure is apparent in the medium engine speed range.

5.11.2 Predicted turbine swallowing characteristics

It may be useful to compare the prediction of swallowing characteristics through the turbine for both cases. This is done by looking at the mass flow parameters for both cases in Figure 5.30.

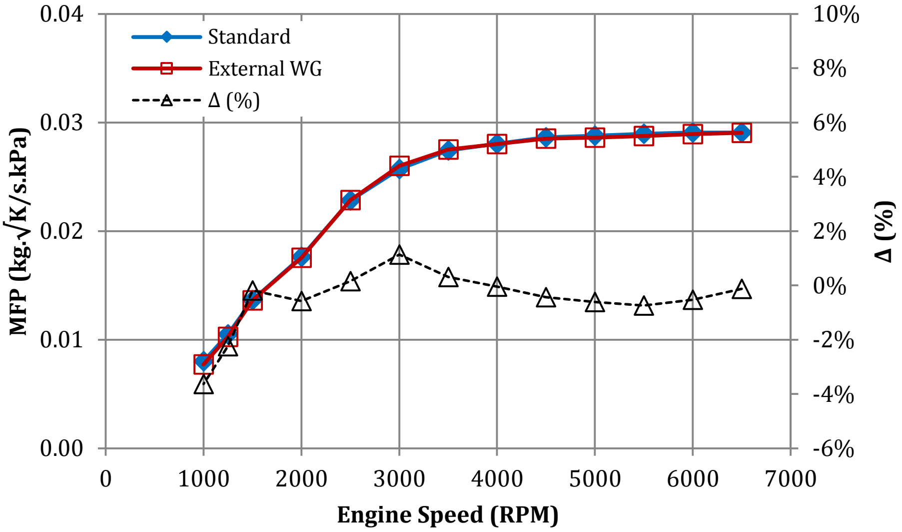

Figure 5.30 Comparison of predicted mass flow parameter for standard and externally modelled waste-gate

It is observed that there is no notable difference between the predicted average mass flow parameters for both cases. A 3.63% maximum difference occurs at 1000 RPM engine speed while the less than 1.15% difference is observed for all other points. This means that the amount of mass swallowed by the turbine is not affected by the presence of the waste-gate. The comparison of mass flow rates through the waste-gate for both cases shows notable difference between the two cases. This is given in Figure 5.31.

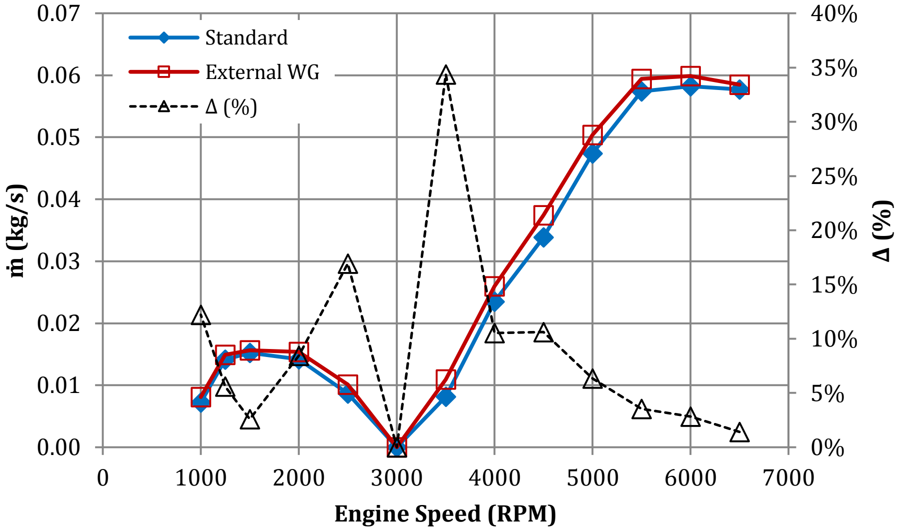

Figure 5.31 Comparison of predicted waste-gate mass flow rate for standard and externally modelled waste-gate

Here, it is seen that the externally modelled waste-gate is passing higher mass flow rate compared to the standard model. At most engine speeds, the difference between the predicted mass flow rate values are less than 17%. At 3500 RPM, a 34.4% difference in predicted mass flow rate is seen. However, the difference in absolute values at this point is only 2.8 g and is small relative to the mass flow rate through the turbine.

5.11.3 Predicted turbine efficiency

It is just as important to look at the predicted efficiency of the turbines for both standard and externally waste-gated cases. This is shown below in Figure 5.32.

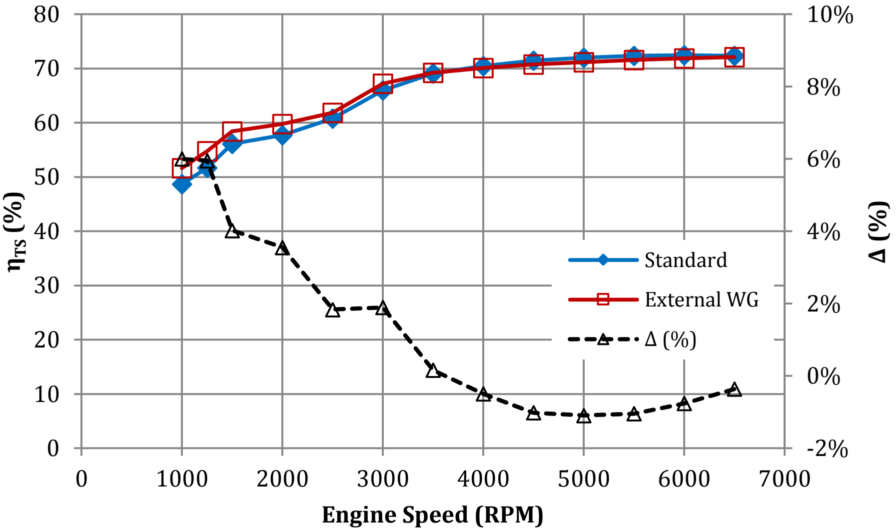

Figure 5.32 Predicted average turbine efficiency against engine speed for standard and externally modelled waste-gate

It can be seen from the figure that by modelling the waste-gate externally, the average efficiency of the turbine is increased particularly at low engine speeds (1000 to 3500 RPM). This is the region where the LP stage is working in tandem with the HP stage. A maximum difference of 6% in predicted efficiency occurs at 1000 RPM engine speed. As the engine speed increases, the difference in predicted efficiency decreases. The increase in efficiency could be due to the decrease in turbine mass flow when the waste-gate is modelled externally. This will result in a reduction in calculated isentropic power, thereby increasing the efficiency.

5.13 Summary

In this chapter, 1-D gas dynamics simulation has been carried out on boosted engines to investigate the impact of turbine map width on the prediction of engine performance. The commercial GT-Power engine simulation code has been adopted for this undertaking. The results show that indeed, the map extrapolations carried out on the same turbine map having different widths of data has produced notable difference in the prediction of the basic engine performance. In this specific case, the use of narrow turbine maps which represents a typical manufacture map results in the under-prediction of engine BMEP (by 9.77%) and over-prediction of engine BSFC (by 10.8%). This can be attributed to the predicted turbine operating points being in less favourable conditions as a result of the map extrapolation performed by the 1-D software.

The second part of the chapter discusses the modelling of a heavily boosted downsized prototype engine, namely the *Ultraboost* engine. This engine utilizes a dual-stage series boosting system comprising a HP supercharger and an LP turbocharger system. The method of modelling the engine and the individual boosting system in a 1-D environment is presented. Also presented is the experimental setup to obtain the supercharger performance map which is used in the simulation. The prediction of engine performance agrees well with experimental data obtained separately on an engine dynamometer.

The predicted performance of the individual boosting system was also discussed in the chapter. The predicted supercharger performance agrees well with test bed results. As far as the LP stage is concerned, the simulation produced satisfactory results. Looking at the turbocharger turbine performance, the speed of the turbocharger was very well replicated by the 1-D simulation. The turbine mass flow parameter also showed satisfactory agreement with the measured data. However, the simulation slightly over-predicts the average turbine pressure ratio across the engine speed range. The difference in pressure ratio prediction is seen to increase as engine speed is increased.

A new method of pressure ratio averaging is proposed to enable plotting the cycle average mass flow from the simulation on a superimposed turbine map. The pressure ratio function (PRF) was introduced such that its time average integral, when used with cycle average mass flow parameter on the turbine map will be representative of the corresponding turbine speed.

The third part of the simulation work involves modelling of an external turbine waste-gate valve to be evaluated against the software standard waste-gate modelling, which assumes the mass flow through the system to be the summation of the mass flow through the turbine and waste-gate. Analysis on the performance of the turbine show slight differences between the two cases. In particular, the inlet and exit static pressures of the turbine are predicted to be lower when a waste-gate is modelled as an external component.

Chapter 6 Conclusions

6.1 Summary of Work

This thesis accounts for work carried out to study the performance of an externally waste-gated turbocharger turbine for use in turbocharger matching of a heavily downsized boosted engines. Extensive experimental work has been carried out in a highly instrumented turbocharger testing facility at Imperial College London. This includes testing of the waste-gated turbine under steady and pulsating inlet conditions under various test configurations. In addition to the experimental work, computational simulations were performed to predict the performance of a prototype highly downsized boosted gasoline engine and the performance of the boosting system. This was achieved by means of 1-D gas dynamics engine simulation software.

6.2 Conclusions

The specific objectives of the thesis were laid out in chapter 1. This forms the basis on which the conclusions are drawn. The main conclusion of the thesis can be arranged in three sections based on the set objectives.

6.2.1 Objective 1

Evaluate the effect of turbine map width on map extrapolation procedures commonly used in turbocharger matching and explain its effect on the prediction of engine performance.

The turbine map extrapolation method employed by a commercial 1-D engine simulation code (GT-Power) was evaluated. The main aim was to assess whether the map extrapolation procedure was able to predict accurately the actual turbine characteristics using a turbine map with limited data range similar to a typical map supplied by a turbocharger manufacturer. This was implemented by way of reducing the swallowing characteristics and efficiency data from a wide map, which was tested on an eddy-current dynamometer. Then the map extrapolation procedure was implemented on this reduced map and the predicted mass flow parameter and efficiency are compared to the wide experimental data. This extrapolation procedure involves fitting curves to normalized values of experimental data which are plotted against normalized velocity ratio.

The use of narrow maps was found to have an effect on the predicted swallowing characteristics and efficiency of the turbine. By comparing the predicted values to the actual experimental data, it was found that the predicted mass flow parameter agree well with experimental data at low speed parameter (1934 RPM/ RPM/√K). However, at high speeds the difference in the prediction of mass flow parameter with experimental values was found to be as high as 7.3% at pressure ratio of 1.352, which is observed at 2892 RPM/√K speed.

The extrapolation of the efficiency characteristic showed low sensitivity to map width at low velocity ratios. This results in a good prediction of turbine efficiency at high pressure ratios. At high pressure ratios (PR>1.9), the difference was found to be less than 2% in all cases at 2892 RPM/√K speed. At the lower turbine speed parameter (1934 RPM/√K), the efficiency prediction at high pressure ratios was also close to within 2% of the actual data. The effect of map width on the prediction of efficiency is largest at low pressure ratios (high velocity ratios) where the use of narrow map result in the zero-efficiency intercept on the normalized velocity ratio axis being at a higher value (1.915) compared to that when a wide map is used (1.747). This results in a large discrepancy between the predicted efficiency and the actual data where a maximum of 58% was observed.

The impact of map extrapolations implemented on different ranges of turbine data on the prediction of engine performance by a 1-D gas dynamics code were also evaluated. The extrapolated maps based on the wide and narrow data range was used to define the turbine element in the GT-Power engine layout and performance simulations were carried out on a virtual 4.7 litre turbocharged Diesel engine. Simulation results show a large difference in the prediction of engine BMEP and BSFC. In this specific case, the use of wider map predicted a higher BMEP with maximum difference of 9.77% over that predicted using the narrow map. The prediction of BSFC was better by 10.8% with the use of the wider map. This improvement seen in BMEP and BSFC can be attributed to the prediction that the turbocharger is operating in the more favourable condition when the wider map is used.

It can be drawn that the use of limited data range in map extrapolations employed by the 1-D gas dynamics code highly influences the prediction of turbine performance parameters in low pressure ratio conditions subsequently affecting the outcome of engine performance predictions.

6.2.2 Objective 2

Develop an experimental method to establish and explore the effect of an external waste-gate on steady turbocharger turbine performance.

Laboratory experiments have been conducted to measure the performance of an externally waste-gated turbine under steady inlet conditions. The experiments are carried out at various turbine speed, load and degrees of waste-gate opening. The waste-gate is characterized so that the mass flow rate through the device can be quantified based on the valve lift. Results show that at a given turbine load, the increase in mass flow rate is accompanied by the decrease in pressure ratio as the degree of waste-gate opening is increased. It was also found that using the current experimental setup results in higher turbine back-pressure as the waste-gate opening area is increased. This is caused by the waste-gate flow stagnating at the junction where it is reintroduced into the main gas flow downstream of the turbine. Another important finding of the experimental study is the interaction between the turbine and the waste-gate in terms of mass flow. It was shown that the mass flow rate through the turbine waste-gate system was less than the summation of the equivalent mass flow through the turbine and the waste-gate if they were operating at the same condition independently. For the cases evaluated, the difference was found to be as high as 6.76% between the measured mass flow rate and that predicted by the independent characteristics of the turbine and the waste-gate summed together.

The measured turbine efficiency was seen to be lower as the waste-gate opening area is increased. This was mainly caused by the increase in measured mass flow rate resulting higher calculated isentropic availability, some of which will be bypassed through the waste-gate and will not produce any useful work output. The apparent efficiency of the turbine was found to decrease by up to 53.7% for the most open waste gate condition tested.

6.2.3 Objective 3

Investigate the unsteady pulsating flow performance of a waste-gated turbine experimentally and provide an insight into the effect of various operating parameters (pulse frequency, turbine loading and degree of waste-gate opening) and investigate how it can be represented in 1-D engine simulation codes.

To achieve this objective, experiments are carried out on the waste-gated turbine subjected to pulsating inlet flow conditions. The unsteady turbine performance parameters are recorded under various turbine loads, pulse frequencies and degrees of waste-gate area openings. A highly instrumented setup with high-speed data measurement system was used in the experiments and was described accordingly in the thesis. The instantaneous measurement of turbine swallowing characteristics and torque was evaluated to provide insight into the effects of turbine load, pulse frequency and waste-gate area opening. Based on the experimental results, it was shown that swallowing characteristics of the turbine under pulsating inlet conditions exhibit a hysteresis loop due to the filling-and-emptying of the turbine volume. By increasing the load applied to the turbine, this loop increases in area, indicating a greater departure from quasi-steady operation. Measurements of time resolved mass flux at waste-gate inlet exhibit a similar behaviour of a hysteresis loop which becomes wider and elongates as the turbine load is increased.

As the waste-gate area opening is increased, its effect on the unsteady characteristic of the turbine system increases. In particular it was found that the pulse amplitude in terms of pressure ratio increases for the same turbine load as the waste-gate is opened due to an increased level of filling-and-emptying enabled by the greater swallowing capacity of the turbine waste-gate system. The pulse amplitude in terms of pressure ratio increases from 0.264 to 0.480 from closed waste-gate condition to 5.0 mm valve lift. The shape of the pressure pulse however, was found to remain similar for different waste-gate openings at the same turbine load and pulse frequency.

The pulse frequency has shown a substantial effect on the dynamic behaviour of the turbine. This was discussed in terms of the measured instantaneous torque for the waste-gated turbine and in terms of MFP and pressure ratio for the non-waste-gated turbine. In all cases it was found that the amplitude of the unsteady effects reduced as the pulse frequency was increased.

The effect of waste-gate opening on the “unsteadiness” experienced by the turbine was quantified by means of three different parameters, namely the Strouhal number, the Ω parameter and I_{MFP}. I_{MFP} was generally found to sit above unity; the maximum value recorded was 1.102 with a 40Hz pulse frequency and 3.0mm waste-gate opening. The minimum value was 0.9969 for the closed waste-gate condition at a 20Hz pulse frequency. As expected, the Strouhal number was seen to correlate very closely to the pulse frequency. The Strouhal number for the waste-gated turbine was found to be lower than that for the non-waste-gated case due to the higher mass flow. The Ω which accounts for the amplitude of the pulse did not correlate as closely with pulse frequency and in most cases indicated a greater unsteadiness for the waste-gated case due to the increase in pulse amplitude.

The experimental setup was modelled numerically in GT-Power in order to assess how well the code was able to capture the unsteady turbine behaviour under waste-gated conditions. A good agreement with the experimental data was found. The turbine speed was predicted well by the simulation for all cases. The shape of the instantaneous torque and MFP traces was captured well by the numerical simulation however, the amplitude of the torque traces was not predicted correctly. For the 1.0mm waste gate lift condition the predicted torque amplitude was 27.4% lower than for the measured data. Nevertheless it was found that the 1-D simulation was able to make a good prediction of the turbine performance under pulsating flow conditions.

In the final chapter, the effect different waste-gate i.e. the GT-Power standard model and an externally modelled waste gate was investigated in terms of the overall engine performance. The different waste-gate models were found to affect the inlet and exit pressures for the turbine by up to 5%. The mass flow through the waste gate was also affected however, because of the relatively small mass flow rate in comparison to the turbine mass flow, this did not have a large effect on the simulation. The efficiency of the turbine was found to be affected particularly at low engine speeds. A maximum difference of 6% was observed at an engine speed of 1000 RPM.

6.3 Future Work

Although this work has allowed a deeper insight into the behaviour of a waste-gated turbine, further investigations would be able to complement the findings in this thesis. In particular the following suggestions are made for future work:

6.3.1 Waste-gate connection geometry.

Only one geometry was considered here, it would be enlightening to study different waste gate connection geometries.

6.3.2 Waste-gate lifting.

In this study a high stiffness spring was used to ensure that the waste-gate did not open unintentionally under high pressures. In a real application this is not the case and the waste gate will lift under high pressures. An investigation of how this affects the engine-turbocharger system would be beneficial to the literature on this topic.

6.3.3 Map extrapolation.

This thesis showed that the effect of map width on the extrapolation of turbine performance can be significant. It is clear that the development of a higher accuracy extrapolation method would be beneficial for 1-D engine simulation.

Bibliography

Anderson, J. S. & Bratos-Anderson, M. (1987) *Solving problems in vibrations*. London, Longman Scientific & Technical.

Andersson, P., & Eriksson, L. (2001) Air-to-Cylinder Observer on a Turbocharged SI-Engine with Wastegate, *SAE Technical Paper*, 2001-01-0262.

Arnold, S., Calta D., Dullack K., Judd, C. & Thompson, G. (2005) Development of an Ultra-High Pressure Ratio Turbocharger. *SAE Technical Paper*, 2005-01-1546.

Baines, N., (2004) Turbocharger turbine pulse flow performance and modelling: 25 years on. *Proceedings of the 9th International Conference on Turbochargers and Turbocharging, 19-20 May 2010, Westminster, London*. Institution of Mechanical Engineers, Information & Library Services, pp. 347-362.

Bandel, W., Fraidl, G. K., Kapus, P. E., Sikiner, H. & Cowland, C. N. (2006) The Turbocharged GDI Engine: Boosted Synergies for High Fuel Economy Plus Ultra-low Emission. *SAE Technical Paper*, 2006-01-1266.

Barlow, T. J., Latham, S., McRae, I. S. & Boulter, P. J. (2009), *A reference book of driving cycles for use in the measurement of road vehicle emissions*. UK, TRL Limited.

Benson, R. S. (1974) Nonsteady Flow in a Turbocharger Nozzleless Radial Gas Turbine. *SAE Technical Paper*, 740739.

Birman, R. (1954) New Developments in Turbocharging. *SAE Technical Paper*, 540017.

British Standards Institution (1983) BS 1042-2.2:1983. *Measurement of fluid flow in closed conduits – Part 2: Velocity area methods*. London, BSI.

Bücker, I., Karhoff, D-C., Klaas, M. & Schröder, W. (2013) Engine In-Cylinder Flow Control via Variable Intake Valve Timing. *SAE Technical Paper*, 2013-24-0055.

Capobianco, M. & Marelli, S. (2007) Waste-Gate Turbocharging Control in Automotive SI Engines: Effect on Steady and Unsteady Turbine Performance. *SAE Technical Paper*, 2007-01-3543.

Chadwell, C. J. & Walls, M. (2010) Analysis of a SuperTurbocharged Downsized Engine Using 1-D CFD Simulation. *SAE Technical Paper*, 2010-01-1231.

Chiong, M. S., Rajoo, S., Costall, A. W., Salim, W. S-I. W., Romagnoli, A. & Martinez-Botas, R. F. (2013) Assessment of Cycle Average Turbocharged Maps through One Dimensional and Mean-Line Coupled Codes. *Proceedings of ASME Turbo Expo 2013: Turbine Technical Conference and Exposition, 3-7 June 2013*, Texas, USA. pp. (V06CT40A026)1-10.

Clenci, A. C., Descombes, G., Podevin, P. & Hara, V. (2007) Some Aspects Concerning the Combination of Downsizing with Turbocharging, Variable Compression Ratio, and Variable Intake Valve Lift. *Proceedings of the Institution of Mechanical Engineers, Part D: Journal of Automobile Engineering*, 221 (10), 1287-1293.

Copeland, C., Martinez-Botas, R. & Seiler, M. (2011) Comparison between Steady and Unsteady Double-Entry Turbine Performance Using the Quasi-Steady Assumption, *Journal of Turbomachinery*, 133 (3), 031001/1-10.

Copeland, C., Martinez-Botas, R., Turner, J., Pearson, R., Luard, N., Carey, C., Richardson, S., Di Martino, P. & Chobola, P. (2012) Boost system selection for a heavily downsized spark ignition prototype engine. *Proceedings of the 10th International Conference on Turbochargers and Turbocharging, 15-16 May 2012, Savoy Place, London*. Cambridge, Woodhead Publishing Limited. pp. 27-41.

Copeland, C., Newton, P. J., Martinez-Botas, R. F. & Seiler, M. (2012) A comparison of timescales within a pulsed flow turbocharger turbine. *Proceedings of the 10th International Conference on Turbochargers and Turbocharging, 15-26 May 2012, Savoy Place, London.* Cambridge, Woodhead Publishing Limited. pp. 389-404.

Costall, A. & Martinez-Botas (2007) Fundamental Characterization of Turbocharger Turbine Unsteady Flow Behavior. *Proceedings of ASME Turbo Expo 2007: Power for Land, Sean and Air, 14-17 May 2007, Montreal, Canada*. pp. 1827-1839.

Costall, A. W., McDavid, R. M., Martinez-Botas, R. F. & Baines, N. C. (2010) Pulse Performance Modeling of a Twin Entry Turbocharger Turbine under Full and Unequal Admission, *Journal of Turbomachinery*, 133 (2), 021005/1-9.

Edson, M. H. (1962) The Influence of Compression Ratio and Dissociation on Ideal Otto Cycle Engine Thermal Efficiency. *SAE Technical Paper*, 620557.

Eriksson, L. (2007) Modeling and Control of Turbocharged SI and DI Engines, *Oil & Gas Science and Technology - Revue de l'IFP Special Issue: IFP International Conference: New Trends on Engine Control, Simulation and Modelling*, 62(4), pp. 523-538.

Flierl, R. & Klüting, M. (2000) The Third Generation of Valve trains – New Fully Variable Valvetrains for Throttle-Free Load Control. *SAE Technical Paper*, 2000-01-1227.

Fraser, N., Blaxill, H., Lumsden, G. & Bassett, M. (2009) Challenges for Increased Efficiency through Gasoline Engine Downsizing. *SAE Technical Paper*, 2009-01-1053.

Galindo, J., Serrano J., Climent H. & Varnier O. (2010) Impact of two-stage turbocharging architectures on pumping losses of automotive engines based on an analytical model. *Energy Conversion Management*, 51 (10), 1958-1969.

Gamma Technologies (2011) *GT-Power Flow Theory*, Gamma Technologies Inc.

Gamma Technologies, (2010) *GT-SUITE Engine Performance Application Manual (Version 7.1)*. Gamma Technologies Inc.

Ghorbanian, K. & Gholamrezaei, M. (2009) An Artificial Neural Network Approach to Compressor Performance Prediction. *Applied Energy*, 86 (7-8), 1210-1221.

Gregg, D. (1928) Performance of a Supercharged Passenger-Car. *SAE Technical Paper*, 280041.

Hancock, D., Fraser, N., Jeremy, M., Sykes, R. & Blaxill, H. (2008) A New 3 Cylinder 1.2l Advanced Downsizing Technology Demonstrator Engine. *SAE Technical Paper*, 2008-01-0611.

Heywood, J. B., (1988) *Internal Combustion Engine Fundamentals*. Singapore, McGraw-Hill.

Honeywell. (2009) Charge Air System flow Diagram. [Online] Available from: http://www51.honeywell.com/ [Accessed 15th October 2014]

Hosaka, T. & Hamazaki, M. (1991) Development of the Variable Valve Timing and Lift (VTEC) Engine for the Honda NSX. *SAE Technical Paper*, 910008.

International Council on Clean Transportation. (2014) *EU CO2 Emission Standards for Passenger Cars and Light-Commercial Vehicles (Update January 2014)*. [Online] Available from: http://www.theicct.org/ [Accessed 15th September 2014]

Jensen, J. P., Kristensen, A. F., Sorenson, S. C., Houbak, N. & Hendricks, E. (1991) Mean Value Modeling of a Small Turbocharged Diesel Engine. *SAE Technical Paper*, 910070.

Jiang, L., Vanier, J., & Yilmaz, H. (2009) Parameterization and Simulation for a Turbocharged Spark Ignition Direct Injection Engine with Variable Valve Timing. *SAE Technical Paper*, 2009-01-0680.

Jung, M., Ford, R., Glover, K., Collings, N., Christen, U. & Watts, M. J. (2002) Parameterization and Transient Validation of a Variable Geometry Turbocharger for Mean-value Modeling at Low and Medium Speed-load Points, *SAE Technical Paper*, 2002-01-2729.

Karamanis, N. & Martinez-Botas, R. F. (2002) Mixed-Flow Turbines for Automotive Turbochargers: Steady and Unsteady Performance. *Int. J. Engine Res.*, 3 (3), 127-138.

Keidel, S., Wetzel, P., Biller, B., Bevan, K. & Birckett, A. (2012) Diesel Engine Fuel Economy Improvement Enabled by Supercharging and Downspeeding. *SAE International Journal of Commercial Vehicles*, 5 (2), 483-493.

King, J., Heaney, M., Bower, E., Jackson, N., Owen, N., Saward, J., Fraser, A., Morris, G., Bloore, P., Cheng, T., Borges-Alejo, J. & Criddle, M. (2012) HyBoost – An intelligent electrified optimized downsized gasoline engine concept. *Proceedings of the 10th International Conference on Turbochargers and Turbocharging, 15-26 May 2012, Savoy Place, London*. Cambridge, Woodhead Publishing Limited. pp. 3-14.

King, L. V. (1914) On the Convection of Heat from Small Cylinders in a Stream of Fluid: Determination of the Convection Constants of Small Platinum Wires, with Applications to Hot-Wire Anemometry. *Proceedings of the Royal Society A, Sept. 1914, London*, 1914 (90), pp. 563-570.

Kirkup, L. (1994) *Experimental Methods: An introduction to the analysis and presentation of data*. Queensland, Australia, John Wiley & Sons Australia.

Kleeberg, H., Tomazic, D., Lang, O. & Habermann, K. (2006) Future Potential and Development Methods for High Output Turbocharged Direct Injected Gasoline Engines. *SAE Technical Paper*, 2006-01-0046.

Königstein, A., Larsson, P-I., Grebe, U. D. & Wu, K-J. (2008) Differentiated Analysis of Downsizing Concepts. *MTZ worldwide*, 69 (6), 4-11.

Lake, T., Stokes, J., Murphy, R., Osborne, R., Schamel, A. (2004) Turbocharging Concepts for Downsized DI Gasoline Engines. *SAE Technical Paper*, 2004-01-0036.

Lang, O., Geiger, J., Habermann, K. & Wittler, M. (2005) Boosting and Direct Injection – Synergies for Future Gasoline Engines. *SAE Technical Paper*, 2005-01-1144.

Lecointe, B. & Monnier, G. (2003) Downsizing a Gasoline Engine using Turbocharging with Direct Injection. *SAE Technical Paper*, 2003-01-0542.

Leduc, P., Dubar, B., Ranini, A. & Monnier, G. (2003) Downsizing for Gasoline Engine: an Efficient Way to Reduce CO2 Emissions. *Oil & Gas Science and Technology – Rev*, 58 (1), pp. 115-127.

Leppard, W. R. (1982) Individual-Cylinder Knock Occurrence and Intensity in Multicylinder Engines. *SAE Technical Paper*, 820074.

Lumsden, G., OudeNijeweme, D., Fraser, N. & Blaxill, H. (2009) Development of a Turbocharged Direct Injection Downsizing Demonstrator Engine. *SAE Technical Paper*, 2009-01-1503.

Luttermann, C., Schünemann, E. & Klauer, N. (2006) Enhanced VALVETRONIC Technology for Meeting SULEV Emission Requirements. *SAE Technical Paper*, 2006-01-0849.

Mamat, A. M. I. (2012) Design and Development of a High Performance LPT for Electric Turbocompounding Energy Recovery Unit in a Heavily Downsized Engine. Ph.D thesis, Imperial College London.

Marelli, S. and Capobianco, M. (2011) Steady and pulsating flow efficiency of a waste-gated turbocharger radial flow turbine for automotive application. *Energy*, 36 (1), 459-465.

Martin, G., Talon, V., Higelin, P., Charlet, A. & Caillol, C. (2009) Implementing Turbomachinery Physics into Data Map-Based Turbocharger Models. *SAE International Journal of Engines*, 2 (1), 211-229.

Martin, G., Talon, V., Higelin, P., Charlet, A. & Caillol, C. (2009) Implementing Turbomachinery Physics into Data Map-Based Turbocharger Models. *SAE International Journal of Engines*, 2 (1), 211-229.

Martinez-Botas, R., Pesiridis, A. & MingYang, Y. (2011) Overview of boosting options for future downsized engines. *Science China Technological Sciences*, 54 (2), 318-331.

McCrometer Inc. (2011) V-Cone Flow Meter Technical Brief, California.

Moraal, P. and I. Kolmanovsky, (1999) Turbocharger Modeling for Automotive Control Applications. *SAE Technical Paper*, 1999-01-0908.

Muranaka, S., Takagi, Y. & Ishida, T. (1987) Factors Limiting the Improvement in Thermal Efficiency of S.I Engine at Higher Compression Ratio. *SAE Technical Paper*, 870548.

Newton, P. J. (2013) *An Experimental and Computational Study of Pulsating Flow within a Double Entry Turbine with Different Nozzle Settings*. Ph.D thesis, Imperial College London.

Pesiridis, A., Salim, W., S-I., W. and Martinez-Botas, R. F., (2012) Turbocharger matching methodology for improved exhaust energy recovery. *Proceedings of the 10th International Conference on Turbochargers and Turbocharging, 15-26 May 2012, Savoy Place, London*. Cambridge, Woodhead Publishing Limited. pp. 203-218.

Petitjean, D., Bernardini, L., Middlemass, C. & Shahed, S. (2004) Advanced Gasoline Engine Turbocharging Technology for Fuel Economy Improvements. *SAE Technical Paper*, 2004-01-0988.

Pohorelsky, L., Brynych, P., Macek, J., Vallaude, P-V., Ricaud, J-C., Obernesser, P. & Tribotté, P. (2012) Air System Conception for a Downsized Two-Stroke Diesel Engine. *SAE Technical Paper*, 2012-01-0831.

Rajoo, S. & Martinez-Botas (2010) Unsteady Effect in a Nozzled Turbocharger Turbine, *Journal of Turbomachinery*, 132 (3), 031001/1-9.

Rajoo, S. & Martinez-Botas, R. (2008) Mixed Flow Turbine Research: A Review. *Journal of Turbomachinery*, 130 (4), 044001/1-12.

Rajoo, S. (2007) *Steady and Unsteady Performance of a Variable Geometry Mixed Flow Turbocharger Turbine*. Ph.D thesis, Imperial College London.

Rajoo, S., Romagnoli, A. & Martinez-Botas, R. F. (2012) Unsteady Performance Analysis of a Twin-entry Variable Geometry Turbocharger Turbine, *Energy*, 38 (1), 176-189.

Raunekk & Stonecypher L. (2009) *Components of a Turbocharger*. [Online] Available from: http://www.brighthubengineering.com/ [Accessed 15th September 2014]

Romagnoli, A., Salim, W. S-I. W., Gurunathan, B. A., Martinez-Botas, R. F., Turner, J. W. G., Luard, N., Jackson, R., Matteucci, L., Copeland, C., Akehurst, S., Lewis, A. G., & Brace, C. J. (2014) Assessment of supercharging boosting component for heavily downsized gasoline engines. *Proceedings of the 11th International Conference on Turbochargers and Turbocharging, 13-14 May 2014, The British Museum, London*. Woodhead Publishing Limited. pp. 13-26.

Salamon, C., McAllister, M., Robinson, R., Richardson, S., Martinez-Botas, R., Romagnoli, A., Copeland, C. & Turner, J. (2012) Improving Fuel Economy by 35% through combined Turbo and Supercharging on a Spark Ignition Engine. *Proceedings of the 21st Aachen Colloquium Automobile and Engine Technology 2012*, 8 – 10 October 2012, Aachen, Germany, pp. 1317-1346.

Saulnier, S. & Guilain, S. (2004) Computational Study of Diesel Engine Downsizing Using Two-Stage Turbocharging. *SAE Technical Paper*, 2004-01-0929.

Serrano, J., Arnau, F., Dolz, V., Tiseira, A. & Cervello, C. (2008) A Model of Turbocharger Radial Turbines Appropriate to be used in Zero- and One-Dimensional Gas Dynamics Codes for Internal Combustion Engines Modelling. *Energy Conversion and Management*, 49 (12), 3729-3745.

Stokes, J., Lake, T. H. & Osborne, R. J. (2000) A Gasoline Engine Concept for Improved Fuel Economy – The Lean Boost System. *SAE Technical Paper*, 2000-01-2902.

Szymko, S. (2006) *The development of an eddy current dynamometer for evaluation of steady and pulsating turbocharger turbine performance*. Ph.D thesis, Imperial College London.

Szymko, S., McGlashan N. R., Martinez-Botas, R. and Pullen K. R. (2006) The development of a dynamometer for torque measurement of automotive turbocharger turbines. *Proceedings of IMechE Part D: J. Automobile Engineering*, 42 (D), 225-239.

The European Commission. (2009) *Setting Emission Performance Standards for New Passenger Cars as part of the Community's Integrated Approach to Reduce CO2 Emissions from Light-Duty Vehicles*. Regulation (EC) No 443/2009 of the European Parliament and of the Council of 23 April 2009.

The International Council on Clean Transportation. (2014) *Global Comparison of Light-Duty Vehicle Fuel Economy/GHG Emission Standards (Update: February 2014)*. [Online]: Available from: http://www.theicct.org/ [Accessed 15th September 2014]

Thomasson, A., Leufve´n, O., Criscuolo, I. & Eriksson, L. (2013) Modeling and Validation of a Boost Pressure Actuation System for a Series Sequentially Turbocharged SI engine, *Control Engineering Practice*, 21 (12), 1860-1870.

Turner, J. W. G., Pearson, R. J., & Kenchington, S. A. (2005) Concepts for Improved Fuel Economy from Gasoline Engines. *International Journal of Engine Research*, 6 (2), 137-157.

Turner, J. W. G., Popplewell, A., Patel, R., Johnson, T. T., Darnton, N. J., Richardson, S., Bredda, S. W., Tudor, R. J., Bithell, C. I., Jackson, R., Remmert S. M., Cracknell, R. F., Fernandes, J. X., Lewis, A. G. J., Akehurst, S., Brace, C. J., Copeland, C., Martinez-Botas, R. Romagnoli, A. & Burluka A. A., (2014) Ultra Boost for Economy: Extending the Limits of Extreme Engine Downsizing, *SAE International Journal of Engines*, 7 (1), 388-417.

Walzer, P. (2001) Future Power Plans for Cars. *SAE Technical Paper*, 2001-01-3192.

Watson, H.C., Milkins, E.E., Roberts, K. & Bryce, W. (1983) Turbocharging for Fuel Economy. *SAE Technical Paper*, 830014.

Watson, N. & Janota, M. S. (1982) *Turbocharging the Internal Combustion Engine*. The Macmillan Press Ltd., London.

Watson, N. & Marzouk, M. (1977) A Non-Linear Digital Simulation of Turbocharged Diesel Engines under Transient Conditions. *SAE Technical Paper*, 770123.

Watson, N. (1979) Turbochargers for the 1980s – Current Trends and Future Prospects. *SAE Technical Paper*, 790063.

Watson, N. (1981) Transient Performance Simulation and Analysis of Turbocharged Diesel Engines. *SAE Technical Paper*, 810338.

Watson, N. (1984) Turbocharged Spark Ignition Engine Simulation. *SAE Technical Paper*, 845042.

Wetzel, P. (2013) Downspeeding a Light Duty Diesel Passenger Car with a Combined Supercharger and Turbocharger Boosting System to Improve Vehicle Drive Cycle Fuel Economy. *SAE Technical Paper*, 2013-01-0932.

Wirth, M., Mayerhofer, U., Piock, W. F. & Fraidl, G. K. (2000) Turbocharging the DI Gasoline Engine. *SAE Technical Paper*, 2000-01-0251.

Wirth, M., Mayerhofer, U., Piock, W. F. & Fraidl, G. K. (2000) Turbocharging the DI Gasoline Engine. *SAE Technical Paper*, 2000-01-0251.

Woods, W. A. & Khan, S. R. (1965) An Experimental Study of Flow through Poppet Valves. *Proceedings of the Institution of Mechanical Engineers, Conference Proceedings 1965 (180:32), June 1965*, SAGE, pp. 32-41.

Yang, M. Y., Padzillah, M. H., Zhuge, W. L, Martinez-Botas, R. F. & Rajoo, S. (2014) Comparison of the Influence of Unsteadiness between Nozzled and Nozzless Mixed Flow Turbocharger Turbine. *Proceedings of the 11th International Conference on Turbochargers and Turbocharging, 13-14 May 2014, London*, pp. 333-345.

Zhang, Q., Pennycott, A. & Brace, C. J. (2013) A review of parallel and series turbocharging for the diesel engine. *Proceedings of the IMechE Part D: J. Automobile Engineering*, 227 (12). 1723-1733.

APPENDIX A

STEADY STATE TURBINE PERFORMANCE

A1. Steady state mass flow parameter (MFP) at various waste-gate valve lifts (l_{wg})

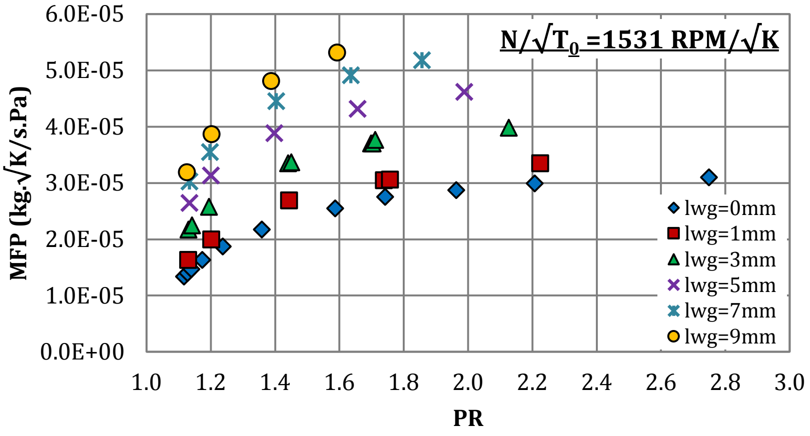

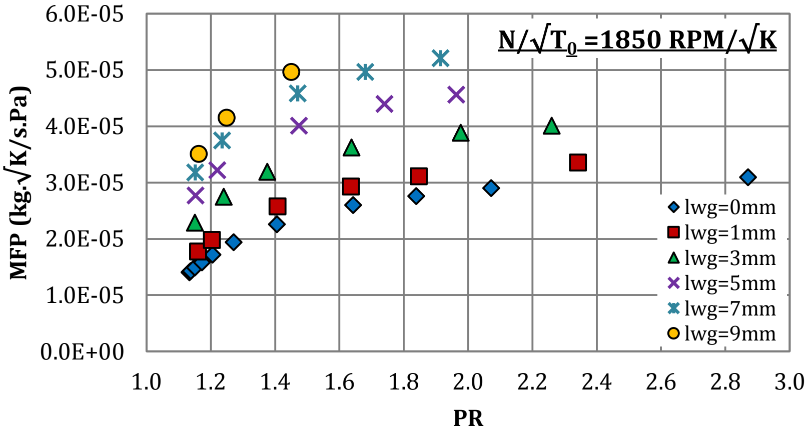

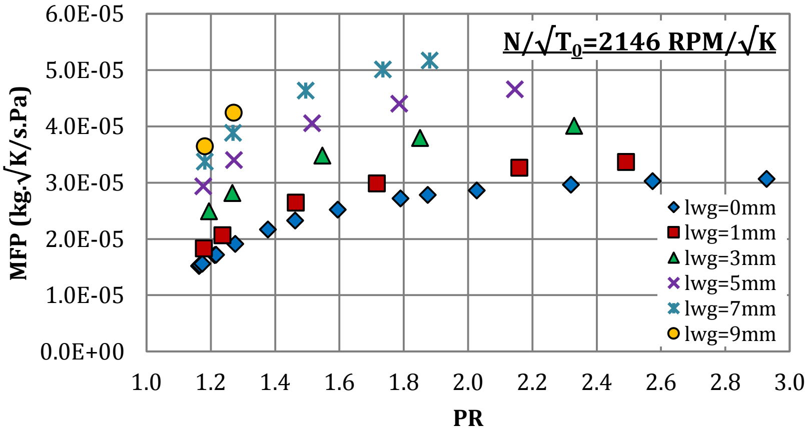

A2. Steady state total-to-static efficiency (η_{TS}) at various waste-gate valve lifts (l_{wg})

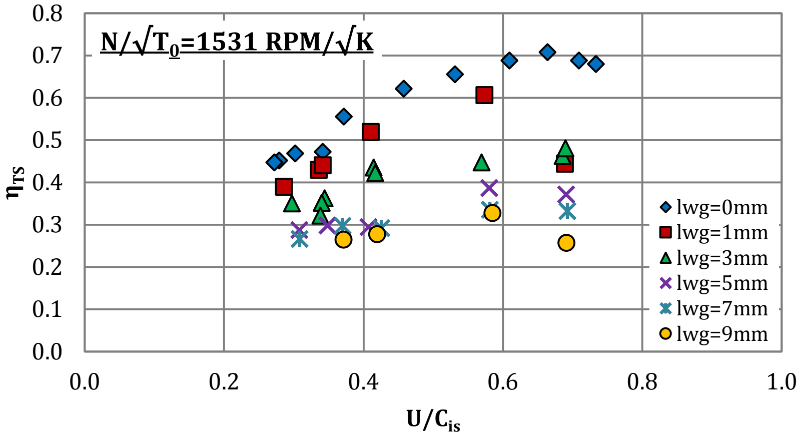

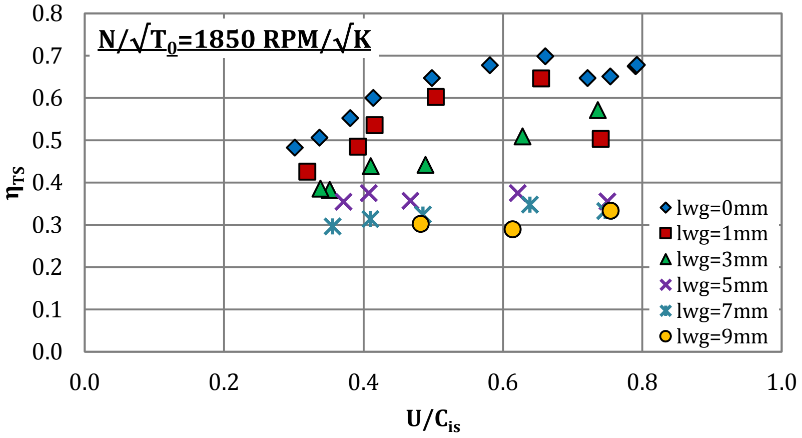

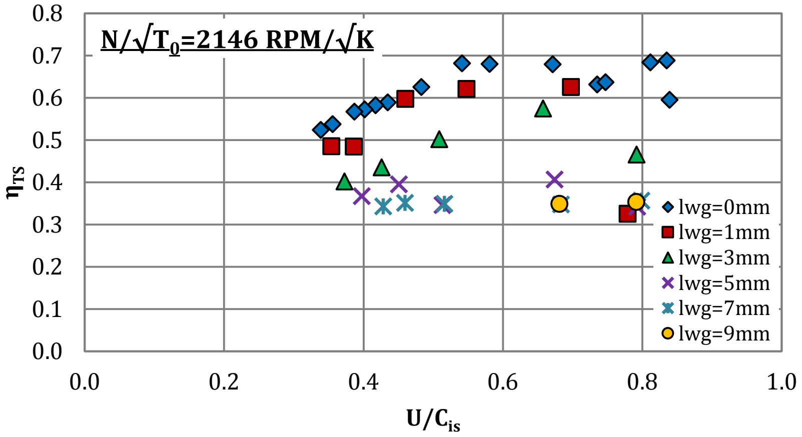

APPENDIX B

UNSTEADY FLOW EXPERIMENTS ($N/\sqrt{T_0}$ = 1850 RPM/$\sqrt{K}$, l_{WG} = 0 mm)

B1. Instantaneous mass flow parameter (MFP) measurements

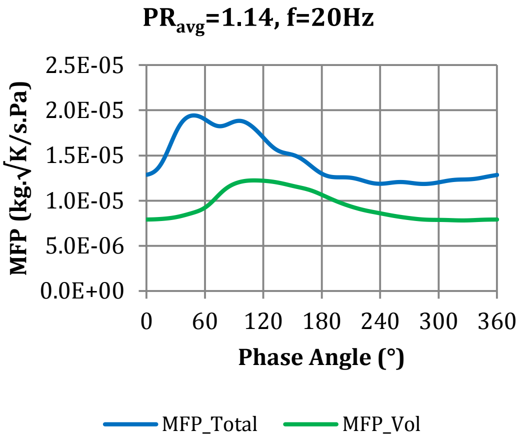

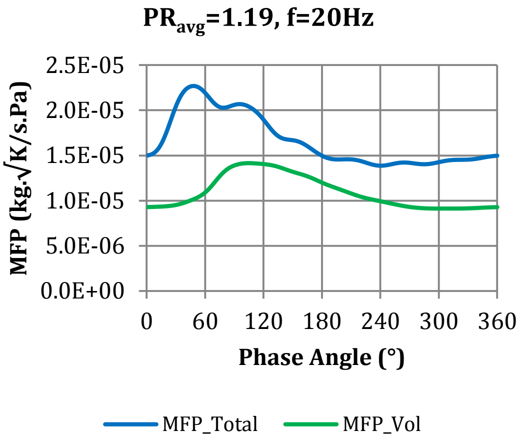

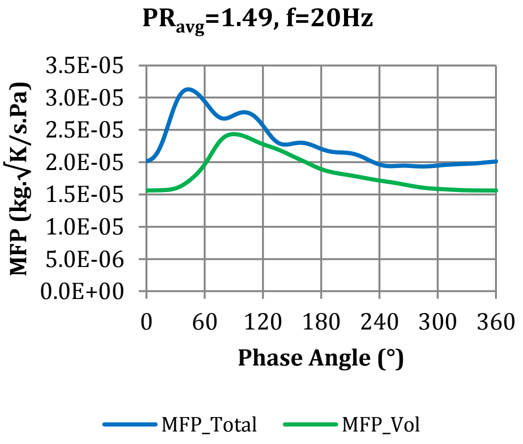

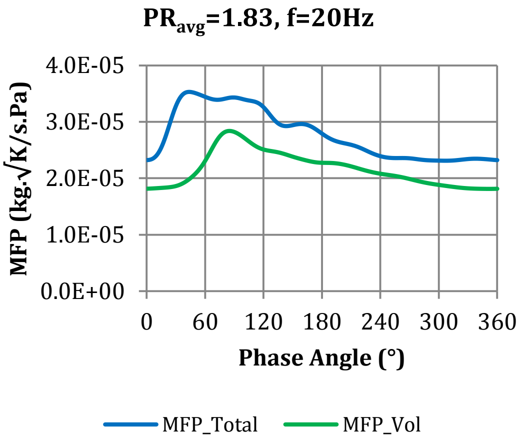

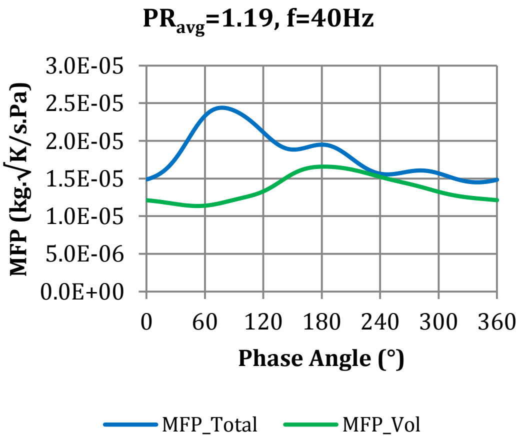

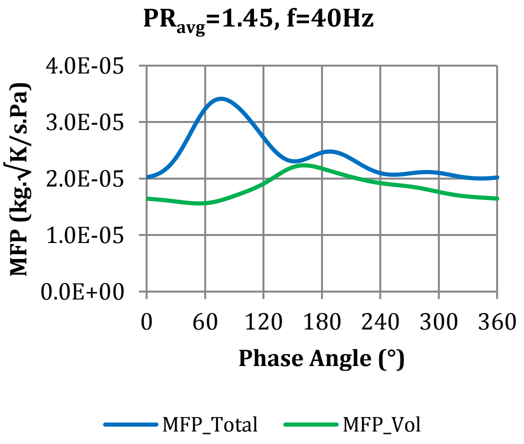

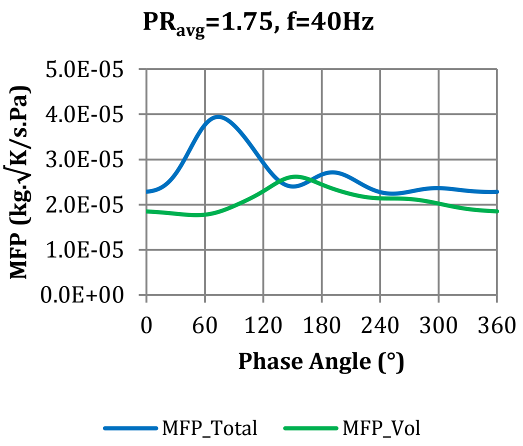
PR_{avg}=1.75, f=40Hz
5.0E-05
4.0E-05
3.0E-05
2.0E-05
1.0E-05
0.0E+00
MFP (kg.√K/s.Pa)
0
60
120
180
240
300
360
Phase Angle (°)
MFP_Total
MFP_Vol

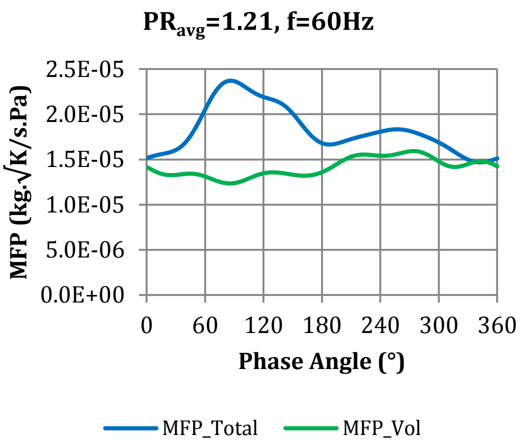
PR_{avg}=1.21, f=60Hz
2.5E-05
2.0E-05
1.5E-05
1.0E-05
5.0E-06
0.0E+00
MFP (kg.√K/s.Pa)
0
60
120
180
240
300
360
Phase Angle (°)
MFP_Total
MFP_Vol

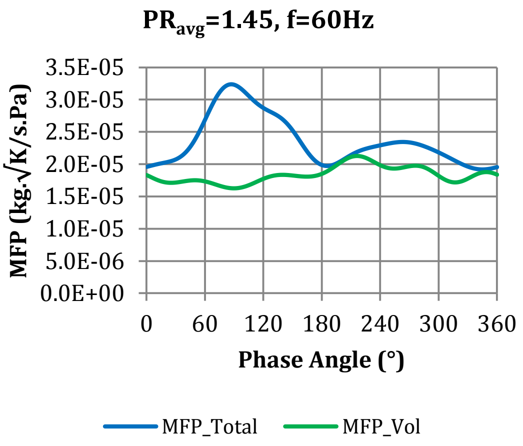
PR_{avg}=1.45, f=60Hz
3.5E-05
3.0E-05
2.5E-05
2.0E-05
1.5E-05
1.0E-05
5.0E-06
0.0E+00
MFP (kg.√K/s.Pa)
0
60
120
180
240
300
360
Phase Angle (°)
MFP_Total
MFP_Vol

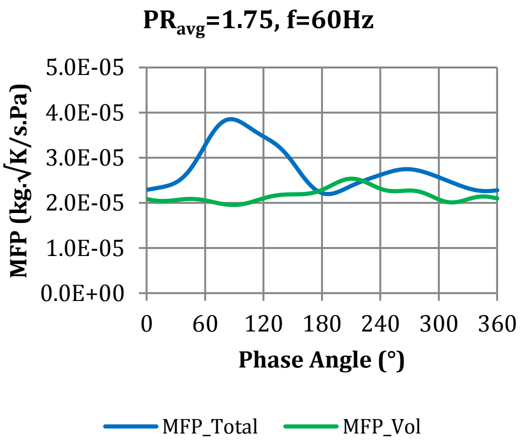
PR_{avg}=1.75, f=60Hz
5.0E-05
4.0E-05
3.0E-05
2.0E-05
1.0E-05
0.0E+00
MFP (kg.√K/s.Pa)
0
60
120
180
240
300
360
Phase Angle (°)
MFP_Total
MFP_Vol

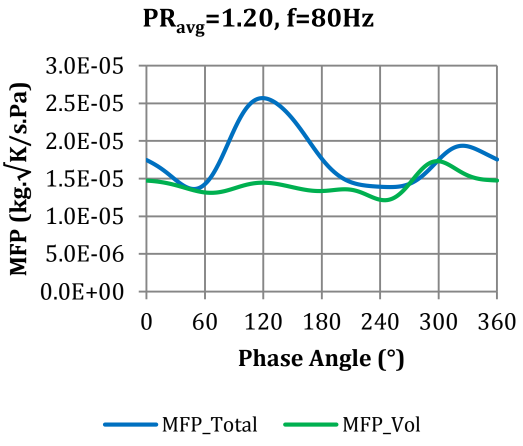
PR_{avg}=1.20, f=80Hz
3.0E-05
2.5E-05
2.0E-05
1.5E-05
1.0E-05
5.0E-06
0.0E+00
MFP (kg.√K/s.Pa)
0
60
120
180
240
300
360
Phase Angle (°)
MFP_Total
MFP_Vol

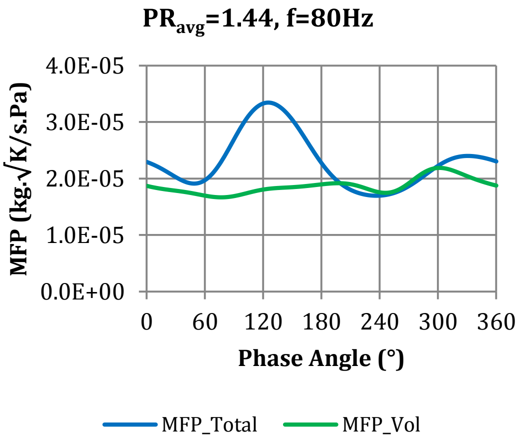
PR_{avg}=1.44, f=80Hz
4.0E-05
3.0E-05
2.0E-05
1.0E-05
0.0E+00
MFP (kg.√K/s.Pa)
0
60
120
180
240
300
360
Phase Angle (°)
MFP_Total
MFP_Vol

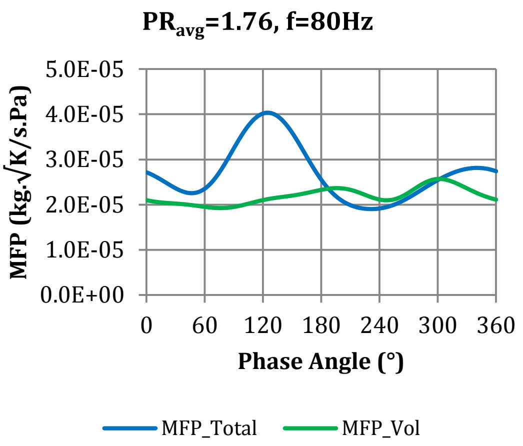

B2. Instantaneous static pressure (P_s) measurements

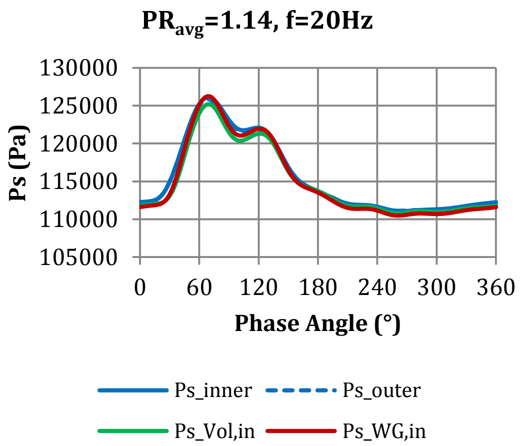

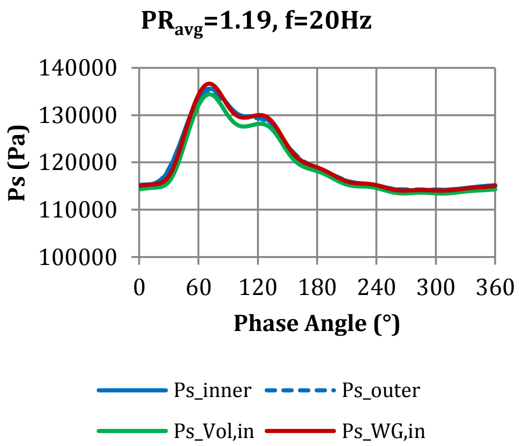

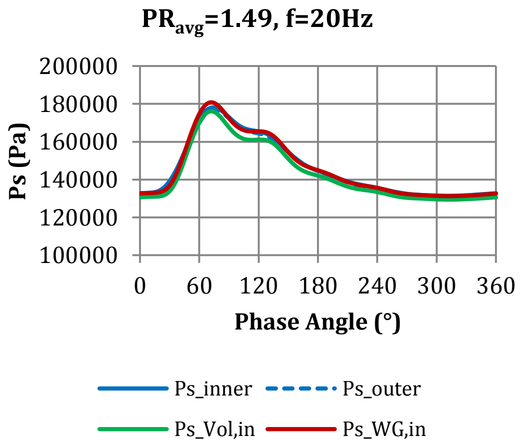

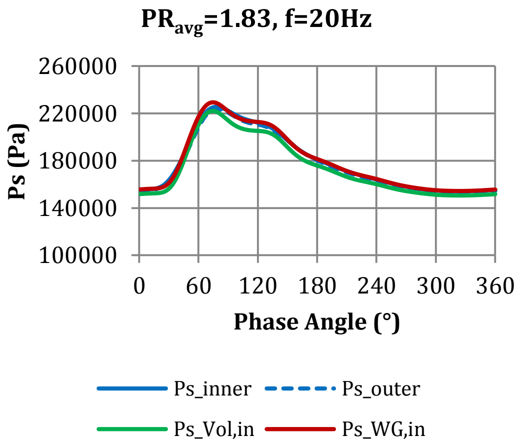

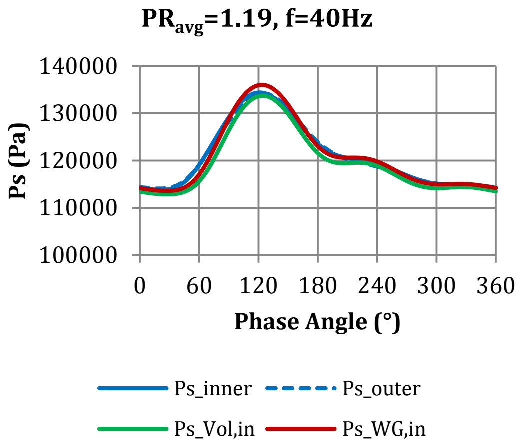
PR$_{avg}$=1.19, f=40Hz
140000
130000
120000
110000
100000
Ps (Pa)
0
60
120
180
240
300
360
Phase Angle (°)
Ps_inner
Ps_outer
Ps_Vol,in
Ps_WG,in

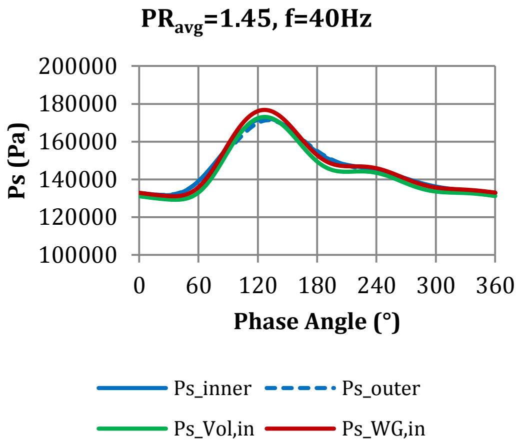
PR$_{avg}$=1.45, f=40Hz
200000
180000
160000
140000
120000
100000
Ps (Pa)
0
60
120
180
240
300
360
Phase Angle (°)
Ps_inner
Ps_outer
Ps_Vol,in
Ps_WG,in

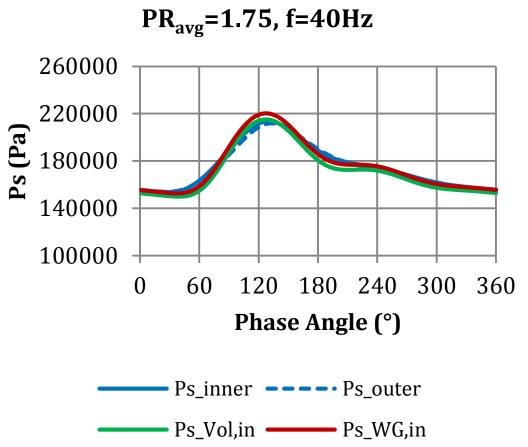
PR$_{avg}$=1.75, f=40Hz
260000
220000
180000
140000
100000
Ps (Pa)
0
60
120
180
240
300
360
Phase Angle (°)
Ps_inner
Ps_outer
Ps_Vol,in
Ps_WG,in

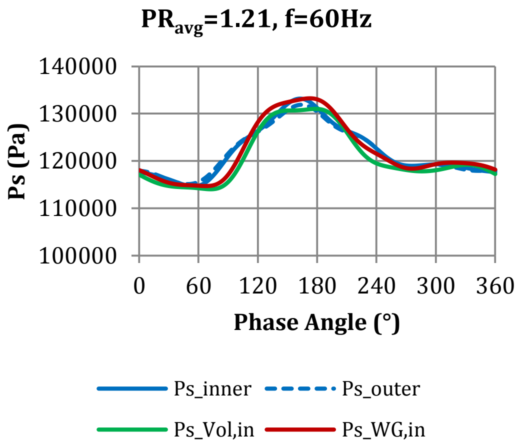
PR$_{avg}$=1.21, f=60Hz
140000
130000
120000
110000
100000
Ps (Pa)
0
60
120
180
240
300
360
Phase Angle (°)
Ps_inner
Ps_outer
Ps_Vol,in
Ps_WG,in

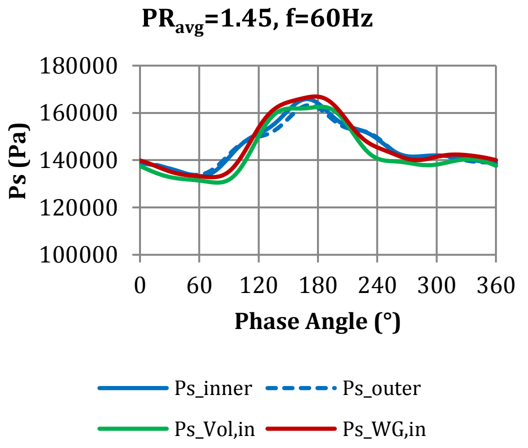
PR$_{avg}$=1.45, f=60Hz
180000
160000
140000
120000
100000
Ps (Pa)
0
60
120
180
240
300
360
Phase Angle (°)
Ps_inner
Ps_outer
Ps_Vol,in
Ps_WG,in

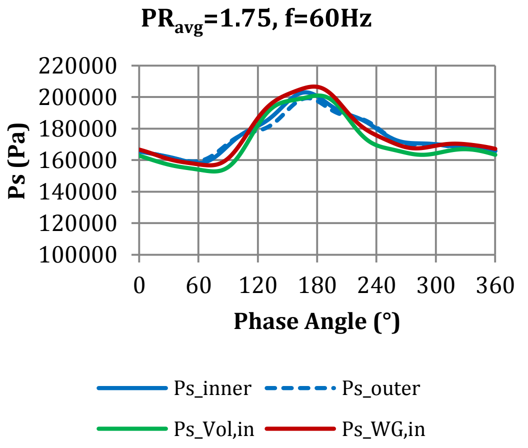
PR$_{avg}$=1.75, f=60Hz
220000
200000
180000
160000
140000
120000
100000
Ps (Pa)
0
60
120
180
240
300
360
Phase Angle (°)
Ps_inner
Ps_outer
Ps_Vol,in
Ps_WG,in

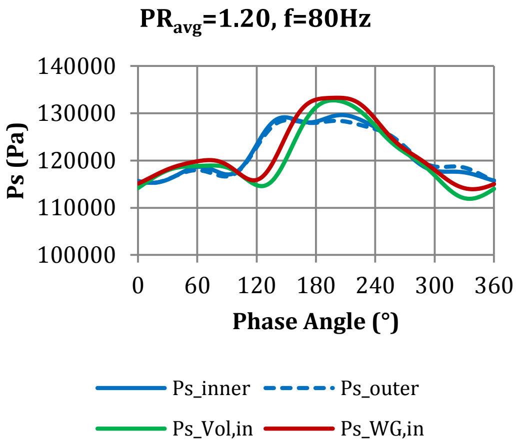

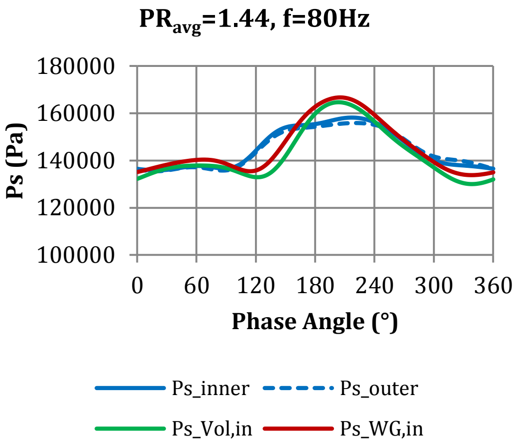

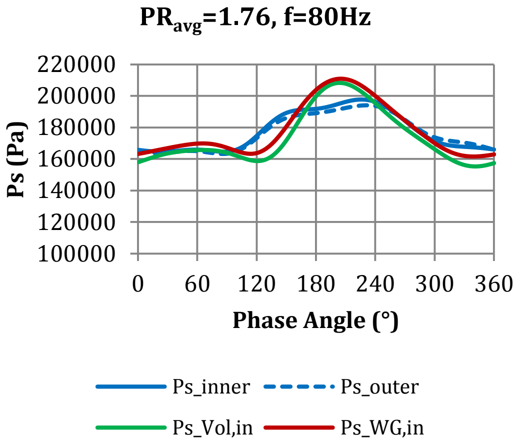

B3. Instantaneous torque measurements

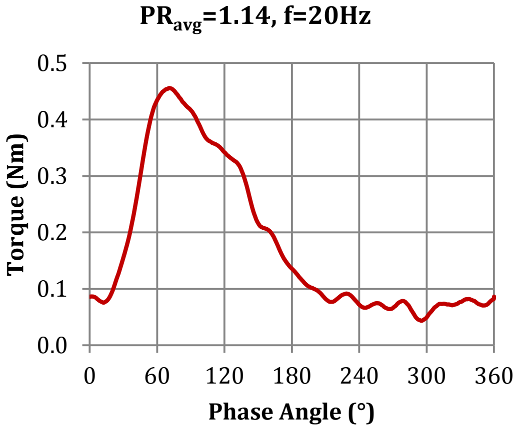

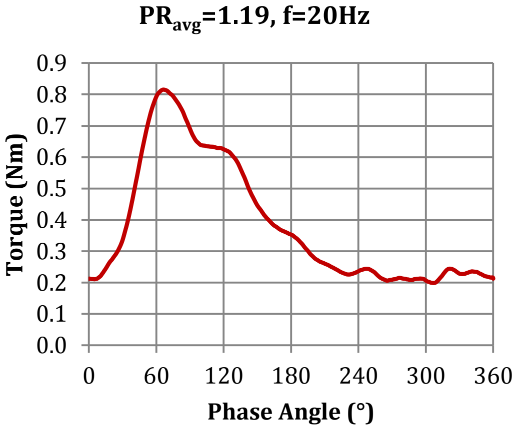

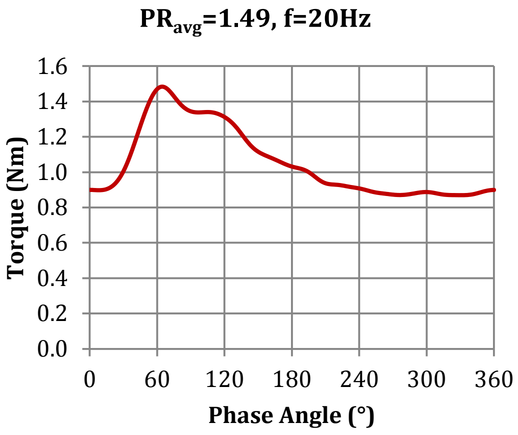
PR$_{avg}$=1.49, f=20Hz

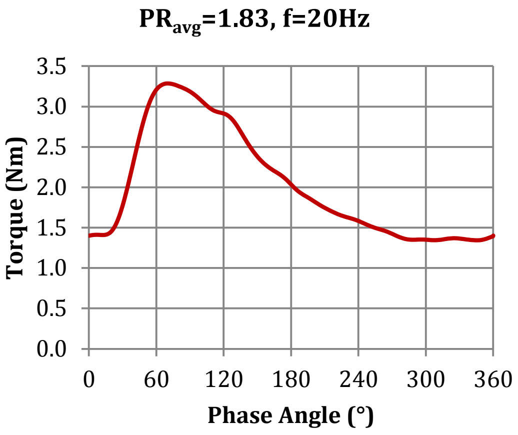
PR$_{avg}$=1.83, f=20Hz

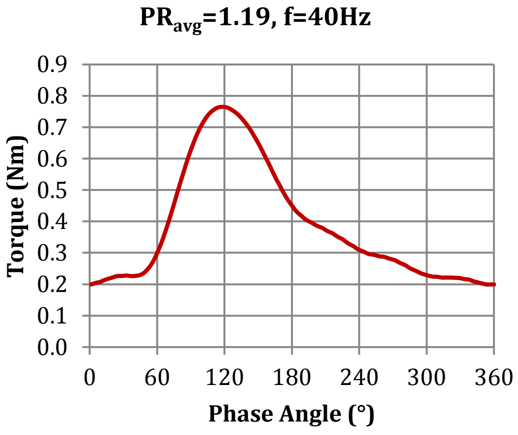
PR$_{avg}$=1.19, f=40Hz

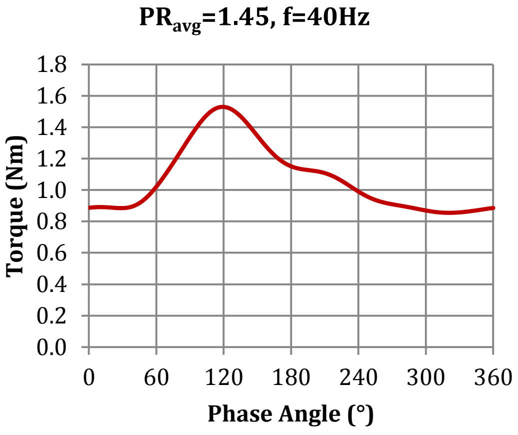
PR$_{avg}$=1.45, f=40Hz

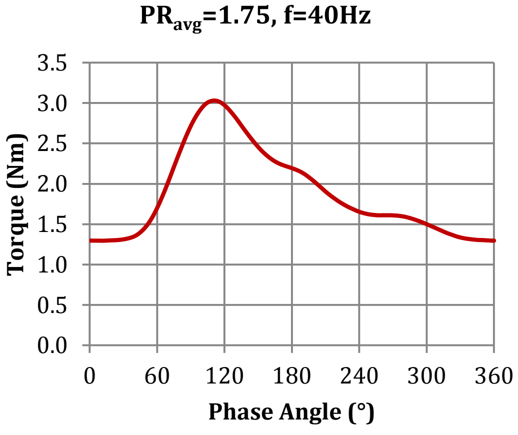
PR$_{avg}$=1.75, f=40Hz

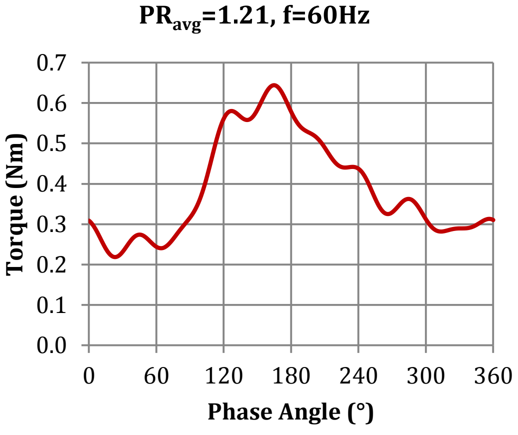
PR$_{avg}$=1.21, f=60Hz

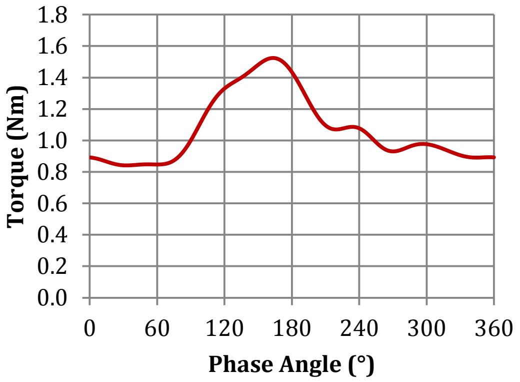

PR$_{avg}$=1.45, f=60Hz

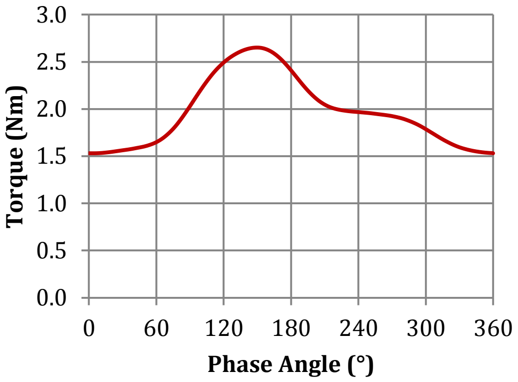

PR$_{avg}$=1.75, f=60Hz

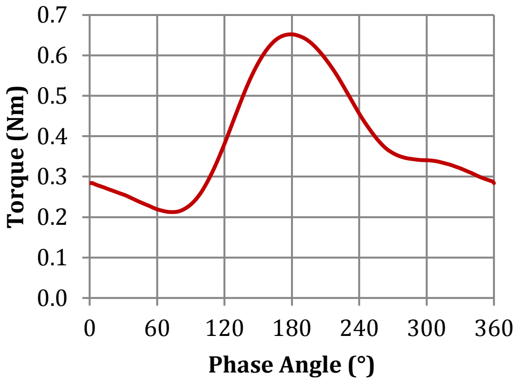

PR$_{avg}$=1.20, f=80Hz

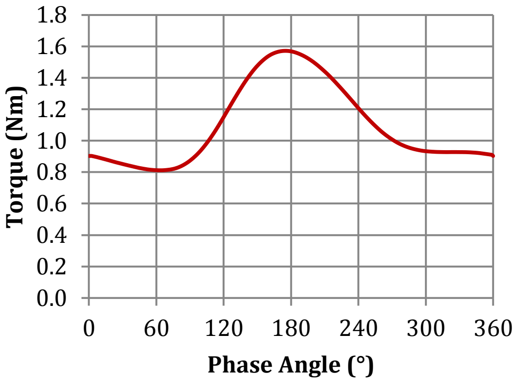

PR$_{avg}$=1.44, f=80Hz

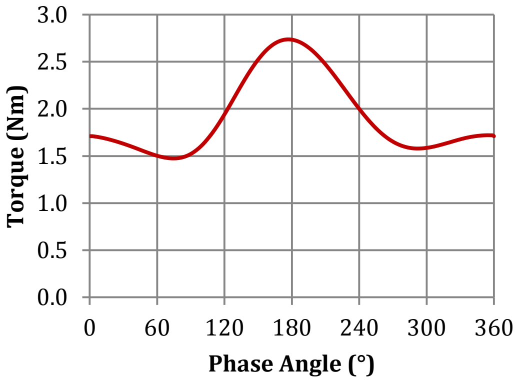

PR$_{avg}$=1.76, f=80Hz

B4. Instantaneous power measurements

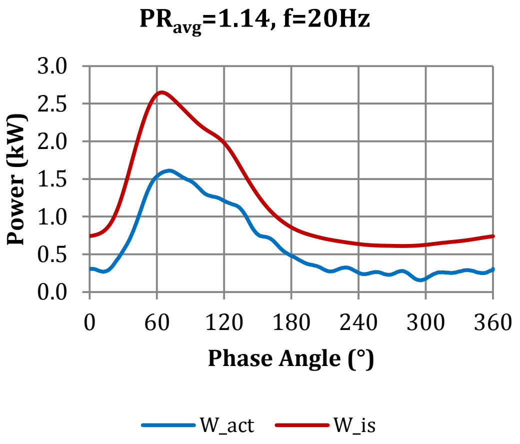

PR_{avg}=1.14, f=20Hz

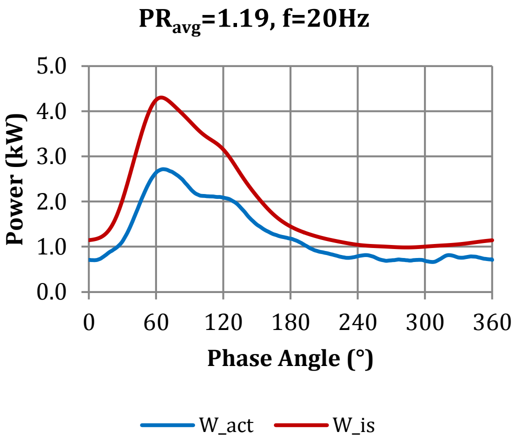

PR_{avg}=1.19, f=20Hz

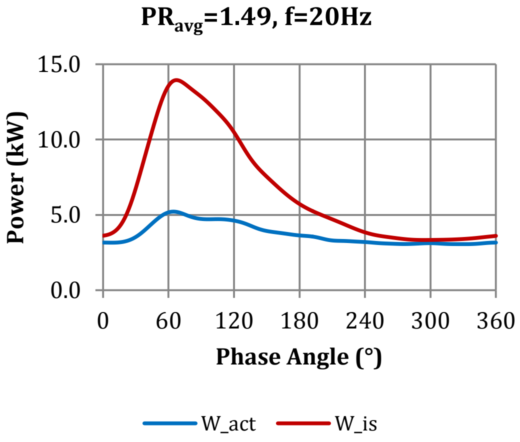

PR_{avg}=1.49, f=20Hz

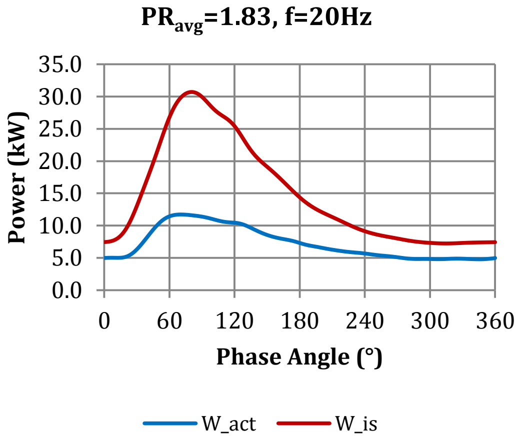

PR_{avg}=1.83, f=20Hz

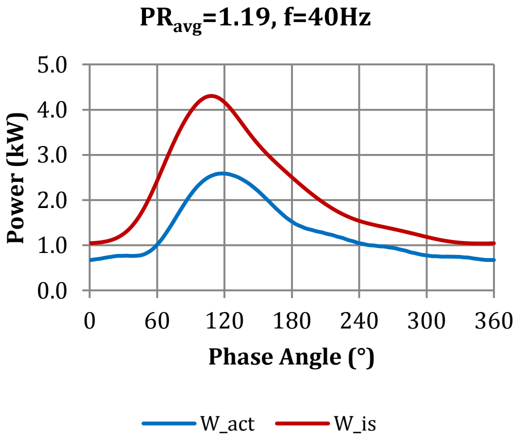

PR_{avg}=1.19, f=40Hz

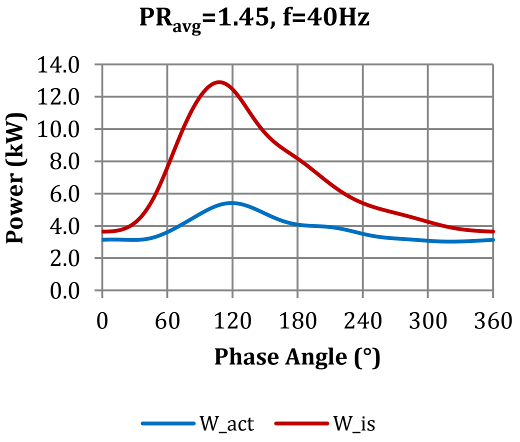

PR_{avg}=1.45, f=40Hz

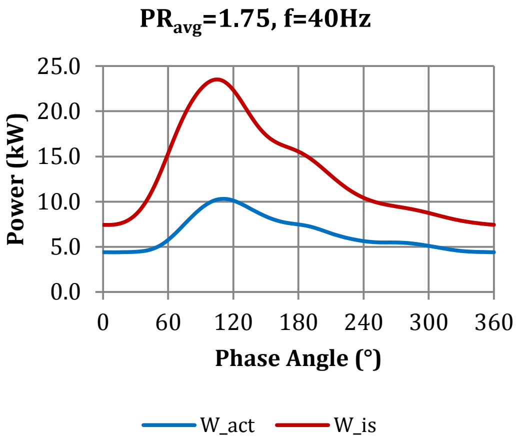
PR_{avg}=1.75, f=40Hz
Power (kW)
25.0
20.0
15.0
10.0
5.0
0.0
0
60
120
180
240
300
360
Phase Angle (°)
W_act
W_is

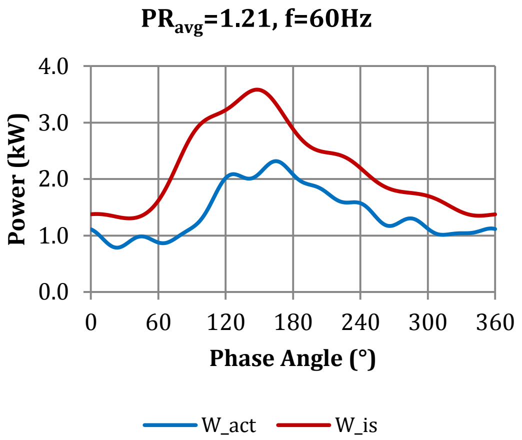
PR_{avg}=1.21, f=60Hz
Power (kW)
4.0
3.0
2.0
1.0
0.0
0
60
120
180
240
300
360
Phase Angle (°)
W_act
W_is

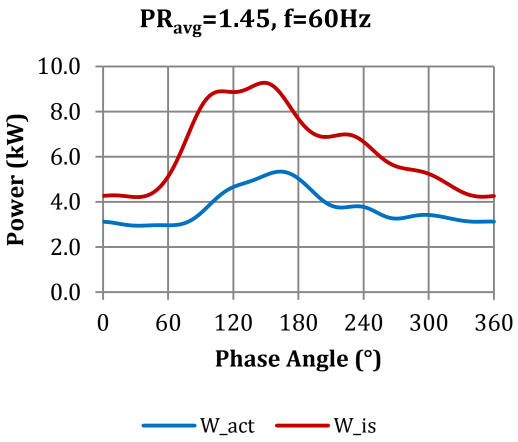
PR_{avg}=1.45, f=60Hz
Power (kW)
10.0
8.0
6.0
4.0
2.0
0.0
0
60
120
180
240
300
360
Phase Angle (°)
W_act
W_is

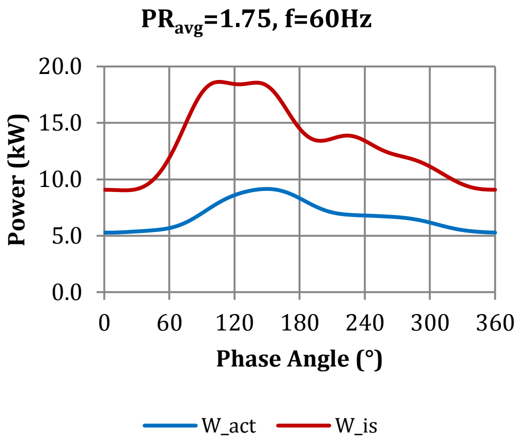
PR_{avg}=1.75, f=60Hz
Power (kW)
20.0
15.0
10.0
5.0
0.0
0
60
120
180
240
300
360
Phase Angle (°)
W_act
W_is

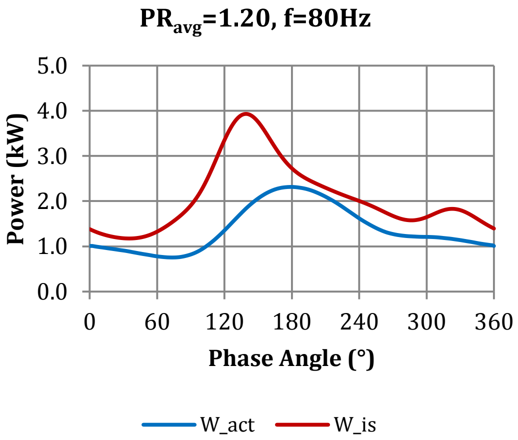
PR_{avg}=1.20, f=80Hz
Power (kW)
5.0
4.0
3.0
2.0
1.0
0.0
0
60
120
180
240
300
360
Phase Angle (°)
W_act
W_is

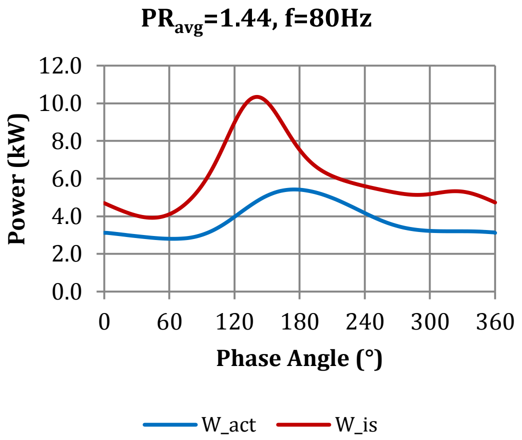
PR_{avg}=1.44, f=80Hz
Power (kW)
12.0
10.0
8.0
6.0
4.0
2.0
0.0
0
60
120
180
240
300
360
Phase Angle (°)
W_act
W_is

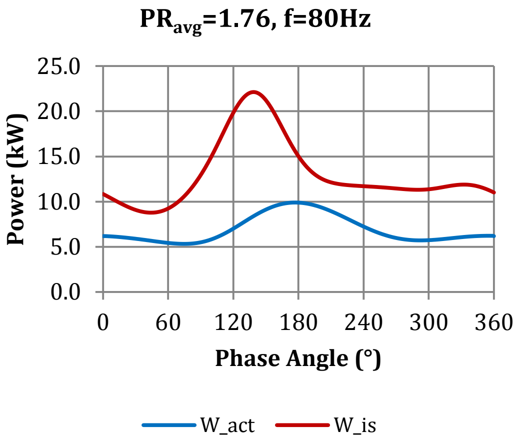
PRavg=1.76, f=80Hz
25.0
20.0
15.0
10.0
5.0
0.0
Power (kW)
0
60
120
180
240
300
360
Phase Angle (°)
W_act
W_is

APPENDIX C

UNSTEADY FLOW EXPERIMENTS ($N/\sqrt{T_0}$ = 1850 RPM/$\sqrt{K}$, l_{WG} = 1 mm)

C1. Instantaneous mass flow parameter (MFP) measurements

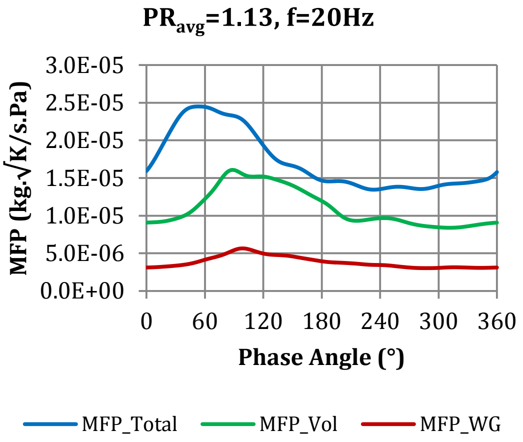
PR_{avg}=1.13, f=20Hz

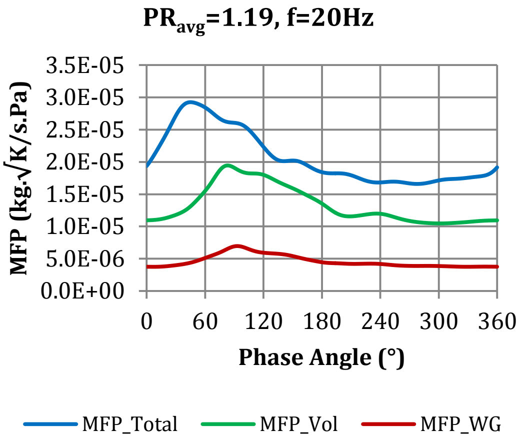
PR_{avg}=1.19, f=20Hz

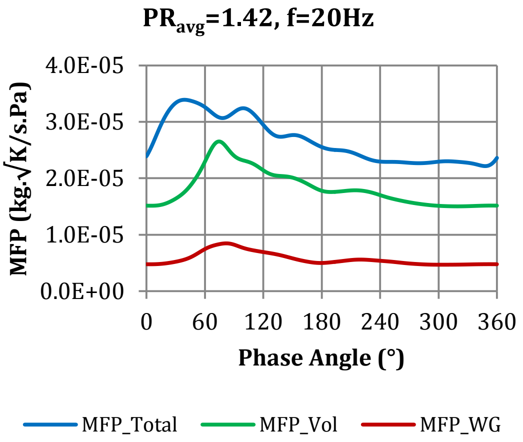
PR_{avg}=1.42, f=20Hz

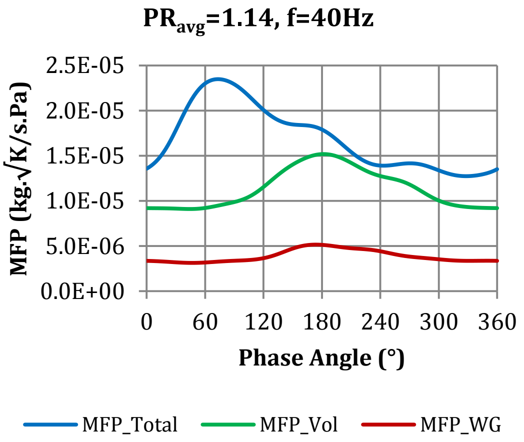
PR_{avg}=1.14, f=40Hz

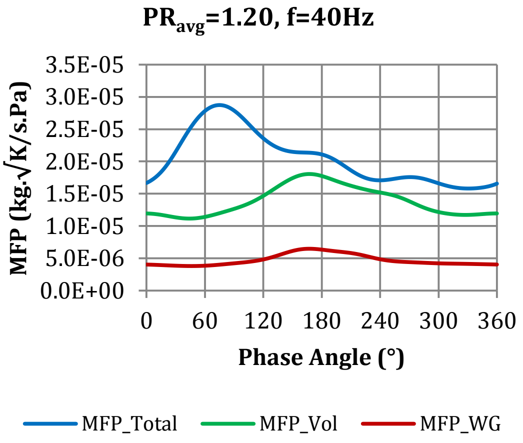
PR_{avg}=1.20, f=40Hz

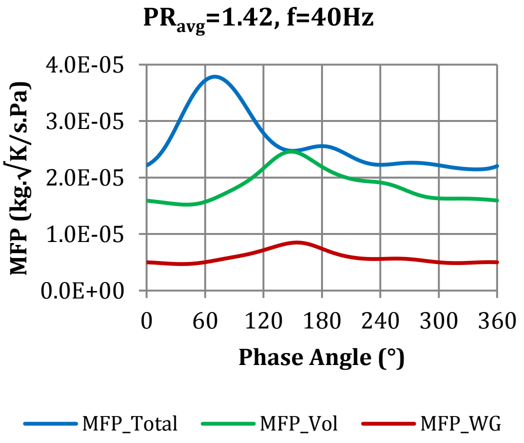
PR_{avg}=1.42, f=40Hz

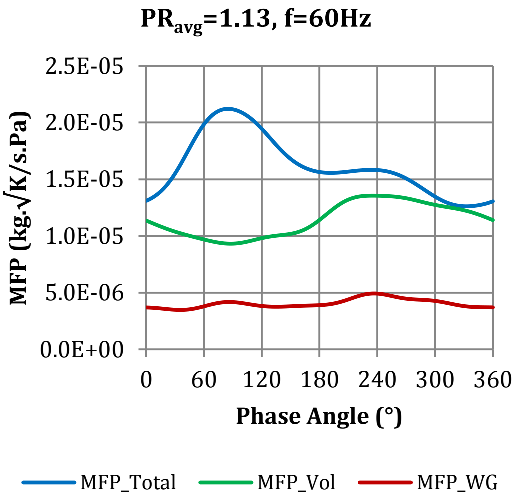

PR_{avg}=1.13, f=60Hz

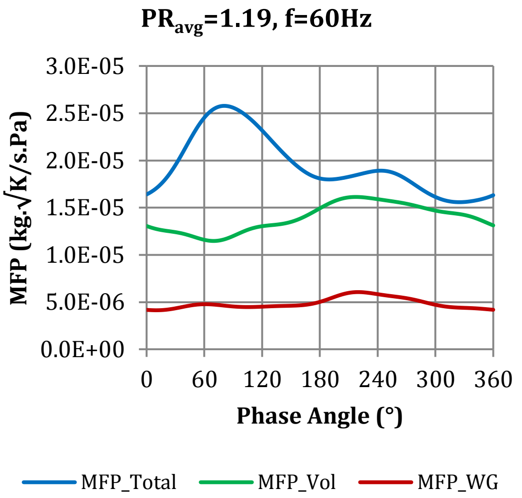

PR_{avg}=1.19, f=60Hz

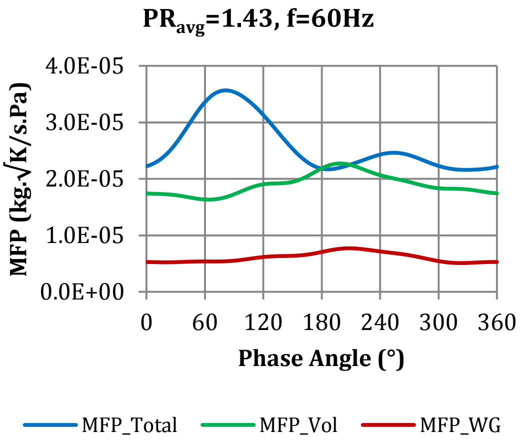

PR_{avg}=1.43, f=60Hz

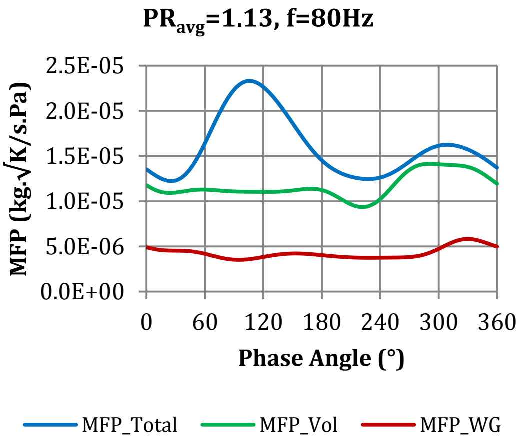

PR_{avg}=1.13, f=80Hz

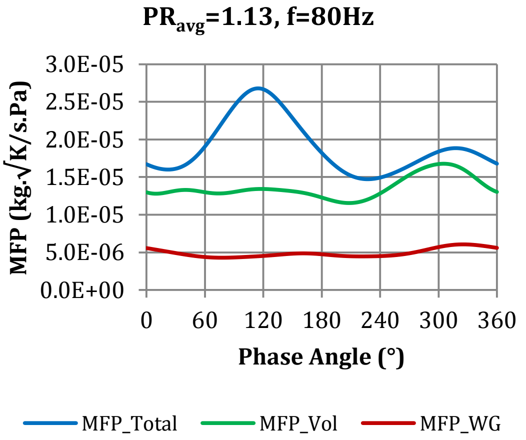

PR_{avg}=1.13, f=80Hz

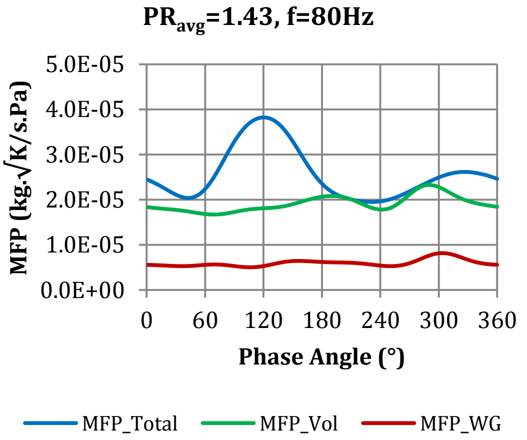

PR_{avg}=1.43, f=80Hz

C2. Instantaneous static pressure (P_s) measurements

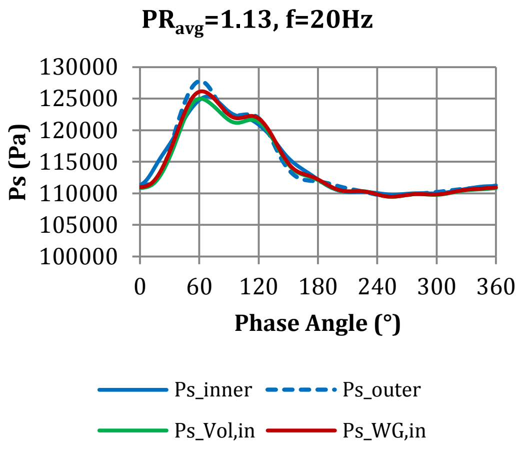

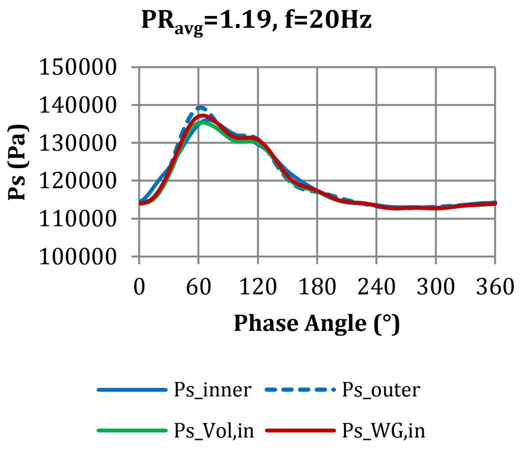

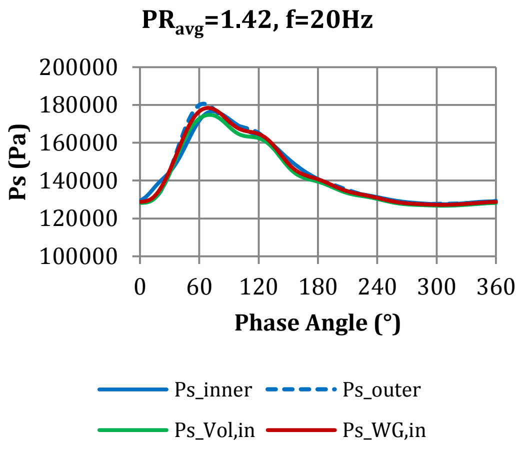

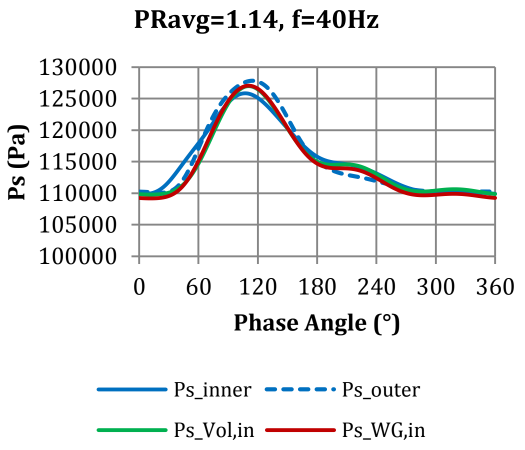

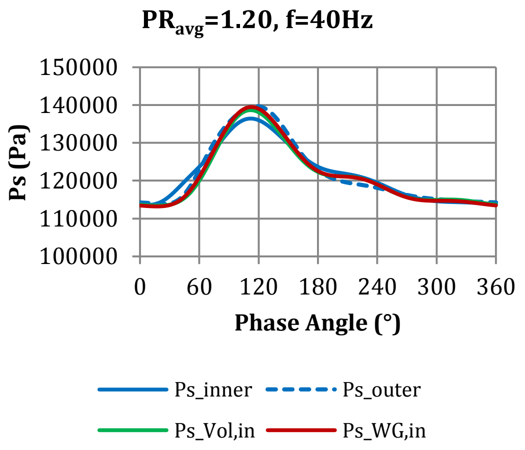

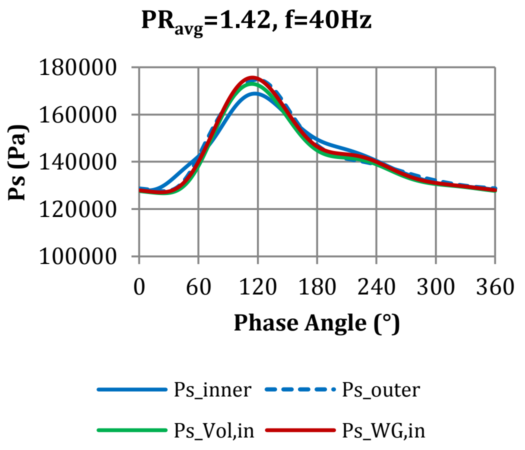

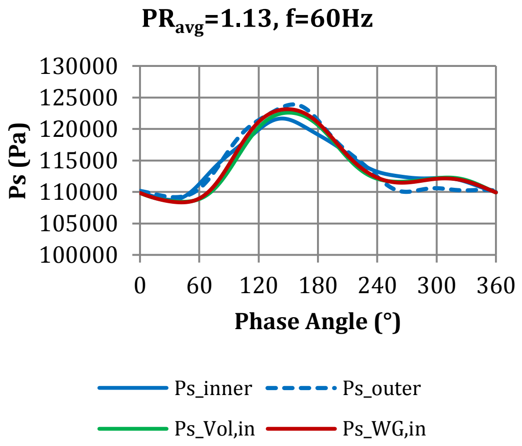
PR_{avg}=1.13, f=60Hz
Ps (Pa)
130000
125000
120000
115000
110000
105000
100000
0
60
120
180
240
300
360
Phase Angle (°)
Ps_inner
Ps_outer
Ps_Vol,in
Ps_WG,in

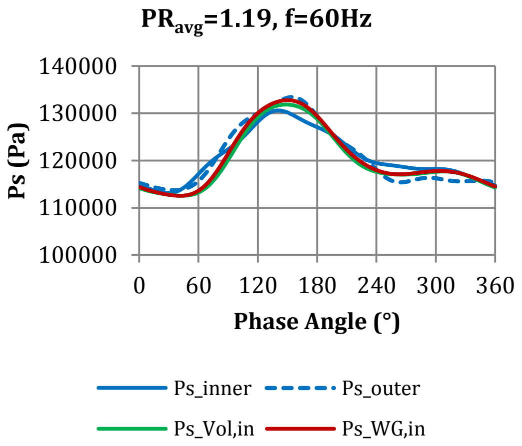
PR_{avg}=1.19, f=60Hz
Ps (Pa)
140000
130000
120000
110000
100000
0
60
120
180
240
300
360
Phase Angle (°)
Ps_inner
Ps_outer
Ps_Vol,in
Ps_WG,in

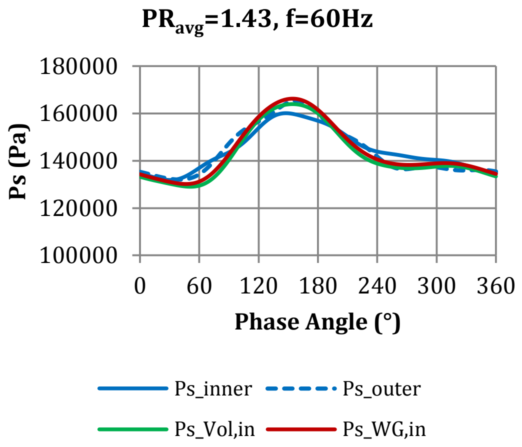
PR_{avg}=1.43, f=60Hz
Ps (Pa)
180000
160000
140000
120000
100000
0
60
120
180
240
300
360
Phase Angle (°)
Ps_inner
Ps_outer
Ps_Vol,in
Ps_WG,in

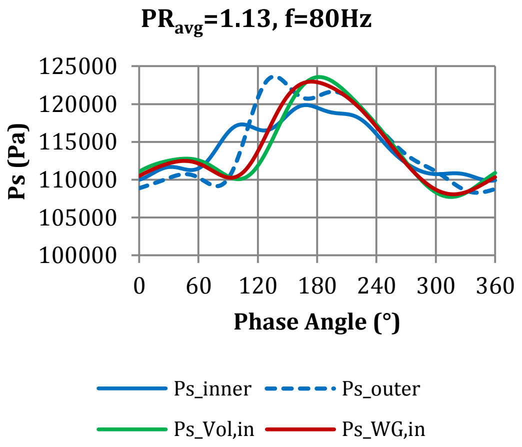
PR_{avg}=1.13, f=80Hz
Ps (Pa)
125000
120000
115000
110000
105000
100000
0
60
120
180
240
300
360
Phase Angle (°)
Ps_inner
Ps_outer
Ps_Vol,in
Ps_WG,in

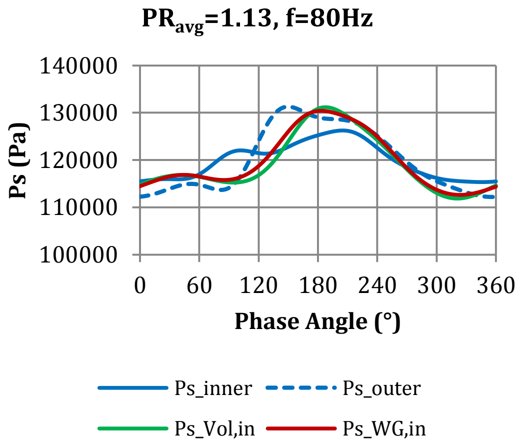
PR_{avg}=1.13, f=80Hz
Ps (Pa)
140000
130000
120000
110000
100000
0
60
120
180
240
300
360
Phase Angle (°)
Ps_inner
Ps_outer
Ps_Vol,in
Ps_WG,in

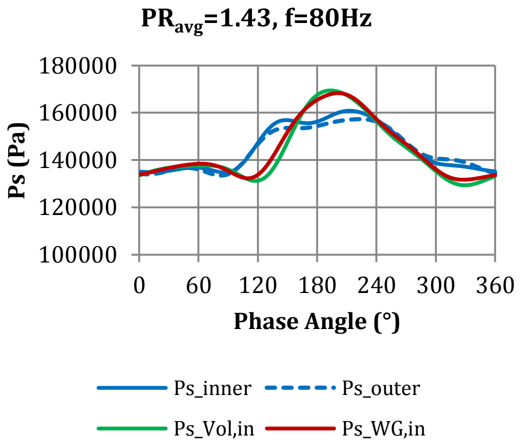
PR_{avg}=1.43, f=80Hz
Ps (Pa)
180000
160000
140000
120000
100000
0
60
120
180
240
300
360
Phase Angle (°)
Ps_inner
Ps_outer
Ps_Vol,in
Ps_WG,in

C3. Instantaneous torque measurements

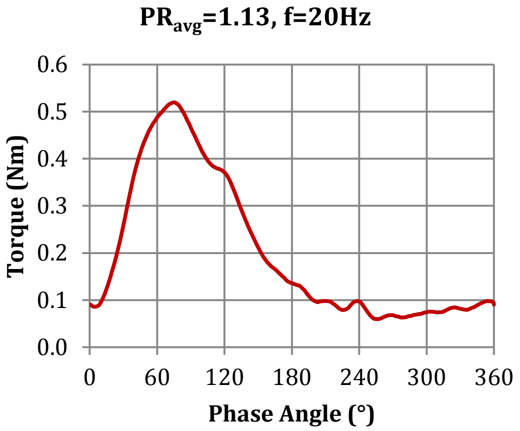
PR_{avg}=1.13, f=20Hz

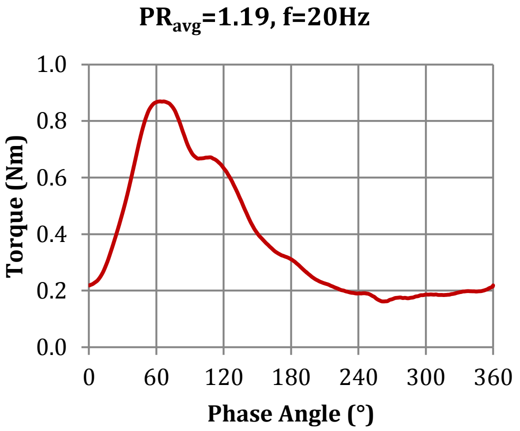
PR_{avg}=1.19, f=20Hz

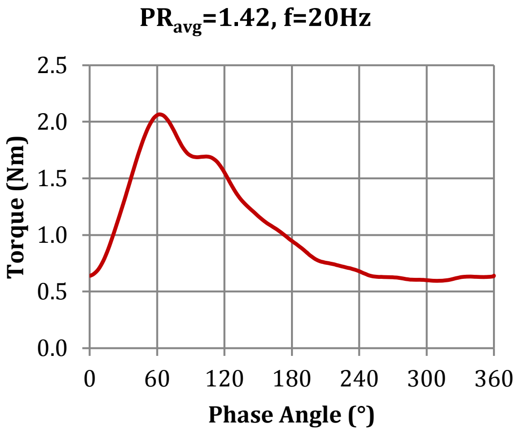
PR_{avg}=1.42, f=20Hz

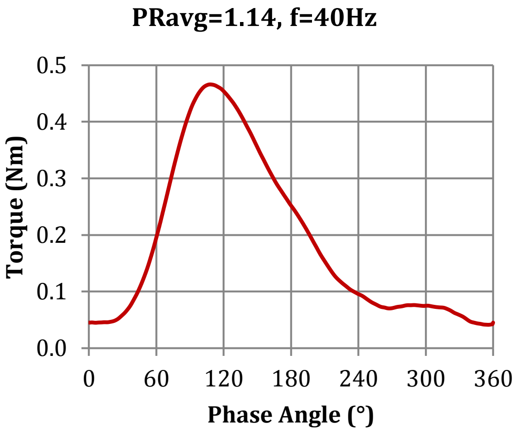
PRavg=1.14, f=40Hz

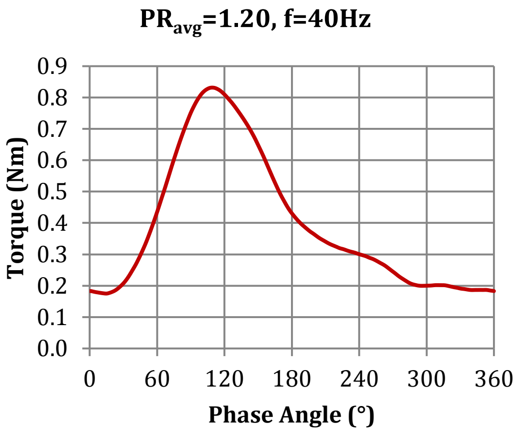
PR_{avg}=1.20, f=40Hz

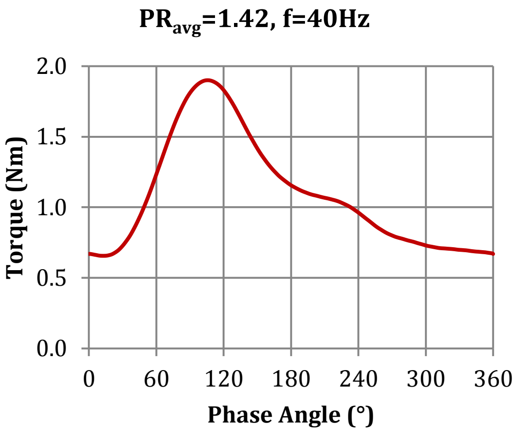
PR_{avg}=1.42, f=40Hz

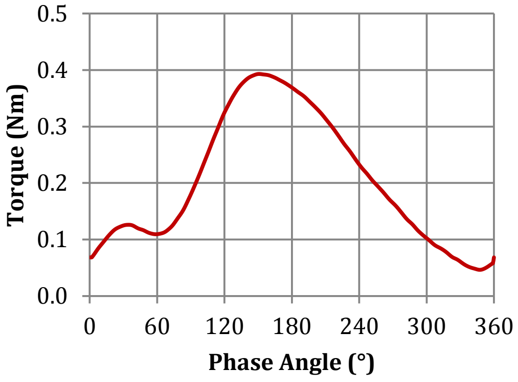

PR_{avg}=1.13, f=60Hz

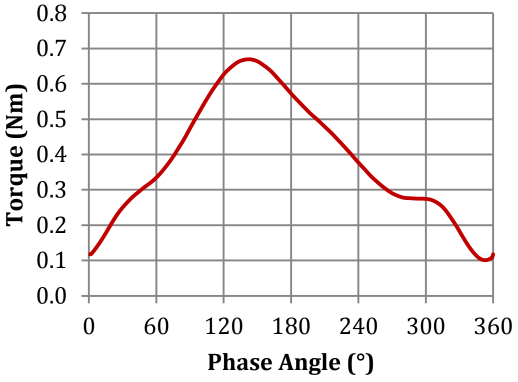

PR_{avg}=1.19, f=60Hz

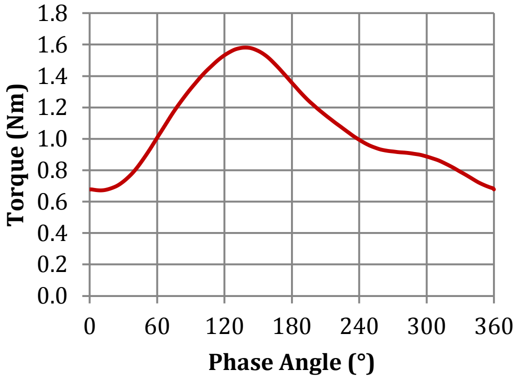

PR_{avg}=1.43, f=60Hz

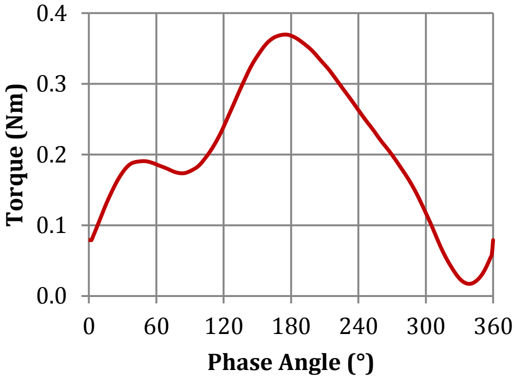

PR_{avg}=1.13, f=80Hz

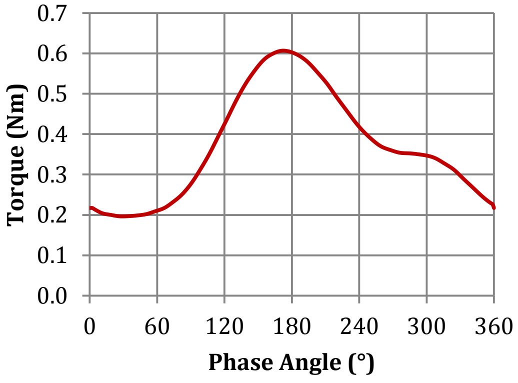

PR_{avg}=1.13, f=80Hz

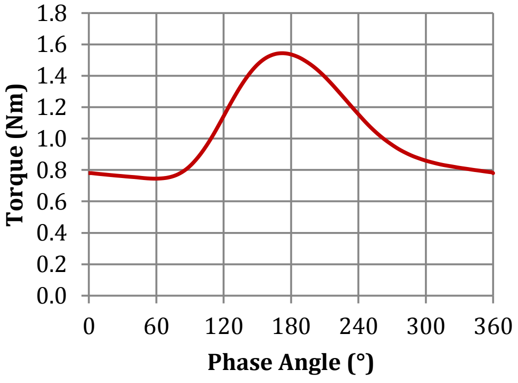

PR_{avg}=1.43, f=80Hz

C4. Instantaneous power measurements

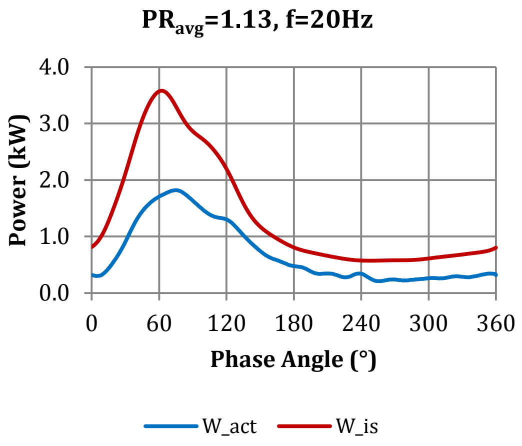
PR_{avg}=1.13, f=20Hz

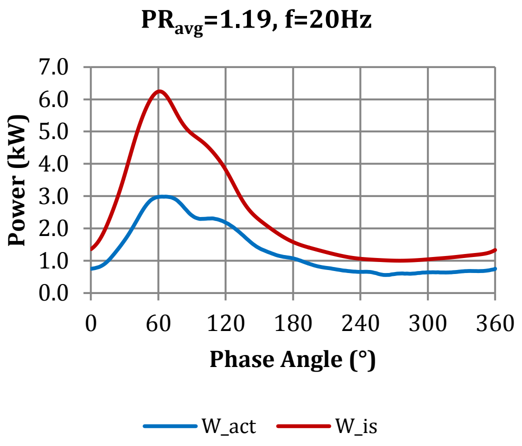
PR_{avg}=1.19, f=20Hz

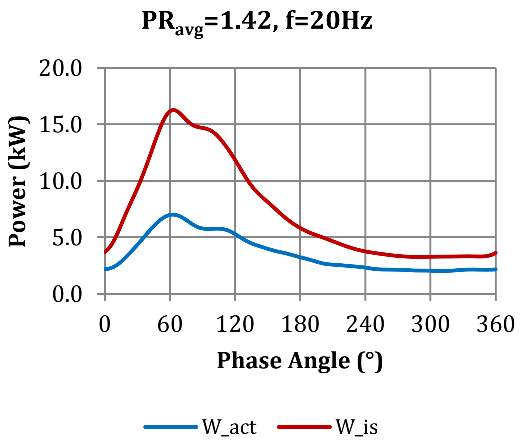
PR_{avg}=1.42, f=20Hz

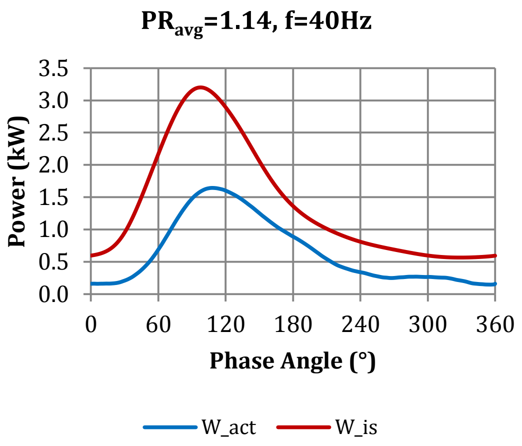
PR_{avg}=1.14, f=40Hz

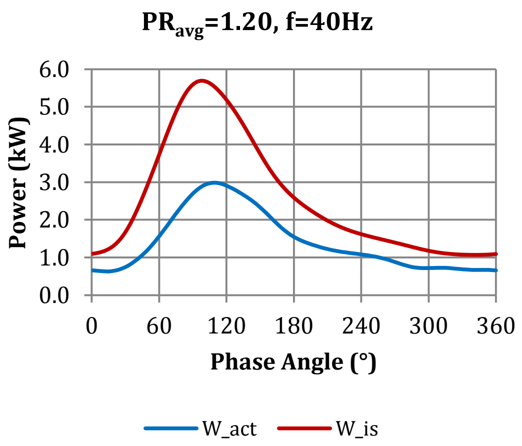
PR_{avg}=1.20, f=40Hz

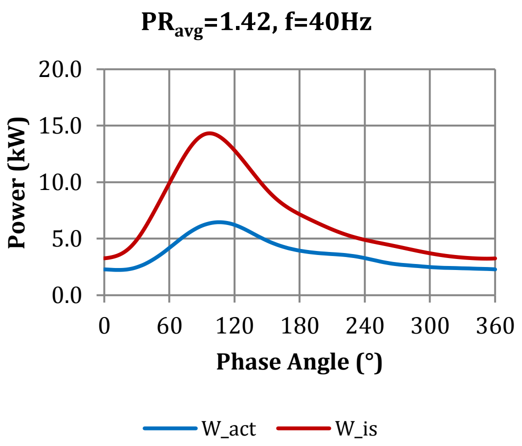
PR_{avg}=1.42, f=40Hz

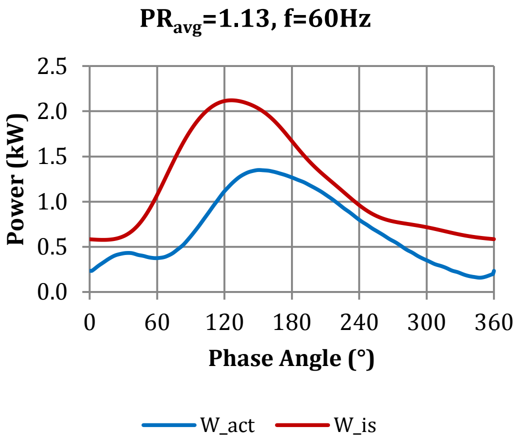
PR$_{avg}$=1.13, f=60Hz

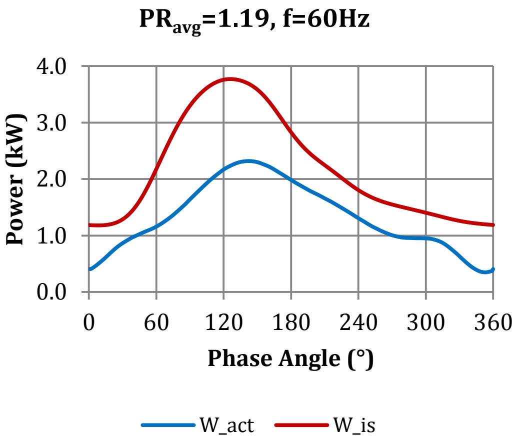
PR$_{avg}$=1.19, f=60Hz

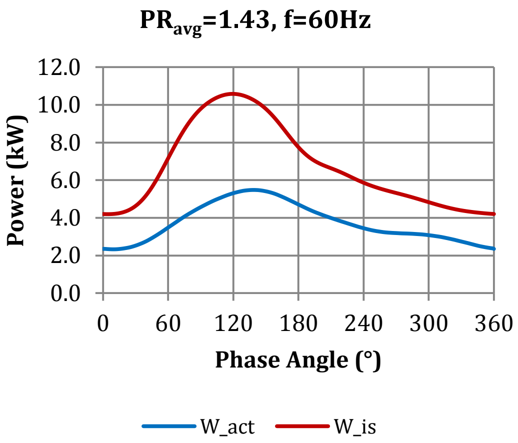
PR$_{avg}$=1.43, f=60Hz

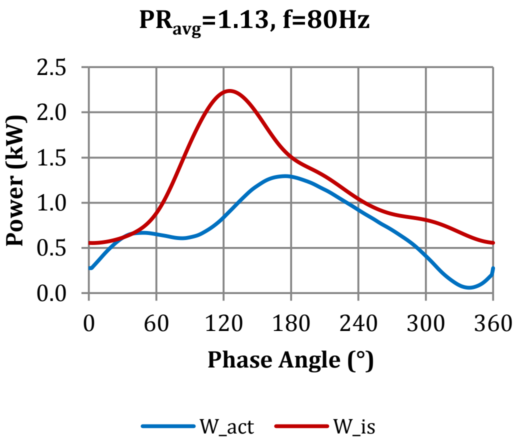
PR$_{avg}$=1.13, f=80Hz

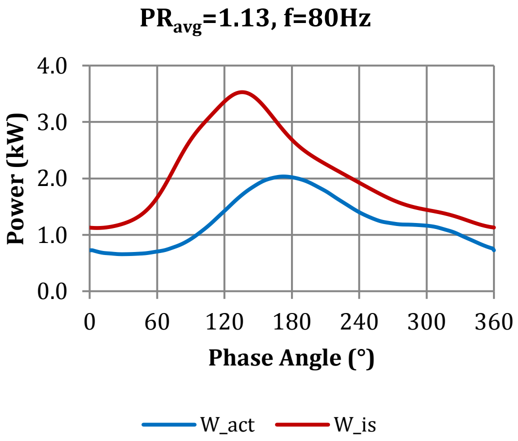
PR$_{avg}$=1.13, f=80Hz

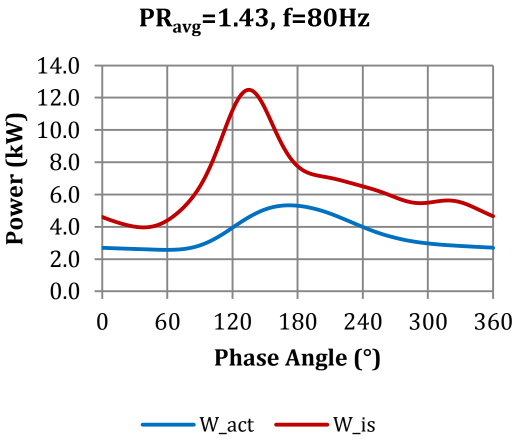
PR$_{avg}$=1.43, f=80Hz

APPENDIX D

UNSTEADY FLOW EXPERIMENTS $(N/\sqrt{T_0} = 1850\ \text{RPM}/\sqrt{K},\ l_{WG} = 3\ \text{mm})$

D1. Instantaneous mass flow parameter (MFP) measurements

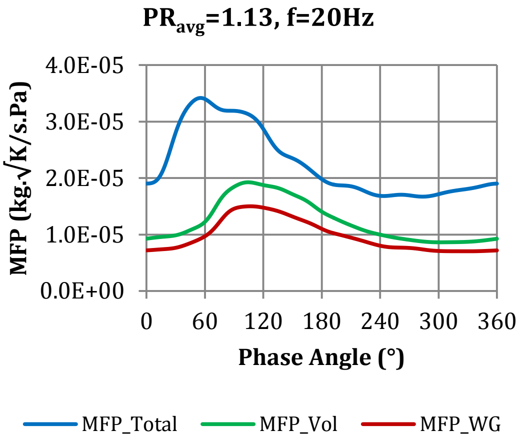

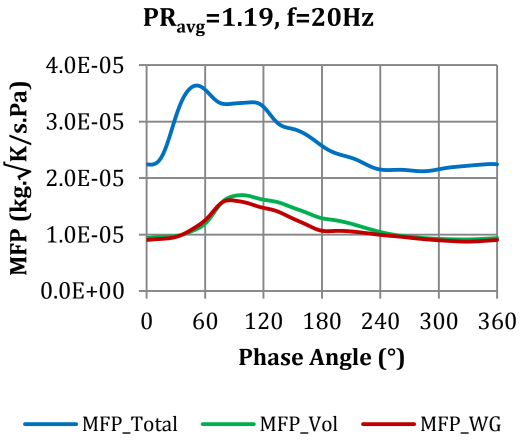

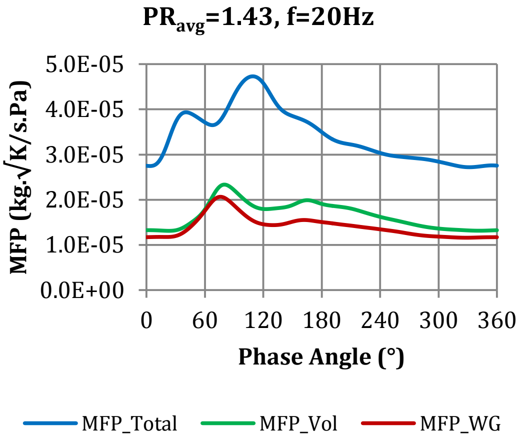

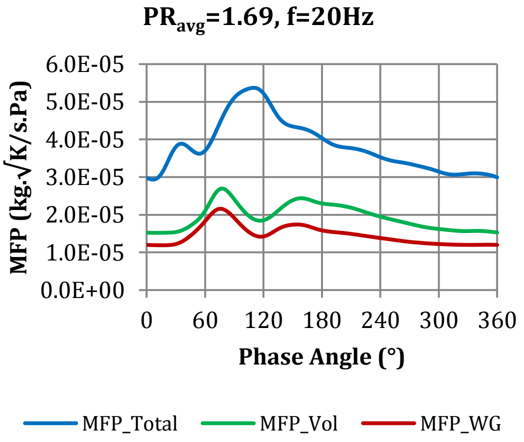

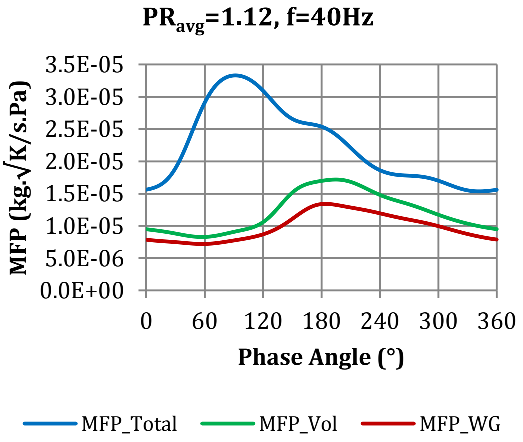

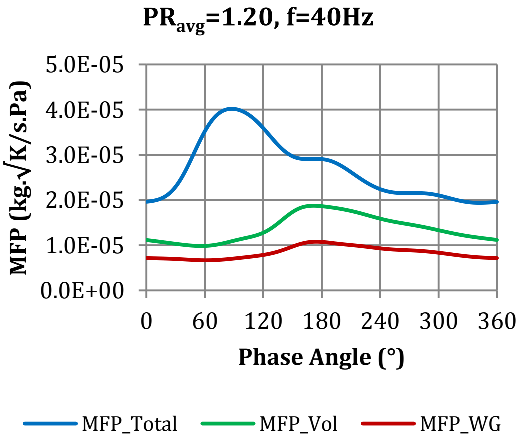

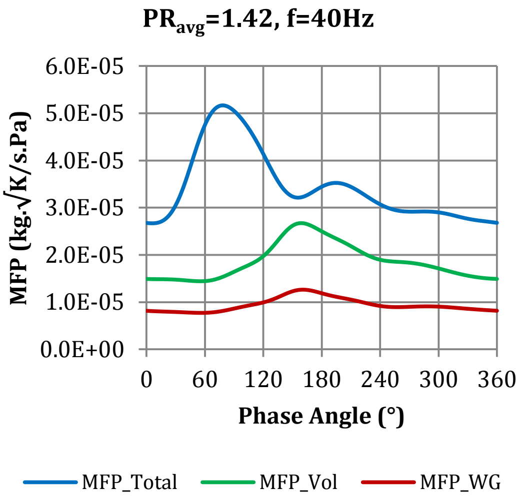
PR$_{avg}$=1.42, f=40Hz

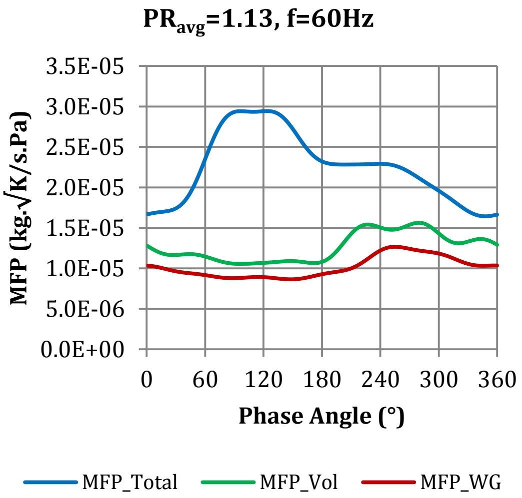
PR$_{avg}$=1.13, f=60Hz

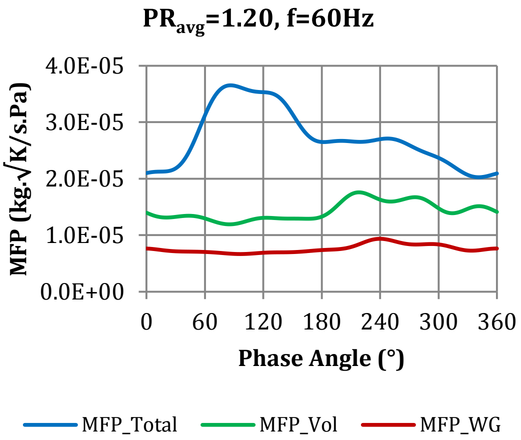
PR$_{avg}$=1.20, f=60Hz

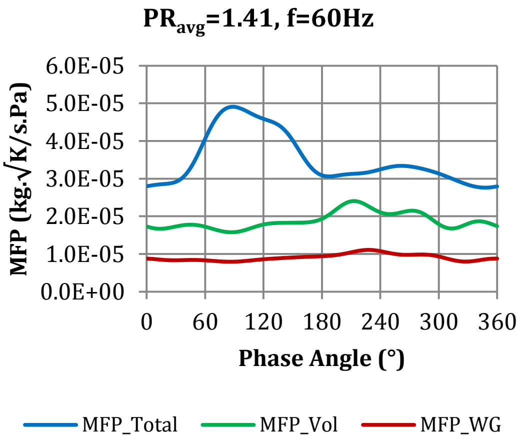
PR$_{avg}$=1.41, f=60Hz

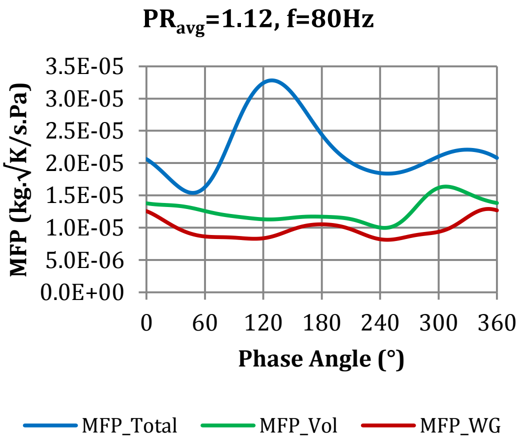
PR$_{avg}$=1.12, f=80Hz

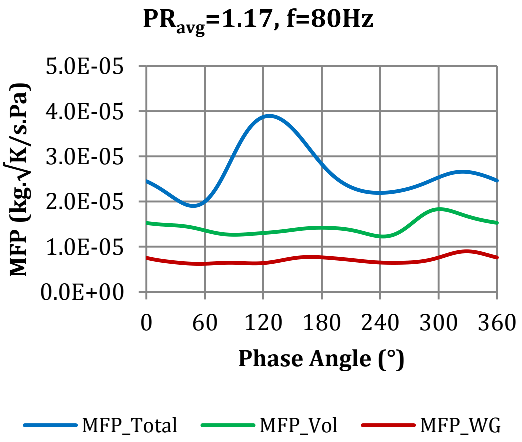
PR$_{avg}$=1.17, f=80Hz

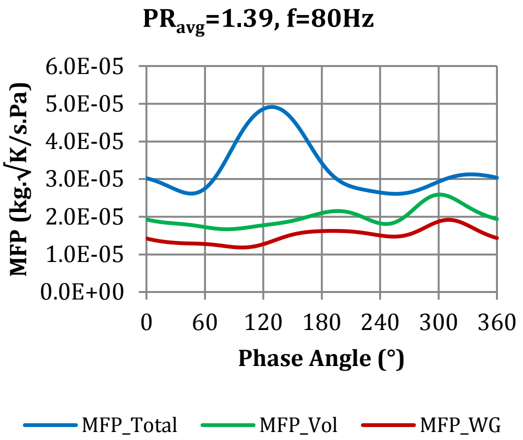

D2. Instantaneous static pressure (P_s) measurements

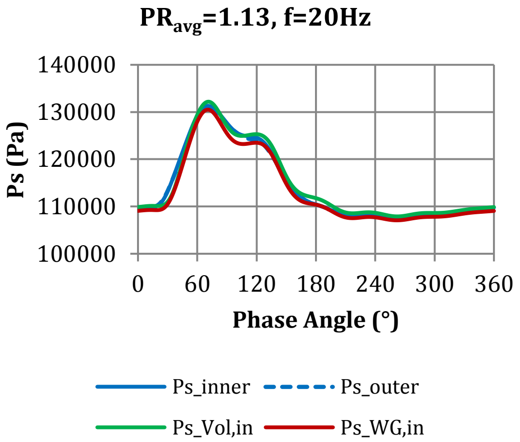

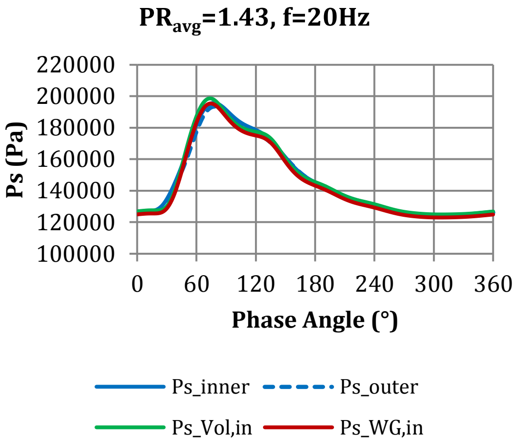

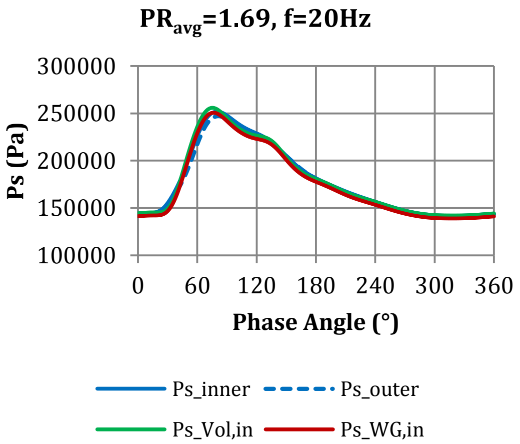

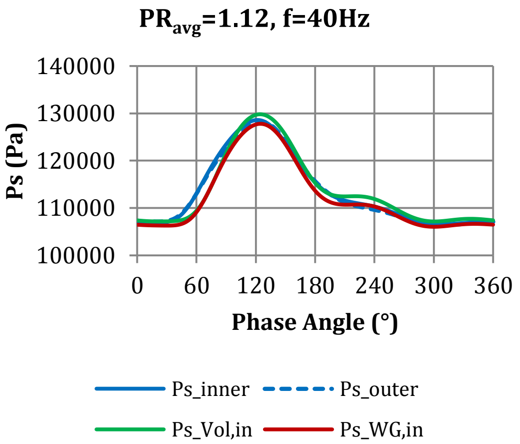

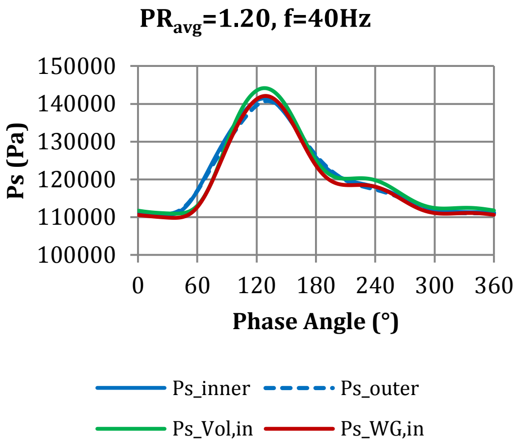
PRavg=1.20, f=40Hz
Ps (Pa)
150000
140000
130000
120000
110000
100000
0
60
120
180
240
300
360
Phase Angle (°)
Ps_inner
Ps_outer
Ps_Vol,in
Ps_WG,in

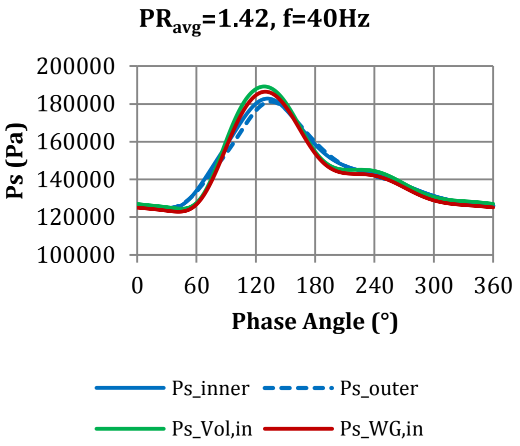
PRavg=1.42, f=40Hz
Ps (Pa)
200000
180000
160000
140000
120000
100000
0
60
120
180
240
300
360
Phase Angle (°)
Ps_inner
Ps_outer
Ps_Vol,in
Ps_WG,in

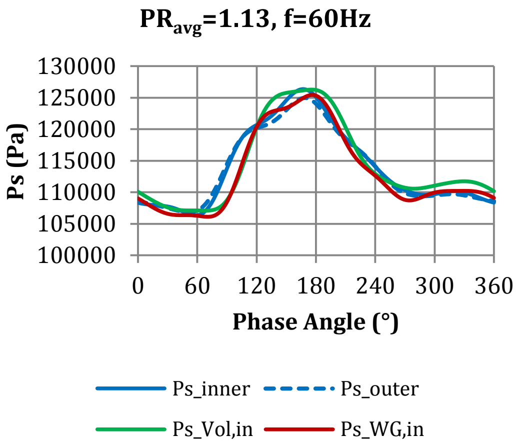
PRavg=1.13, f=60Hz
Ps (Pa)
130000
125000
120000
115000
110000
105000
100000
0
60
120
180
240
300
360
Phase Angle (°)
Ps_inner
Ps_outer
Ps_Vol,in
Ps_WG,in

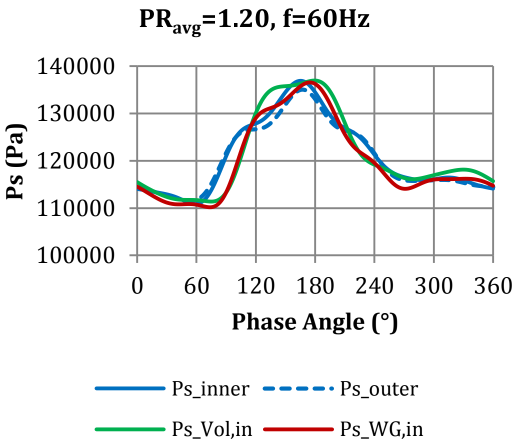
PRavg=1.20, f=60Hz
Ps (Pa)
140000
130000
120000
110000
100000
0
60
120
180
240
300
360
Phase Angle (°)
Ps_inner
Ps_outer
Ps_Vol,in
Ps_WG,in

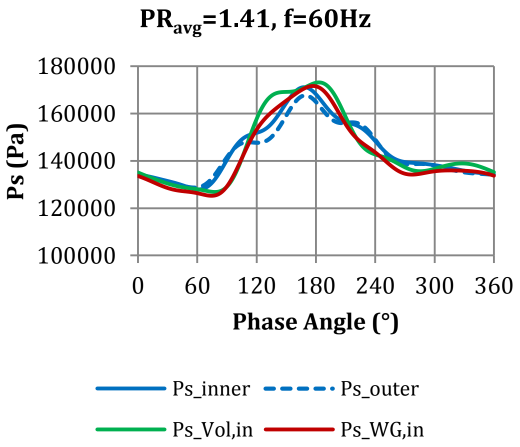
PRavg=1.41, f=60Hz
Ps (Pa)
180000
160000
140000
120000
100000
0
60
120
180
240
300
360
Phase Angle (°)
Ps_inner
Ps_outer
Ps_Vol,in
Ps_WG,in

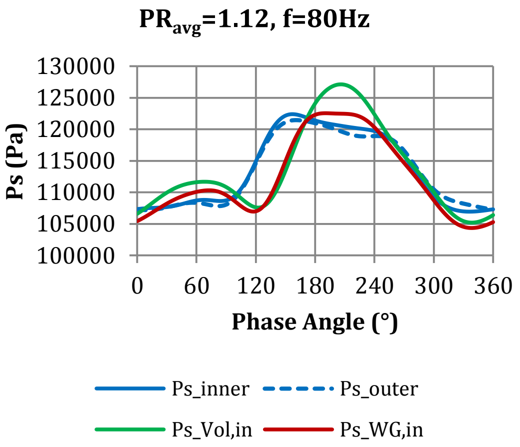
PRavg=1.12, f=80Hz
Ps (Pa)
130000
125000
120000
115000
110000
105000
100000
0
60
120
180
240
300
360
Phase Angle (°)
Ps_inner
Ps_outer
Ps_Vol,in
Ps_WG,in

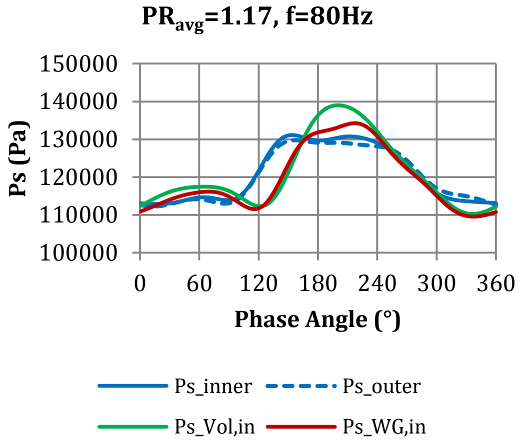
PR$_{avg}$=1.17, f=80Hz

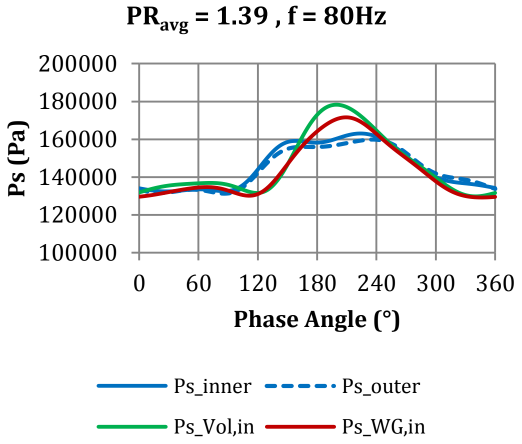
PR$_{avg}$ = 1.39 , f = 80Hz

D3. Instantaneous torque measurements

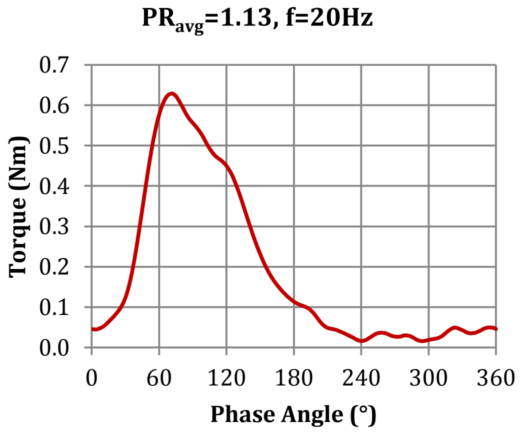
PR$_{avg}$=1.13, f=20Hz

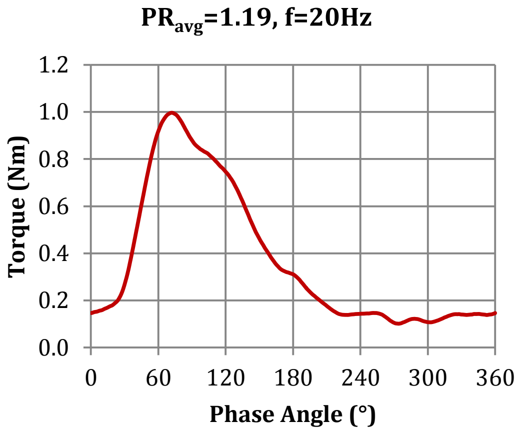
PR$_{avg}$=1.19, f=20Hz

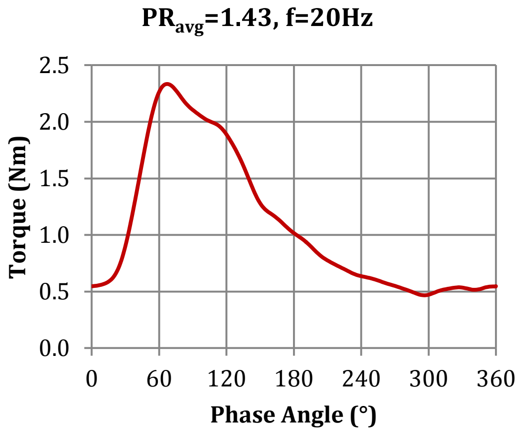
PR$_{avg}$=1.43, f=20Hz

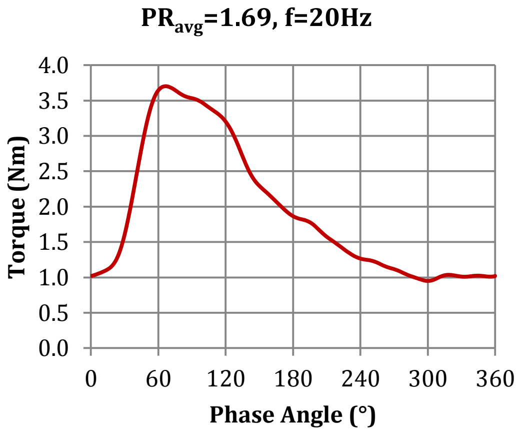
PR$_{avg}$=1.69, f=20Hz

PR_{avg}=1.12, f=40Hz

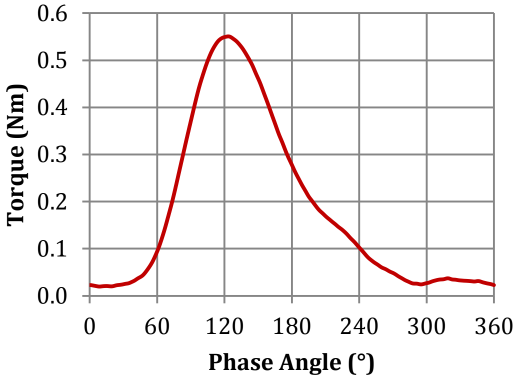

PR_{avg}=1.20, f=40Hz

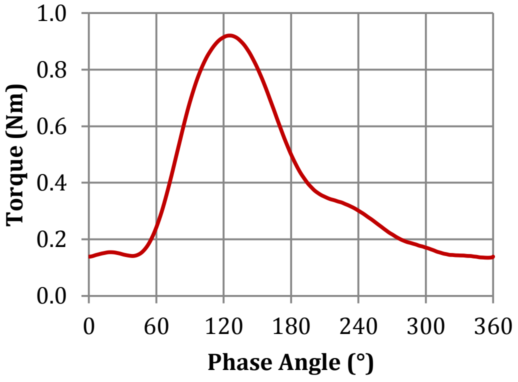

PR_{avg}=1.42, f=40Hz

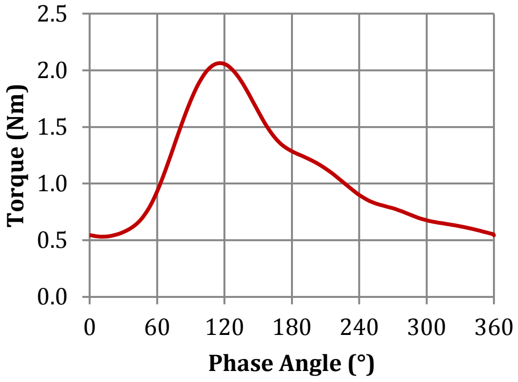

PR_{avg}=1.13, f=60Hz

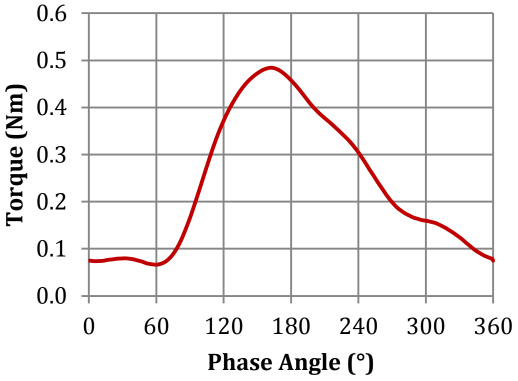

PR_{avg}=1.20, f=60Hz

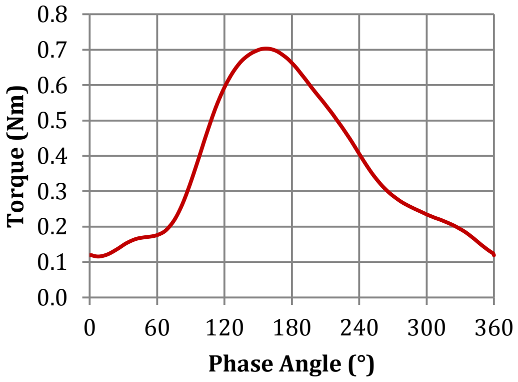

PR_{avg}=1.41, f=60Hz

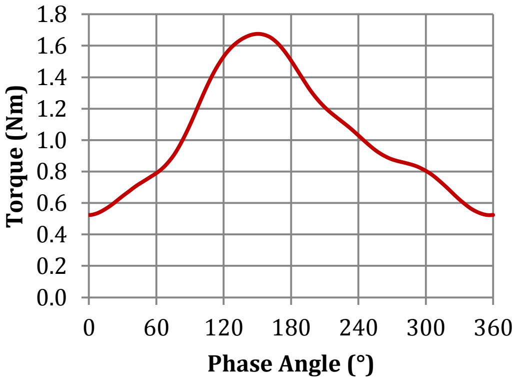

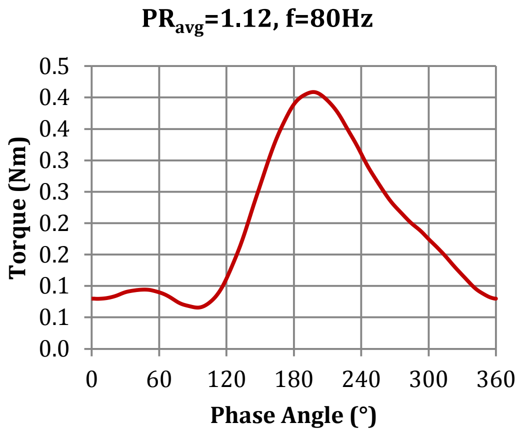

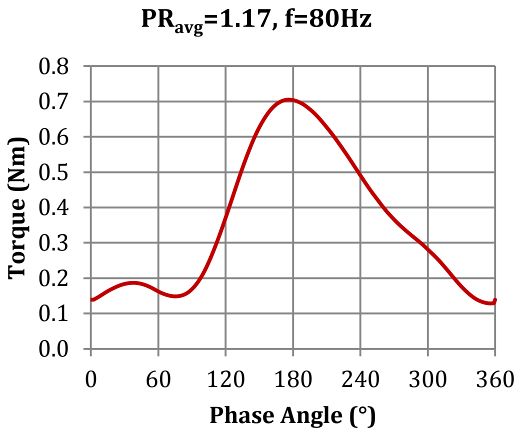

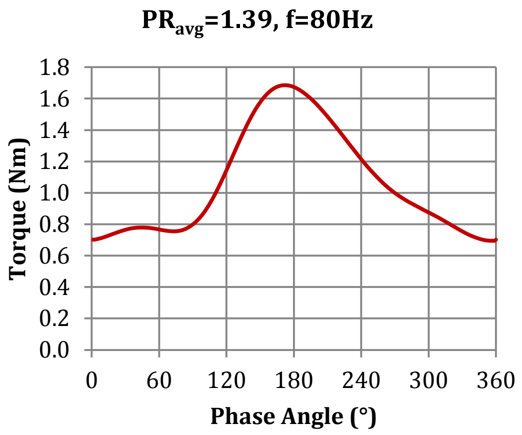

D4. Instantaneous power measurements

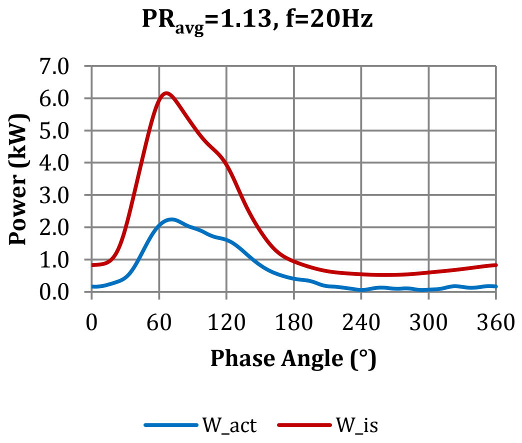

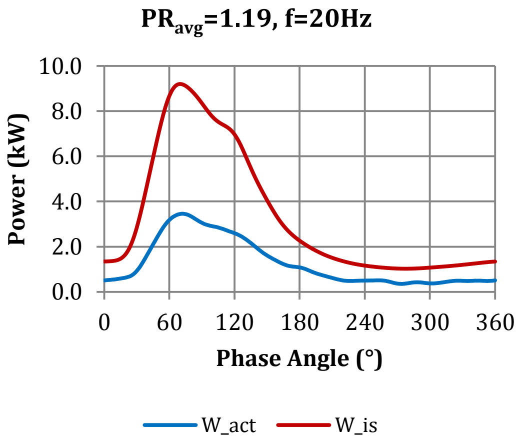

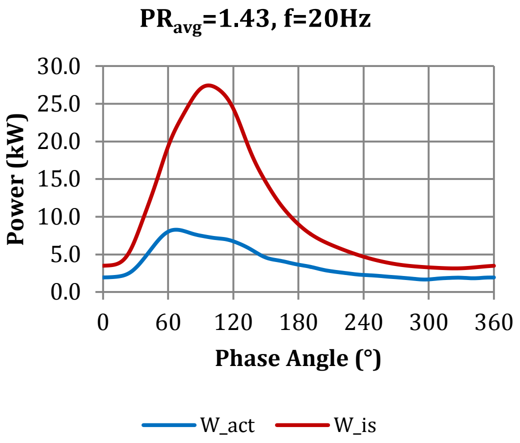
PR_{avg}=1.43, f=20Hz
Power (kW)
30.0
25.0
20.0
15.0
10.0
5.0
0.0
0
60
120
180
240
300
360
Phase Angle (°)
W_act
W_is

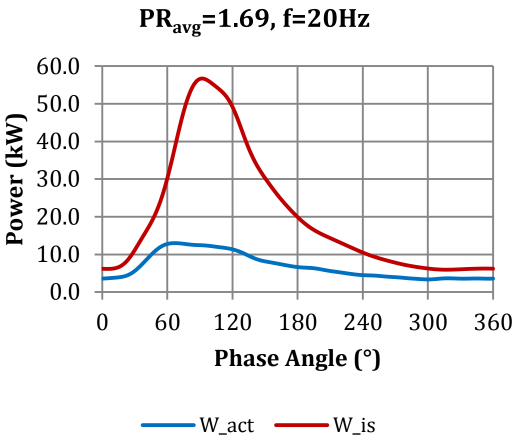
PR_{avg}=1.69, f=20Hz
Power (kW)
60.0
50.0
40.0
30.0
20.0
10.0
0.0
0
60
120
180
240
300
360
Phase Angle (°)
W_act
W_is

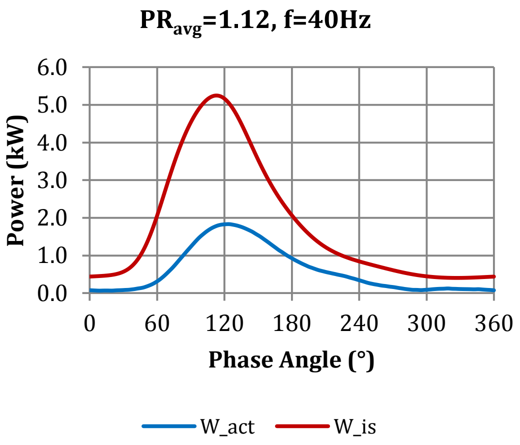
PR_{avg}=1.12, f=40Hz
Power (kW)
6.0
5.0
4.0
3.0
2.0
1.0
0.0
0
60
120
180
240
300
360
Phase Angle (°)
W_act
W_is

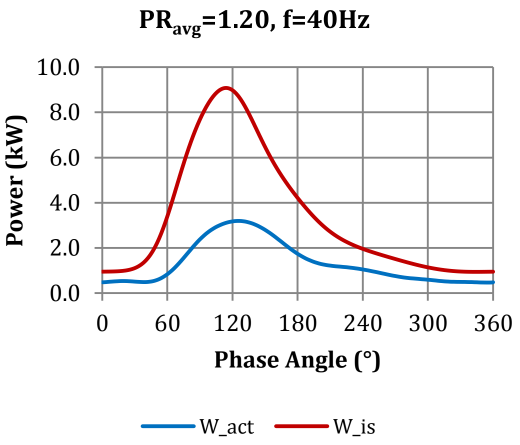
PR_{avg}=1.20, f=40Hz
Power (kW)
10.0
8.0
6.0
4.0
2.0
0.0
0
60
120
180
240
300
360
Phase Angle (°)
W_act
W_is

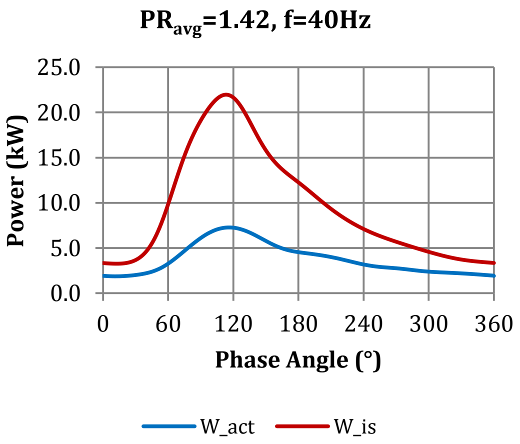
PR_{avg}=1.42, f=40Hz
Power (kW)
25.0
20.0
15.0
10.0
5.0
0.0
0
60
120
180
240
300
360
Phase Angle (°)
W_act
W_is

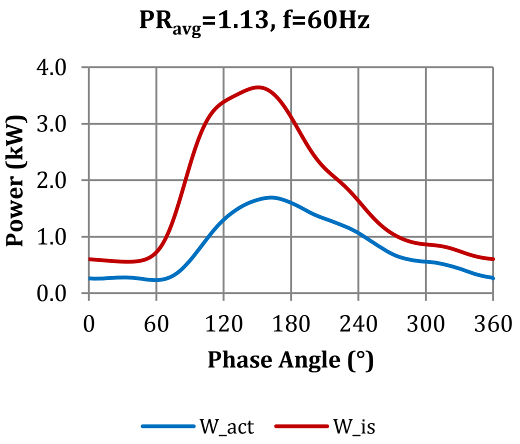
PR_{avg}=1.13, f=60Hz
Power (kW)
4.0
3.0
2.0
1.0
0.0
0
60
120
180
240
300
360
Phase Angle (°)
W_act
W_is

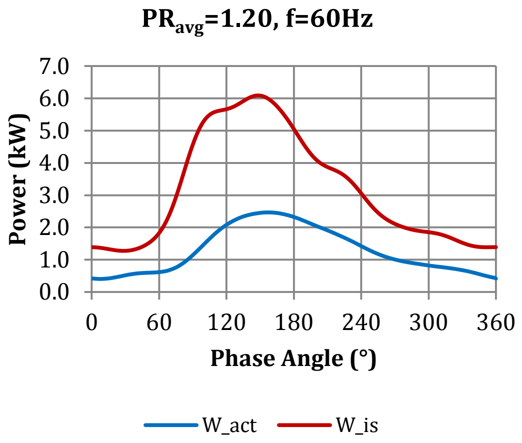
PR_{avg}=1.20, f=60Hz
Power (kW)
7.0
6.0
5.0
4.0
3.0
2.0
1.0
0.0
0
60
120
180
240
300
360
Phase Angle (°)
W_act
W_is

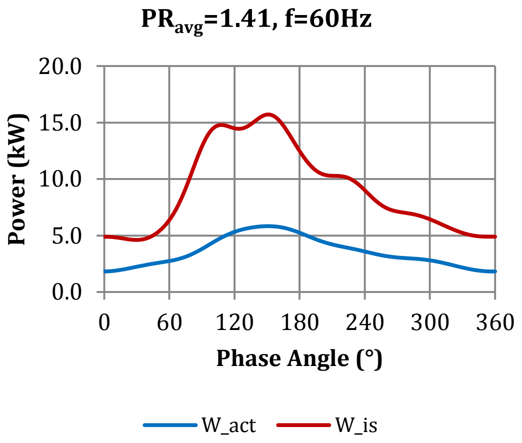
PR_{avg}=1.41, f=60Hz
Power (kW)
20.0
15.0
10.0
5.0
0.0
0
60
120
180
240
300
360
Phase Angle (°)
W_act
W_is

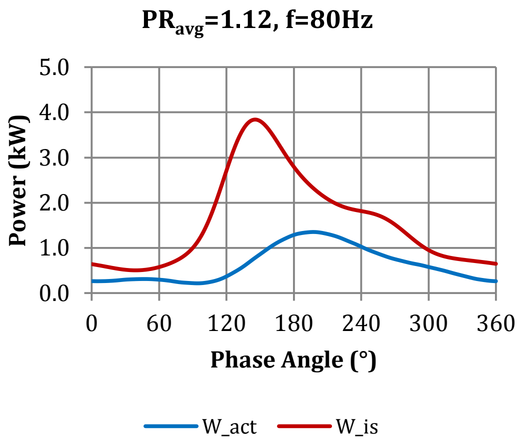
PR_{avg}=1.12, f=80Hz
Power (kW)
5.0
4.0
3.0
2.0
1.0
0.0
0
60
120
180
240
300
360
Phase Angle (°)
W_act
W_is

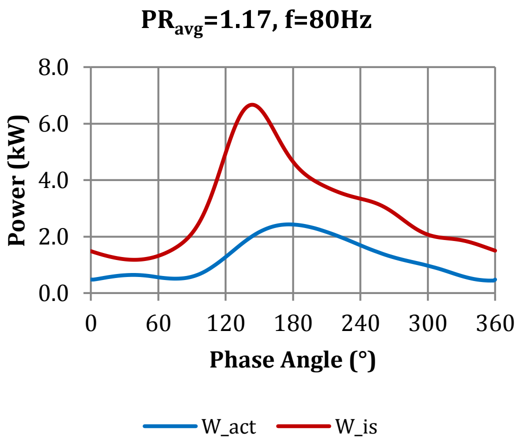
PR_{avg}=1.17, f=80Hz
Power (kW)
8.0
6.0
4.0
2.0
0.0
0
60
120
180
240
300
360
Phase Angle (°)
W_act
W_is

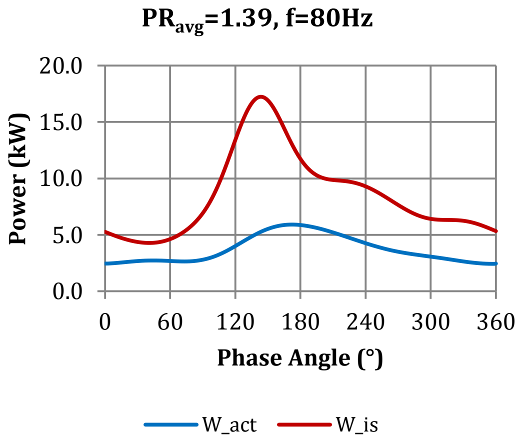
PR_{avg}=1.39, f=80Hz
Power (kW)
20.0
15.0
10.0
5.0
0.0
0
60
120
180
240
300
360
Phase Angle (°)
W_act
W_is

APPENDIX E

UNSTEADY FLOW EXPERIMENTS ($N/\sqrt{T_0}$ = 1850 RPM/$\sqrt{K}$, l_{WG} = 5 mm)

E1. Instantaneous mass flow parameter (MFP) measurements

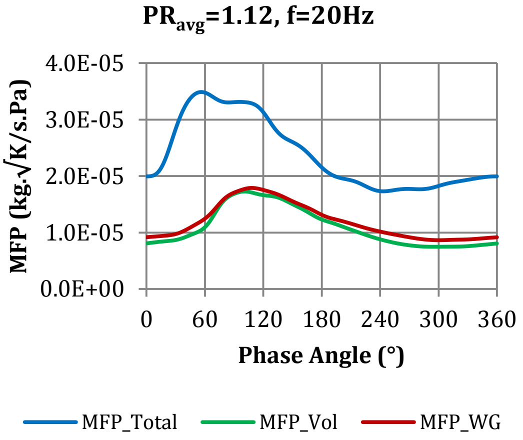
PR_{avg}=1.12, f=20Hz

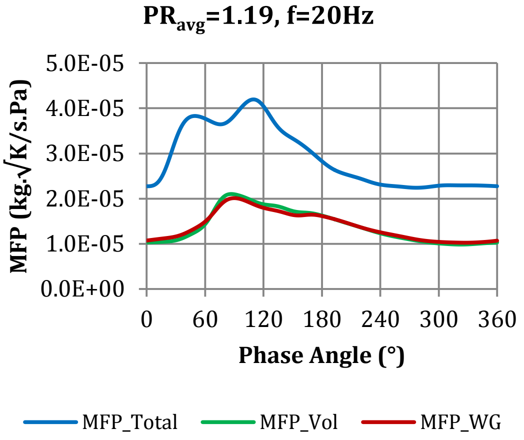
PR_{avg}=1.19, f=20Hz

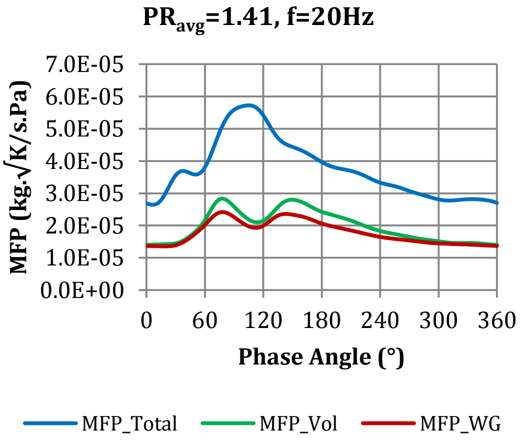
PR_{avg}=1.41, f=20Hz

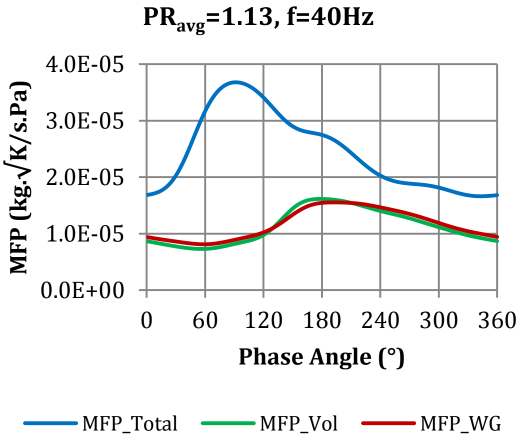
PR_{avg}=1.13, f=40Hz

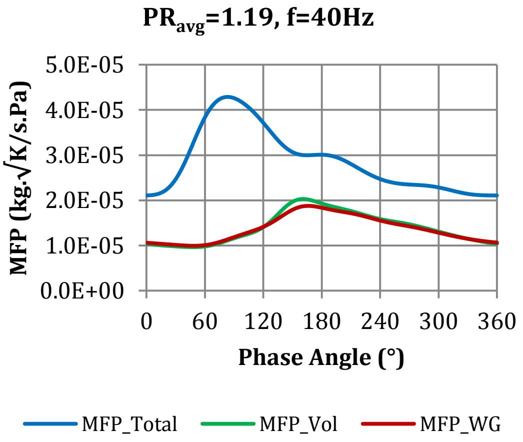
PR_{avg}=1.19, f=40Hz

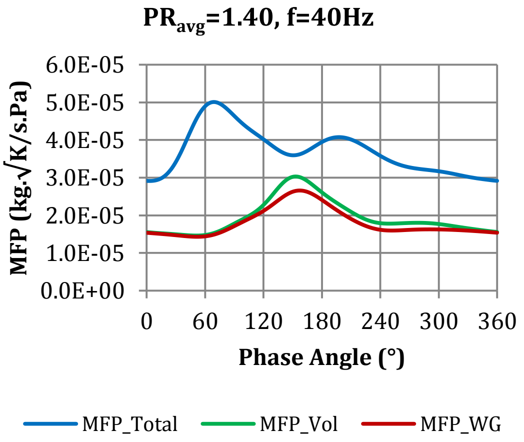
PR_{avg}=1.40, f=40Hz

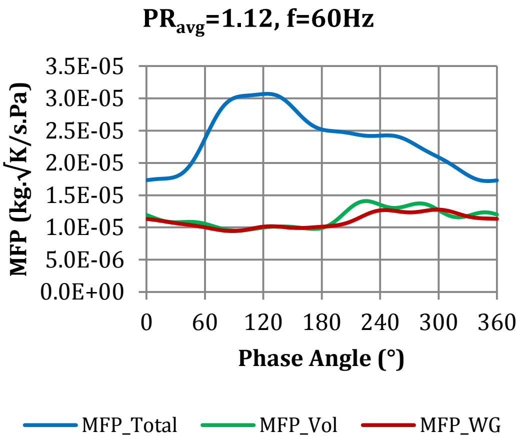
PR$_{avg}$=1.12, f=60Hz
MFP (kg.√K/s.Pa)
3.5E-05
3.0E-05
2.5E-05
2.0E-05
1.5E-05
1.0E-05
5.0E-06
0.0E+00
0
60
120
180
240
300
360
Phase Angle (°)
MFP_Total
MFP_Vol
MFP_WG

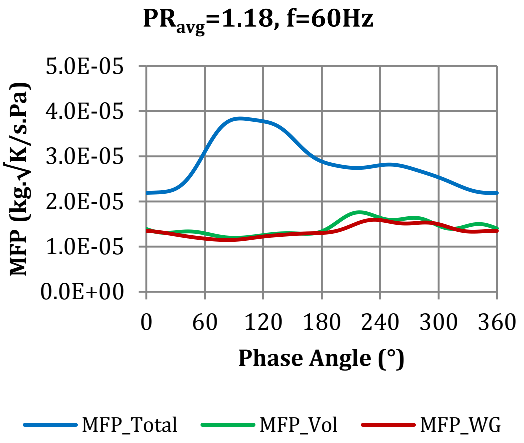
PR$_{avg}$=1.18, f=60Hz
MFP (kg.√K/s.Pa)
5.0E-05
4.0E-05
3.0E-05
2.0E-05
1.0E-05
0.0E+00
0
60
120
180
240
300
360
Phase Angle (°)
MFP_Total
MFP_Vol
MFP_WG

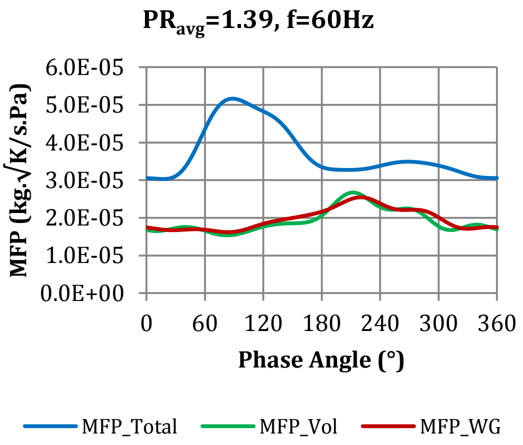
PR$_{avg}$=1.39, f=60Hz
MFP (kg.√K/s.Pa)
6.0E-05
5.0E-05
4.0E-05
3.0E-05
2.0E-05
1.0E-05
0.0E+00
0
60
120
180
240
300
360
Phase Angle (°)
MFP_Total
MFP_Vol
MFP_WG

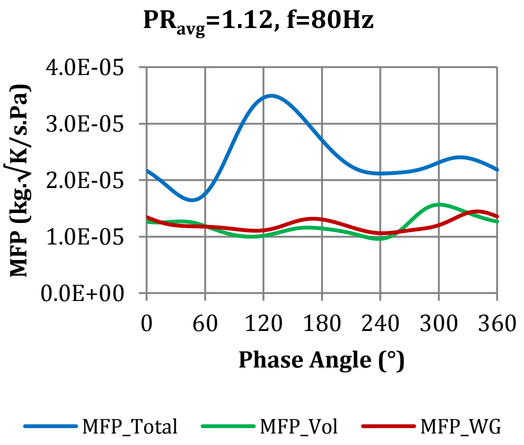
PR$_{avg}$=1.12, f=80Hz
MFP (kg.√K/s.Pa)
4.0E-05
3.0E-05
2.0E-05
1.0E-05
0.0E+00
0
60
120
180
240
300
360
Phase Angle (°)
MFP_Total
MFP_Vol
MFP_WG

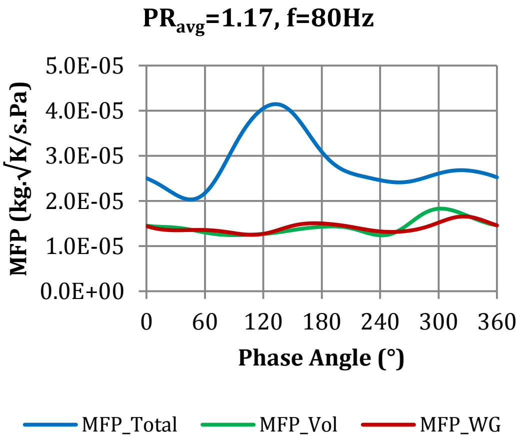
PR$_{avg}$=1.17, f=80Hz
MFP (kg.√K/s.Pa)
5.0E-05
4.0E-05
3.0E-05
2.0E-05
1.0E-05
0.0E+00
0
60
120
180
240
300
360
Phase Angle (°)
MFP_Total
MFP_Vol
MFP_WG

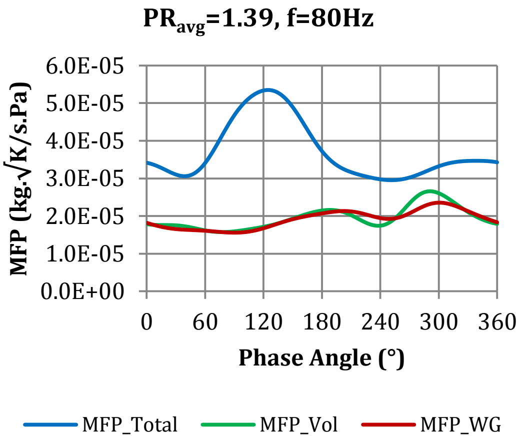
PR$_{avg}$=1.39, f=80Hz
MFP (kg.√K/s.Pa)
6.0E-05
5.0E-05
4.0E-05
3.0E-05
2.0E-05
1.0E-05
0.0E+00
0
60
120
180
240
300
360
Phase Angle (°)
MFP_Total
MFP_Vol
MFP_WG

E2. Instantaneous static pressure (P_s) measurements

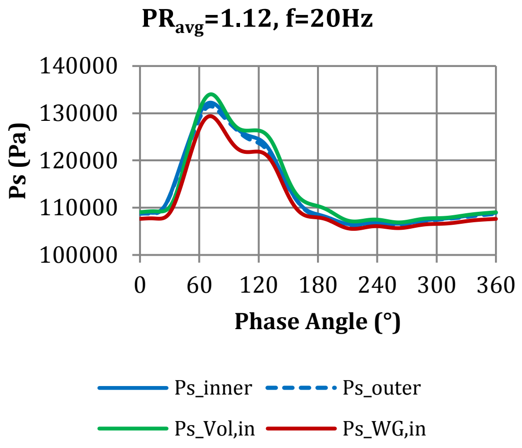
PR_{avg}=1.12, f=20Hz

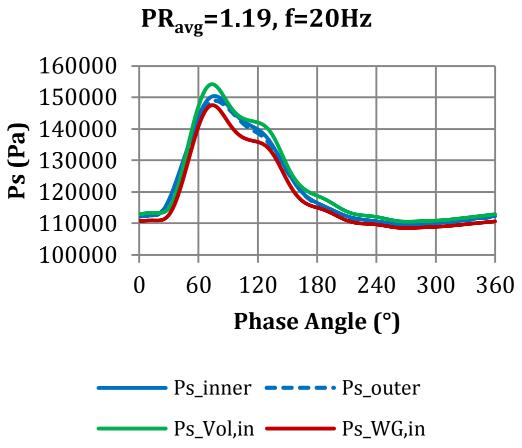
PR_{avg}=1.19, f=20Hz

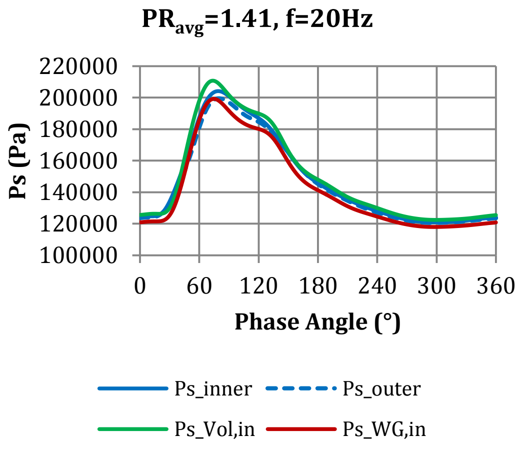
PR_{avg}=1.41, f=20Hz

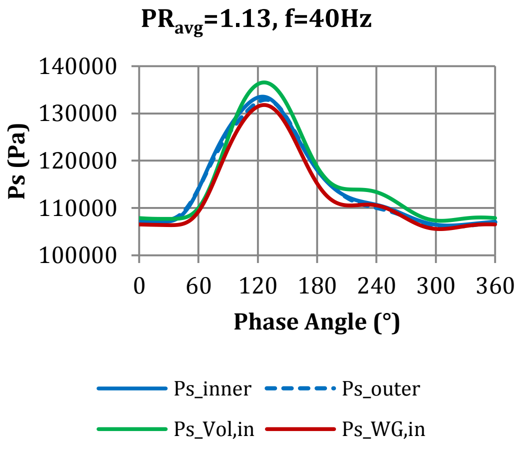
PR_{avg}=1.13, f=40Hz

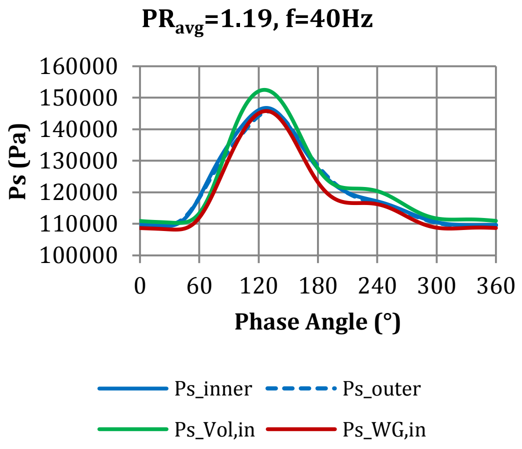
PR_{avg}=1.19, f=40Hz

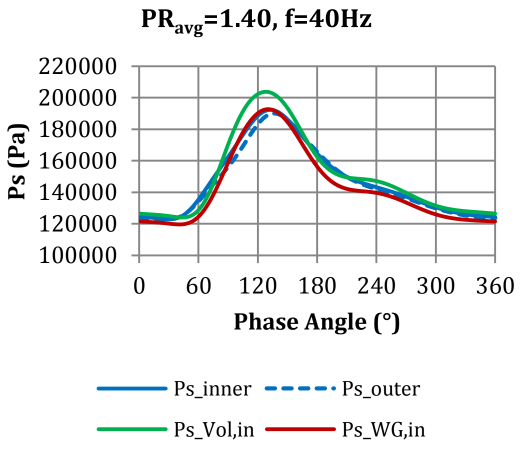
PR_{avg}=1.40, f=40Hz

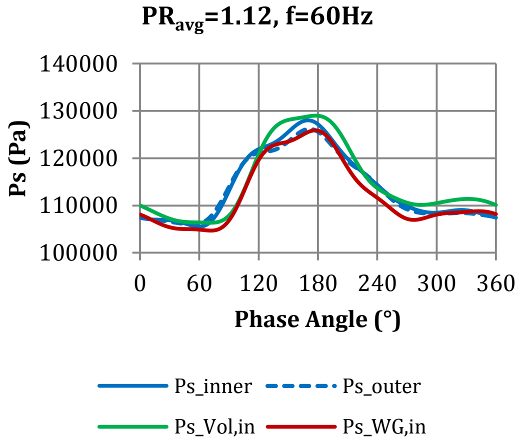
PR$_{avg}$=1.12, f=60Hz
Ps (Pa)
140000
130000
120000
110000
100000
0
60
120
180
240
300
360
Phase Angle (°)
Ps_inner
Ps_outer
Ps_Vol,in
Ps_WG,in

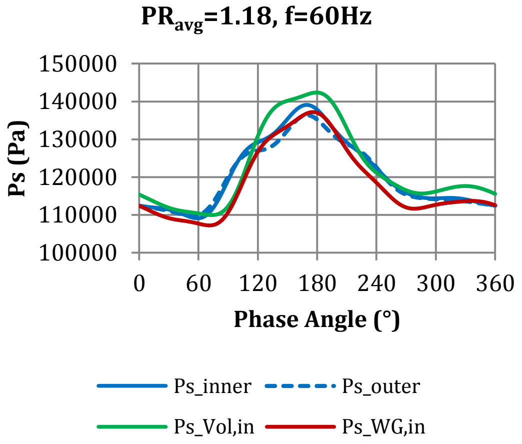
PR$_{avg}$=1.18, f=60Hz
Ps (Pa)
150000
140000
130000
120000
110000
100000
0
60
120
180
240
300
360
Phase Angle (°)
Ps_inner
Ps_outer
Ps_Vol,in
Ps_WG,in

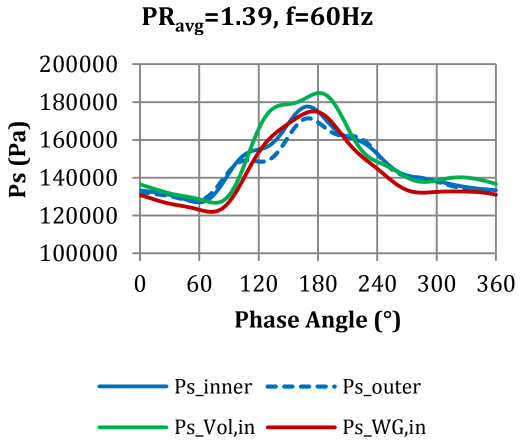
PR$_{avg}$=1.39, f=60Hz
Ps (Pa)
200000
180000
160000
140000
120000
100000
0
60
120
180
240
300
360
Phase Angle (°)
Ps_inner
Ps_outer
Ps_Vol,in
Ps_WG,in

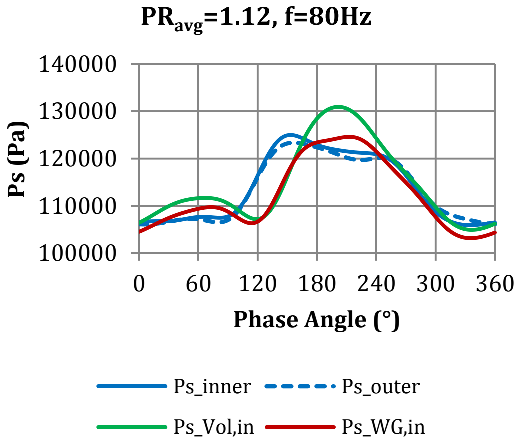
PR$_{avg}$=1.12, f=80Hz
Ps (Pa)
140000
130000
120000
110000
100000
0
60
120
180
240
300
360
Phase Angle (°)
Ps_inner
Ps_outer
Ps_Vol,in
Ps_WG,in

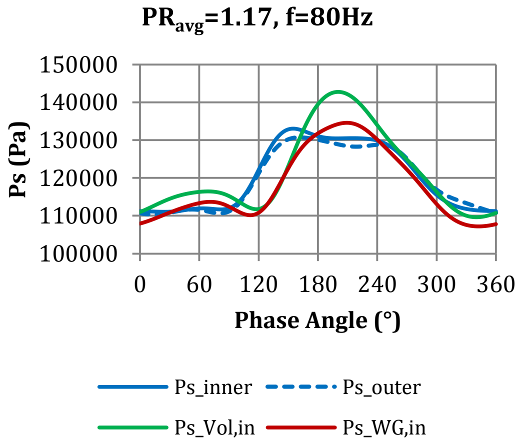
PR$_{avg}$=1.17, f=80Hz
Ps (Pa)
150000
140000
130000
120000
110000
100000
0
60
120
180
240
300
360
Phase Angle (°)
Ps_inner
Ps_outer
Ps_Vol,in
Ps_WG,in

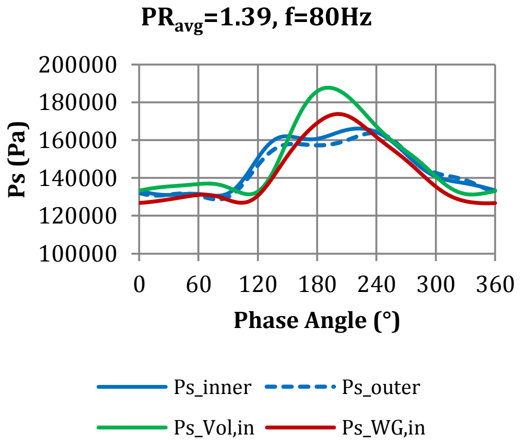
PR$_{avg}$=1.39, f=80Hz
Ps (Pa)
200000
180000
160000
140000
120000
100000
0
60
120
180
240
300
360
Phase Angle (°)
Ps_inner
Ps_outer
Ps_Vol,in
Ps_WG,in

E3. Instantaneous torque measurements

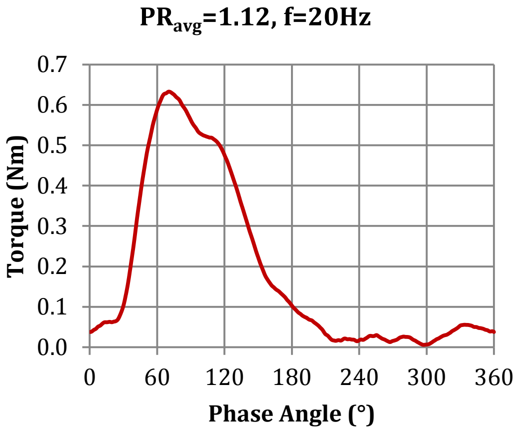
PR$_{avg}$=1.12, f=20Hz

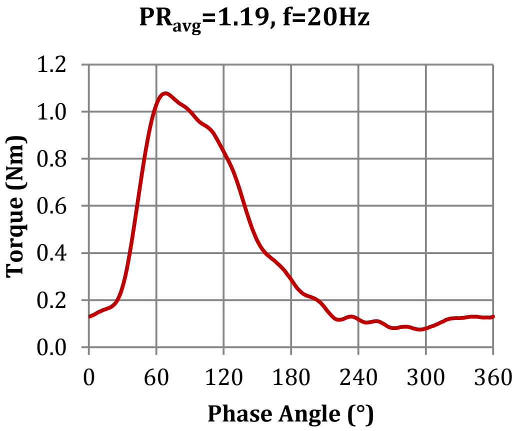
PR$_{avg}$=1.19, f=20Hz

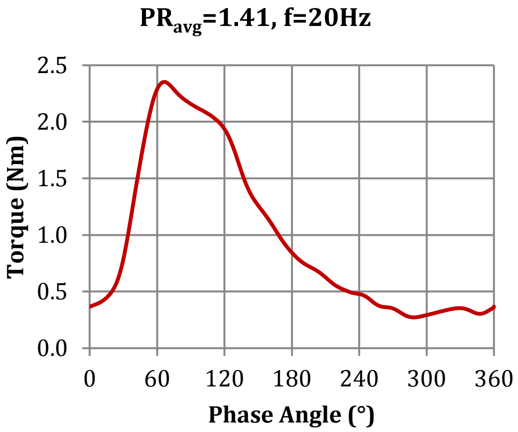
PR$_{avg}$=1.41, f=20Hz

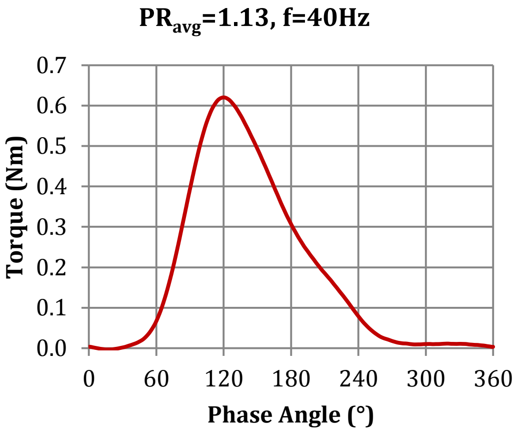
PR$_{avg}$=1.13, f=40Hz

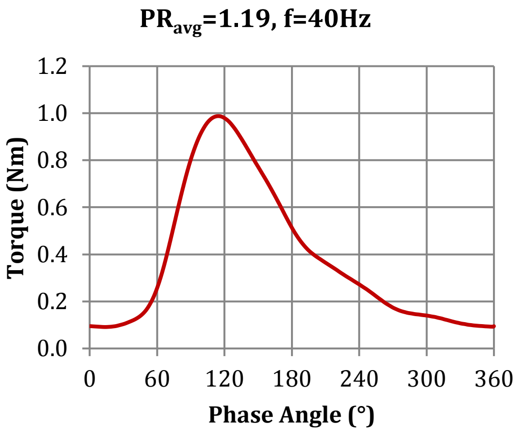
PR$_{avg}$=1.19, f=40Hz

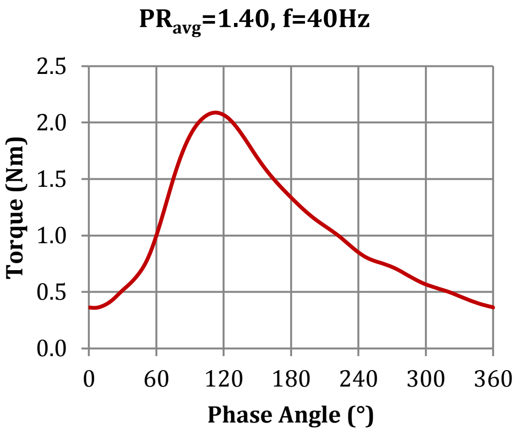
PR$_{avg}$=1.40, f=40Hz

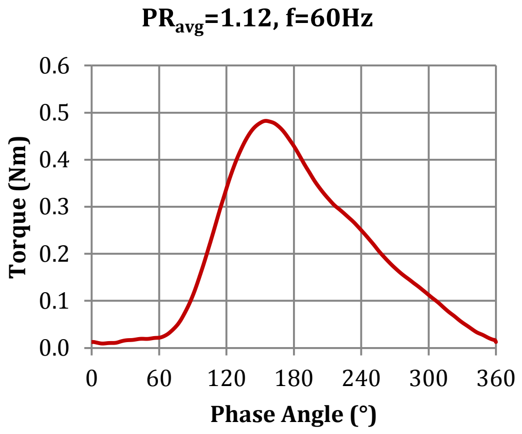

PR_{avg}=1.12, f=60Hz

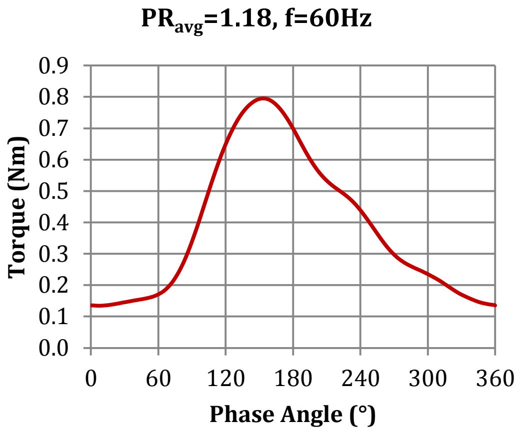

PR_{avg}=1.18, f=60Hz

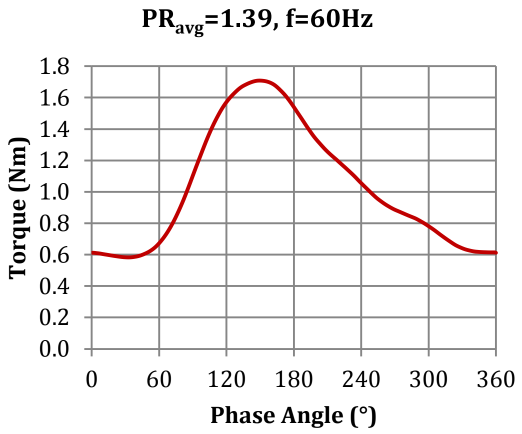

PR_{avg}=1.39, f=60Hz

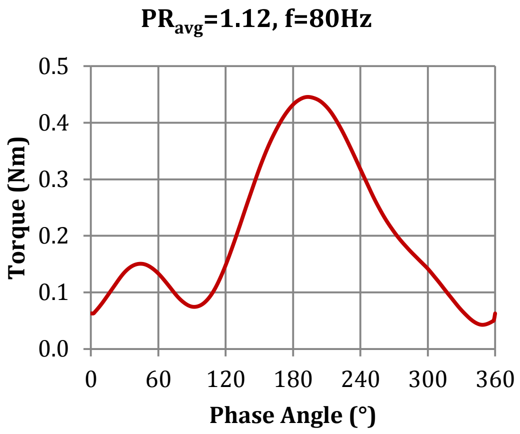

PR_{avg}=1.12, f=80Hz

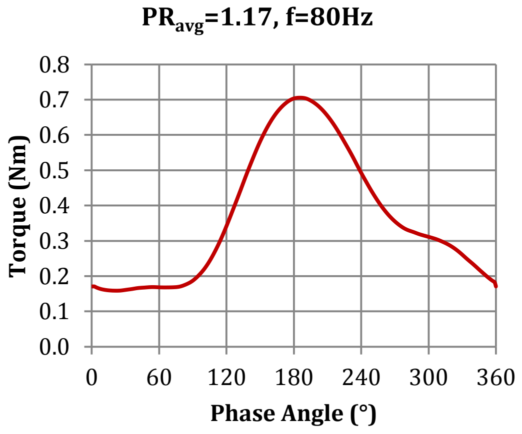

PR_{avg}=1.17, f=80Hz

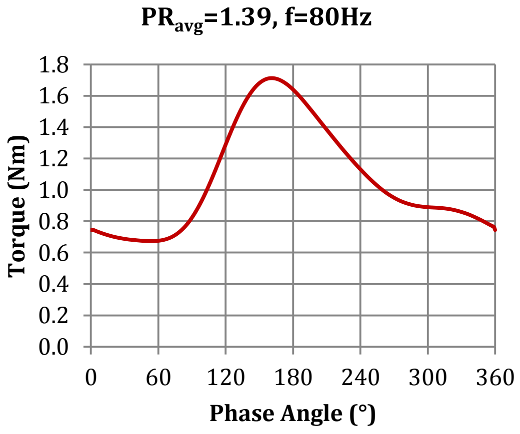

PR_{avg}=1.39, f=80Hz

E4. Instantaneous power measurements

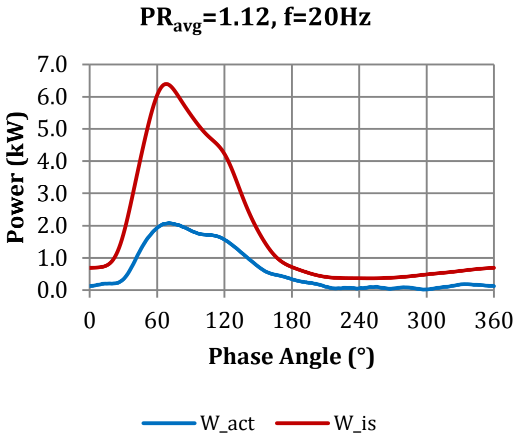
$PR_{avg}=1.12$, f=20Hz

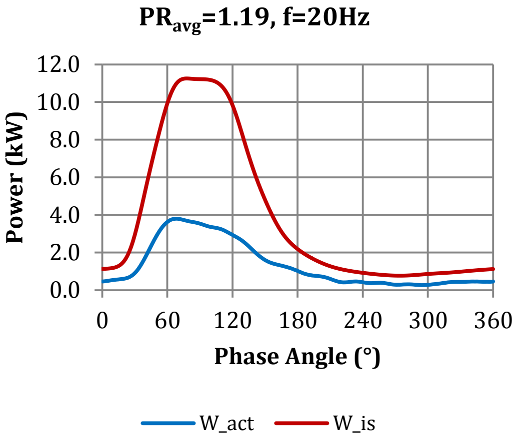
$PR_{avg}=1.19$, f=20Hz

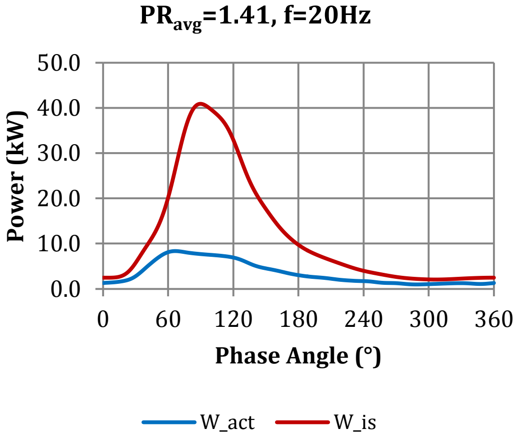
$PR_{avg}=1.41$, f=20Hz

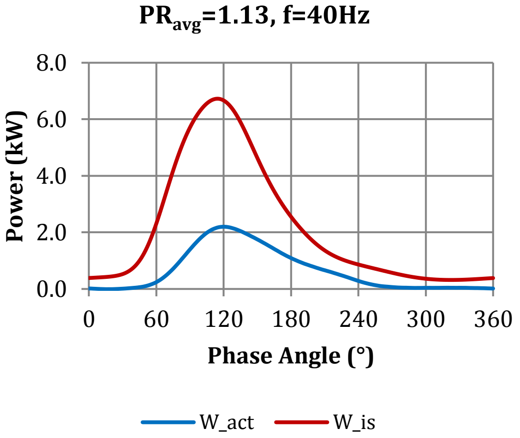
$PR_{avg}=1.13$, f=40Hz

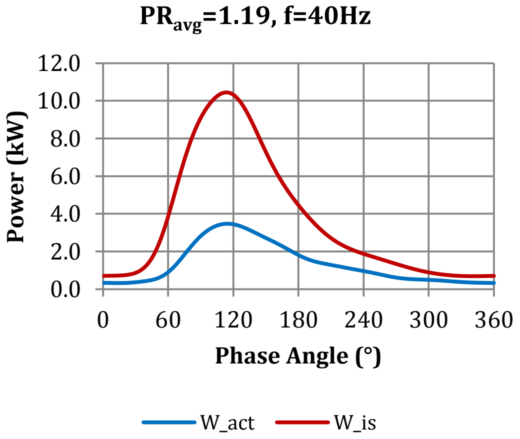
$PR_{avg}=1.19$, f=40Hz

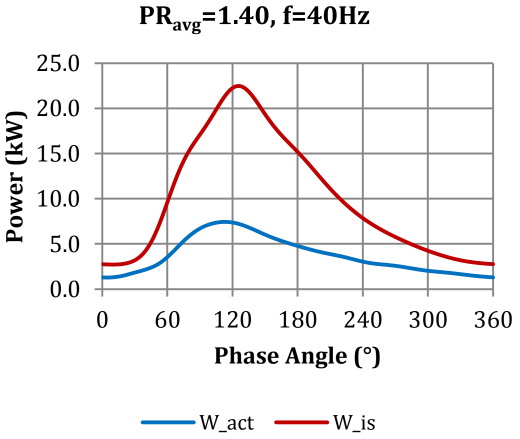
$PR_{avg}=1.40$, f=40Hz

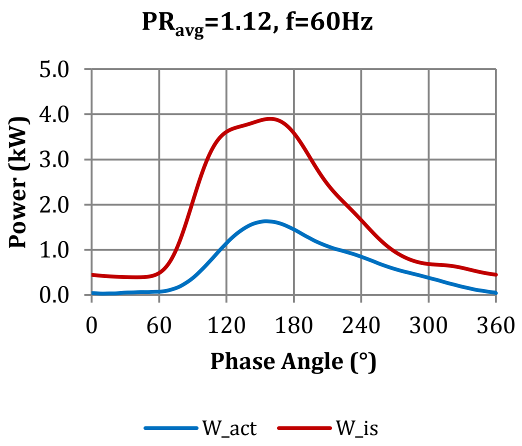
PR$_{avg}$=1.12, f=60Hz

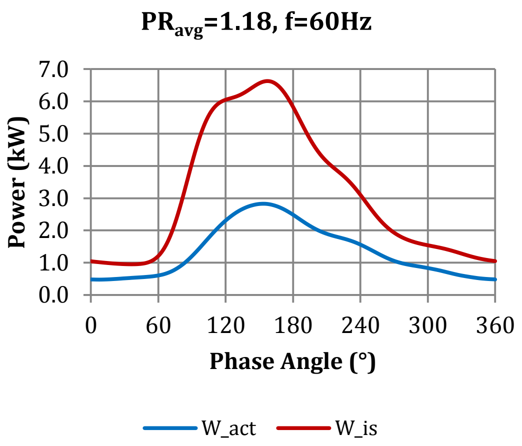
PR$_{avg}$=1.18, f=60Hz

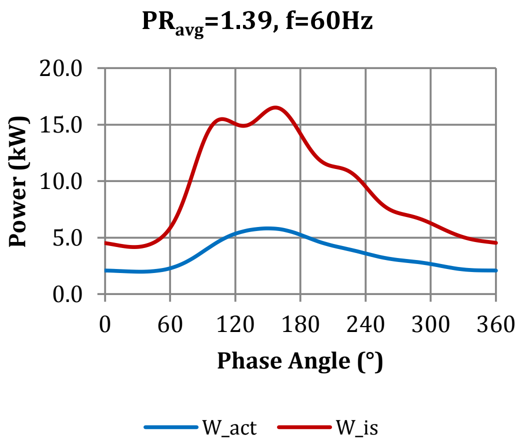
PR$_{avg}$=1.39, f=60Hz

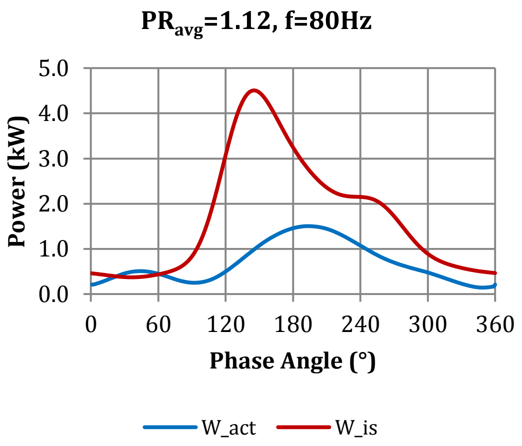
PR$_{avg}$=1.12, f=80Hz

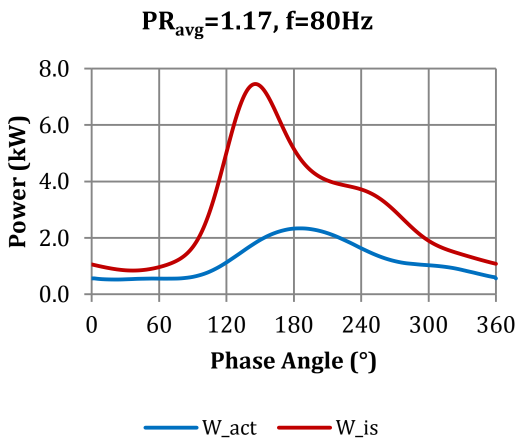
PR$_{avg}$=1.17, f=80Hz

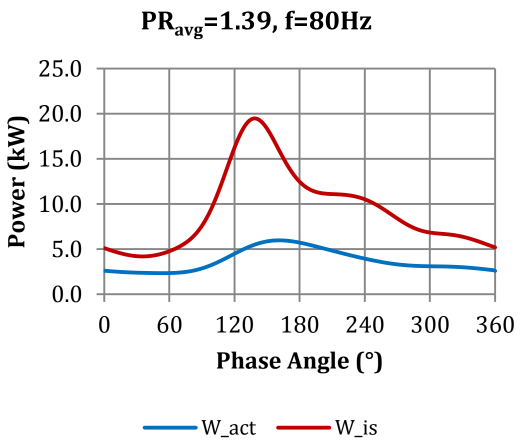
PR$_{avg}$=1.39, f=80Hz

APPENDIX F

UNSTEADY FLOW EXPERIMENTS ($N/\sqrt{T_0}$ = 2146 RPM/$\sqrt{K}$, l_{WG} = 0 mm)

F1. Instantaneous mass flow parameter (MFP) measurements

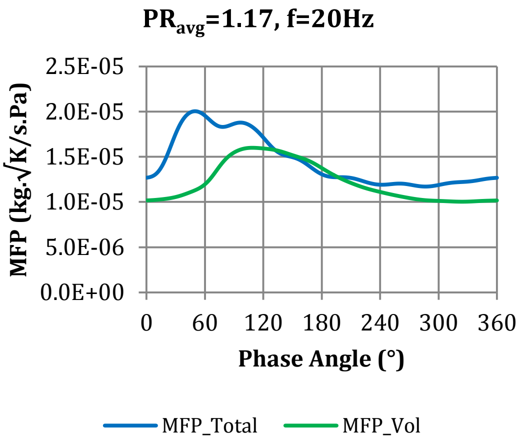

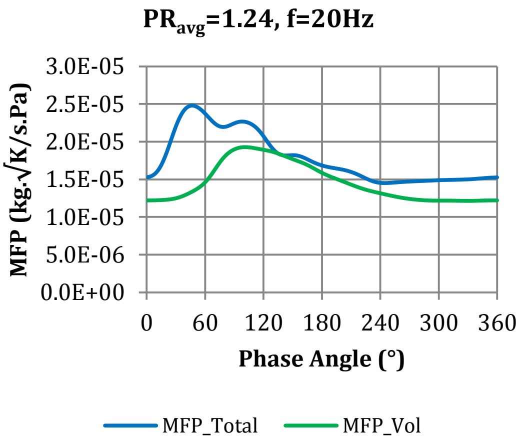

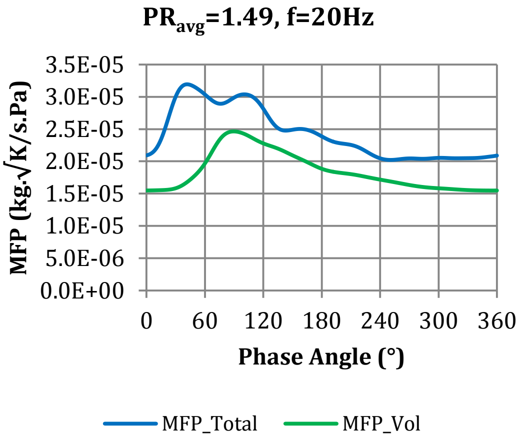

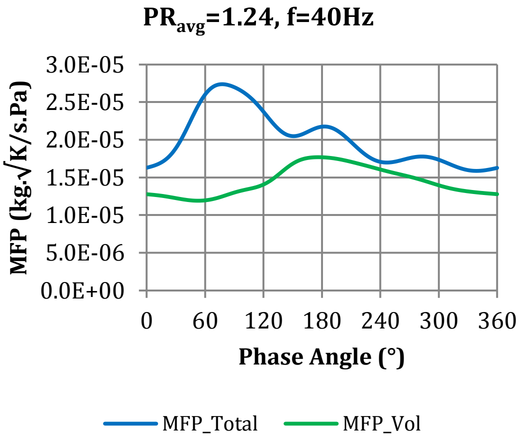

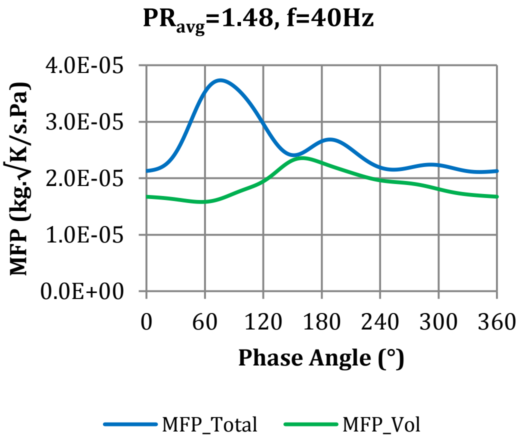

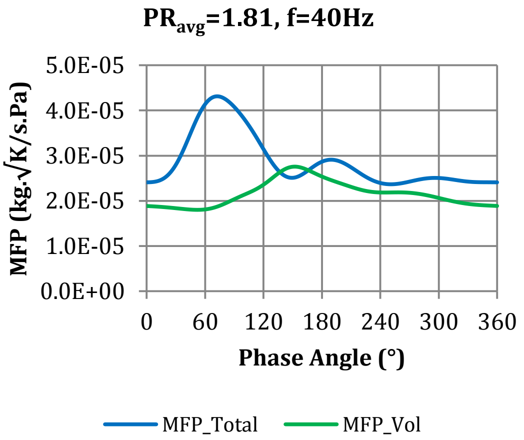

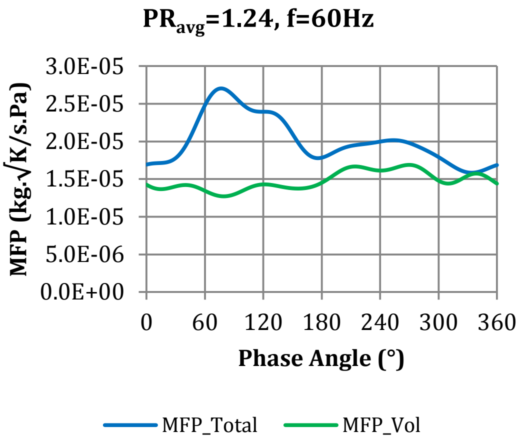
PR$_{avg}$=1.24, f=60Hz
MFP (kg.√K/s.Pa)
3.0E-05
2.5E-05
2.0E-05
1.5E-05
1.0E-05
5.0E-06
0.0E+00
0
60
120
180
240
300
360
Phase Angle (°)
MFP_Total
MFP_Vol

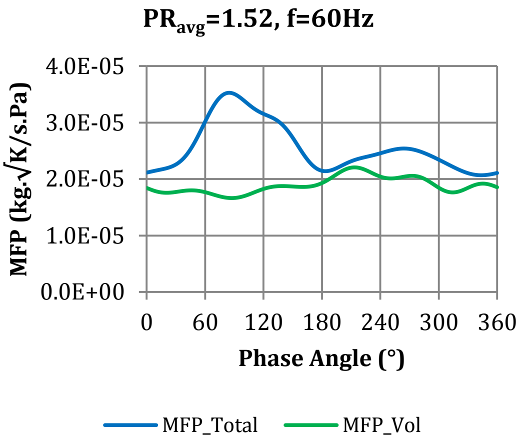
PR$_{avg}$=1.52, f=60Hz
MFP (kg.√K/s.Pa)
4.0E-05
3.0E-05
2.0E-05
1.0E-05
0.0E+00
0
60
120
180
240
300
360
Phase Angle (°)
MFP_Total
MFP_Vol

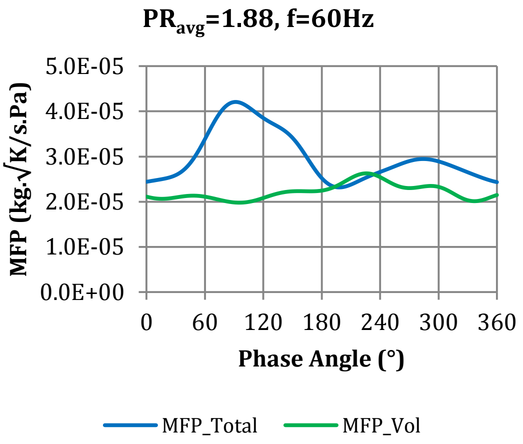
PR$_{avg}$=1.88, f=60Hz
MFP (kg.√K/s.Pa)
5.0E-05
4.0E-05
3.0E-05
2.0E-05
1.0E-05
0.0E+00
0
60
120
180
240
300
360
Phase Angle (°)
MFP_Total
MFP_Vol

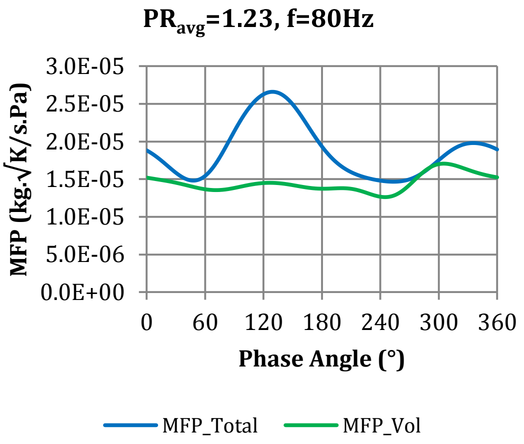
PR$_{avg}$=1.23, f=80Hz
MFP (kg.√K/s.Pa)
3.0E-05
2.5E-05
2.0E-05
1.5E-05
1.0E-05
5.0E-06
0.0E+00
0
60
120
180
240
300
360
Phase Angle (°)
MFP_Total
MFP_Vol

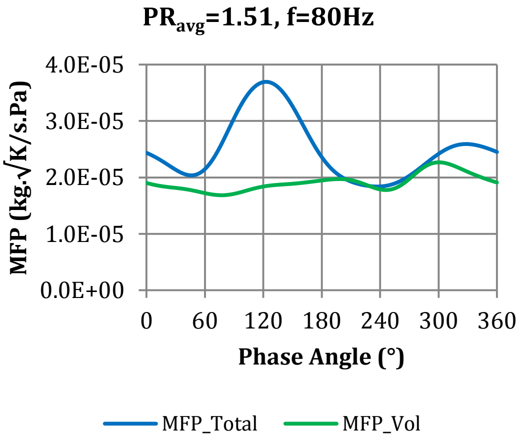
PR$_{avg}$=1.51, f=80Hz
MFP (kg.√K/s.Pa)
4.0E-05
3.0E-05
2.0E-05
1.0E-05
0.0E+00
0
60
120
180
240
300
360
Phase Angle (°)
MFP_Total
MFP_Vol

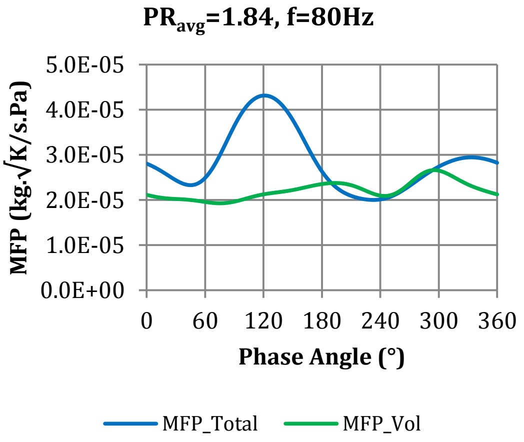
PR$_{avg}$=1.84, f=80Hz
MFP (kg.√K/s.Pa)
5.0E-05
4.0E-05
3.0E-05
2.0E-05
1.0E-05
0.0E+00
0
60
120
180
240
300
360
Phase Angle (°)
MFP_Total
MFP_Vol

F2. Instantaneous static pressure (P_s) measurements

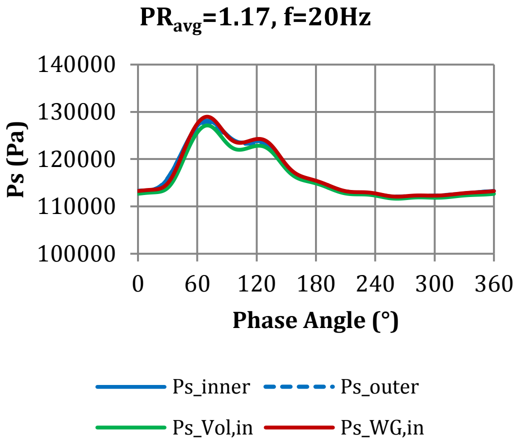

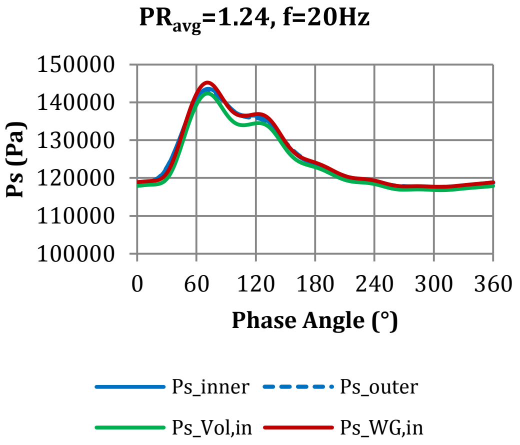

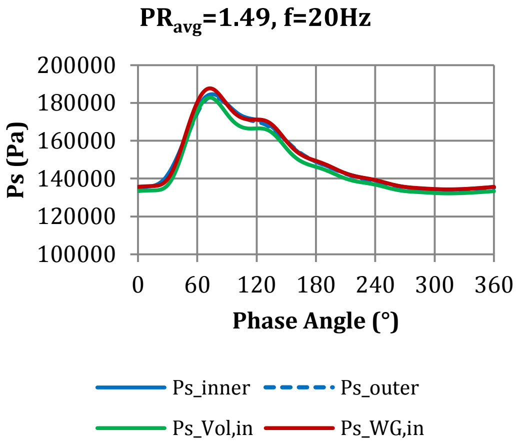

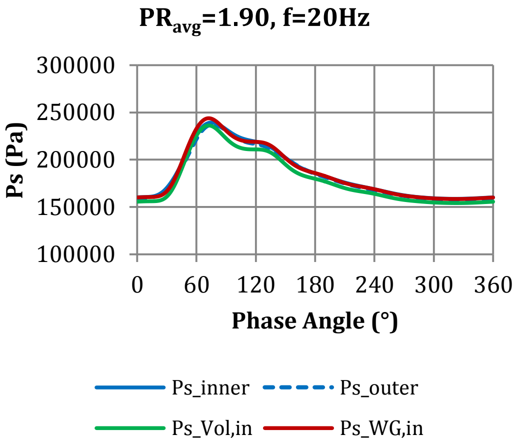

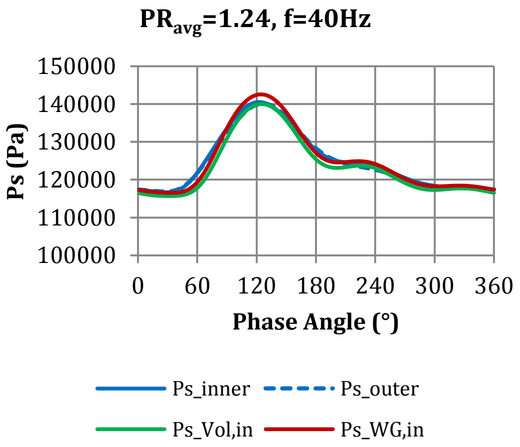

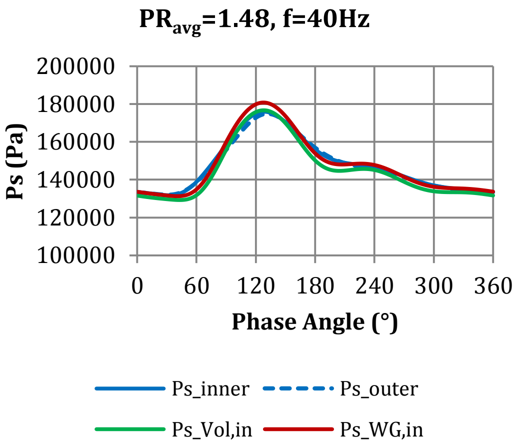

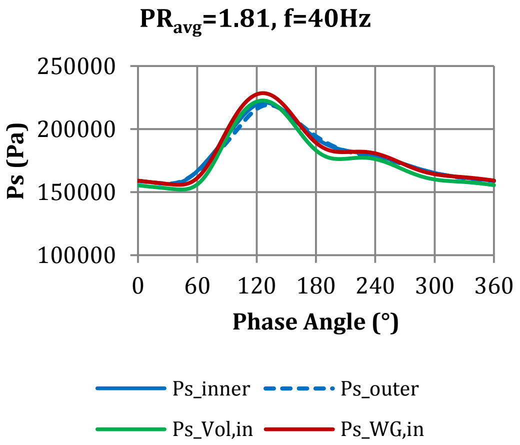
PR$_{avg}$=1.81, f=40Hz
Ps (Pa)
250000
200000
150000
100000
0
60
120
180
240
300
360
Phase Angle (°)
Ps_inner
Ps_outer
Ps_Vol,in
Ps_WG,in

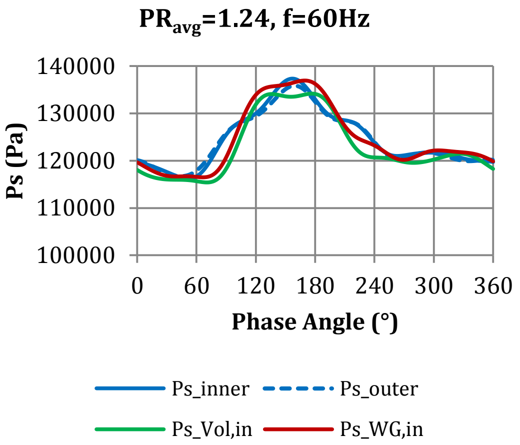
PR$_{avg}$=1.24, f=60Hz
Ps (Pa)
140000
130000
120000
110000
100000
0
60
120
180
240
300
360
Phase Angle (°)
Ps_inner
Ps_outer
Ps_Vol,in
Ps_WG,in

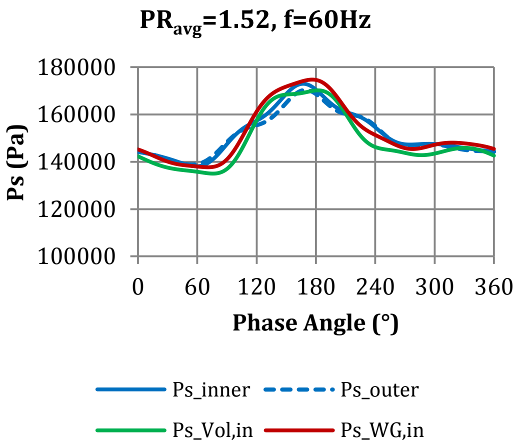
PR$_{avg}$=1.52, f=60Hz
Ps (Pa)
180000
160000
140000
120000
100000
0
60
120
180
240
300
360
Phase Angle (°)
Ps_inner
Ps_outer
Ps_Vol,in
Ps_WG,in

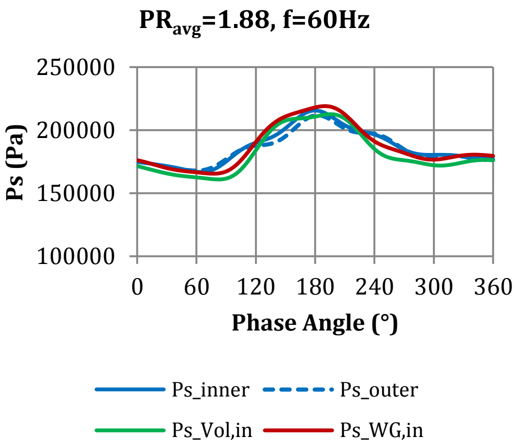
PR$_{avg}$=1.88, f=60Hz
Ps (Pa)
250000
200000
150000
100000
0
60
120
180
240
300
360
Phase Angle (°)
Ps_inner
Ps_outer
Ps_Vol,in
Ps_WG,in

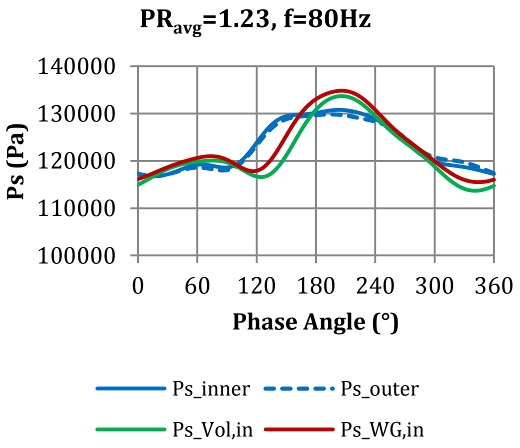
PR$_{avg}$=1.23, f=80Hz
Ps (Pa)
140000
130000
120000
110000
100000
0
60
120
180
240
300
360
Phase Angle (°)
Ps_inner
Ps_outer
Ps_Vol,in
Ps_WG,in

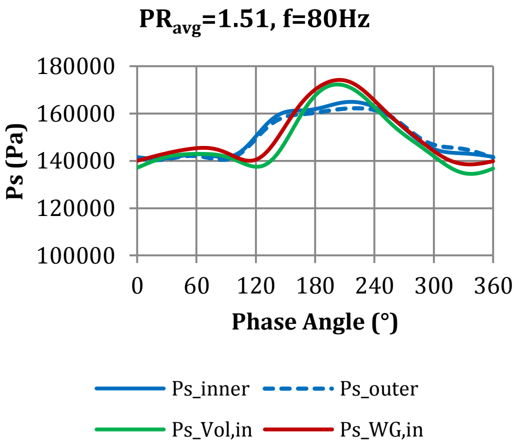
PR$_{avg}$=1.51, f=80Hz
Ps (Pa)
180000
160000
140000
120000
100000
0
60
120
180
240
300
360
Phase Angle (°)
Ps_inner
Ps_outer
Ps_Vol,in
Ps_WG,in

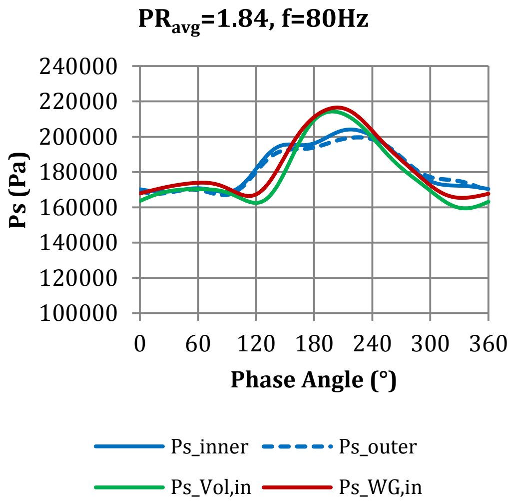

F3. Instantaneous torque measurements

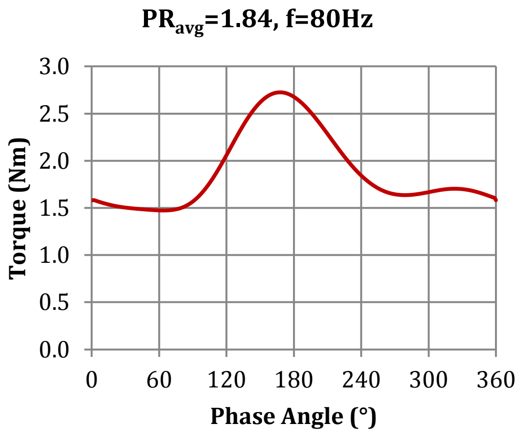

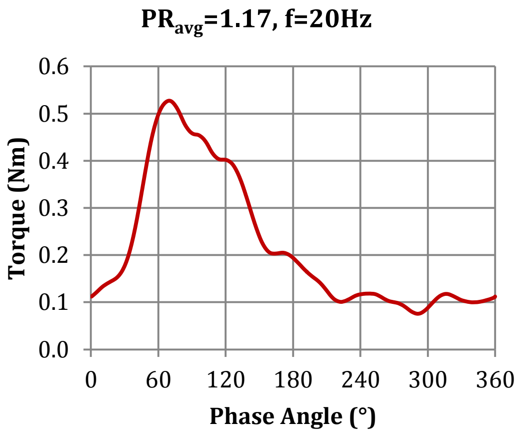

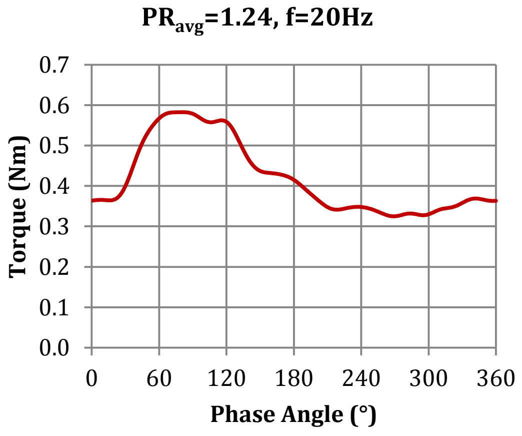

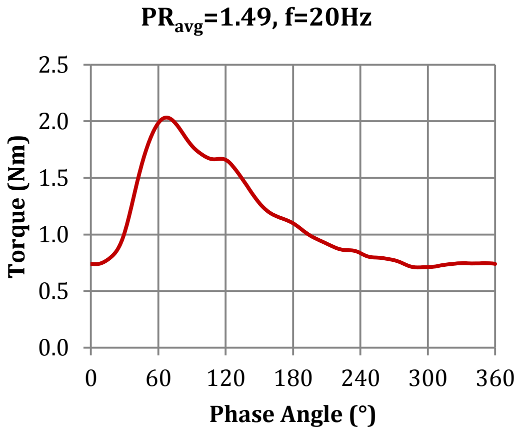

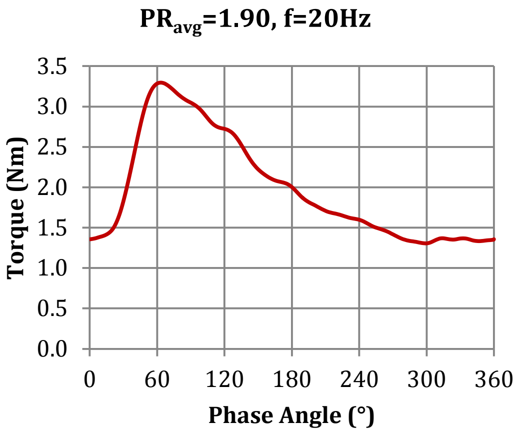
PR$_{avg}$=1.90, f=20Hz
Torque (Nm)
3.5
3.0
2.5
2.0
1.5
1.0
0.5
0.0
0
60
120
180
240
300
360
Phase Angle (°)

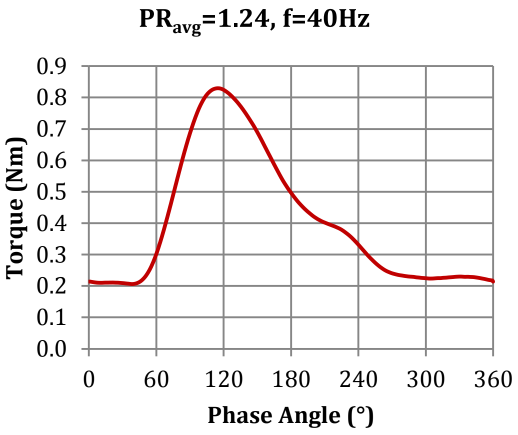
PR$_{avg}$=1.24, f=40Hz
Torque (Nm)
0.9
0.8
0.7
0.6
0.5
0.4
0.3
0.2
0.1
0.0
0
60
120
180
240
300
360
Phase Angle (°)

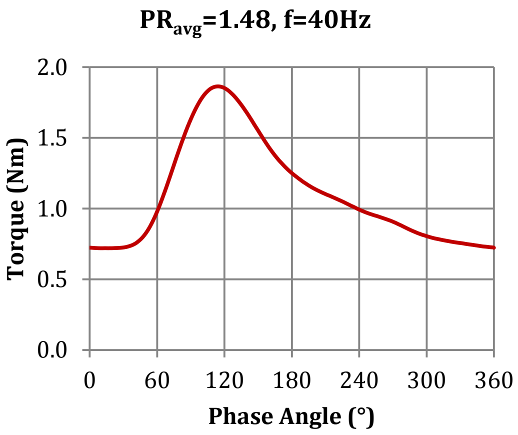
PR$_{avg}$=1.48, f=40Hz
Torque (Nm)
2.0
1.5
1.0
0.5
0.0
0
60
120
180
240
300
360
Phase Angle (°)

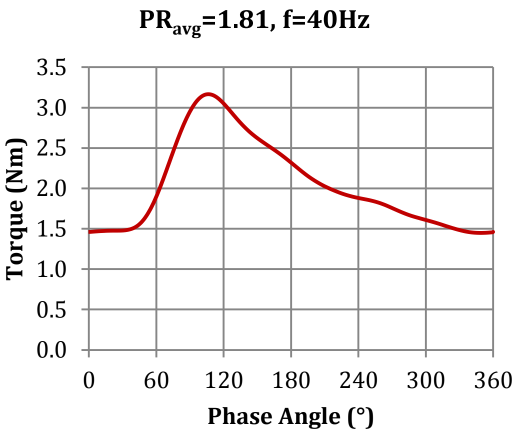
PR$_{avg}$=1.81, f=40Hz
Torque (Nm)
3.5
3.0
2.5
2.0
1.5
1.0
0.5
0.0
0
60
120
180
240
300
360
Phase Angle (°)

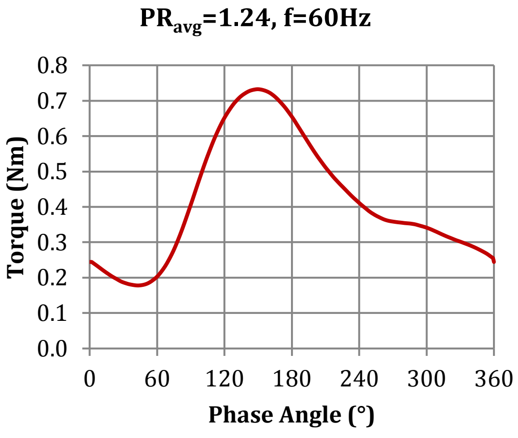
PR$_{avg}$=1.24, f=60Hz
Torque (Nm)
0.8
0.7
0.6
0.5
0.4
0.3
0.2
0.1
0.0
0
60
120
180
240
300
360
Phase Angle (°)

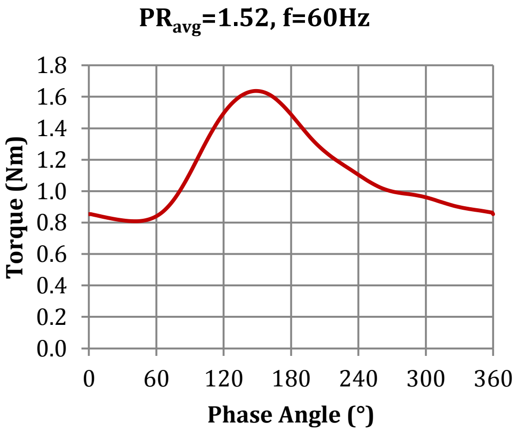
PR$_{avg}$=1.52, f=60Hz
Torque (Nm)
1.8
1.6
1.4
1.2
1.0
0.8
0.6
0.4
0.2
0.0
0
60
120
180
240
300
360
Phase Angle (°)

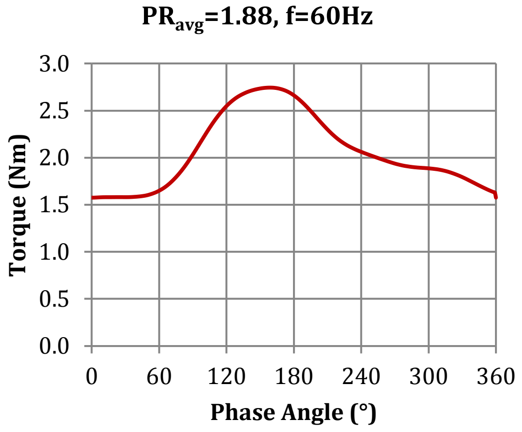
PR$_{avg}$=1.88, f=60Hz

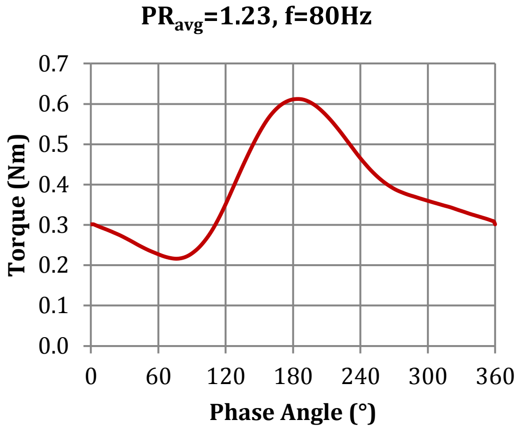
PR$_{avg}$=1.23, f=80Hz

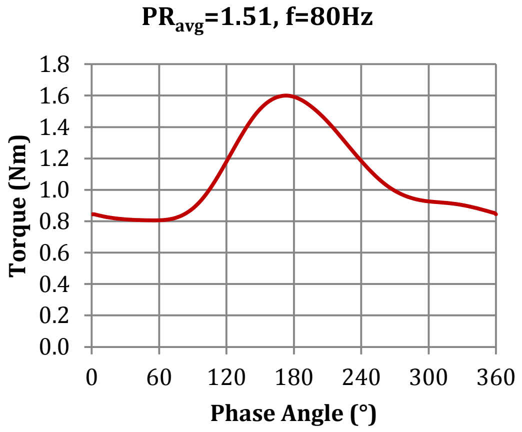
PR$_{avg}$=1.51, f=80Hz

E4. Instantaneous power measurements

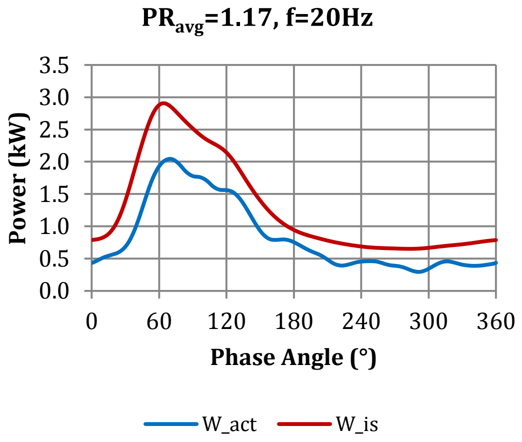
PR$_{avg}$=1.17, f=20Hz

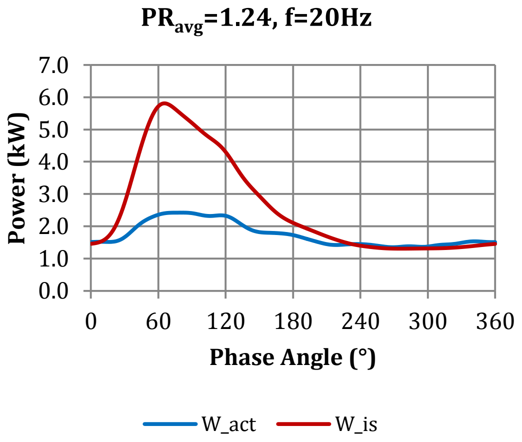
PR$_{avg}$=1.24, f=20Hz

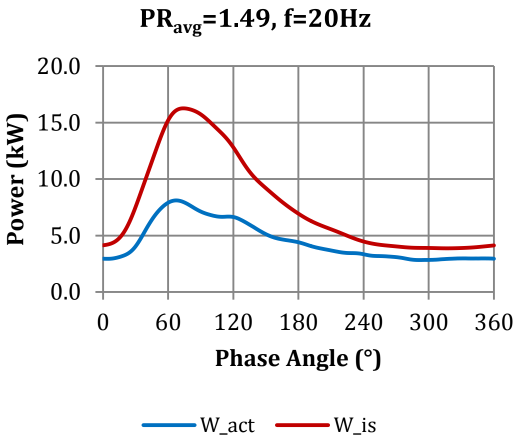
PR_{avg}=1.49, f=20Hz
Power (kW)
20.0
15.0
10.0
5.0
0.0
0
60
120
180
240
300
360
Phase Angle (°)
W_act
W_is

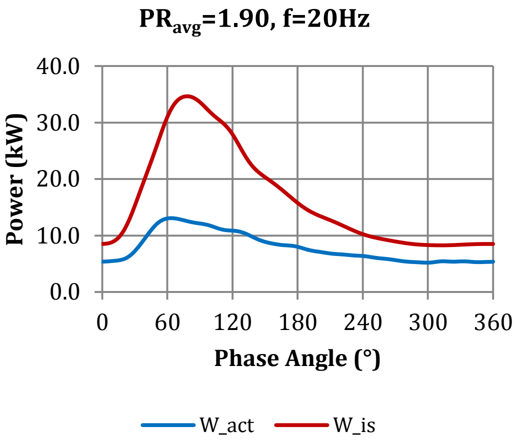
PR_{avg}=1.90, f=20Hz
Power (kW)
40.0
30.0
20.0
10.0
0.0
0
60
120
180
240
300
360
Phase Angle (°)
W_act
W_is

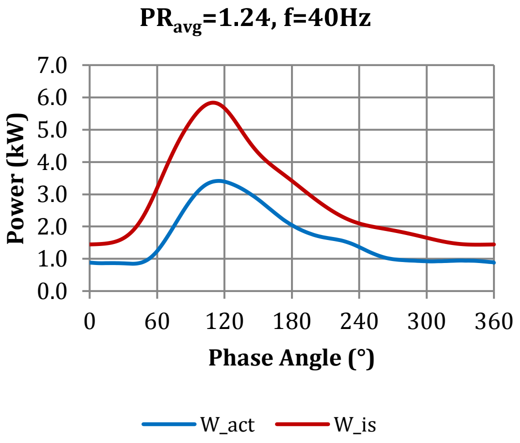
PR_{avg}=1.24, f=40Hz
Power (kW)
7.0
6.0
5.0
4.0
3.0
2.0
1.0
0.0
0
60
120
180
240
300
360
Phase Angle (°)
W_act
W_is

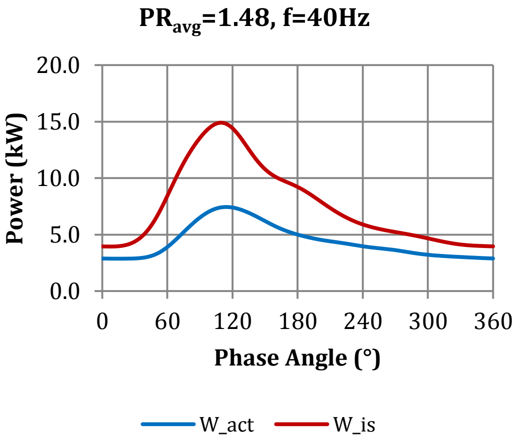
PR_{avg}=1.48, f=40Hz
Power (kW)
20.0
15.0
10.0
5.0
0.0
0
60
120
180
240
300
360
Phase Angle (°)
W_act
W_is

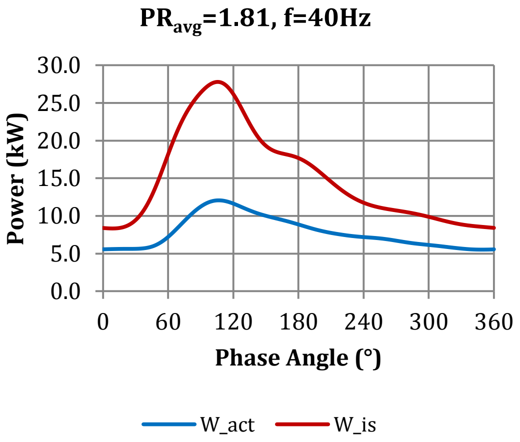
PR_{avg}=1.81, f=40Hz
Power (kW)
30.0
25.0
20.0
15.0
10.0
5.0
0.0
0
60
120
180
240
300
360
Phase Angle (°)
W_act
W_is

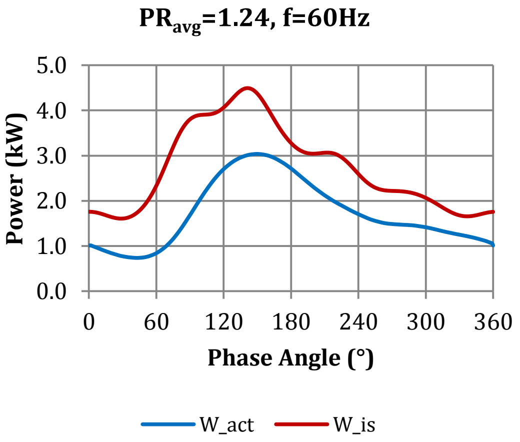
PR_{avg}=1.24, f=60Hz
Power (kW)
5.0
4.0
3.0
2.0
1.0
0.0
0
60
120
180
240
300
360
Phase Angle (°)
W_act
W_is

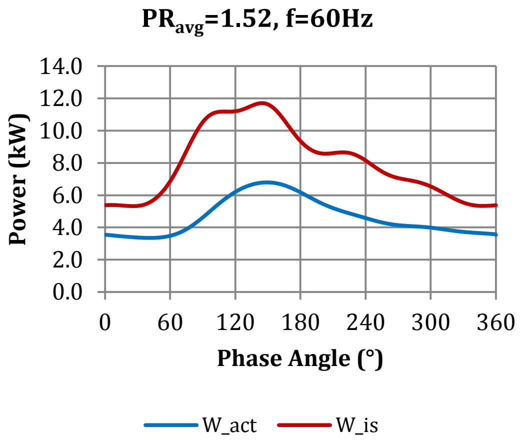
PR_{avg}=1.52, f=60Hz
Power (kW)
14.0
12.0
10.0
8.0
6.0
4.0
2.0
0.0
0
60
120
180
240
300
360
Phase Angle (°)
W_act
W_is

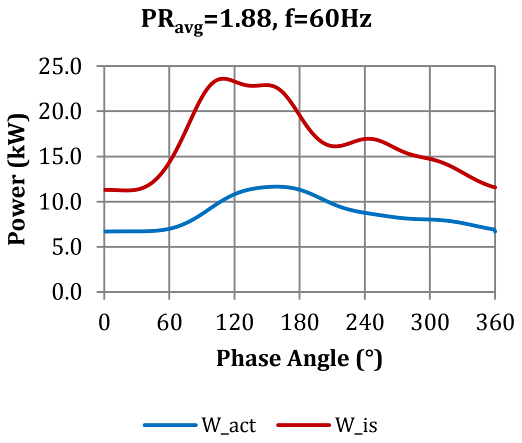
PR_{avg}=1.88, f=60Hz
Power (kW)
25.0
20.0
15.0
10.0
5.0
0.0
0
60
120
180
240
300
360
Phase Angle (°)
W_act
W_is

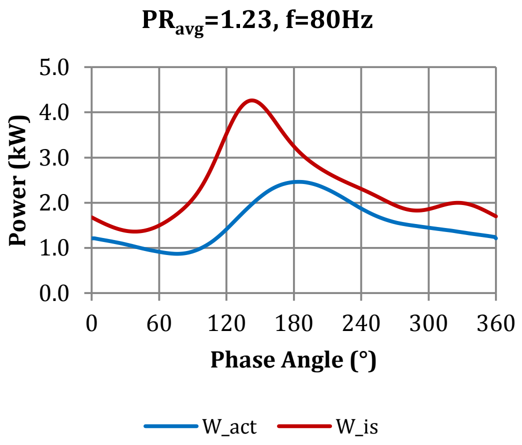
PR_{avg}=1.23, f=80Hz
Power (kW)
5.0
4.0
3.0
2.0
1.0
0.0
0
60
120
180
240
300
360
Phase Angle (°)
W_act
W_is

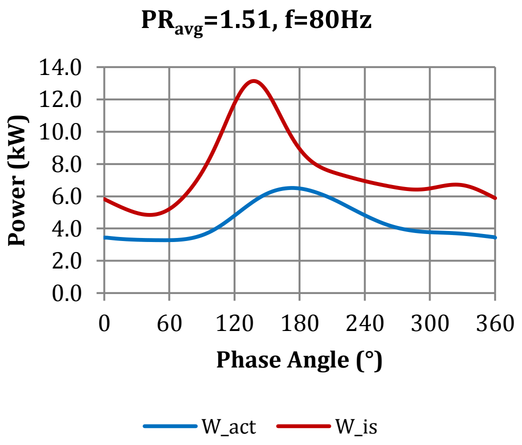
PR_{avg}=1.51, f=80Hz
Power (kW)
14.0
12.0
10.0
8.0
6.0
4.0
2.0
0.0
0
60
120
180
240
300
360
Phase Angle (°)
W_act
W_is

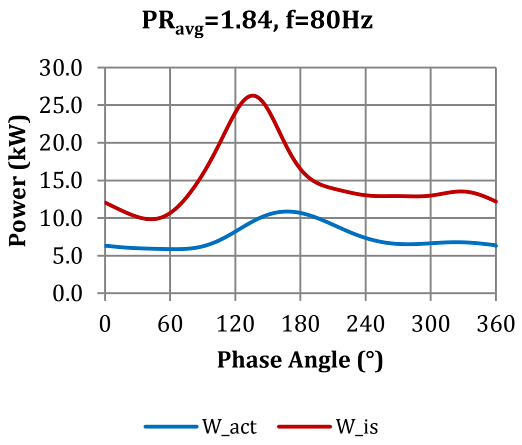
PR_{avg}=1.84, f=80Hz
Power (kW)
30.0
25.0
20.0
15.0
10.0
5.0
0.0
0
60
120
180
240
300
360
Phase Angle (°)
W_act
W_is

APPENDIX F

UNSTEADY FLOW EXPERIMENTS ($N/\sqrt{T_0}$ = 2146 RPM/$\sqrt{K}$, l_{WG} = 1 mm)

F1. Instantaneous mass flow parameter (MFP) measurements

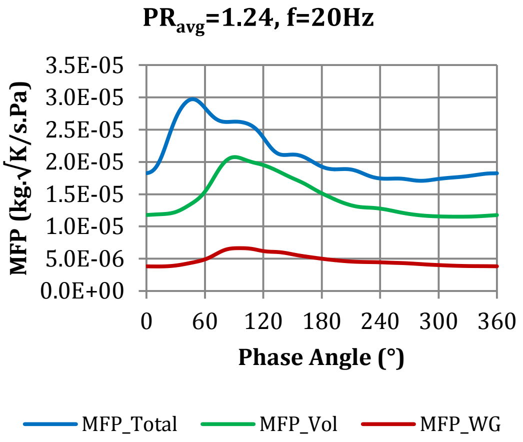
PR_{avg}=1.24, f=20Hz

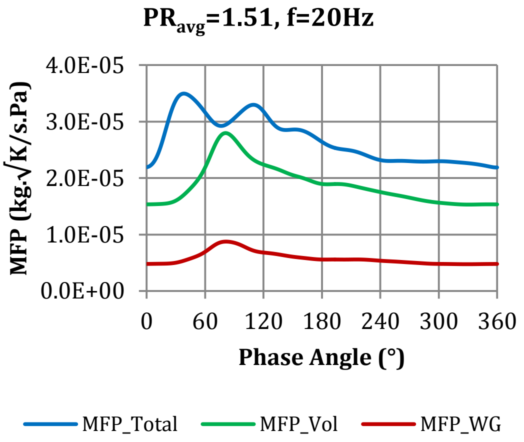
PR_{avg}=1.51, f=20Hz

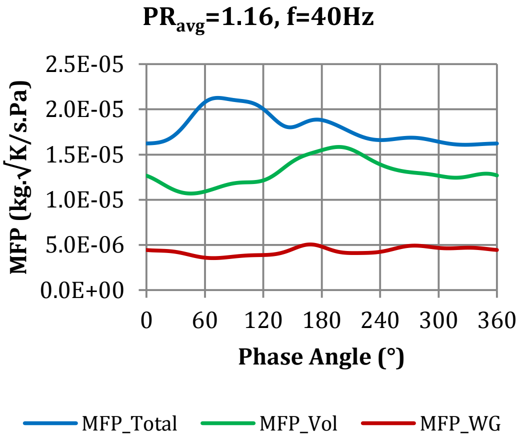
PR_{avg}=1.16, f=40Hz

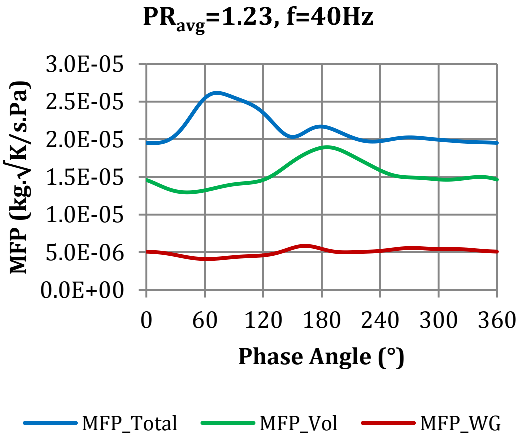
PR_{avg}=1.23, f=40Hz

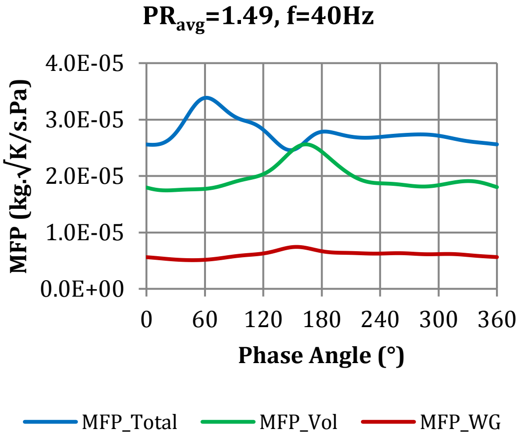
PR_{avg}=1.49, f=40Hz

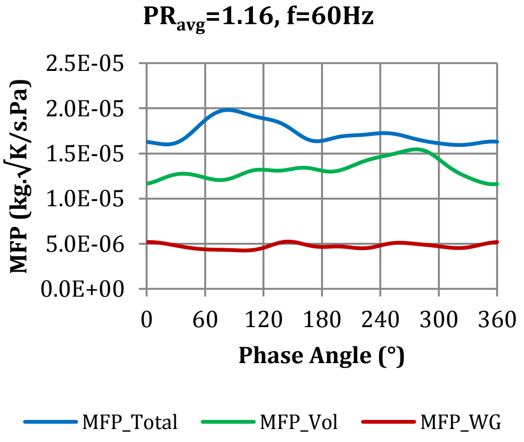
PR_{avg}=1.16, f=60Hz

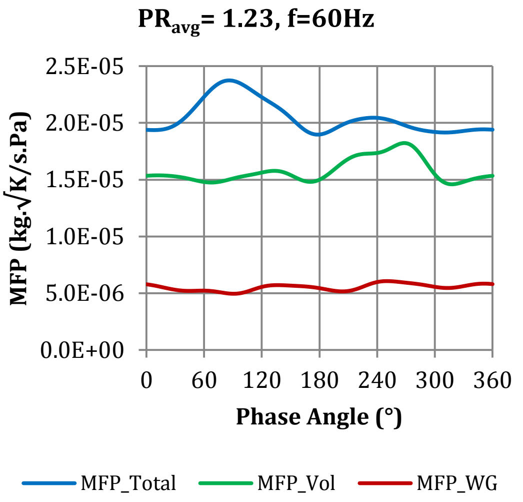
PR$_{avg}$= 1.23, f=60Hz

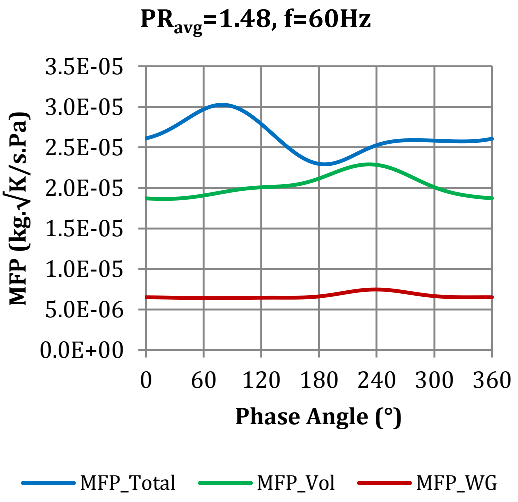
PR$_{avg}$=1.48, f=60Hz

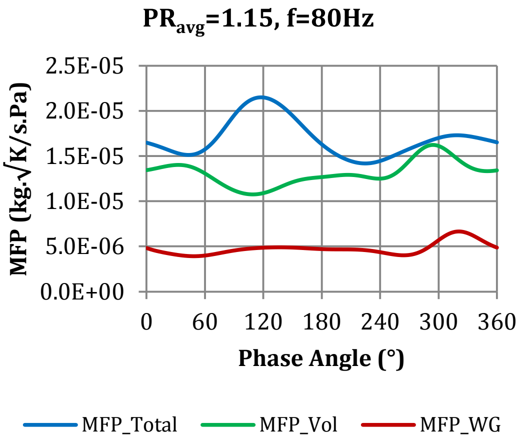
PR$_{avg}$=1.15, f=80Hz

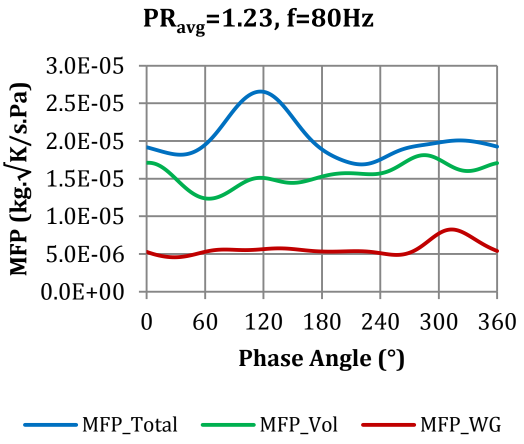
PR$_{avg}$=1.23, f=80Hz

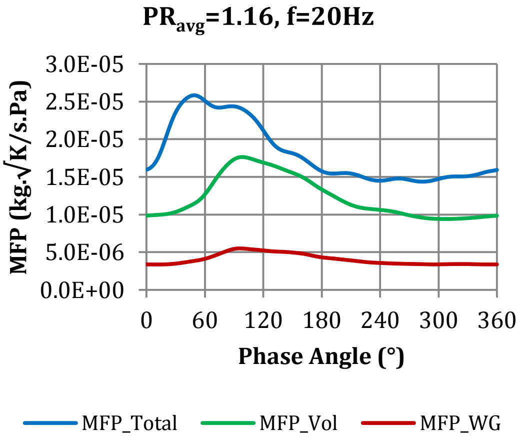
PR$_{avg}$=1.16, f=20Hz

F2. Instantaneous static pressure (P_s) measurements

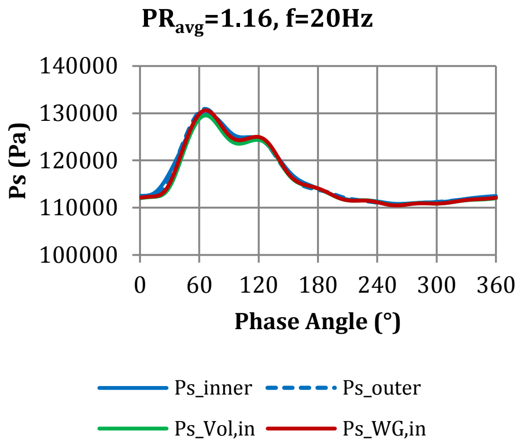

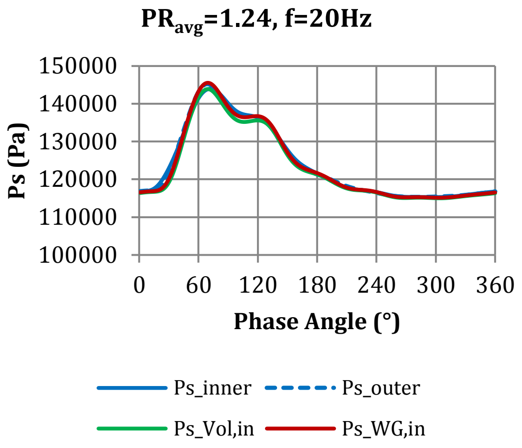

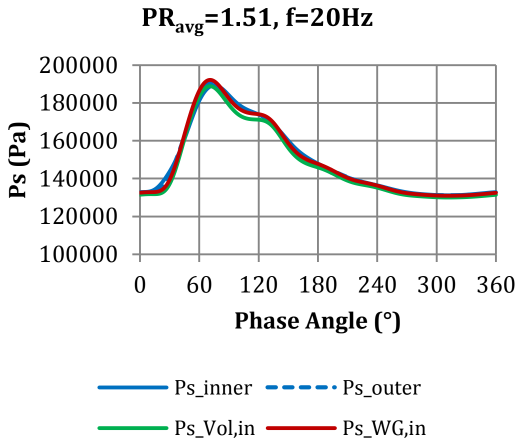

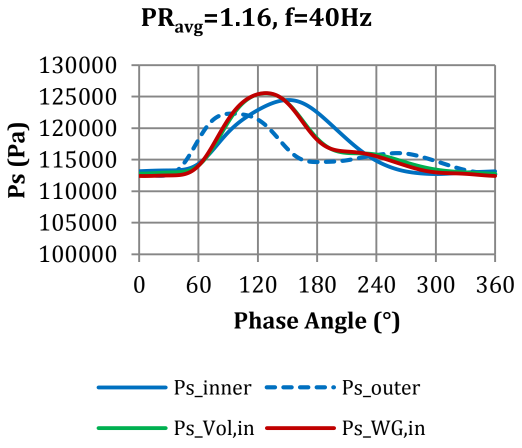

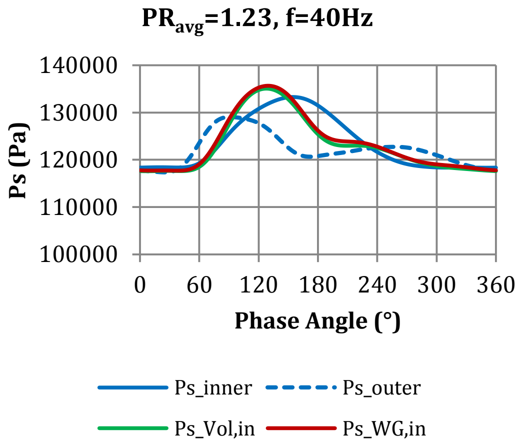

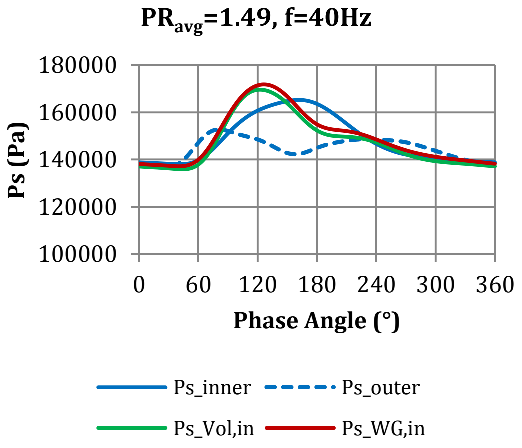

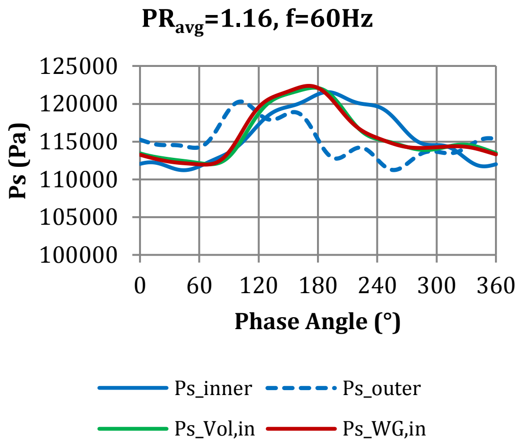
PRavg=1.16, f=60Hz
Ps (Pa)
125000
120000
115000
110000
105000
100000
0
60
120
180
240
300
360
Phase Angle (°)
Ps_inner
Ps_outer
Ps_Vol,in
Ps_WG,in

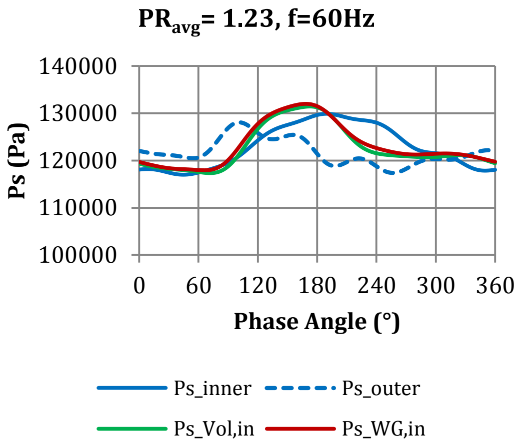
PRavg= 1.23, f=60Hz
Ps (Pa)
140000
130000
120000
110000
100000
0
60
120
180
240
300
360
Phase Angle (°)
Ps_inner
Ps_outer
Ps_Vol,in
Ps_WG,in

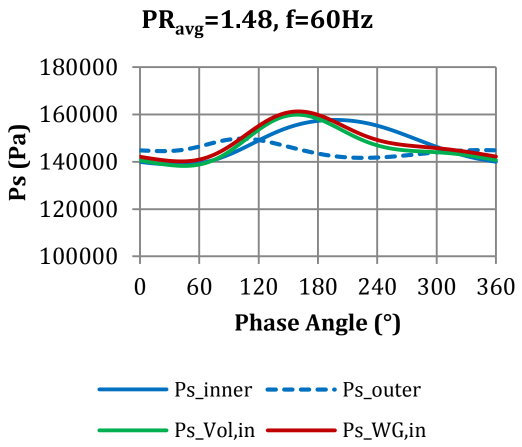
PRavg=1.48, f=60Hz
Ps (Pa)
180000
160000
140000
120000
100000
0
60
120
180
240
300
360
Phase Angle (°)
Ps_inner
Ps_outer
Ps_Vol,in
Ps_WG,in

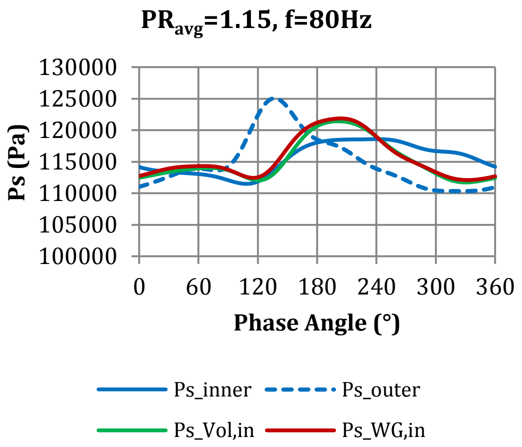
PRavg=1.15, f=80Hz
Ps (Pa)
130000
125000
120000
115000
110000
105000
100000
0
60
120
180
240
300
360
Phase Angle (°)
Ps_inner
Ps_outer
Ps_Vol,in
Ps_WG,in

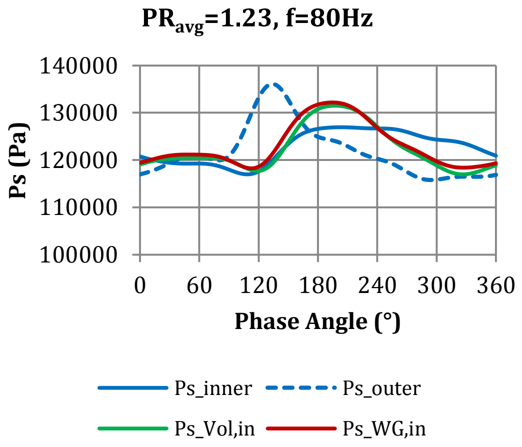
PRavg=1.23, f=80Hz
Ps (Pa)
140000
130000
120000
110000
100000
0
60
120
180
240
300
360
Phase Angle (°)
Ps_inner
Ps_outer
Ps_Vol,in
Ps_WG,in

F3. Instantaneous torque measurements

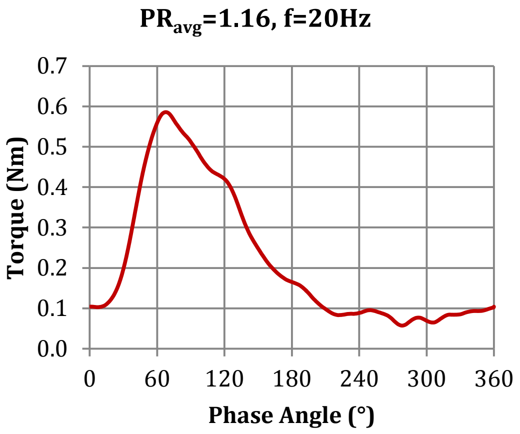

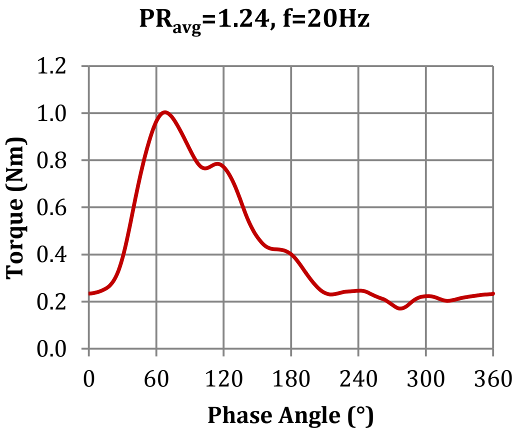

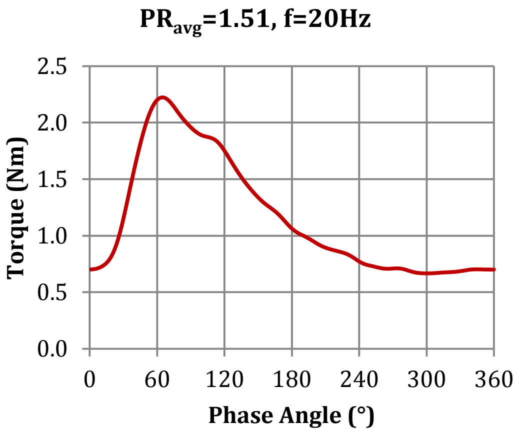

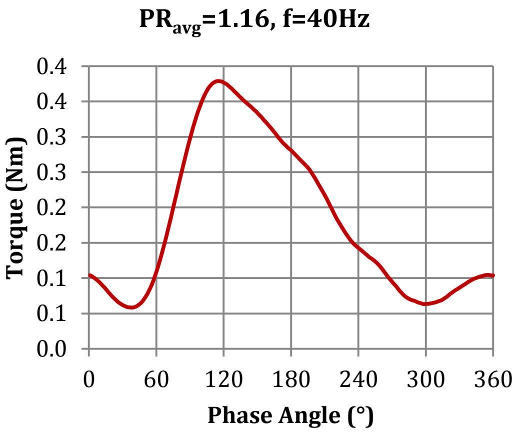

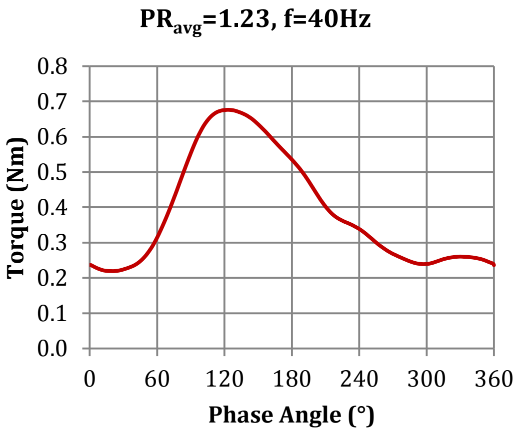

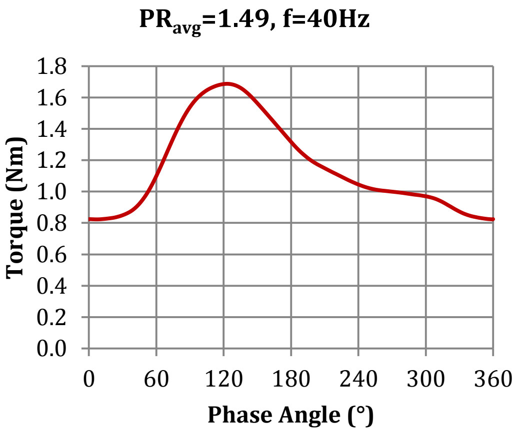

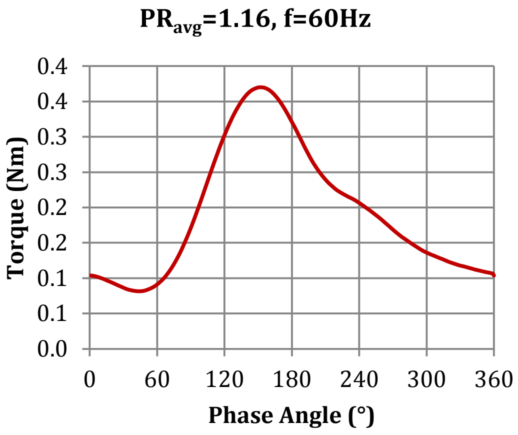
PR_{avg}=1.16, f=60Hz

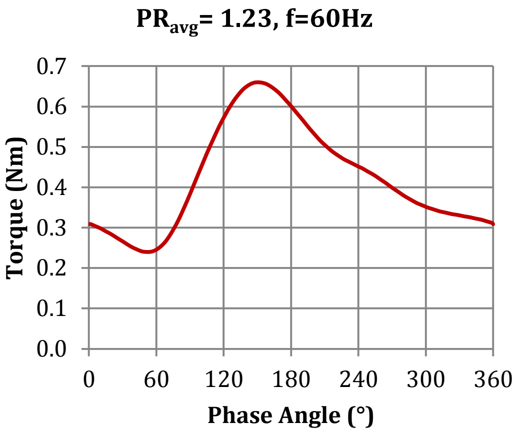
PR_{avg}= 1.23, f=60Hz

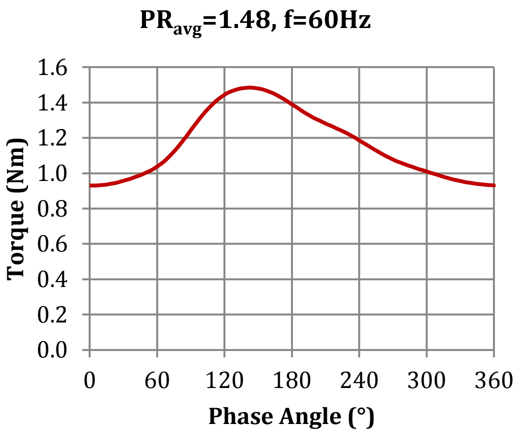
PR_{avg}=1.48, f=60Hz

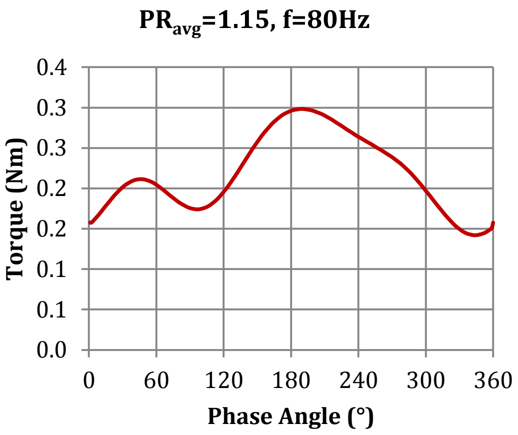
PR_{avg}=1.15, f=80Hz

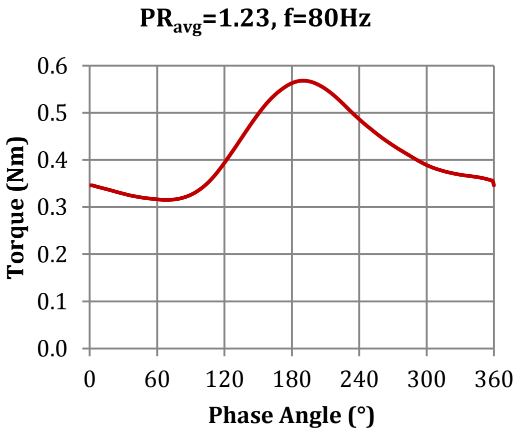
PR_{avg}=1.23, f=80Hz

F4. Instantaneous power measurements

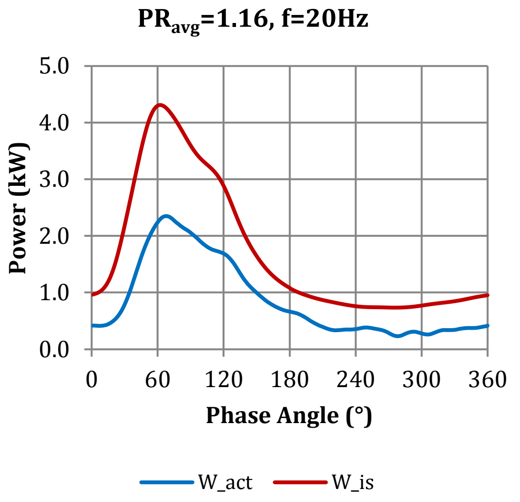
PR$_{avg}$=1.16, f=20Hz

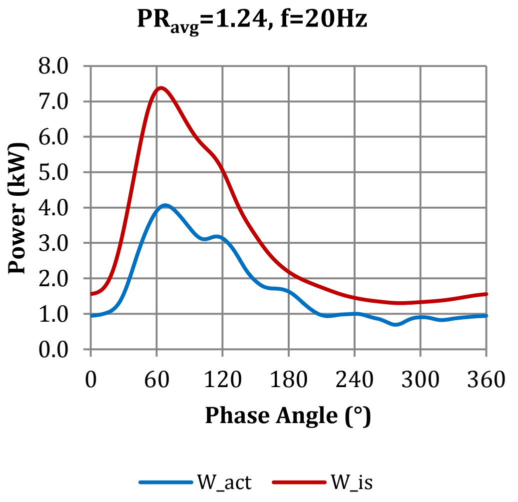
PR$_{avg}$=1.24, f=20Hz

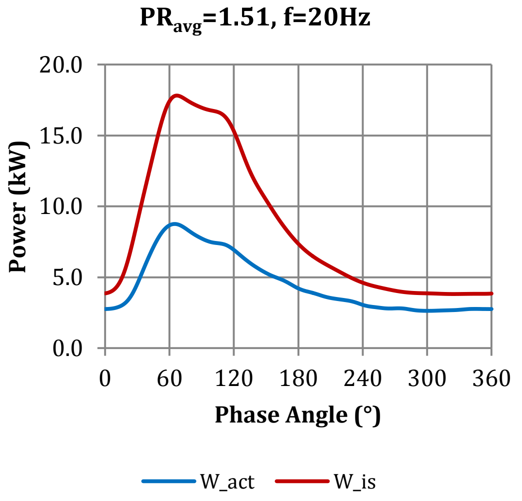
PR$_{avg}$=1.51, f=20Hz

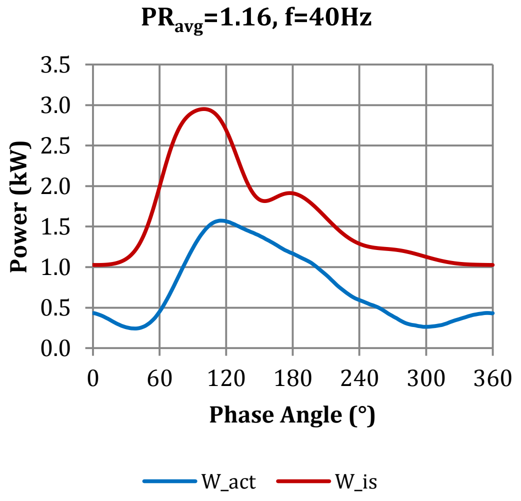
PR$_{avg}$=1.16, f=40Hz

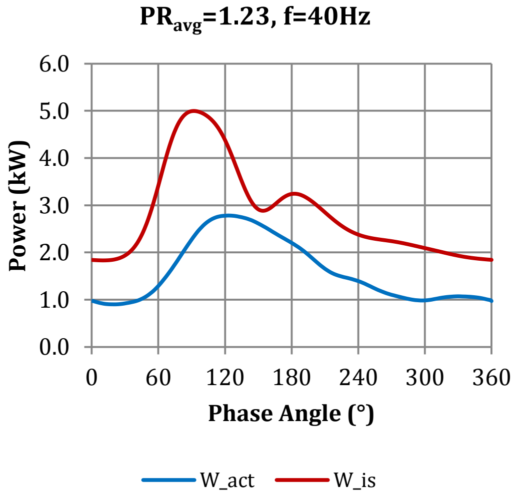
PR$_{avg}$=1.23, f=40Hz

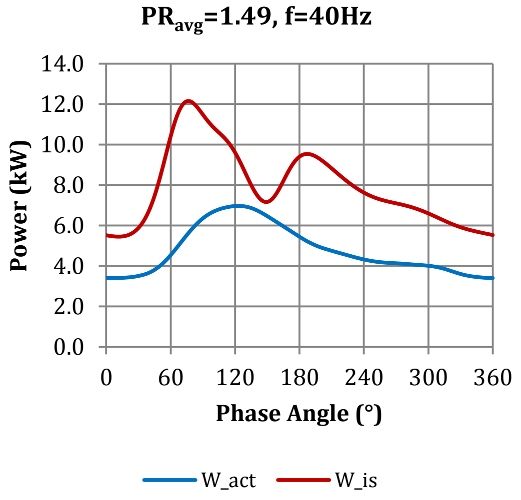
PR$_{avg}$=1.49, f=40Hz

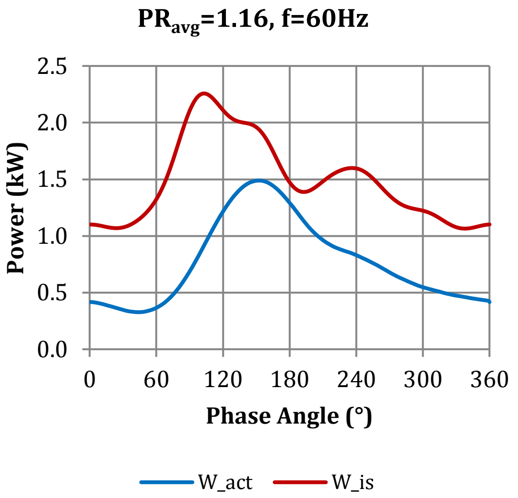
PR_{avg}=1.16, f=60Hz

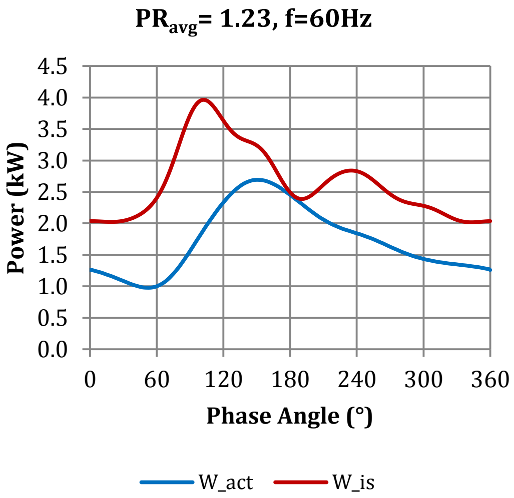
PR_{avg}= 1.23, f=60Hz

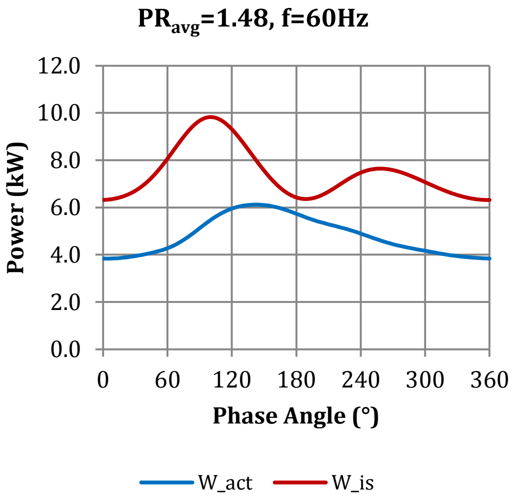
PR_{avg}=1.48, f=60Hz

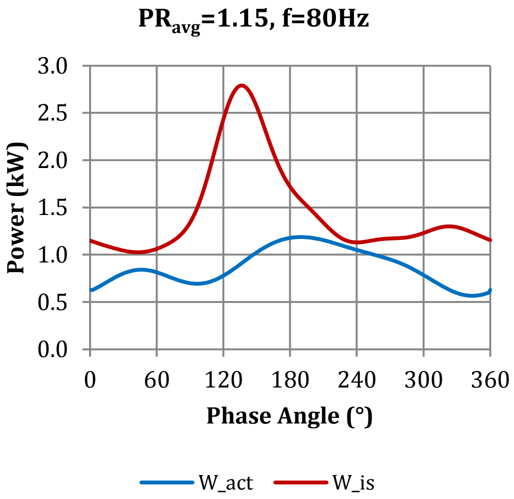
PR_{avg}=1.15, f=80Hz

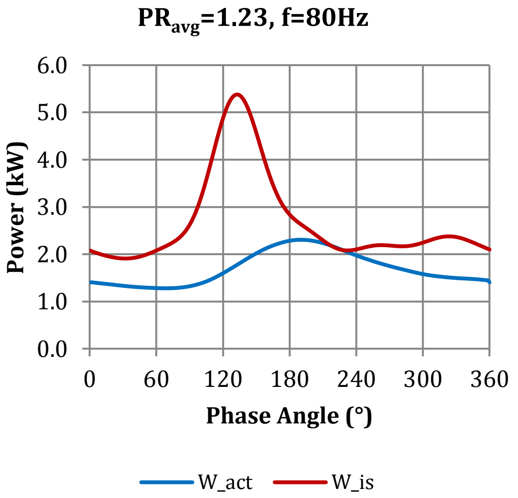
PR_{avg}=1.23, f=80Hz

APPENDIX G

UNSTEADY FLOW EXPERIMENTS ($N/\sqrt{T_0}$ = 2146 RPM/$\sqrt{K}$, l_{WG} = 3 mm)

G1. Instantaneous mass flow parameter (MFP) measurements

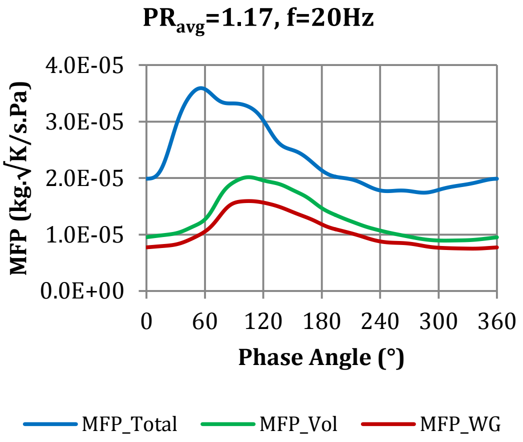

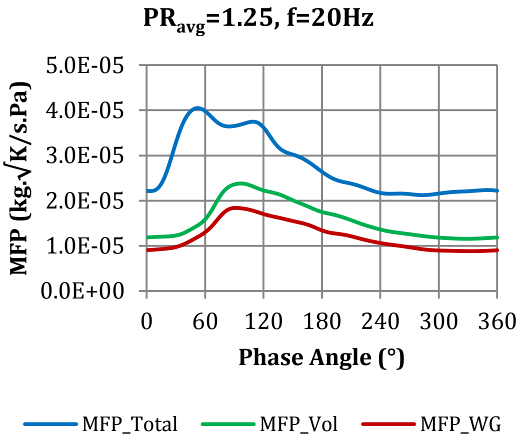

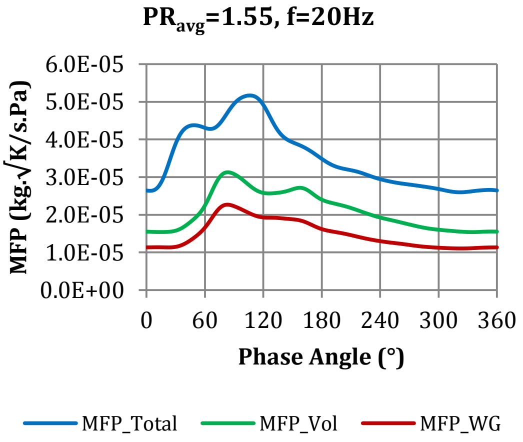

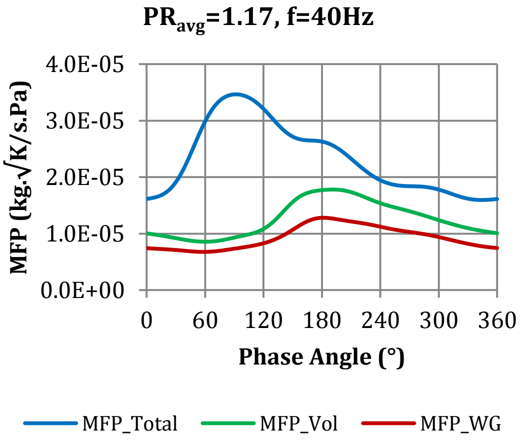

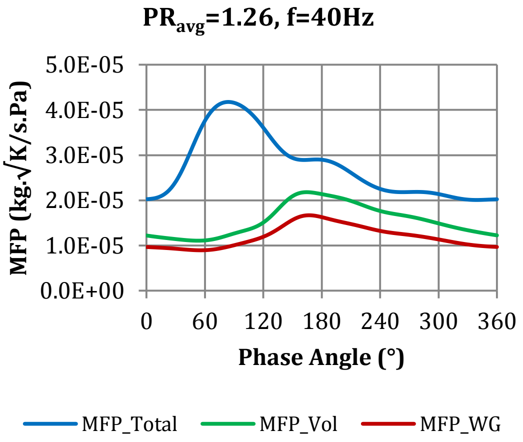

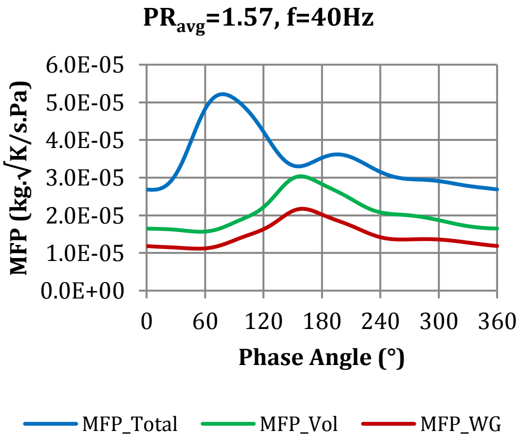

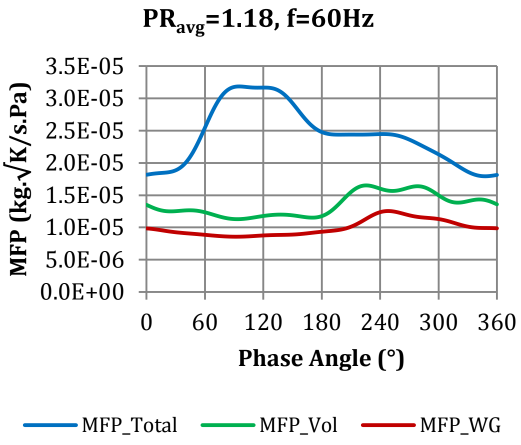

PR_{avg}=1.18, f=60Hz

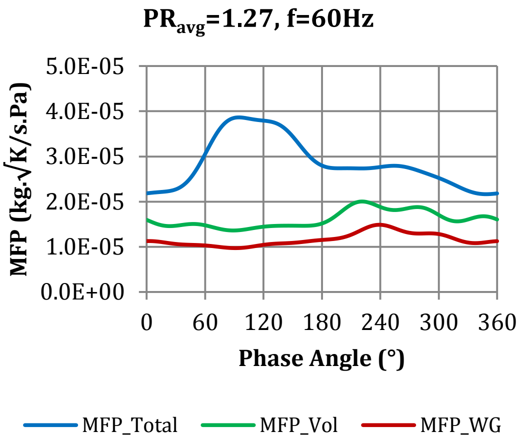

PR_{avg}=1.27, f=60Hz

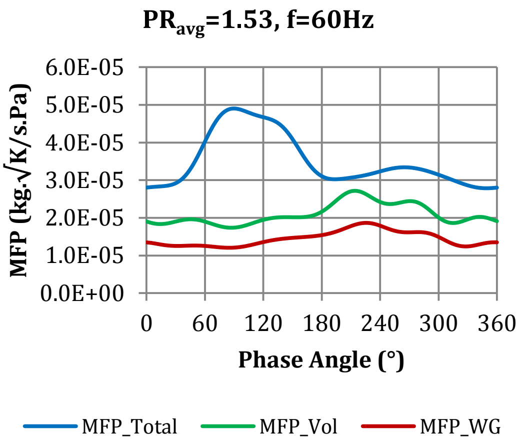

PR_{avg}=1.53, f=60Hz

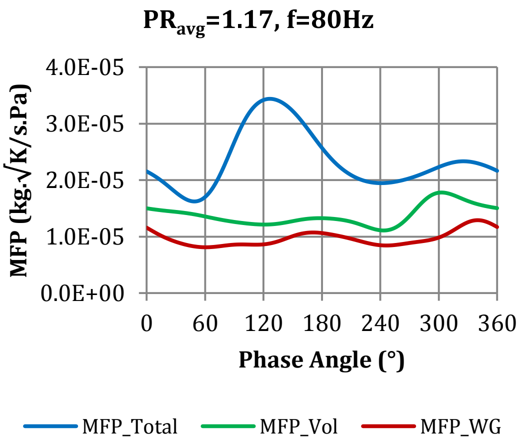

PR_{avg}=1.17, f=80Hz

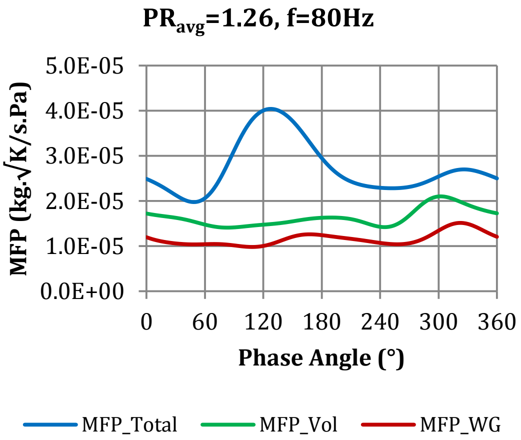

PR_{avg}=1.26, f=80Hz

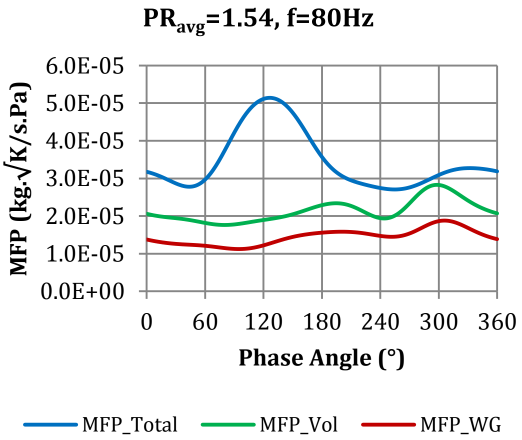

PR_{avg}=1.54, f=80Hz

G2. Instantaneous static pressure (P_s) measurements

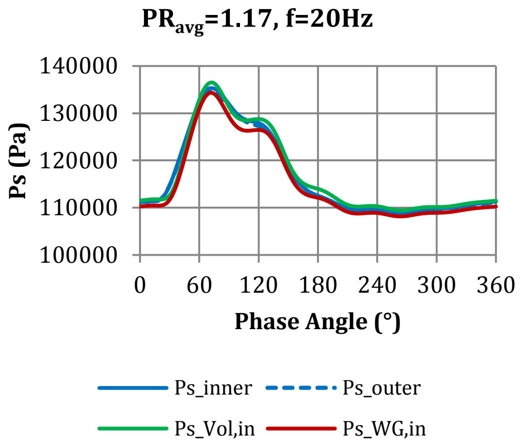

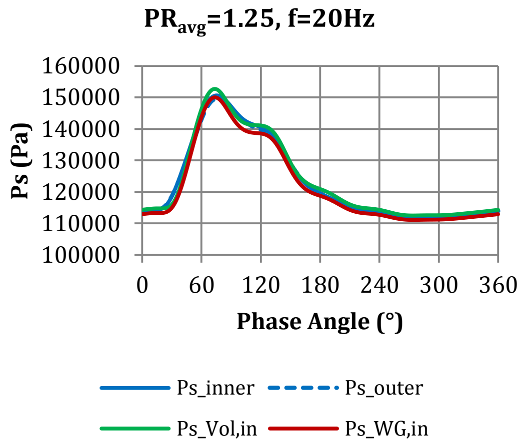

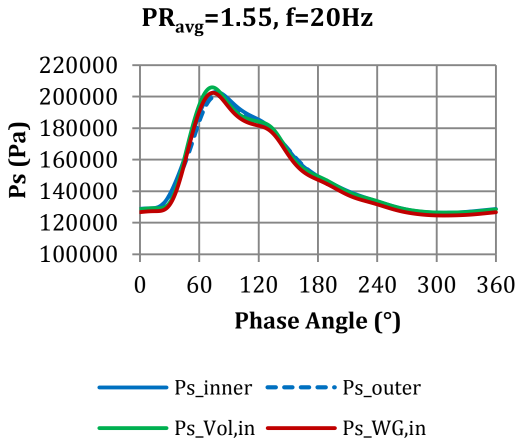

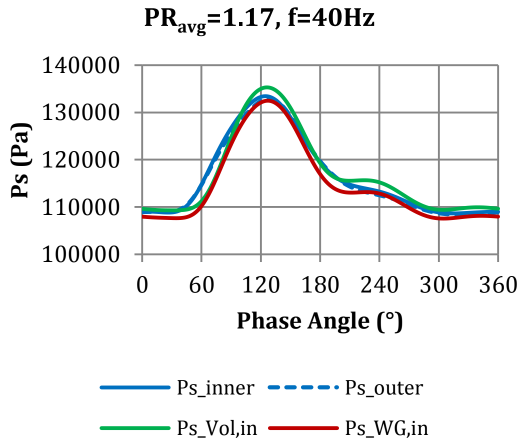

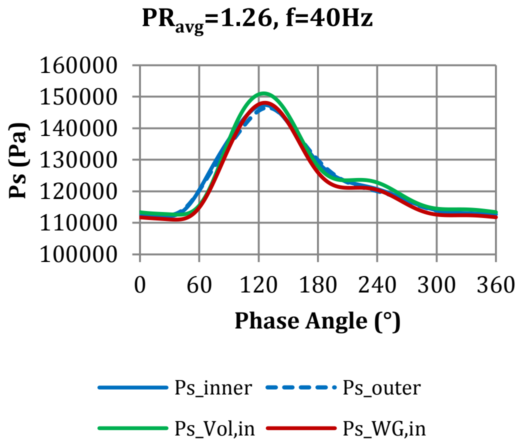

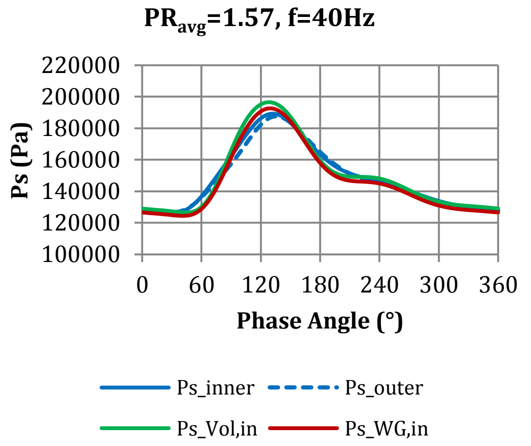

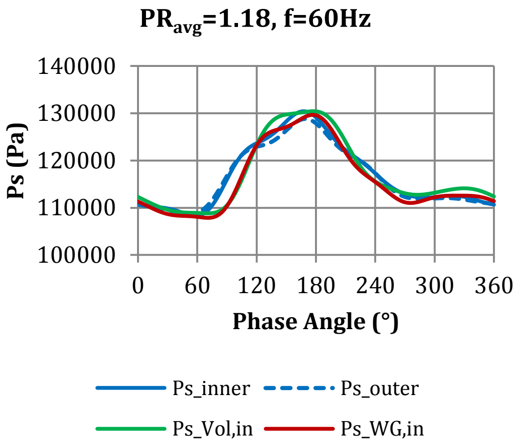
PR_avg=1.18, f=60Hz
Ps (Pa)
140000
130000
120000
110000
100000
0
60
120
180
240
300
360
Phase Angle (°)
Ps_inner
Ps_outer
Ps_Vol,in
Ps_WG,in

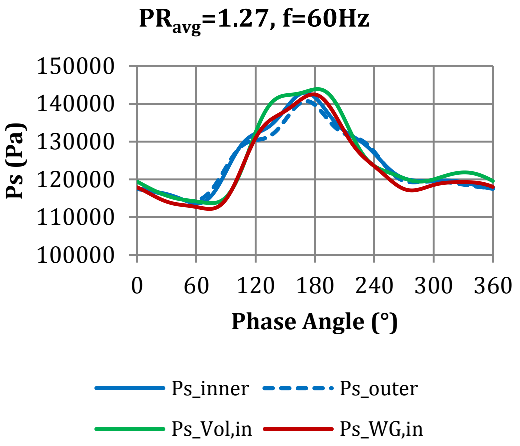
PR_avg=1.27, f=60Hz
Ps (Pa)
150000
140000
130000
120000
110000
100000
0
60
120
180
240
300
360
Phase Angle (°)
Ps_inner
Ps_outer
Ps_Vol,in
Ps_WG,in

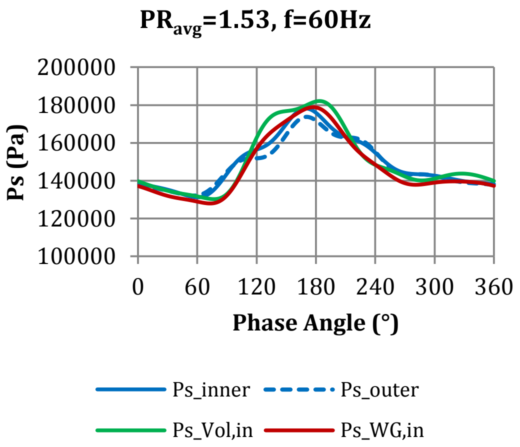
PR_avg=1.53, f=60Hz
Ps (Pa)
200000
180000
160000
140000
120000
100000
0
60
120
180
240
300
360
Phase Angle (°)
Ps_inner
Ps_outer
Ps_Vol,in
Ps_WG,in

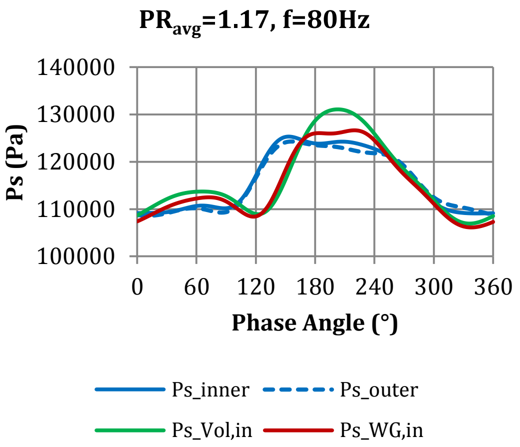
PR_avg=1.17, f=80Hz
Ps (Pa)
140000
130000
120000
110000
100000
0
60
120
180
240
300
360
Phase Angle (°)
Ps_inner
Ps_outer
Ps_Vol,in
Ps_WG,in

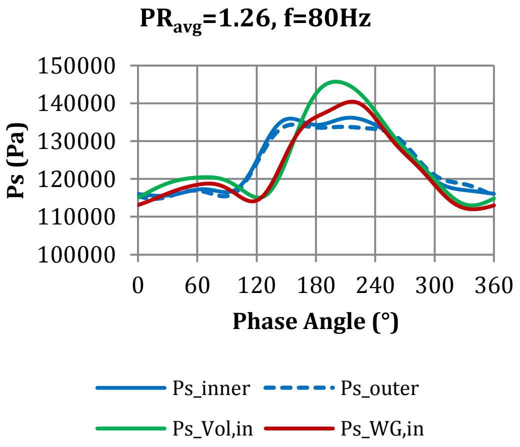
PR_avg=1.26, f=80Hz
Ps (Pa)
150000
140000
130000
120000
110000
100000
0
60
120
180
240
300
360
Phase Angle (°)
Ps_inner
Ps_outer
Ps_Vol,in
Ps_WG,in

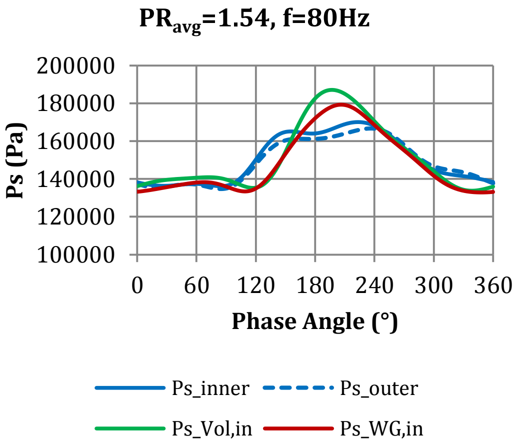
PR_avg=1.54, f=80Hz
Ps (Pa)
200000
180000
160000
140000
120000
100000
0
60
120
180
240
300
360
Phase Angle (°)
Ps_inner
Ps_outer
Ps_Vol,in
Ps_WG,in

G3. Instantaneous torque measurements

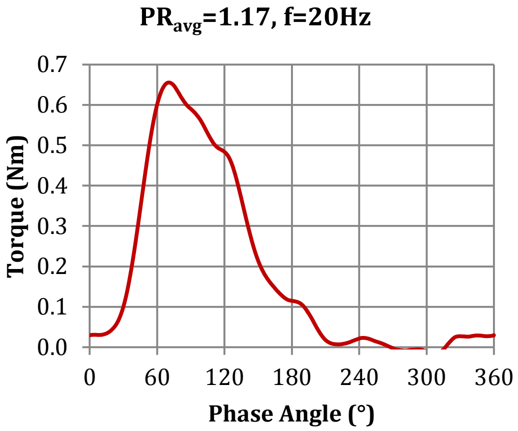
PR_{avg}=1.17, f=20Hz

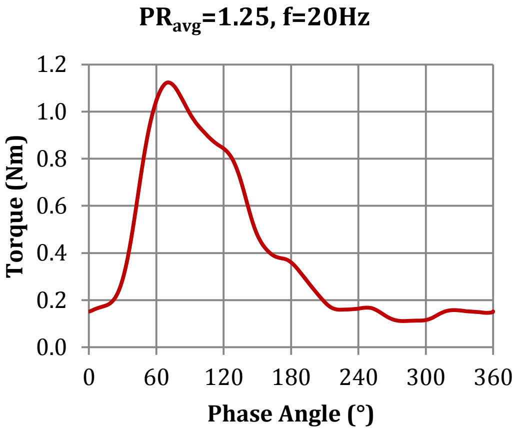
PR_{avg}=1.25, f=20Hz

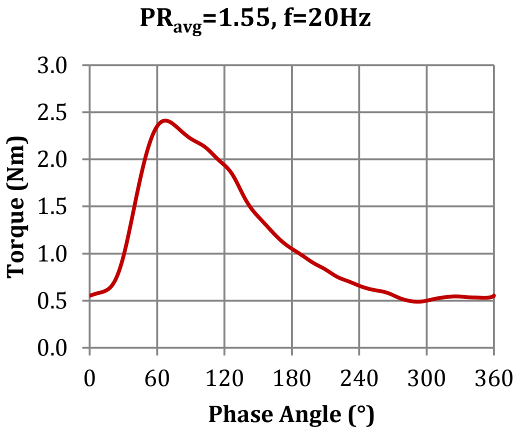
PR_{avg}=1.55, f=20Hz

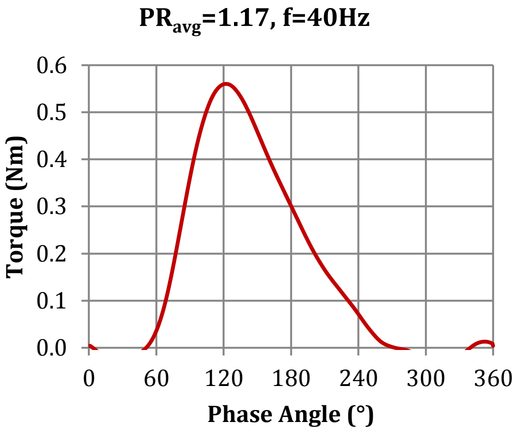
PR_{avg}=1.17, f=40Hz

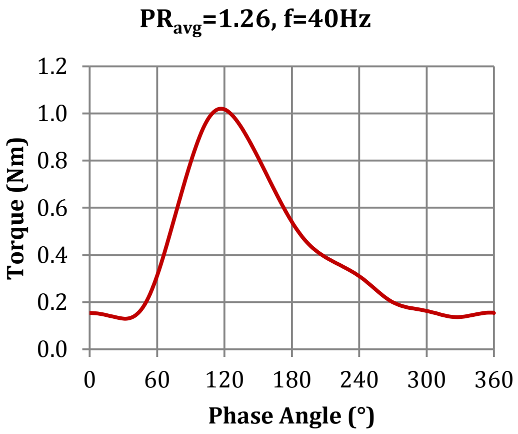
PR_{avg}=1.26, f=40Hz

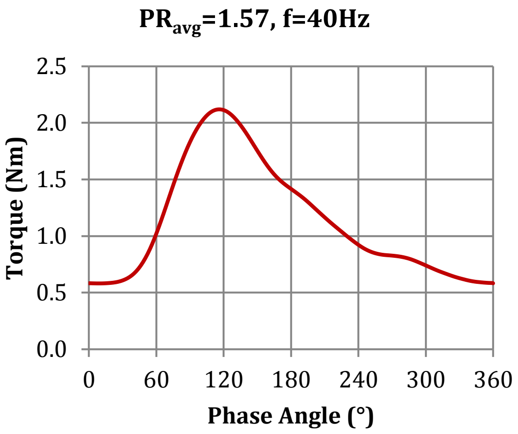
PR_{avg}=1.57, f=40Hz

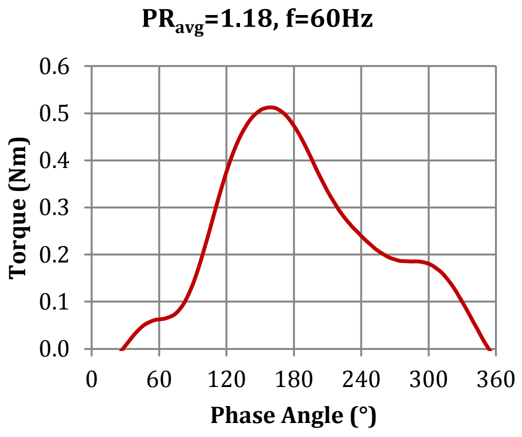
PR_{avg}=1.18, f=60Hz
Torque (Nm)
0.6
0.5
0.4
0.3
0.2
0.1
0.0
0
60
120
180
240
300
360
Phase Angle (°)

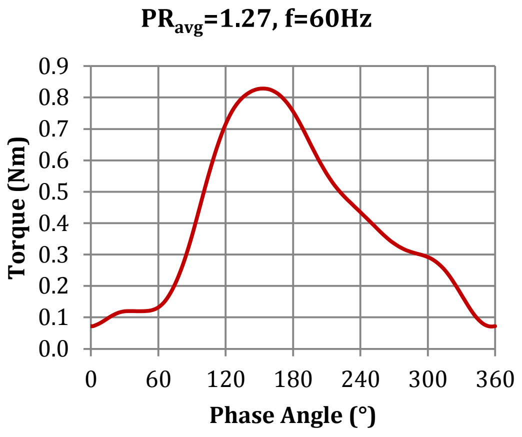
PR_{avg}=1.27, f=60Hz
Torque (Nm)
0.9
0.8
0.7
0.6
0.5
0.4
0.3
0.2
0.1
0.0
0
60
120
180
240
300
360
Phase Angle (°)

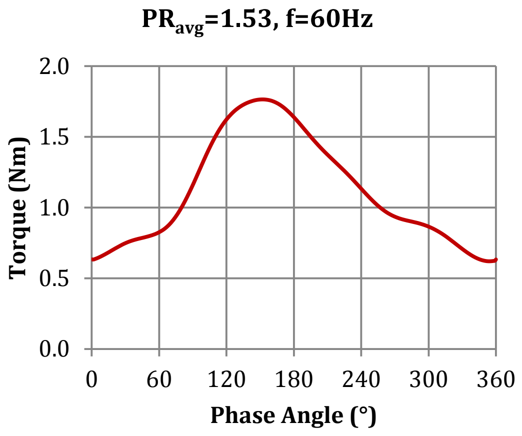
PR_{avg}=1.53, f=60Hz
Torque (Nm)
2.0
1.5
1.0
0.5
0.0
0
60
120
180
240
300
360
Phase Angle (°)

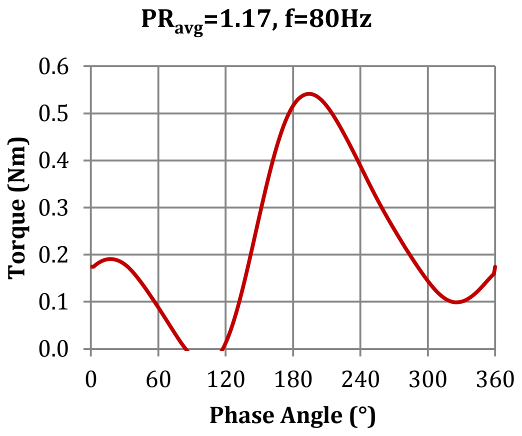
PR_{avg}=1.17, f=80Hz
Torque (Nm)
0.6
0.5
0.4
0.3
0.2
0.1
0.0
0
60
120
180
240
300
360
Phase Angle (°)

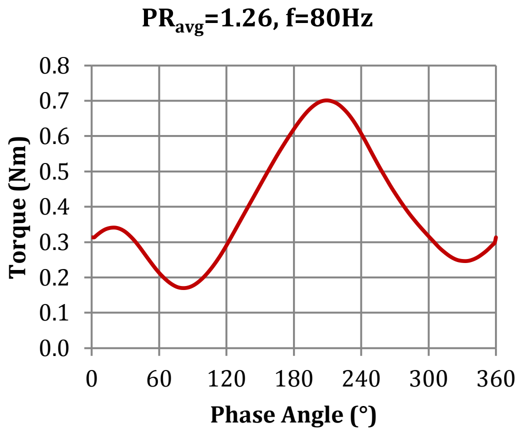
PR_{avg}=1.26, f=80Hz
Torque (Nm)
0.8
0.7
0.6
0.5
0.4
0.3
0.2
0.1
0.0
0
60
120
180
240
300
360
Phase Angle (°)

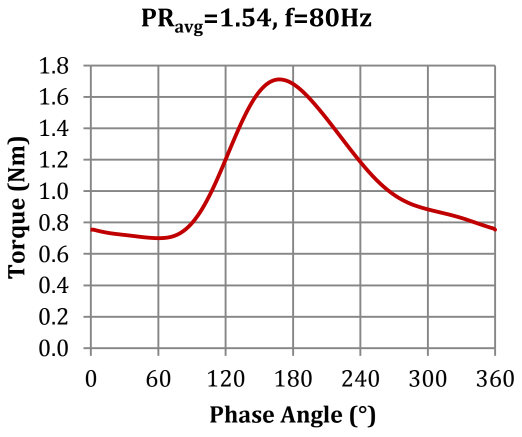
PR_{avg}=1.54, f=80Hz
Torque (Nm)
1.8
1.6
1.4
1.2
1.0
0.8
0.6
0.4
0.2
0.0
0
60
120
180
240
300
360
Phase Angle (°)

G4. Instantaneous power measurements

PR_{avg}=1.17, f=20Hz

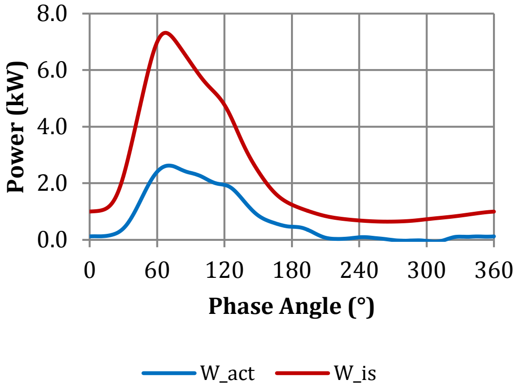

PR_{avg}=1.25, f=20Hz

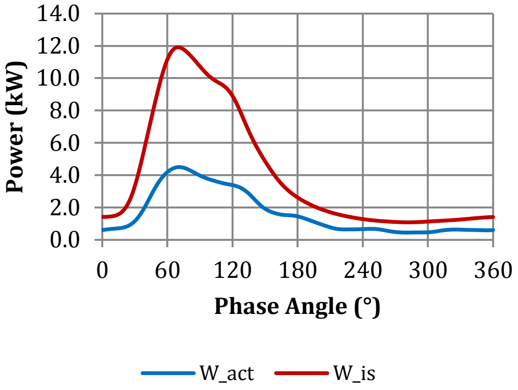

PR_{avg}=1.55, f=20Hz

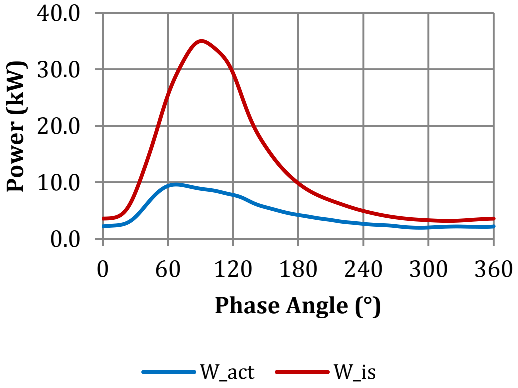

PR_{avg}=1.17, f=40Hz

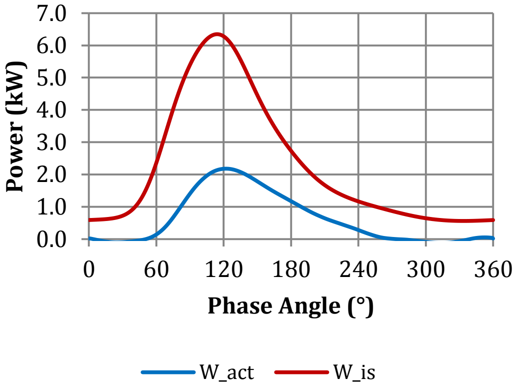

PR_{avg}=1.26, f=40Hz

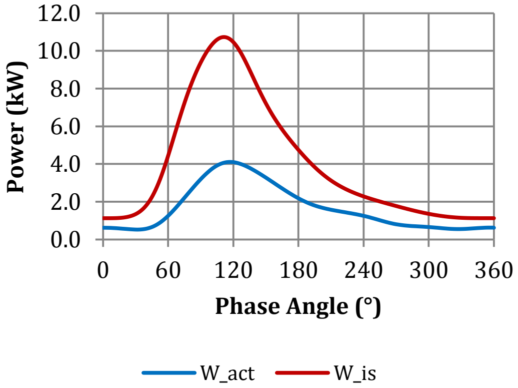

PR_{avg}=1.57, f=40Hz

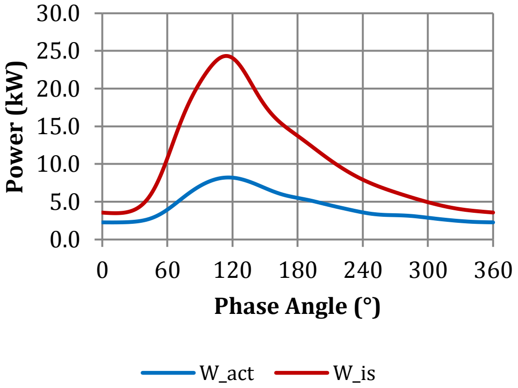

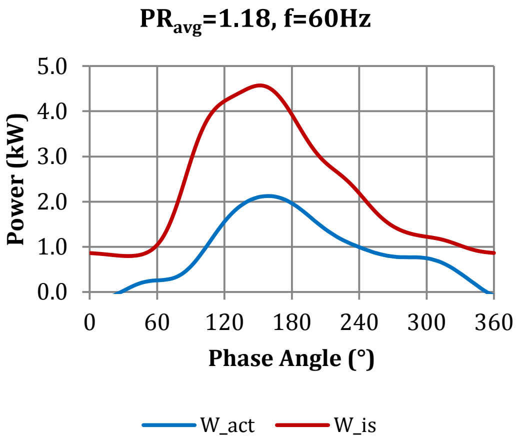
PR$_{avg}$=1.18, f=60Hz
Power (kW)
5.0
4.0
3.0
2.0
1.0
0.0
0
60
120
180
240
300
360
Phase Angle (°)
W_act
W_is

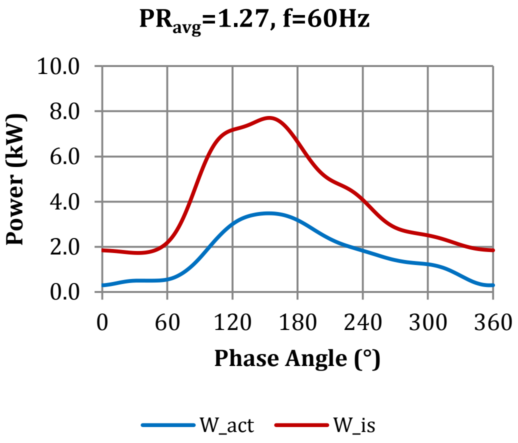
PR$_{avg}$=1.27, f=60Hz
Power (kW)
10.0
8.0
6.0
4.0
2.0
0.0
0
60
120
180
240
300
360
Phase Angle (°)
W_act
W_is

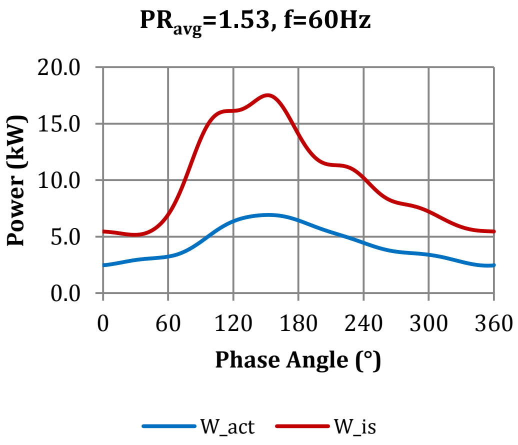
PR$_{avg}$=1.53, f=60Hz
Power (kW)
20.0
15.0
10.0
5.0
0.0
0
60
120
180
240
300
360
Phase Angle (°)
W_act
W_is

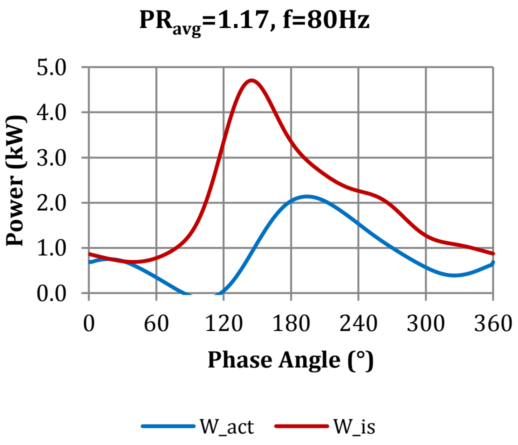
PR$_{avg}$=1.17, f=80Hz
Power (kW)
5.0
4.0
3.0
2.0
1.0
0.0
0
60
120
180
240
300
360
Phase Angle (°)
W_act
W_is

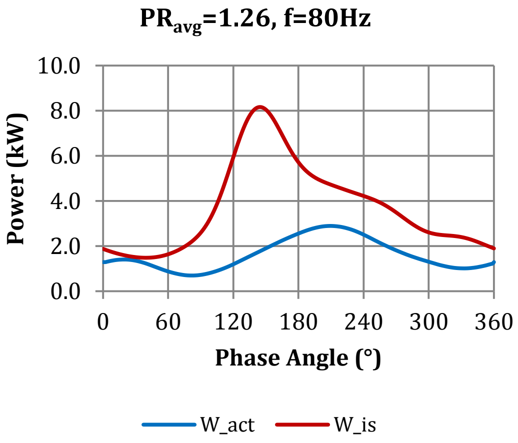
PR$_{avg}$=1.26, f=80Hz
Power (kW)
10.0
8.0
6.0
4.0
2.0
0.0
0
60
120
180
240
300
360
Phase Angle (°)
W_act
W_is

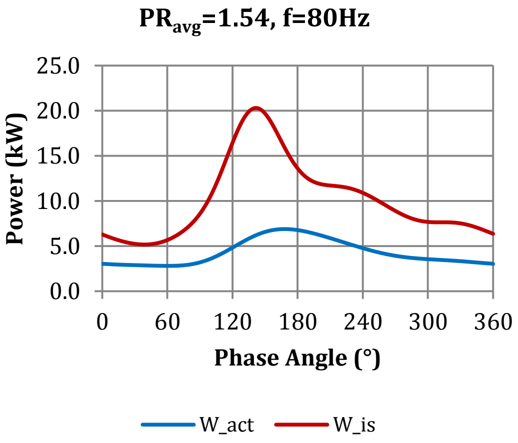
PR$_{avg}$=1.54, f=80Hz
Power (kW)
25.0
20.0
15.0
10.0
5.0
0.0
0
60
120
180
240
300
360
Phase Angle (°)
W_act
W_is

APPENDIX H

UNSTEADY FLOW EXPERIMENTS ($N/\sqrt{T_0}$ = 2146 RPM/$\sqrt{K}$, l_{WG} = 5 mm)

H1. Instantaneous mass flow parameter (MFP) measurements

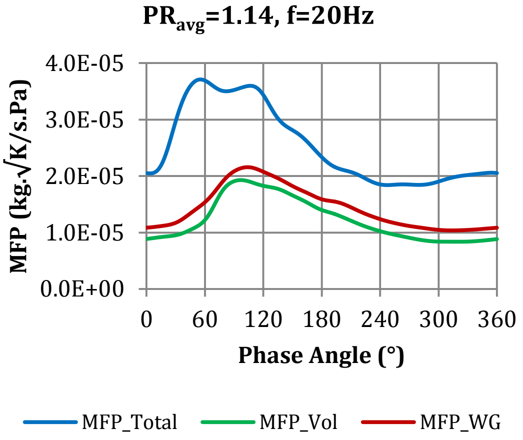

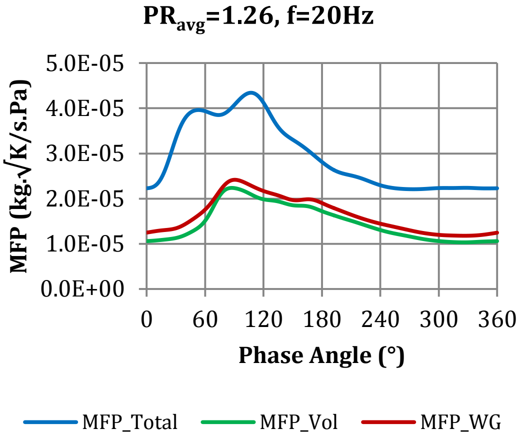

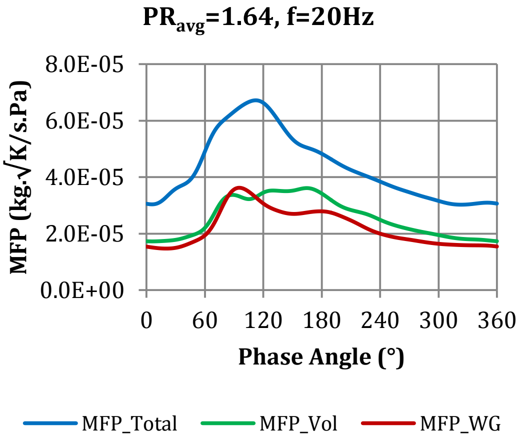

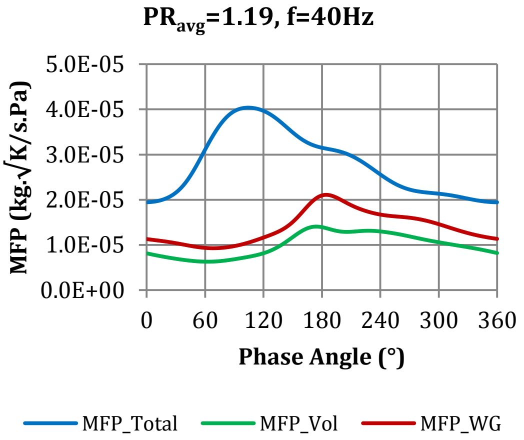

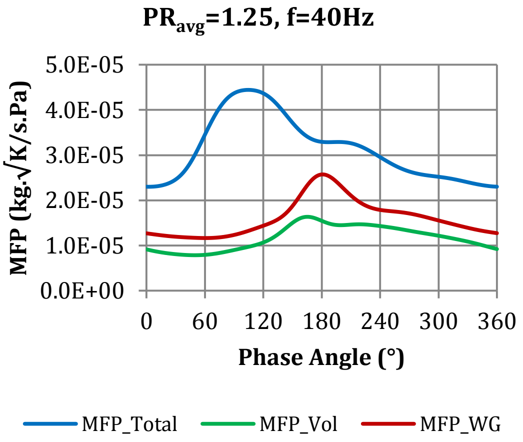

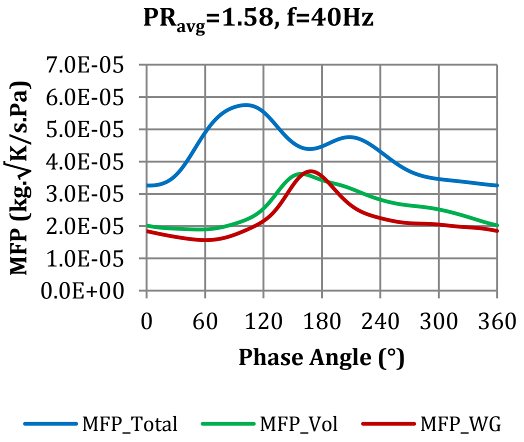

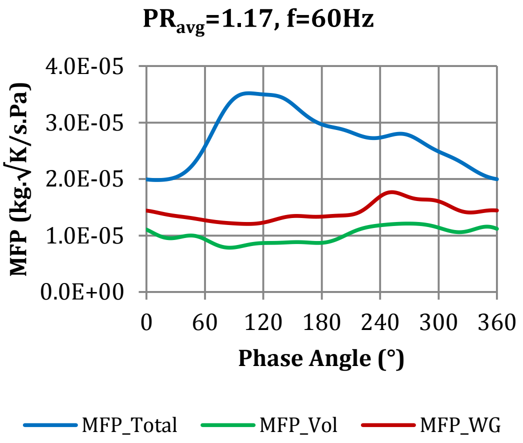
PR$_{avg}$=1.17, f=60Hz

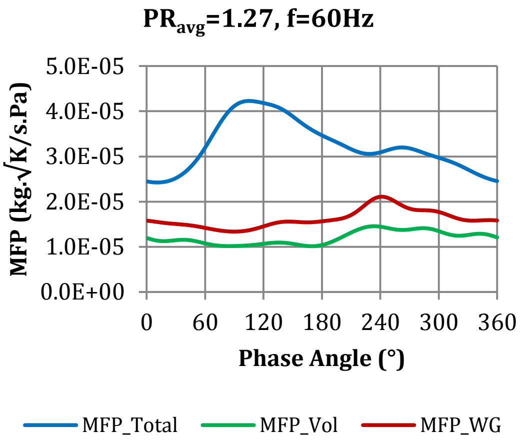
PR$_{avg}$=1.27, f=60Hz

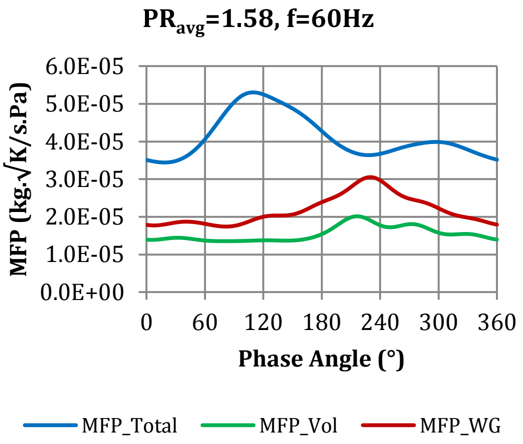
PR$_{avg}$=1.58, f=60Hz

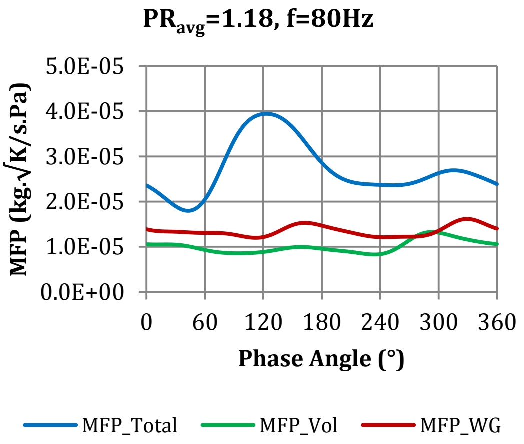
PR$_{avg}$=1.18, f=80Hz

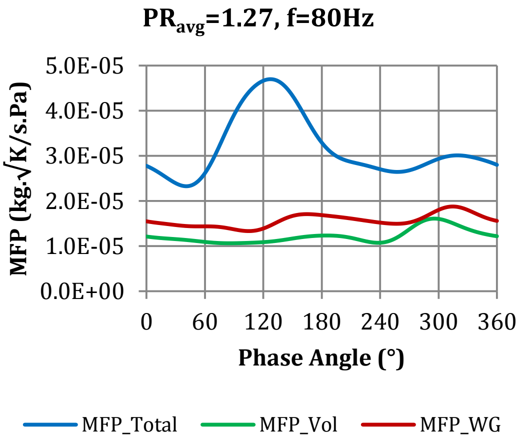
PR$_{avg}$=1.27, f=80Hz

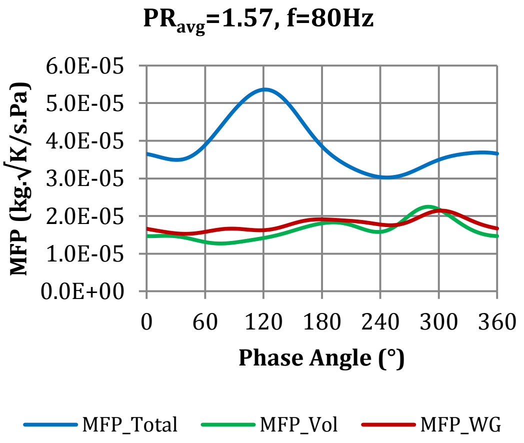
PR$_{avg}$=1.57, f=80Hz

H2. Instantaneous static pressure (P_s) measurements

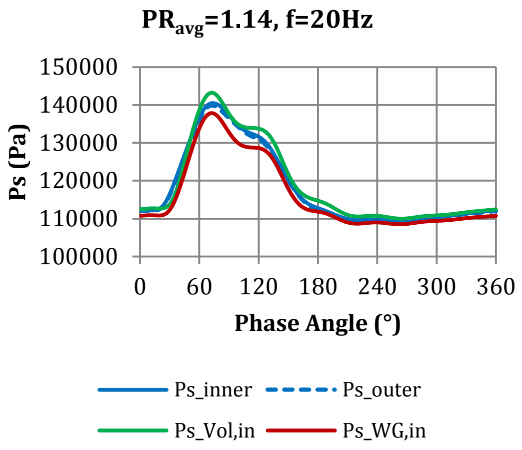

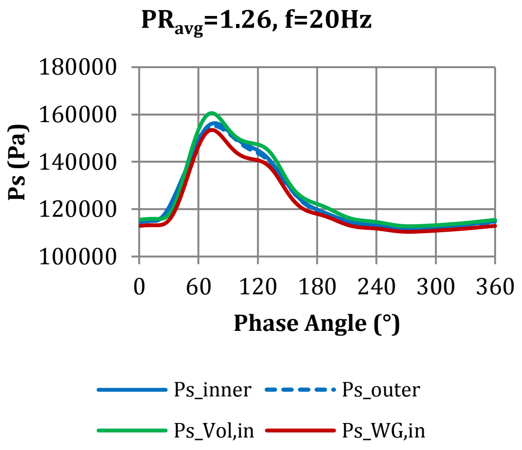

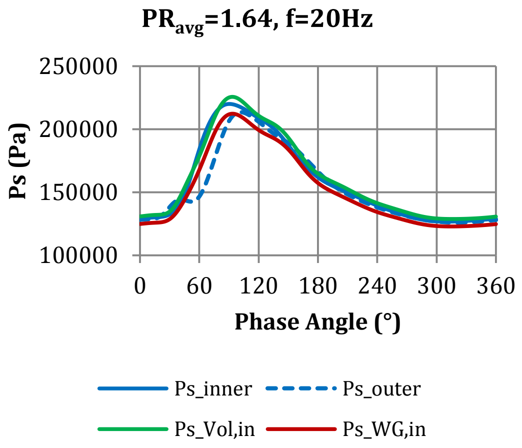

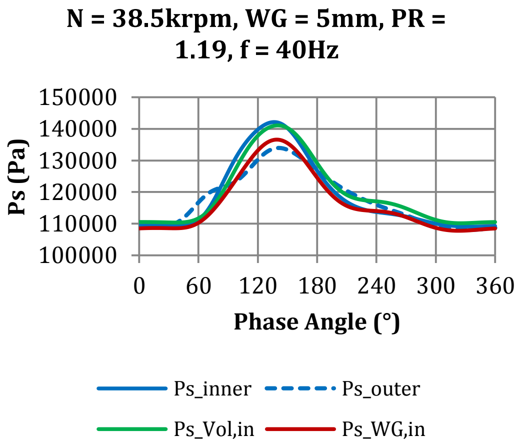

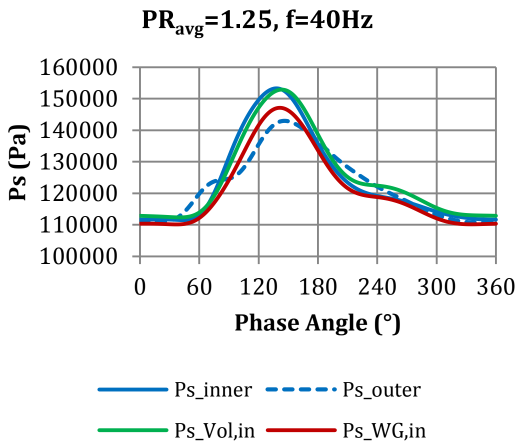

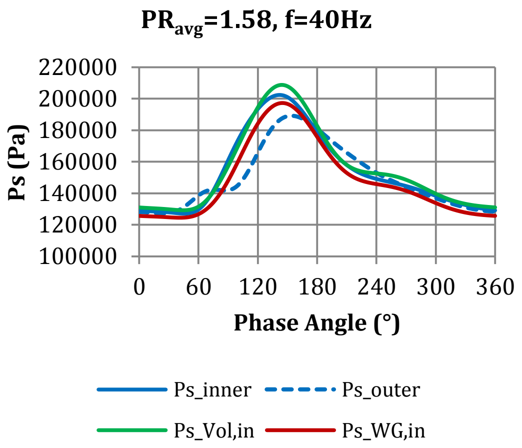

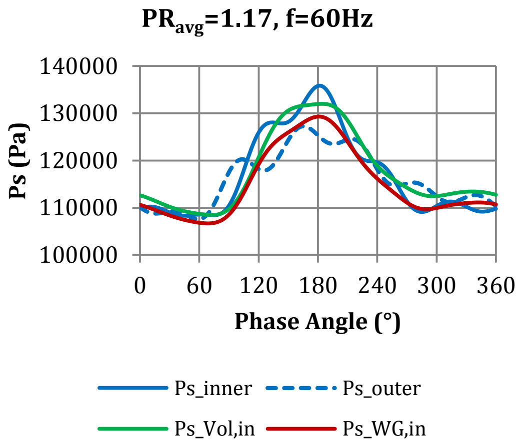
PRavg=1.17, f=60Hz
Ps (Pa)
140000
130000
120000
110000
100000
0
60
120
180
240
300
360
Phase Angle (°)
Ps_inner
Ps_outer
Ps_Vol,in
Ps_WG,in

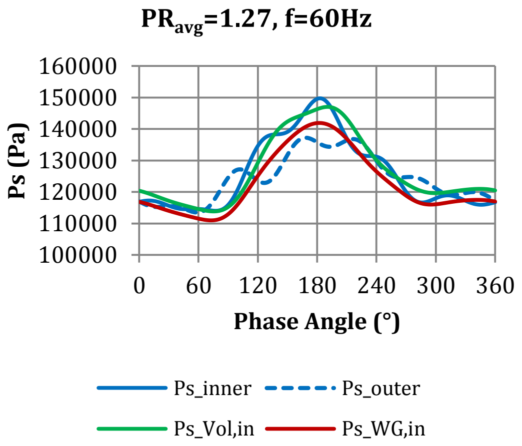
PRavg=1.27, f=60Hz
Ps (Pa)
160000
150000
140000
130000
120000
110000
100000
0
60
120
180
240
300
360
Phase Angle (°)
Ps_inner
Ps_outer
Ps_Vol,in
Ps_WG,in

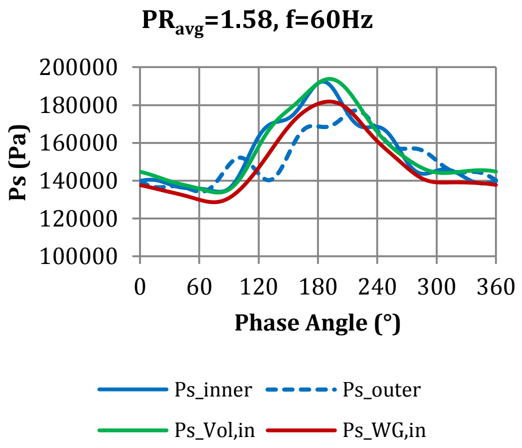
PRavg=1.58, f=60Hz
Ps (Pa)
200000
180000
160000
140000
120000
100000
0
60
120
180
240
300
360
Phase Angle (°)
Ps_inner
Ps_outer
Ps_Vol,in
Ps_WG,in

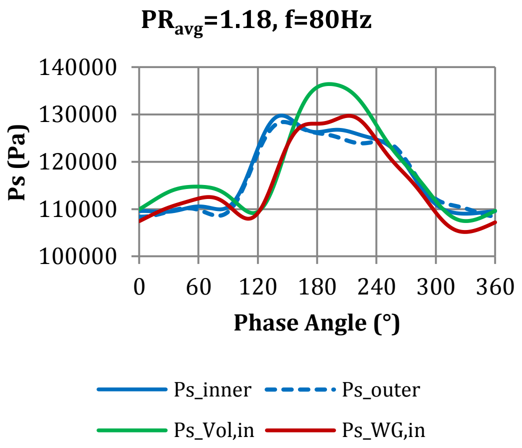
PRavg=1.18, f=80Hz
Ps (Pa)
140000
130000
120000
110000
100000
0
60
120
180
240
300
360
Phase Angle (°)
Ps_inner
Ps_outer
Ps_Vol,in
Ps_WG,in

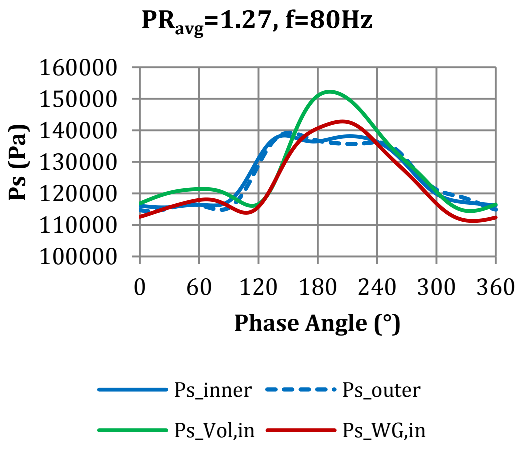
PRavg=1.27, f=80Hz
Ps (Pa)
160000
150000
140000
130000
120000
110000
100000
0
60
120
180
240
300
360
Phase Angle (°)
Ps_inner
Ps_outer
Ps_Vol,in
Ps_WG,in

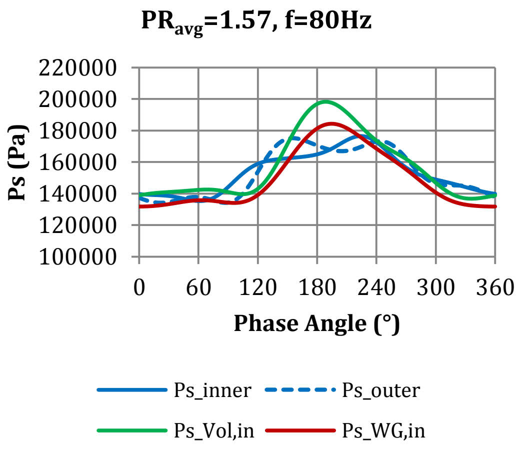
PRavg=1.57, f=80Hz
Ps (Pa)
220000
200000
180000
160000
140000
120000
100000
0
60
120
180
240
300
360
Phase Angle (°)
Ps_inner
Ps_outer
Ps_Vol,in
Ps_WG,in

H3. Instantaneous torque measurements

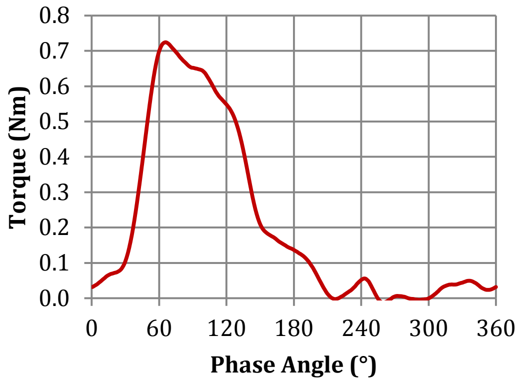
PR_{avg}=1.14, f=20Hz

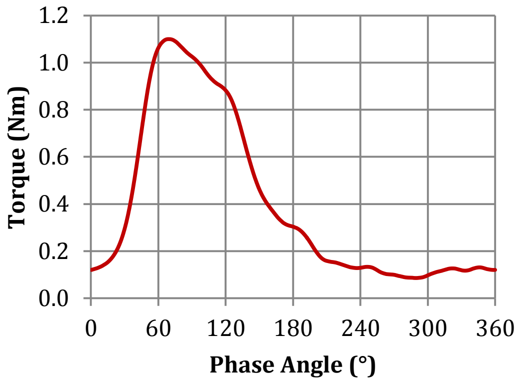
PR_{avg}=1.26, f=20Hz

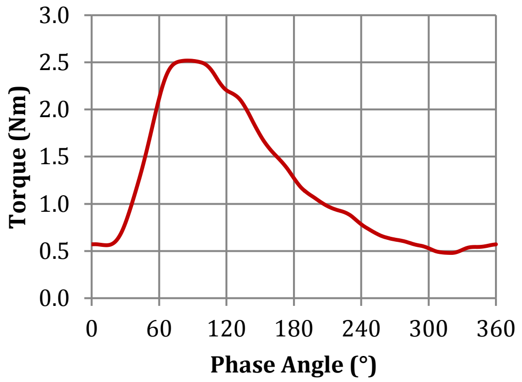
PR_{avg}=1.64, f=20Hz

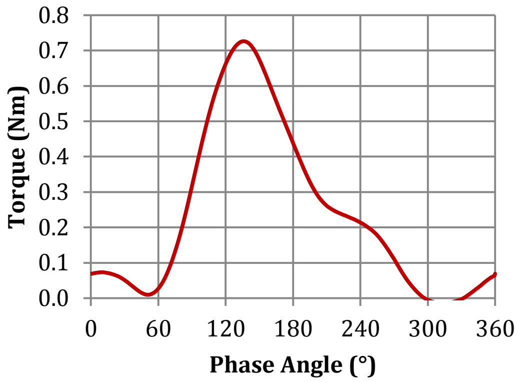
PR_{avg}=1.19, f=40Hz

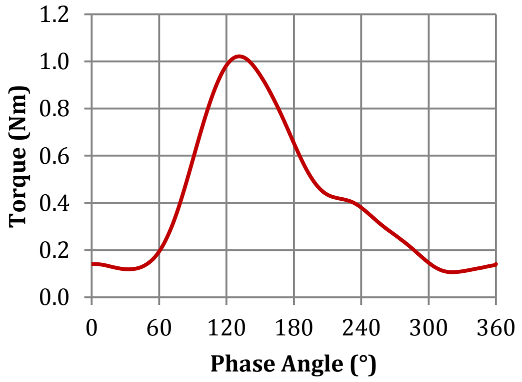
PR_{avg}=1.25, f=40Hz

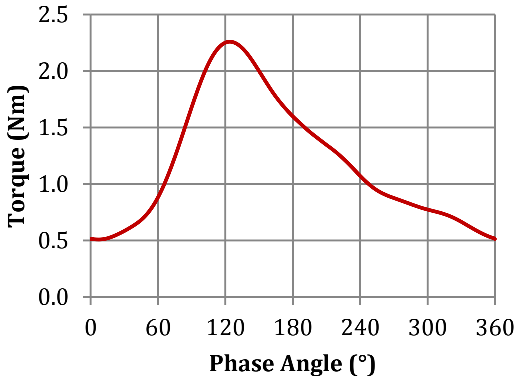
PR_{avg}=1.58, f=40Hz

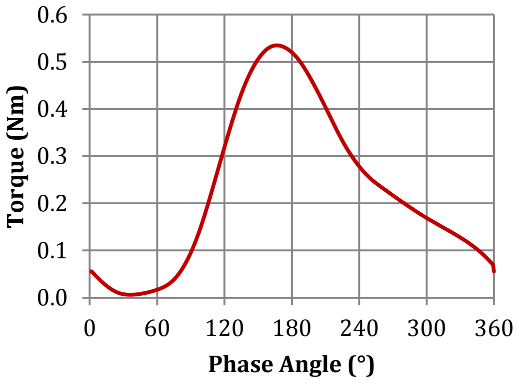
PR$_{avg}$=1.17, f=60Hz

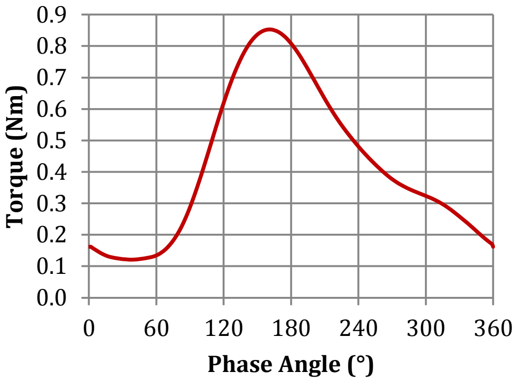
PR$_{avg}$=1.27, f=60Hz

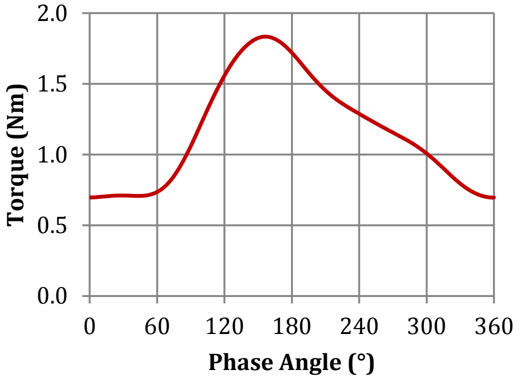
PR$_{avg}$=1.58, f=60Hz

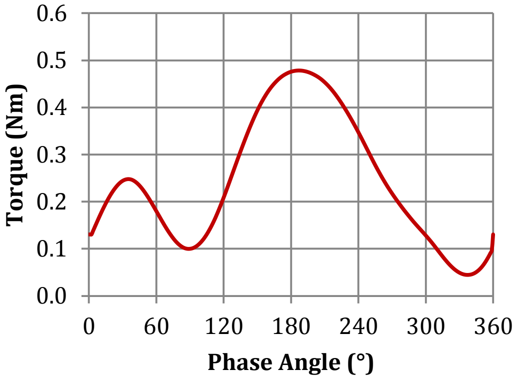
PR$_{avg}$=1.18, f=80Hz

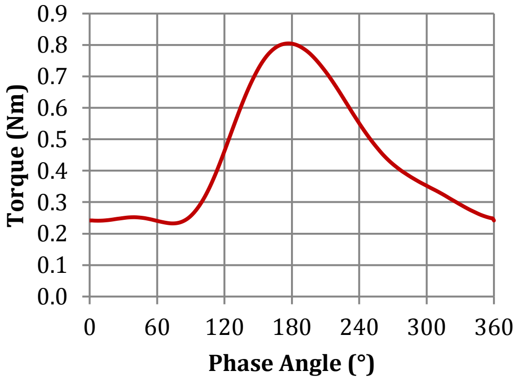
PR$_{avg}$=1.27, f=80Hz

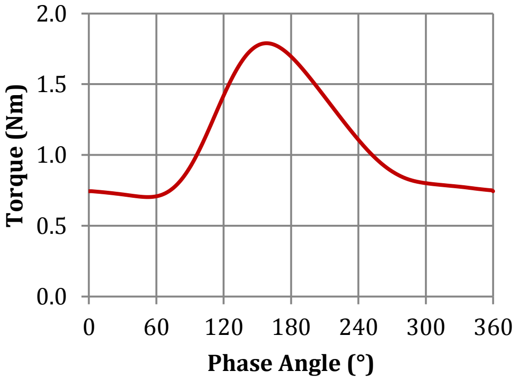
PR$_{avg}$=1.57, f=80Hz

H4. Instantaneous power measurements

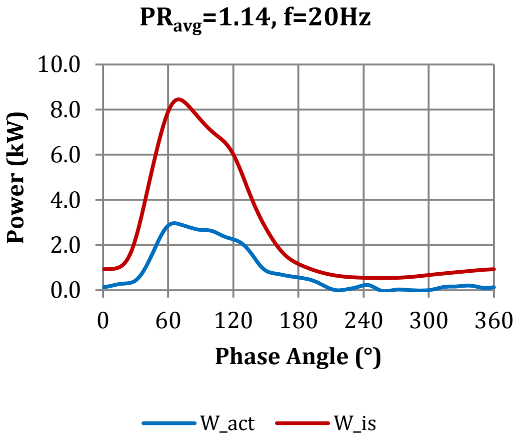

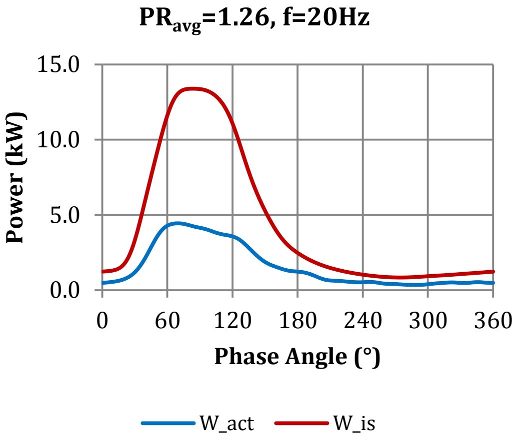

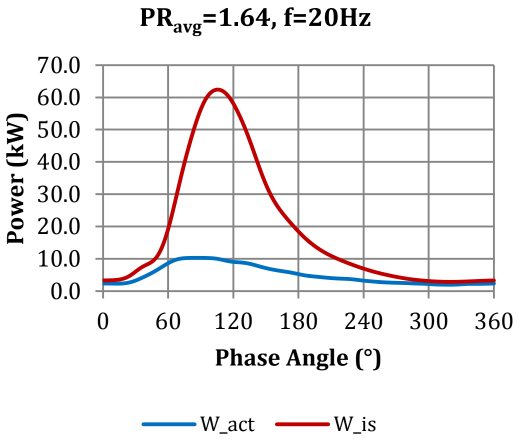

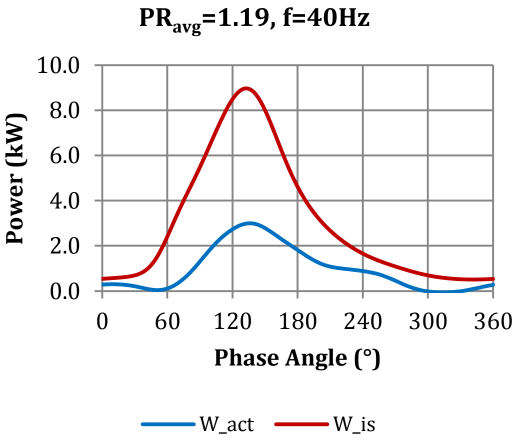

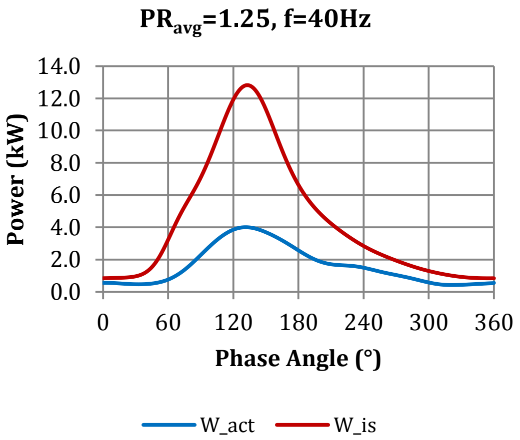

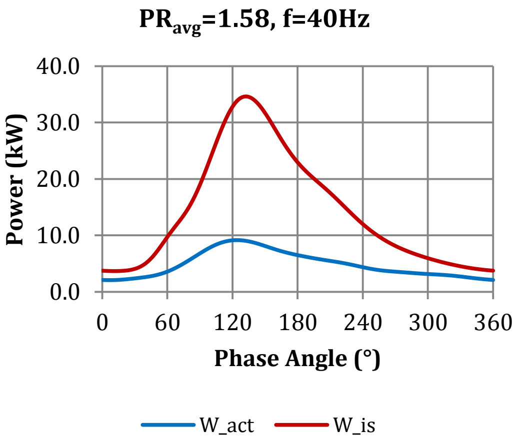

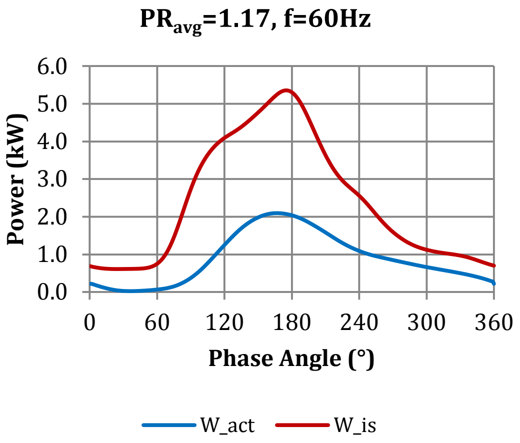
PR$_{avg}$=1.17, f=60Hz
Power (kW)
6.0
5.0
4.0
3.0
2.0
1.0
0.0
0
60
120
180
240
300
360
Phase Angle (°)
W_act
W_is

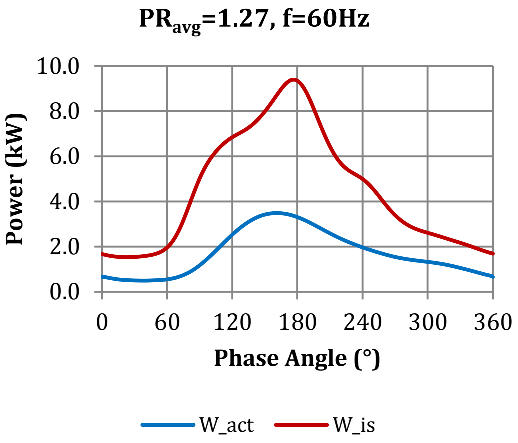
PR$_{avg}$=1.27, f=60Hz
Power (kW)
10.0
8.0
6.0
4.0
2.0
0.0
0
60
120
180
240
300
360
Phase Angle (°)
W_act
W_is

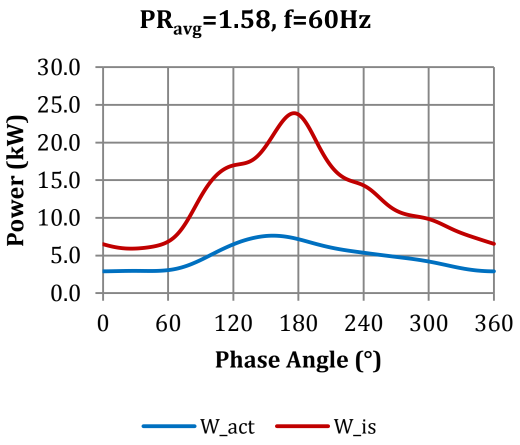
PR$_{avg}$=1.58, f=60Hz
Power (kW)
30.0
25.0
20.0
15.0
10.0
5.0
0.0
0
60
120
180
240
300
360
Phase Angle (°)
W_act
W_is

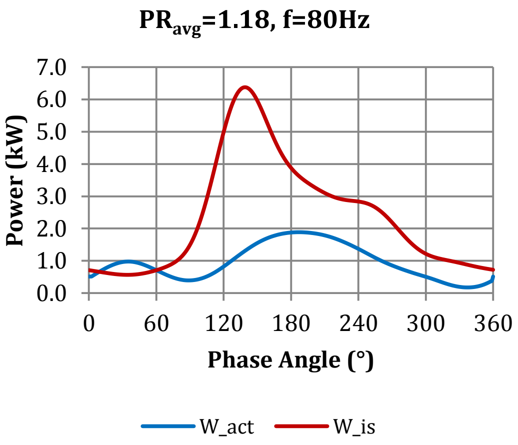
PR$_{avg}$=1.18, f=80Hz
Power (kW)
7.0
6.0
5.0
4.0
3.0
2.0
1.0
0.0
0
60
120
180
240
300
360
Phase Angle (°)
W_act
W_is

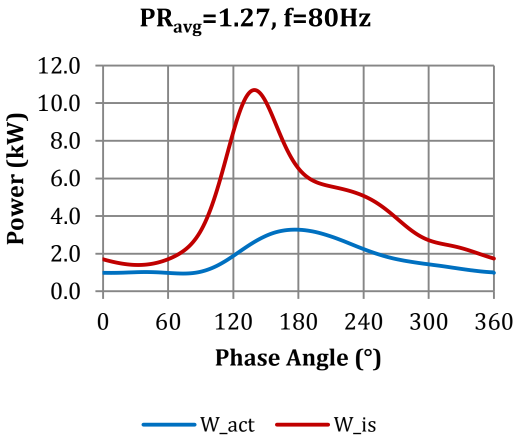
PR$_{avg}$=1.27, f=80Hz
Power (kW)
12.0
10.0
8.0
6.0
4.0
2.0
0.0
0
60
120
180
240
300
360
Phase Angle (°)
W_act
W_is

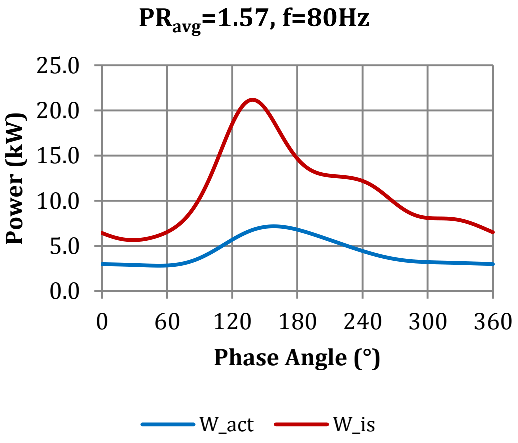
PR$_{avg}$=1.57, f=80Hz
Power (kW)
25.0
20.0
15.0
10.0
5.0
0.0
0
60
120
180
240
300
360
Phase Angle (°)
W_act
W_is

APPENDIX I

I 1 The Measure of Turbine Unsteadiness

It was shown in Chapter 4 that turbine behaviour under pulsating inlet conditions is not quasi-steady in nature. This then begs another question as to how the level of unsteadiness can quantified. Since the quasi-steady assumption is widely applied in turbocharger matching procedures, an estimate for the level of unsteadiness in turbine operation can act as an indicator as to how accurate and reliable the matching process is.

I 1.1 Influence Factor

In view of this, it seems that the most intuitive approach would be to have a parameter that relates the performance of the turbine under unsteady and steady state conditions. On this basis, a parameter called the influence factor (I), which is the ratio of the unsteady parameter to its quasi-steady prediction on a cycle-average basis was proposed by Benson (1974) and was used in the work of Capobianco and Marelli (2010) and Newton (2013). For mass flow, the influence factor (I_{MFP}) is calculated by taking the average mass flow over a pulse cycle and dividing it with the average quasi-steady mass flow as follows:

$$I_{MFP} = \frac{\overline{MFP}_{cyc,US}}{\overline{MFP}_{cyc,QS}} \quad \text{... (I.1);}$$

where $\overline{MFP}_{cyc,US}$ and $\overline{MFP}_{cyc,QS}$ denotes the cycle average value of the measured mass flow parameter and the calculated quasi-steady values respectively. This parameter can also be extended to evaluate other turbine performance parameters such as torque and efficiency.

I 1.2 Strouhal Number

In consideration of unsteady effects within the system, several authors have utilized the dimensionless parameter Strouhal number (St), or its derivatives as means to characterize the unsteadiness of turbine behaviour (Szymko, 2006, Rajoo, 2007, Mamat, 2012 and Newton, 2013). The standard form of this dimensionless parameter is given by:

$$St = \frac{fL_c}{\bar{U}} = \frac{T}{t} \quad \text{... (I.2);}$$

where, f is the frequency of the oscillation, L_c is the characteristic length, $\overline{U}$ is the reference velocity obtained as the cycle average flow velocity from the knowledge of mass flow rate and the flow area. Strouhal number can also be expressed as the ratio of time taken for a fluid to travel over a length at a given velocity (T) to the time associated with the oscillation frequency (t). In its conservative use, a value of 0.1 is perceived as the limit where unsteady effects become significant on the flow.

A normalized version of Strouhal number is presented by Szymko by introducing a factor ϕ to incorporate the pulse event over a wavelength. This is taken as 0.5, which indicates that the pulse event encompasses one half of the entire cycle wavelength. The normalized Strouhal number (St^*) is therefore expressed as follows:

$$St^* = \frac{fL_c}{\overline{U}}\frac{1}{2\phi} \quad \ldots \text{(I.3)};$$

where ϕ is the pulse period fraction over the pulse cycle.

I 1.3 Amplitude-Weighted Strouhal Number (Ω)

The experimental results discussed above reveals that the unsteadiness of the turbine behaviour under pulsating inlet conditions is dependent not only on the frequency of the pulse, but also the amplitude of the fluctuating parameters as in the case of varying turbine loads and waste-gate area openings. The effect of amplitude on the level of unsteadiness was pointed out by Copeland et al (2012).

Newton (2013) developed a parameter referred to here as the amplitude-weighted Strouhal number (Ω), which incorporates the effects of fluctuating amplitudes in the prediction of unsteadiness. By implementing an order of magnitude analysis on the mass flow rate and the periodic change of mass within a fluid domain, a weighting factor (Π) is introduced in the calculation of Strouhal number. This is given in the expression below:

$$\Omega = \frac{2\Delta\rho_{in}}{\rho_{ref}}.St \quad \ldots \text{(I.4)};$$

where $\Delta\rho$ and ρ_{ref} is the amplitude of density and reference density respectively. For an adiabatic system, the density term may be interchanged with pressure giving the final form of the expression as:

$$\Omega = \frac{2\Delta P_{in}}{P_{ref}}.St = \Pi.St \ \ldots \text{(I.5)}$$

For the calculation of this parameter, the reference pressure is taken as the cycle average static pressure over a pulse.

I 2 Analysis on the Level of Unsteadiness

It is now possible to assess the level of unsteadiness based on the evaluation of the amplitude-weighted Strouhal number above for test conditions discussed in the preceding sections. For the sake of comparison, the influence factor (I_{MFP}) values are also calculated and included in the analysis.

I 2.1 Effect of waste-gate opening

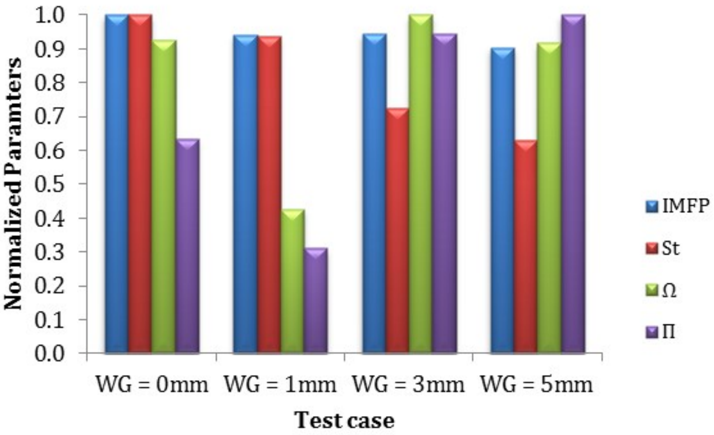

Figure I.1 Histogram showing normalized values of unsteady parameters for different waste-gate area openings at 2146 RPM/√K speed parameter and 1.25 mean pressure ratio

Figure I.1 shows the normalized values of unsteady parameters, namely I_{MFP}, St and Ω for evaluation of the effect of waste-gate area opening on unsteadiness. The values of each parameter are normalized by their maximum so that the unsteadiness level predicted by the different parameters may be compared relative to each other. The calculated values of the parameters are shown in Table I.1. The weighting factor Π is also included for reference. For this analysis, the case of the turbine tested at 2146 RPM/√K with constant load ($PR \approx 1.25$) and pulse frequency (*f*=20Hz) is revisited. The values of influence factor evaluated based on quasi-steady analysis do not indicate a significant change in the level of unsteadiness. The values of Strouhal number decrease with valve lift due to the flow velocity being higher as a result of the increase in mass flow rate at opened waste-gate conditions. On the other hand, the level of unsteadiness represented by the parameter Ω does not show any notable trend. Ω is seen to fall initially from closed waste-gate to 1.0 mm valve lift condition and then increase to a maximum value at 3.0mm and decrease again at 5.0mm valve lifts. The weighting factor, Π, being largest at 5.0mm opening does not yield the highest value of Ω due to the relatively small contribution of Strouhal number at this setting.

Table I.1 Unsteady parameters calculated for different valve lifts

Waste-gate valve lift	I_{MFP}	***St****	**Ω**	**Π**
l_{wg} = 0mm	1.1052	0.6313	0.1701	0.2695
l_{wg} = 1mm	1.0400	0.5911	0.0783	0.1325
l_{wg} = 3mm	1.0447	0.4582	0.1838	0.4011
l_{wg} = 5mm	0.9985	0.3971	0.1687	0.4249

I 2.2 Effect of pulse frequency

The effect of frequency on the unsteady parameters is presented in Figure I.2 with the calculated values of the corresponding parameters in Table I.2. The unsteadiness levels are evaluated for closed (l_{wg} = 0mm) and opened waste-gated conditions at 3.0 mm valve lift for the same speed and mean turbine load. It can be seen that there is no significant change in the calculated influence factor for all the cases shown. Here, the impact of frequency is most notable on Strouhal number with the values being higher as frequency is increased.

For the closed waste-gate case, the weighting factor describing mass imbalance at 40Hz pulse frequency is the highest accompanied by the highest predicted unsteadiness level (Ω). The other frequencies in the closed waste-gate condition show similar values of weighting factor. For the 3.0mm lift waste-gated condition, the weighting factor is seen to decrease as the frequency increases. In this case, at low frequency, where the weighting factor is large, Ω is relatively low suggesting that the unsteadiness is less influenced by the mass imbalance for the lower frequency waste-gated cases. At 60Hz, where the predicted level of unsteadiness is the highest according to the Ω criterion, it is seen that the contributions of Strouhal number and the weighting factor are similar. As the frequency increases further to 80Hz the value of Π falls significantly, this is compensated by an increase in Strouhal number leading to an overall similar value of Ω with the 60Hz case.

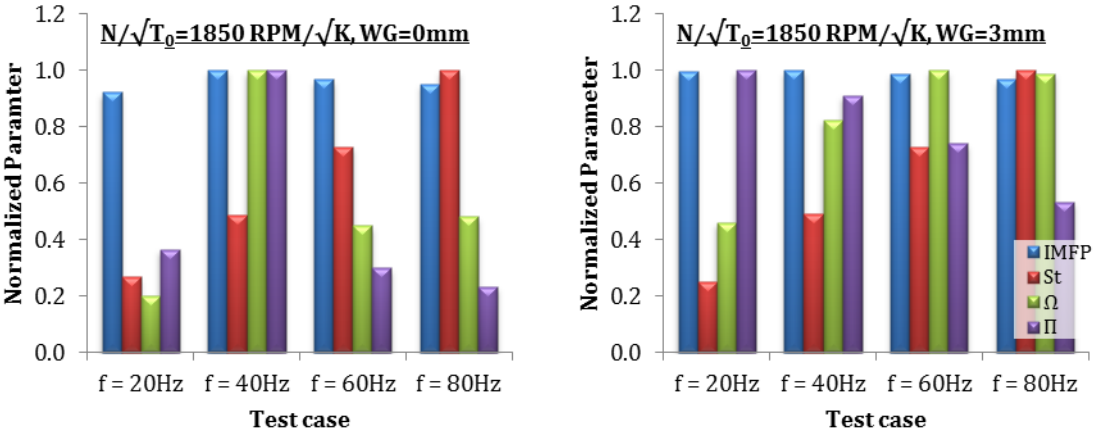

Figure I.2 Histogram showing normalized values of unsteady parameters for different pulse frequencies

Table I.2 Unsteady parameters calculated for different pulse frequencies for closed and opened waste-gate

Test Condition	**Pulse Frequency**	I_{MFP}	St^*	**Ω**	**Π**
Closed waste-gate	f = 20Hz	0.9969	0.3832	0.0963	0.2513
	f = 40Hz	1.0797	0.6972	0.4772	0.6845
	f = 60Hz	1.0466	1.0432	0.2154	0.2065
	f = 80Hz	1.0283	1.4290	0.2306	0.1613
Opened waste-gate (l_{wg} = 3mm)	f = 20Hz	1.0987	0.2376	0.0937	0.3944
	f = 40Hz	1.1016	0.4669	0.1678	0.3594
	f = 60Hz	1.0892	0.6940	0.2030	0.2925
	f = 80Hz	1.0670	0.9502	0.2006	0.2111

I 2.3 Effect of turbine load

Finally, the same analysis is carried out to investigate the unsteadiness level of the turbine at different loads. This is shown in Figure I.3 along with Table I.3 showing the values of each parameter.

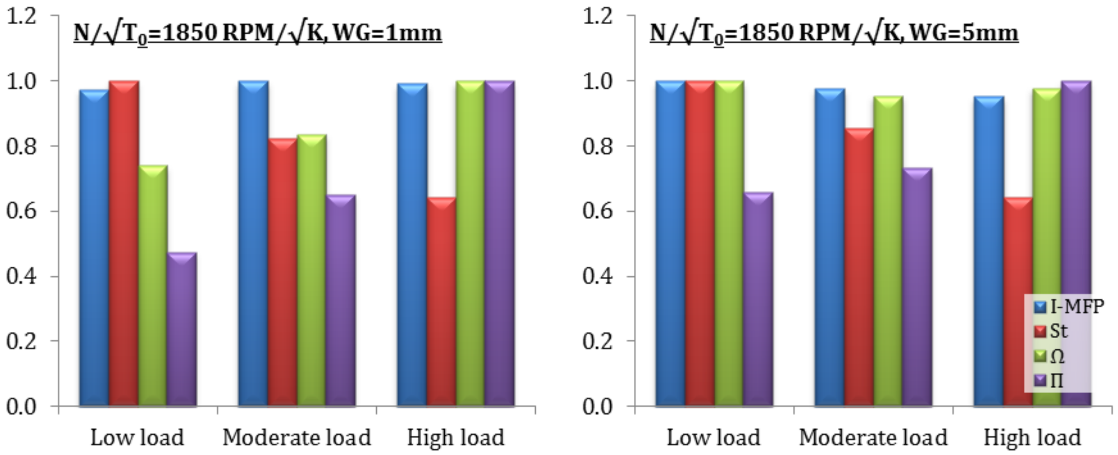

Figure I.3 Histogram showing normalized values of unsteady parameters for different mean turbine loads at two different waste-gate valve lifts

Table I.3 Unsteady parameters calculated for different turbine loads at two waste-gate valve lifts

	Turbine load	I_{MFP}	***St****	**Ω**	**Π**
WG = 1mm	Low load	1.009373	0.751618	0.155699	0.207152
	Moderate load	1.035869	0.61965	0.175785	0.283684
	High load	1.028477	0.482307	0.210406	0.436248
WG = 5mm	Low load	1.037458	1.046253	0.235121	0.224726
	Moderate load	1.011751	0.89317	0.224487	0.251337
	High load	0.988226	0.67235	0.230016	0.342107

Again, the calculated influence factor does not seem to signify any substantial change in the level of unsteadiness of the turbine. Strouhal numbers for both cases (1mm and 5mm lift) decrease with increasing turbine loads and this is attributed to increase in the contribution of mean flow velocity as the load is increased. At small waste-gate area opening (1.0 mm lift), the predicted level of unsteadiness is seen to increase with turbine load along with the weighting factor. This suggests that the unsteadiness of the turbine at this condition is largely influenced by the mass imbalance. At 5.0 mm waste-gate lift a similar trend is seen with Strouhal number decreasing and the weighting factor increasing with load. However, the predicted unsteadiness is relatively closer at different loads in the case of the 5.0 mm waste-gate lift. It can therefore be gathered that the effect of load on the level of unsteadiness is diminished at larger waste-gate openings.